UNIVERSITÀ DEGLI STUDI DI MILANO

Scuola di Dottorato in Fisica, Astrofisica e Fisica Applicata
Dipartimento di Fisica

Corso di Dottorato in Fisica, Astrofisica e Fisica Applicata
Ciclo XXXVI

Kinematics and dynamics of self-gravitating protostellar discs

Settore Scientifico Disciplinare FIS/05

Supervisore: Professor Giuseppe Lodato

Coordinatore: Professoressa Roberta Vecchi

Tesi di Dottorato di:
Cristiano Longarini

Anno Accademico 2022 - 2023

Panel of the final exam:

External Referee:
Myriam Benisty
Cathie J. Clarke

External Member:
Myriam Benisty
Cathie J. Clarke

Internal Member:
Giuseppe Lodato

Final examination:

Date 9th of January 2024

Università degli Studi di Milano, Dipartimento di Fisica, Milano, Italy

Per Marghe,
così sarai costretta ad aprire questa tesi almeno una volta!

Cover illustration:

Snapshot of a Smoothed Particle Hydrodynamics simulation
of a gas and dust gravitatonally unstable protostellar disc.

MIUR subjects:

FIS/05

PACS:

97.10.Gz, 47.20.Cq

Contents

Thesis overview

Structure of the thesis

The present thesis consists of one introductory chapter, three parts and a final chapter, for a total of eleven chapters. The first chapter set the stage by introducing the themes that will be discussed, providing a general overview of the research landscape in which my doctoral thesis unfolds. The first part is composed of 4 chapters, and it is devoted to the presentation of the classical viscous theory of protoplanetary discs. In particular, chapter 2 focus on the gas dynamics in protostellar discs, chapter 3 address the role of the self-gravity and gravitational instability, chapter 4 is devoted to the study of gas kinematics in protostellar discs and chapter 5 to the dust dynamics. In the second and third part, we get to the core of my research. The second part presents the gas kinematics in self-gravitating discs, and it includes three chapters. chapter 6 is devoted to the study of kinematic signatures of gravitational instability, chapter 7 focusses on a method to weigh and size discs through the kinematics and chapter 8 presents kinematic analysis of a gravitationally unstable disc. Part III consists of two chapters, and it focusses on the dust dynamics in gravitationally unstable discs. In particular, chapter 9 presents an analytical framework to study the stability of gas and dust in protostellar discs, and chapter 10 tackles this problem through numerical simulations, showing that gravitational instability is a pathway to form planetary cores in young protostellar systems.

Most of the results of part 2 and part 3 have appeared as refereed publications in scientific journals. Some variations have been made in the presentation of previously published results, to maintain consistency of style and content structure through the dissertation. Here, I briefly summarize the content of chapters.

Chapter 1: The synergy between theory and observations in the high resolution era

In this introductory chapter, I set the stage by presenting the current research panorama in the field of exoplanet and planet formation. I underline the strong connection between theory and observations of protoplanetary discs. I introduce the issue of early planet formation, the starting point of my research.

Chapter 2: Gas dynamics in protostellar discs

I describe the dynamics of gas in accretion discs, with a particular focus on protostellar environments. The basic dynamical equations are presented and discussed, and a particular attention is devoted to the transport of angular momentum and the nature of the viscosity in these environments.

Chapter 3: Self-gravity and gravitational instability in protostellar discs

I thoroughly discuss the role of self-gravity and gravitational instability in protostellar environments. After characterizing the basic state of a self-gravitating protostellar disc, I introduce the concept of gravitational instability, investigating both the linear and non-linear regime. Finally, I discuss whether the standard picture of gravitational instability can be a viable way to form planets.

Chapter 4: Gas kinematics in protostellar discs

I introduce the molecular line emission processes in protoplanetary discs, explaining how they can trace the gas kinematics. I analyse the kinematics of protostellar discs, discussing azimuthal, radial and vertical motions. In addition, I present the power of kinematics in studying protoplanetary discs structure and temperature. Finally, I introduce kinematic signatures of different processes that can happen in a protoplanetary disc, such as embedded planets and instabilities.

Chapter 5: Dust in protostellar discs

I discuss the role of dust in protostellar discs, the aerodynamical coupling with the gas and the resulting dynamics. The Core Accretion theory for planet formation is presented, with its advantages and caveats, and finally we introduce the interplay between dust dynamics and self-gravity.

Chapter 6: Kinematic signatures of gravitational instability

I present an analytical framework to characterize kinematic signatures of gravitational instability in protoplanetary discs. I derive the analytical expression for the velocity field perturbations generated by gravitational instability, and we discuss the physical parameters involved. Interestingly, the cooling factor plays a fundamental role in this context, and the possibility of constraining it is discussed and tested.

Chapter 7: Weighing and sizing protoplanetary discs with gravity

I present a method to infer disc masses and sizes through high resolution CO isotopologues rotation curves. I benchmark the method against numerical simulations, and I present a generalization for a thermal stratified disc. I finally apply this method to the MAPS sample.

Chapter 8: Kinematic study of a gravitational unstable disc : Elias 2-27

I present a kinematical study of the protoplanetary disc Elias 2-27, revealing indications of gravitational instability. In particular, I analyse global kinematic deviations and, assuming that they are generated by gravitational instability, I constrain the cooling factor. Consequently, I estimate the amount of angular momentum transported through gravitational instability. To validate this analysis, I compare the expected accretion rate onto the central object with the observed one, showing a very good agreement.

Chapter 9: The interplay between drag force and gravitational instability

I present an analytical framework to describe the stability of a fluid composed of two phases that interact through a drag force. Starting from previous works in the context of galactic dynamics, I generalize them to the field of protoplanetary discs, and I discuss the role of the drag force. I show that for typical protoplanetary discs parameter, the dynamical role of the dust can be important in determining the global stability of the flow.

Chapter 10: Planetary cores formation through dust collapse in gravitationally unstable discs

Strong of the analytical background, I perform numerical SPH simulation of gas and dust protostellar discs undergoing gravitational instability. I focus my attention on the interplay between cooling, drag force and dust excitation. I identify a sweet spot within our parameter space where dust collapse in gas spiral arms becomes possible. The consequence of this collapse is the formation of planetary bodies with masses on the order of Earth's mass. I speculate about the possibility of them to be the cradle of the ALMA planets.

Table 1: Values of the relevant physical constant assumed in this thesis.

Quantity	Value
$M_\odot$	1.99×10^{33} g
M_{jup}	1.90×10^{30} g
$M_\oplus$	5.97×10^{27} g
$R_\odot$	6.69×10^{10} g
$L_\odot$	3.90×10^{33} erg s^{-1}
G	6.67×10^{-8} g^{-1}cm^{3}s^{-2}
au	1.5×10^{13} cm
pc	3.09×10^{18} cm
k_B	1.38×10^{-16} erg K^{-1}
m_p	1.66×10^{24} g
σ_{SB}	5.67×10^{-5} erg cm^{-2}s^{-1}K^{-4}
h	6.63×10^{-27} erg s

CHAPTER 1

The synergy between theory and observation in the high resolution era

Planets are definitely the most familiar astrophysical objects: we live on one of them, and we know very well the ones belonging to our planetary system. The initial planets discovered by humans were part of our solar system, visible to the naked eye. Their swift motions in contrast to the background stars indicated their distinct nature. The 20th century marked the era of space exploration within our solar system, with significant advancements in the understanding of celestial bodies. During this time, we ventured closer to the planets within our system, allowing for detailed and close-up studies of their characteristics. Important space missions such as Voyager, Cassini, Rosetta, New Horizons, and Juno played pivotal roles in unravelling the mysteries of our solar system.

In 1995, a paradigm-shifting moment occurred with the detection of the first exoplanet orbiting around a Sun-like star, 51 Pegasi. The incredible discovery was made by Mayor and Queloz (Mayor & Queloz 1995), Nobel Prize 2019. This discovery completely changed our perspective, since it was the first time that a planet not belonging to our planetary system was seen, and also because the properties of this planet are completely different from ours. Indeed, it is really close to the host star, and its mass is higher compared to Jupiter, and for this reason it is called "hot Jupiter". To this day, there are more than 5000 confirmed exoplanets, whose properties are extremely diverse. From a dynamical point of view, figure 1.1 shows the semi-major axis - planetary mass diagram for the current exoplanet population, where the colour indicates the planetary eccentricity. This figure shows that hot Jupiters, as 51 Peg B, are very common in our Galaxy. In addition, there is a large number of planets with sub-au orbital separation, and higher mass compared to the Earth. These bodies are referred to as "Super Earths". As for the orbital eccentricity, there is an almost uniform distribution over all eccentricity values, reaching very high values $e \sim 0.9$. In this context, our planetary system is a really peculiar subset of the whole exoplanet population, not showing giant planets at sub-au orbital distances, with all the bodies in almost circular orbits. How can we reconcile all these differences? How is it possible to create such a diverse set of features? To answer these questions, investigating the process of planet formation is of paramount importance.

The planet formation process takes places in protostellar discs, that are structures around newborn stars. These astrophysical objects play an important dynamical role in the star formation process, since it is through them that the protostars accrete material, and they are the cradle of planets. The reason why a disc-like geometry forms in such environments is a direct consequence of angular momentum conservation. Stars form through the collapse of a molecular cloud core. In principle, without angular momentum, the molecular cloud core can collapse freely, forming a compact protostar. However, even a small amount of rotation prevents the collapse, allowing the gas to sink

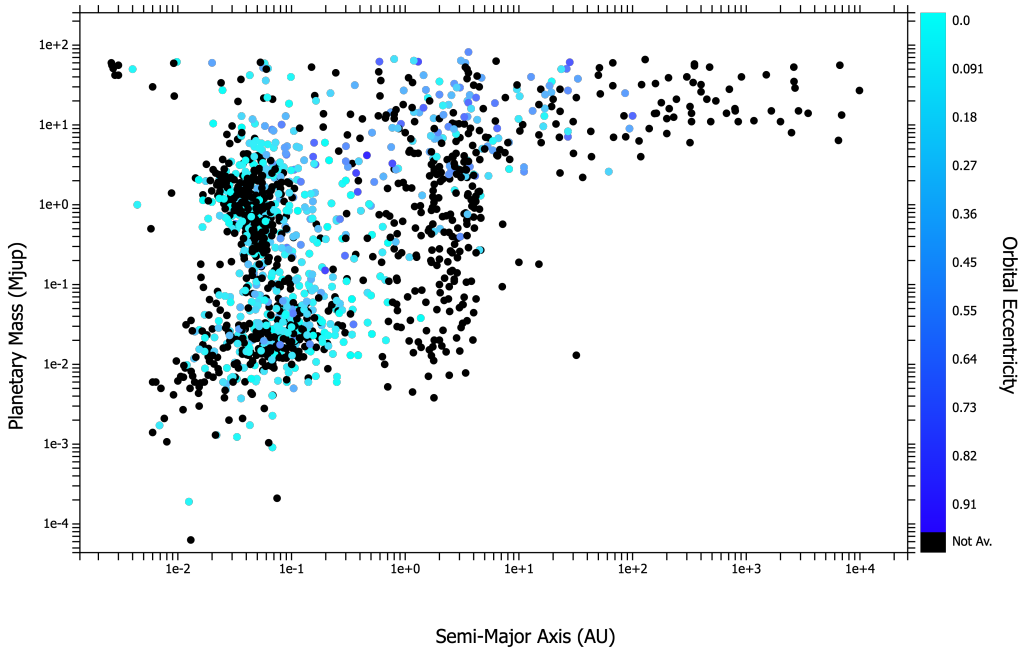

Figure 1.1: Semi-major axis - planetary mass plot for the exoplanet population. The colour of the points refers to the planet eccentricity.

down only to a minimum distance from the centre, called circularization radius. At this distance, the centrifugal force completely balances the gravitational one, allowing the formation of a flattened structure, that is the circumstellar disc. Typical values of circularisation radius are $\sim$ 300au, much larger than the stellar radius. Hence, a star could not form from a simple gravitational collapse of a rotating core because of the centrifugal barrier, unless the angular momentum is lost or transferred to something else, and this is the role played by the accretion disc.

A system composed of a young star and an envelope, from which the protostar is still gathering mass, is usually called Young Stellar Object (YSO). Typically, YSOs are classified according to their infrared spectral energy distribution (Lada & Wilking 1984), and different classes are interpreted as different evolutionary stages (Adams et al. 1988). The spectral energy distribution represents how the energy radiated from the system is redistributed over frequencies after being reprocessed by the disc material. The spectral index is defined as

$$s = \frac{\mathrm{d}\log(\lambda F_\lambda)}{\mathrm{d}\log\lambda}, \tag{1.1}$$

where F_λ is the emitted flux per wavelength λ. The infrared spectral index is usually defined between 2μm and 100μm. Figure 1.2 shows the four classes of YSOs, their spectral energy distribution and the evolutionary stage. Class 0 and Class I objects are characterized by $s > 0$, meaning that the spectrum rises towards higher wavelengths, indicating the presence of a cold envelope that dominates the emission. Such objects are the youngest ones, being the protostar still embedded into the molecular cloud. Class II objects have a spectral index $-4/3 < s < 0$, meaning that the spectrum declines in the infrared region, and they show a significant excess of emission with respect to the

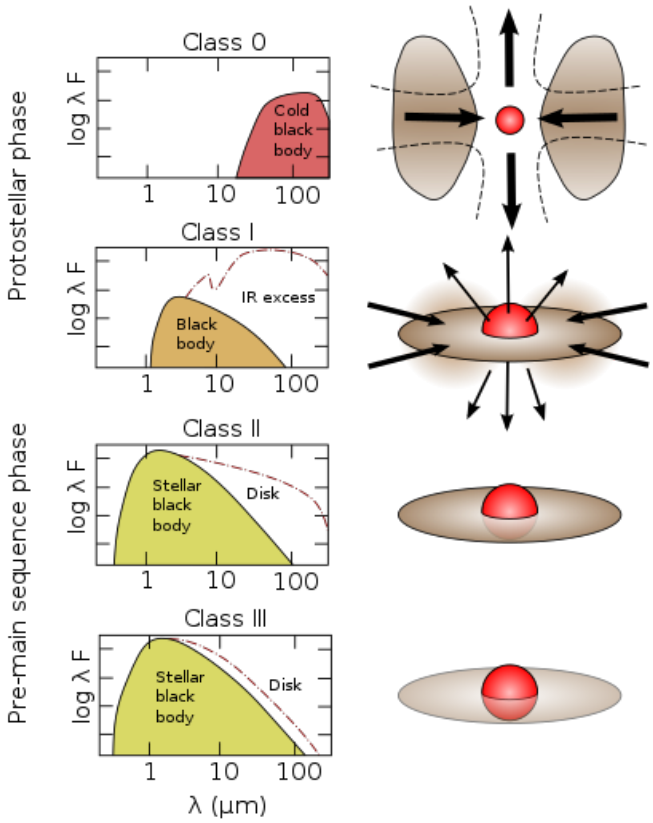

Figure 1.2: Infrared classification of Young Stellar Objects (Andre et al. 2000).

standard stellar photosphere. This feature, often referred to as IR excess, is thought to be mostly due to the disc, which can be accreting or simply reprocessing the stellar emission. These systems are known as "Classical T-Tauri" stars. To conclude, Class III objects are characterized by $s < -4/3$, typically $s = -3$, and here the emission is dominated by the star, showing a very small IR excess. At this stage, most of the protostellar material has been accreted, and thus they represent the last stage of a YSO. Usually, these objects are known as "Weak T-Tauri stars".

Being the result of molecular cloud core collapse, circumstellar discs are essentially composed of gas and dust. Typically, the gas-to-dust mass ratio is inferred from the composition of the interstellar medium (Draine 2011), and it is often taken ~ 100. Due to its abundance, the gas controls the dynamics of the system. On the other hand, because of its opacity, the dust is responsible for the radiative transport, as it absorbs and reprocesses stellar radiation, emitting in infrared-millimetric wavelengths. In addition to that, gas is a viscous fluid, which is subject to pressure forces, while dust is pressureless and inviscid. These properties imply different dynamical behaviours, that have several implications on planet formation. The gas content of protoplanetary discs is mainly made up of molecular hydrogen. This molecule is symmetric, and hence it does not emit through roto-vibrational transitions, making it impossible to be observed. Almost the entirety of the gas mass is invisible, thus one should rely on other tracers. Molecular

tracers are CO isotopologues, which have a relative abundance to the H_2 of the order of $10^{-6} - 10^{-5}$. Clearly, another tracer is the dust. Solid particles in protoplanetary are mainly composed by silicates. The emission in mid-infrared wavelengths is generated by sub-μ - 10μ particles. This part of the spectrum contains several spectral resonances whose features can be related to the shape and composition of dust grains (Bouwman et al. 2001; van Boekel et al. 2003; Kessler-Silacci et al. 2006; Min et al. 2016). Observations at longer wavelengths are dominated by the thermal emission from large dust grains.

Since the primary emission of protoplanetary discs occurs within the millimetric range of wavelengths, to achieve high-resolution observations of these environments, the use of interferometric techniques becomes crucial. In this field of study, the revolution came thanks to the Atacama Large Millimetre Array (ALMA). ALMA is a radio interferometer located on the Chajnantor Plateau in the Atacama Desert, Chile, one of the highest and driest places on Earth. Currently, ALMA is the largest radio telescope in the world. This achievement is the result of an international collaboration between Europe (ESO), North America (NRAO) and East Asia (NAOJ). It is composed of 66 high-precision antennas, which operate on wavelengths of 0.32 to 3.6mm. ALMA has the flexibility to arrange its antennas in various configurations, allowing for adjustable spacing ranging from 150 meters to 16 kilometres. This feature provides ALMA with a formidable "zoom" capability, reaching incredible spatial resolutions and sensitivity. From 2015, ALMA is collecting incredible images of the cold universe, including planet forming environments. The first image of a protoplanetary disc was released in 2015 (ALMA Partnership et al. 2015), and consists of dust continuum and spectral line emission from the HL Tau region. The incredible image is shown in the left panel of figure 1.3, showcasing a number of gaps and rings, rather than a smooth emission. Soon, this became the norm, as nearly every protoplanetary disc, when observed with sufficient spatial resolution, exhibits substructures such as rings, gaps, spirals, or asymmetric features in dust continuum emission. Figure 1.4 shows a collection of dust substructures in protoplanetary discs observed by ALMA.

In addition to dust continuum emission, ALMA is capable of observing gas line emission at high spectral resolution. The main targets are CO isotopologues, being the most abundant gas tracers in protostellar environments. This kind of observation allows probing the kinematics of these systems, offering a complementary window to study them.

Such progress in the observational field requires a strong theoretical effort to disclose the potential of these data. This happens through the advancement of hydrodynamical simulations. These simulations have truly revolutionized our comprehension of protoplanetary disc dynamics, and have allowed us to understand the information hidden within the wealth of observational data. Key to this transformation are the sophisticated algorithms capable of accurately modelling the hydrodynamics of gas and dust within these discs. Noteworthy examples include PHANTOM - Price et al. (2018b) and FARGO - Benítez-Llambay & Masset (2016). Moreover, it is crucial to highlight the synergy between hydrodynamic simulations, which describe the dynamics of these systems, and radiative transport simulations. Radiative transport codes, such as MCFOST Pinte et al. (2006, 2009) and RADMC-3D Dullemond et al. (2012), play a pivotal role in generating synthetic observations that can be one-to-one compared with the data obtained from ALMA. This powerful combination enables to bridge the gap between theoretical predictions and observations, unlocking unprecedented insights into protoplanetary disc evolution and planet formation. An incredible example of the synergy between theory and observations is presented in figure 1.3. Following the release of the initial image of a protoplanetary disc by ALMA (ALMA Partnership et al. 2015), Dipierro et al. (2015b) conducted hydrodynamical simulations using the PHANTOM code to explore planet for-

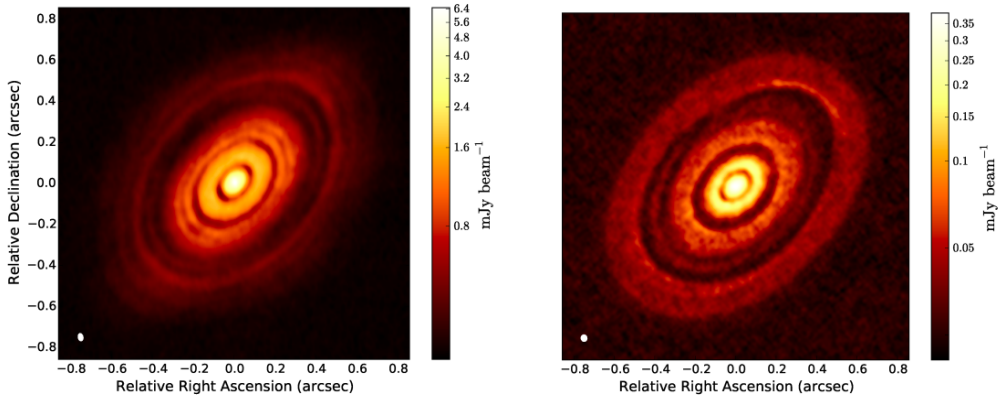

Figure 1.3: Comparison between the ALMA image of HL Tau (left panel) with simulated observations (right panel) at band 6 (continuum emission at 233 GHz), taken from Dipierro et al. (2015b).

mation in HL Tau. They found good agreement between the actual observations and the synthetic ones, generated from the hydrodynamical simulation. The axisymmetric gaps seen in the observations of the HL Tau protoplanetary disc with ALMA are explained as being due to the different response of gas and dust to three embedded protoplanets.

The ubiquity of substructures in protoplanetary discs shown by ALMA has opened debate as to how the timescales for planet formation align with the established evolutionary sequence for Young Stellar Objects. Under the hypothesis of the planetary interpretation, a robust conclusion is that a substantial part of the planet formation process must overlap with the time when protostellar discs are likely to be young. These findings completely changed our perspective on the timescale for planet formation. Indeed, ALMA observations have indicated that the planet formation process must occur within the first Myr of the disc's life, a timescale one order of magnitude earlier than previously believed. This shift in perspective poses a challenge to existing planet formation theories, such as the Core Accretion model. At this stage, most of the mass content of the disc has not yet been accreted by the central object. The disc to star mass ratio can be considerably high, making the role of the disc self-gravity of paramount importance. A key consequence of the self-gravity is the development of gravitational instability, that can lead to the formation of grand designed spiral structures, that deeply influence the structure and the dynamics of the disc, and the physical processes happening within. As a matter of fact, it is well known (Lynden-Bell & Kalnajs 1972) that gravitational instability is responsible for the transport of angular momentum, possibly solving the angular momentum problem, at least during the first stages of the disc lifetime. Historically (Boss 1997), gravitational instability has been proposed as a pathway for planetary formation, due to the limitations of the core accretion model. However, it lost favour due to the higher likelihood of forming stellar companions rather than planets (Kratter & Lodato 2016). Nevertheless, recently, this scenario has gained new interest (Rice et al. 2004, 2006; Booth & Clarke 2016; Baehr & Zhu 2021a), when the synergy between gravitational instability and dust dynamics is considered. Nowadays, it is believed to have the potential to contribute to planet formation.

The work presented in this thesis fits into this line of research. The question we address in this dissertation is: is gravitational instability a viable way to form planets in young protostellar discs? To tackle this, we first focus our attention into characterizing

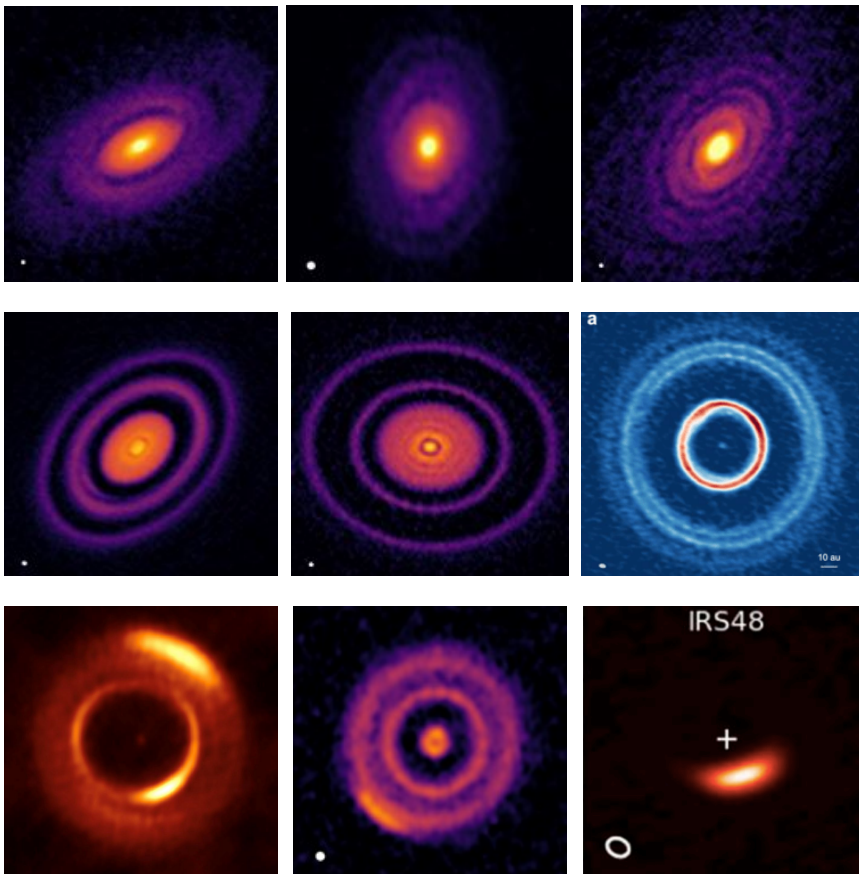

Figure 1.4: Examples of substructures in protoplanetary discs collected in dust continuum emission from ALMA telescope. Top row: spirals, Elias 2-27 (Pérez et al. 2016; Andrews et al. 2018), WaOph6 (Andrews et al. 2018), IM Lup (Andrews et al. 2018). Central row: rings and gaps, HD 163296 (Andrews et al. 2018), AS 209 (Andrews et al. 2018), HD 169142 (Pérez et al. 2019). Bottom row: asymmetric features, MWC 758 (Dong et al. 2018), HD 143006 (Andrews et al. 2018) and IRS48 (van der Marel et al. 2013).

the kinematic signatures of gravitational instability in protoplanetary discs (chapter 6). This approach allows us to get insight about the ability of such process to transport angular momentum throughout the disc, and can be applied to actual systems that show hints of gravitational instability (chapter 8). Additionally, the kinematics of such systems provides important information about their mass content, that is the building blocks of planets (chapter 7). In light of this, we investigate the dust dynamics in gravitationally unstable systems. Building on prior research and on a strong analytic background (chapter 9), we exploit high resolution hydrodynamical simulations to assess the viability for gravitational instability to form planets (chapter 10).

Part I

Viscous theory of accretion discs

CHAPTER 2

Gas dynamics in protostellar discs

The content presented in this chapter is mainly taken from Lodato (2008); Armitage (2013); Clarke & Carswell (2014); Hartmann (2009).

2.1 Description of an accretion disc

A first important distinction for protostellar discs is based on their luminosity. If the disc luminosity is generated by internal dynamical mechanisms, i.e. accretion, the disc is active, and its luminosity is given by

$$L_{\rm acc} = \frac{GM_\star \dot{M}}{2R_\star}, \tag{2.1}$$

where $M_\star$ and $R_\star$ are the mass and the radius of the star, and $\dot{M}$ is the accretion rate. Conversely, if the luminosity is generated by reprocessing the stellar one, the disc is passive, and the luminosity is

$$L_{\rm irr} = \frac{L_\star}{4}, \tag{2.2}$$

where $L_\star$ is the star luminosity. The threshold between active and passive discs can be obtained by equating $L_{\rm acc}$ with $L_{\rm irr}$, and can be expressed in terms of accretion rate. In particular, a disc is active if its accretion rate is

$$\dot{M} \geq \frac{L_\star}{2GM_\star R_\star} \simeq 10^{-8}\frac{\rm M_\odot}{\rm yr}, \tag{2.3}$$

where we have used $L_\star = L_\odot$, $M_\star = M_\odot$ and $R_\star = R_\odot$. Typical T-Tauri accretion rates vary from 10^{-6} to $10^{-8}\rm M_\odot/yr$ (Hartmann et al. 1998), being at the border between active and passive discs.

From simple geometrical arguments, it is possible to characterize the temperature profile of a passive thin disc, that scales as

$$T \propto R^{-3/4}. \tag{2.4}$$

However, a thin irradiated disc model is not realistic, and a degree of flaring should be considered. Hence, self-consistent models of flared irradiated discs show that the temperature profile scales as

$$T \propto R^{-1/2}. \tag{2.5}$$

Conversely, to understand how active discs work, a thorough analysis of the accretion processes is needed.

Protoplanetary discs are accretion discs, meaning that, through redistribution of angular momentum, the disc material is accreted onto the central object. In order to describe an accretion disc, we hypothesize that the system is thin. The thickness of the disc can be measured by comparing the height of the disc H with the radial extent R. The quantity H/R is called the aspect ratio. The thin disc approximation translates into

$$\frac{H}{R} << 1. \tag{2.6}$$

This ratio can be evaluated for different astrophysical systems. In particular, in accretion discs around black holes or AGN disc, this approximation is satisfied since $H/R \simeq 10^{-3}$; as for protostellar discs, the typical value is 10^{-1}, meaning that this hypothesis is marginally satisfied. The thin disc approximation implies that the azimuthal velocity is supersonic. Indeed, according to the hydrostatic equilibrium for a Keplerian disc (see section 2.1.1), the height of the disc H can be written as $H = c_s/\Omega_k$, where c_s is the sound speed and $\Omega_k = \sqrt{GM_\star/R^3}$ is the Keplerian frequency. Hence, the aspect ratio can be written as

$$\frac{H}{R} = \frac{c_s}{R\Omega_k} = \frac{c_s}{v_k} << 1; \tag{2.7}$$

where $v_k = R\Omega_k = \sqrt{GM_\star/R}$ is the azimuthal Keplerian velocity. Thanks to the thin disc approximation, it is convenient to use vertically integrated quantities, as the surface density

$$\Sigma(R,t) = \int_{-\infty}^{+\infty} \mathrm{d}z \rho(R,z,t). \tag{2.8}$$

In the following paragraphs, we will also assume that the disc is axisymmetric and non self-gravitating. We will discuss the effects of self-gravity in chapter 3.

2.1.1 Hydrodynamical equations

The equations that govern the dynamics of an accretion disc are the fluid equations, namely the conservation of mass (continuity equation) and the conservation of angular momentum (Navier Stokes equation). We consider an axisymmetric thin accretion disc in cylindrical coordinates. The continuity and Navier Stokes equations are

$$\frac{\partial \Sigma}{\partial t} + \frac{1}{R}\frac{\partial}{\partial R}(R\Sigma v_R) = 0, \tag{2.9}$$

$$\rho\left[\frac{\partial \mathbf{v}}{\partial t} + (\mathbf{v}\cdot\nabla)\mathbf{v}\right] = -\nabla P - \rho\nabla\Phi + \nabla\cdot\sigma, \tag{2.10}$$

where $\mathbf{v}$ is the velocity vector, P is the pressure, Φ the gravitational potential and σ the stress viscosity tensor. The components of this object are

$$\sigma_{ij} = \eta\left(\frac{\partial v_i}{\partial x_j} + \frac{\partial v_j}{\partial x_i} - \frac{2}{3}(\nabla_k v_k)\delta_{ij}\right) + \zeta(\nabla_k v_k)\delta_{ij}, \tag{2.11}$$

where η is the shear viscosity coefficient, ζ the bulk viscosity one and δ_{ij} is the Kronecker delta. We assume, as a first approximation, that the disc is Keplerian. This means that $\Omega = \Omega_k \propto R^{-3/2}$, implying that the inner rings rotate faster, and thus viscous shear forces act between a ring and another one, because of their difference in azimuthal velocity.

These forces are caused by the radial gradient of azimuthal velocity, consequently the only non-vanishing component of the viscous stress tensor is $R\phi$, that is

$$\sigma_{R\phi} = \eta R \frac{\mathrm{d}\Omega}{\mathrm{d}R}. \tag{2.12}$$

In general, the viscosity generates a surface force that opposes to the velocity gradients, and thus for a uniform circular motion it vanishes. For this reason, it is described through a tensor, and not simply a vector. In the limit of non self-gravitating disc, the gravitational potential is the Keplerian one generated by the central object, that is

$$\Phi = -\frac{GM_\star}{r}, \tag{2.13}$$

where $M_\star$ is the mass of the central star and r is the spherical radius $\left(r = \sqrt{R^2 + z^2}\right)$. Finally, we consider the gas to be barotropic, meaning that the pressure only depends on density. In this case, the sound speed is defined as

$$c_s^2 = \frac{\mathrm{d}P}{\mathrm{d}\rho}. \tag{2.14}$$

A noteworthy case is represented by a locally isothermal fluid, where the relationship between pressure and density is simply

$$P = c_s^2 \rho. \tag{2.15}$$

In the next paragraphs we will separately study the vertical, radial and azimuthal component of the Navier Stokes equation. We will show that the vertical component simply reduces to the hydrostatic equilibrium, the radial one to the centrifugal balance and the azimuthal one to the conservation of angular momentum.

Vertical component

We consider the vertical component of equation 2.10. Because of the thin disc approximation, we neglect vertical motions, and hence the left part is zero. In addition, the viscosity does not act in the vertical direction, thus the Navier Stokes equation reduces to

$$\frac{1}{\rho}\frac{\partial P}{\partial z} = -\frac{\partial \Phi}{\partial z}, \tag{2.16}$$

that is the vertical hydrostatic equilibrium. The right side is just the derivative along z of equation 2.13. As a consequence of the barotropic hypothesis, the left side can be written as a function of the density. Equation 2.16 then becomes

$$\frac{c_s^2}{\rho}\frac{\partial \rho}{\partial z} = -\frac{\partial \Phi}{\partial z}, \tag{2.17}$$

where we assume that the disc is vertically isothermal, meaning that the sound speed does not change with z. A study of the effects of thermal stratification is presented in chapter 7. Since we hypothesize that the disc is thin, $z << R$ and hence we can approximate the spherical radius r with the cylindrical one R. The hydrostatic equilibrium is then

$$\frac{c_s^2}{\rho}\frac{\partial \rho}{\partial z} = -\frac{GM_\star}{R^3} z = -\Omega_k^2 z. \tag{2.18}$$

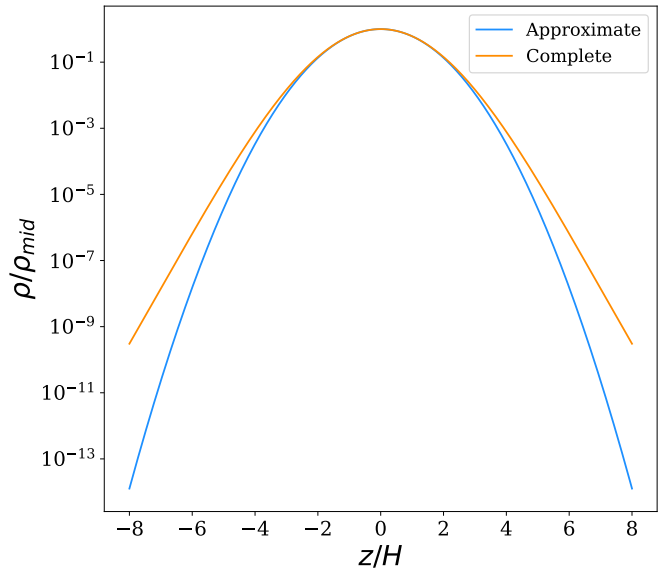

Figure 2.1: Density ρ as a function of z for the approximate gravitational potential (eq. (2.19)) and the complete one (eq. (2.21)). In this plot, $R = 100$au and $H = 10$au, resulting in an aspect ratio of $H/R = 0.1$.

To solve this equation, we define the dimensionless quantity $\zeta = z/z_0$, where $z_0 = c_s/\Omega_k$ is the typical scale height of the problem, and we call it H. The solution of eq. (2.18) is

$$\rho(R, z) = \rho_{\text{mid}}(R) \exp\left[-\frac{z^2}{2H^2}\right], \tag{2.19}$$

that is a Gaussian along the z direction, and $\rho_{\text{mid}}(R)$ is the density at the midplane.

It is possible to solve the hydrostatic equilibrium without approximating the gravitational potential, and just by computing its vertical gradient. In this case, the hydrostatic equilibrium is

$$\frac{c_s^2}{\rho}\frac{\partial \rho}{\partial z} = -\frac{GM_\star z}{(R^2 + z^2)^{3/2}}, \tag{2.20}$$

and the solution

$$\rho(R, z) = \rho_{\text{mid}}(R) \exp\left[-\frac{R^2}{H^2}\left(1 - \frac{1}{\sqrt{1 + z^2/R^2}}\right)\right]. \tag{2.21}$$

We underline that the last equation reduces to the standard Gaussian in the limit of $z << R$. Figure 2.1 shows the difference between the two solutions, for a set of standard disc parameters.

Radial component

We now consider the radial component of eq. (2.10). Since accretion happens on a long timescale, we can neglect the radial component of the velocity. In addition, the viscosity

does not act on the radial direction, hence the tensor stress contribution is zero. The Navier Stokes equation in the radial direction hence reduces to the centrifugal balance, and it reads

$$v_\phi^2 = R\frac{\partial \Phi}{\partial R} + \frac{R}{\rho}\frac{\partial P}{\partial R}. \tag{2.22}$$

The azimuthal velocity is determined by two contributions: the first one is simply the gravitational field of the central star; the second one is the so called "pressure gradient", that is, typically, a negative contribution. Its meaning relates to the fact that a particle is pushed to move from a high to low pressure region. Indeed, the pressure profile of a protostellar disc usually decreases with the radius, and hence the pressure gradient tends to slow gas particles.

The first term of eq. (2.22) can be written as

$$R\frac{\partial \Phi}{\partial R} = \frac{GM_\star R^2}{(R^2+z^2)^{3/2}} = v_k^2\left(1+\frac{z^2}{R^2}\right)^{-3/2} \tag{2.23}$$

and the second one

$$\frac{R}{\rho}\frac{\partial P}{\partial R} = c_s^2\frac{\partial \log \rho}{\partial \log R} = v_k^2\left(\frac{H}{R}\right)^2\frac{\partial \log \rho}{\partial \log R}, \tag{2.24}$$

and hence the azimuthal velocity is

$$v_\phi^2 = v_k^2\left[\left(1+\frac{z^2}{R^2}\right)^{-3/2} + \left(\frac{H}{R}\right)^2\frac{\partial \log \rho}{\partial \log R}\right]. \tag{2.25}$$

As a first order estimate, we can assume that the density in the radial direction is simply a power law $\rho \propto R^{-n}$. At the disc midplane ($z = 0$), the azimuthal velocity is

$$v_\phi = v_k\left[1 - n\left(\frac{H}{R}\right)^2\right]^{1/2}. \tag{2.26}$$

Here it is clear how the pressure gradient is slowing gas particle rotation. As a matter of fact, we usually refer to the gas azimuthal velocity as sub-Keplerian. The sub-Keplerian correction scales with $(H/R)^2$, that is small, but non-negligible. In some cases, the pressure corrections play an important role, as for the radial drift of solid particles, that will be presented in chapter 5.

Azimuthal component

Finally, we discuss the azimuthal component of the Navier Stokes equation, where, the viscous term plays an important role. The gravitational and pressure term give zero contribution, and the vertically integrated equation reads

$$\Sigma\left[\frac{\partial v_\phi}{\partial t} + v_R\left(\frac{v_\phi}{R}+\frac{\partial v_\phi}{\partial R}\right)\right] = \nabla\cdot\mathbf{T}|_\phi \tag{2.27}$$

where $\mathbf{T}$ is the vertically integrated stress tensor, whose only non-vanishing term is

$$T_{R\phi} = \nu\Sigma R\Omega'. \tag{2.28}$$

In eq. (2.28) the vertically integrated kinematics viscosity ν is defined through

$$\nu\Sigma = \int_{-\infty}^{+\infty} \mathrm{d}z\eta. \tag{2.29}$$

Combining eq. (2.27) with the continuity one, we obtain the angular momentum conservation for a viscous disc

$$\frac{\partial}{\partial t}\left(\Sigma R v_\phi\right) + \frac{1}{R}\frac{\partial}{\partial R}\left(R v_R \Sigma R v_\phi\right) = \frac{1}{R}\frac{\partial}{\partial R}\left(\nu\Sigma R^3\Omega'\right). \tag{2.30}$$

The above equation is a continuity equation for the quantity $\Sigma R v_\phi$, that is the angular momentum per unit area. The left-hand side is the Lagrangian derivative of this quantity, while the right one is the torque per unit area exerted by viscous forces. We underline that the right-hand side term is a divergence, hence a surface term. It is not a dissipative term but a transport one. Indeed, viscosity redistributes angular momentum throughout the disc, and it does not dissipate it. To make this clear, imagine integrating the above equation all over the disc: because of the Stokes theorem, the divergence term give a contribution only at the borders, meaning that the angular momentum is transported throughout the disc, and it exits from the borders. Multiplying the right-hand term by $2\pi R\mathrm{d}R$, we get the net torque on an annulus of width $\mathrm{d}R$. Thus, the flux of angular momentum across an annulus at distance R from the central object is given by

$$G(R) = 2\pi R^2 T_{R\phi} = 2\pi\nu\Sigma R^3\Omega', \tag{2.31}$$

where the sign convention is such that a positive $G(R)$ implies inward flux. As expected, in a rigidly rotating disc ($\Omega = \text{const}$), the flux of angular momentum is zero. Conversely, for a Keplerian disc ($\Omega_k' = -3\Omega_k/2R$), the angular momentum is transported outward with a net torque given by

$$G_k(R) = -3\pi\nu\Sigma R^2\Omega_k. \tag{2.32}$$

With the help of the continuity equation, from eq. (2.30) we obtain an expression for the radial velocity

$$v_R = \frac{1}{R\Sigma(R^2\Omega)'}\frac{\partial}{\partial R}\left(\nu\Sigma R^3\Omega'\right). \tag{2.33}$$

The above equation is valid for a general potential, and in the Keplerian case it yields

$$v_R = -\frac{3}{\Sigma R^{1/2}}\frac{\partial}{\partial R}\left(\nu\Sigma R^{1/2}\right). \tag{2.34}$$

Combining the above equation back with the continuity one, we obtain the equation for the evolution of the surface density Σ

$$\frac{\partial\Sigma}{\partial t} = -\frac{1}{R}\frac{\partial}{\partial R}\left[\frac{1}{(R^2\Omega)'}\frac{\partial}{\partial R}\left(\nu\Sigma R^2\Omega'\right)\right], \tag{2.35}$$

that, for a Keplerian disc, reads

$$\frac{\partial\Sigma}{\partial t} = \frac{3}{R}\frac{\partial}{\partial R}\left[R^{1/2}\frac{\partial}{\partial R}\left(\nu\Sigma R^{1/2}\right)\right]. \tag{2.36}$$

The equation provided depicts the temporal evolution of the surface density of a viscous accretion disc, that is clearly a diffusion mechanism. We want to underline that the

evolution strongly depends on the viscosity ν, which sets the typical diffusive timescale. Indeed, from a simple dimensional analysis of eq. (2.35), the surface density evolves on a timescale t_ν, called viscous timescale, of the order of

$$t_\nu = \frac{R^2}{\nu}. \tag{2.37}$$

2.2 Transport of angular momentum : solutions to the diffusion equation

In this section, we solve the diffusion equation for the surface density (2.35) for a number of relevant cases. In order to solve (2.35), one should determine how the kinematic viscosity ν changes with the radius. We will analyse the case of constant ν ("spreading ring solution") and of power law profile $\nu \propto R^\gamma$. In the following paragraphs, we will also assume that the disc is Keplerian, hence we will solve eq. (2.36). Finally, it is useful to define two quantities that will appear in the following parts, that are the enclosed disc mass within a radius R

$$M_d(R,t) = 2\pi \int_0^R \mathrm{d}R' \Sigma(R',t) R', \tag{2.38}$$

and the accretion rate

$$\dot{M}(R,t) = -2\pi R v_R(R,t), \tag{2.39}$$

where v_R is given by (2.34).

Spreading ring

A simple but instructive case to consider is when the viscosity coefficient ν is constant with the radius. In this case, the diffusion equation for the surface density can be solved analytically (Lynden-Bell & Pringle 1974). We assume that, initially, the mass of the disc M_d is concentrated on an infinitesimally thin ring at radius R_0

$$\Sigma(R, t=0) = \frac{M_d}{2\pi R_0} \delta(R - R_0), \tag{2.40}$$

where δ is the Dirac δ function. The solution of the eq. (2.35) is

$$\Sigma(x,\tau) = \frac{M_d}{\pi R_0^2} \frac{x^{-1/4}}{\tau} \exp\left[-\frac{1+x^2}{\tau}\right] I_{1/4}\left(\frac{2x}{\tau}\right), \tag{2.41}$$

where $x = R/R_0$, $\tau = 12\nu t/R_0^2$ and $I_{1/4}$ is the modified Bessel function of the first kind. τ is the typical timescale of the problem, and it represents the ratio between t and viscous time. This solution is called spreading ring, since the initial ring of mass spreads both inward and outward, rather than simply accreting. Figure 2.2 shows the evolution of the surface density for $\tau = [0.01, 0.05, 0.1, 0.2]$. In figure 2.2 we see that, in order to accrete, the disc needs to spread outward. In particular, the transition between the inward and outward evolution occurs at a radius of order of $R_{\rm tr} \simeq R_0 t/t_\nu$, being an increasing function of time. This means that for $t \to \infty$ all the ring mass is accreted, and the angular momentum is transported to infinitely large radii by a negligible amount of mass.

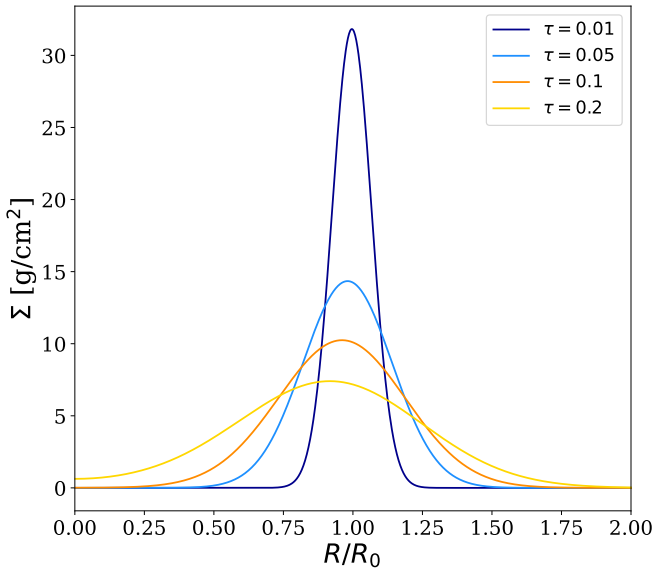

Figure 2.2: Evolution of the surface density of a Keplerian spreading ring under the effect of viscosity ν, for different times ν.

Self Similar

Another class of solutions for the diffusion equation are derived under the hypothesis that the viscosity varies with the radius, following a power law $\nu \propto R^{\gamma}$. Power-law viscosity profiles are often employed in numerical simulations of accretion discs due to their simplicity and the ability to capture various physical phenomena in a computationally efficient manner. We assume that the initial density profile follows

$$\Sigma(R, t=0) = \frac{C}{3\pi\nu(R)} \exp\left[-\left(\frac{R}{R_c}\right)^{2-\gamma}\right], \tag{2.42}$$

where C is a constant, with the dimension of mass over time, γ is the power law coefficient of the viscosity profile and R_c is the typical length of the problem, i.e. the scale radius of the density profile. The viscosity $\nu(R)$ can be expressed as

$$\nu = \nu_c \left(\frac{R}{R_c}\right)^{\gamma}, \tag{2.43}$$

so that the surface density scales as $\Sigma \propto R^{-\gamma} \exp[-(R/R_c)^{2-\gamma}]$. The solution of the diffusion equation with this initial condition is known as self-similar, since its functional form is the same at all times. The solution has been derived by Lynden-Bell & Pringle (1974), and it reads

$$\Sigma(R, T) = \frac{C}{3\pi\nu(R)} T^{-\frac{5/2-\gamma}{2-\gamma}} \exp\left[-\frac{1}{T}\left(\frac{R}{R_c}\right)^{2-\gamma}\right], \tag{2.44}$$

where the dimensionless time coordinate T is defined as

$$T = 1 + \frac{t}{t_\nu}, \quad t_\nu = \frac{1}{3(2-\gamma)^2}\frac{R_c^2}{\nu_c}, \tag{2.45}$$

where $\nu_c = \nu(R_c)$. We note that choosing a typical length R_c defines a typical timescale, the viscous time t_ν. By examining the equation (2.44), we observe that as T increases, the normalization of the surface density decreases while the truncation shifts towards larger radii. This means that the disc looses mass, since the central object accretes, and the size of the disc increases: this mechanism is called viscous spreading, and it is fundamental in the viscous theory of accretion discs. Hence, in order to accrete onto the central object, a small part of the disc mass migrates outwards, subtracting angular momentum. The spread of the disc extent can be seen by inspecting how the scale radius changes as a function of time

$$R_c(T) = R_{c,0} T^{\frac{1}{2-\gamma}}. \tag{2.46}$$

As for the enclosed disc mass, it varies with the radius and the time according to

$$M_d(R,t) = \frac{2CR_c^2}{3\nu_c(2-\gamma)} T^{-\frac{1}{2(2-\gamma)}} \left\{ 1 - \exp\left[-\frac{1}{T}\left(\frac{R}{R_c}\right)^{2-\gamma} \right] \right\}. \tag{2.47}$$

It is possible to compute the total mass of the disc, by integrating the surface density from 0 to infinity

$$M_d(T) = \frac{2CR_c^2}{3\nu_c(2-\gamma)} T^{-\frac{1}{2(2-\gamma)}} = M_{d,0} T^{-\frac{1}{2(2-\gamma)}}, \tag{2.48}$$

where $M_{d,0} = 2CR_c^2/3\nu_c(2-\gamma)$ is the initial mass. Using the above expression, we can re-write the surface density, removing the C constant

$$\Sigma(R,t) = \frac{(2-\gamma)M_{d,0}}{2\pi R_c^2} T^{-\frac{5/2-\gamma}{2-\gamma}} \exp\left[-\frac{1}{T}\left(\frac{R}{R_c}\right)^{2-\gamma} \right], \tag{2.49}$$

and now its meaning is clearer. Indeed, the surface density at time T is given by the initial mass $M_{d,0}$ divided by a circular area of radius R_c times the time dependent part. Now, using eq. (2.34), we write the radial velocity as a function of radius and time

$$v_R(R,t) = -\frac{3\pi\nu_c}{R}\left[1 - \frac{2}{T}\left(\frac{R}{R_c}\right)^{2-\gamma} \right]. \tag{2.50}$$

Here, it is clear that the inner part of the disc undergoes accretion, having a negative radial velocity, while the outer part migrates outwards. In particular, this inversion happens at $R_c/2^{2-\gamma}$. Finally, it is instructive to obtain the accretion rate, that is given by

$$\dot{M} = \frac{3M_{d,0}\nu_c(2-\gamma)}{2R_c^2} \exp\left[-\frac{1}{T}\left(\frac{R}{R_c}\right)^{2-\gamma} \right] \left[1 - \frac{2}{T}\left(\frac{R}{R_c}\right)^{2-\gamma} \right] T^{-\frac{5/2-\gamma}{2-\gamma}}. \tag{2.51}$$

As for the radial velocity, also the accretion rate changes sign at $R_c/2^{2-\gamma}$, being positive in the inner part (accretion) and negative in the outer one (outward migration). As time increases, the scale radius becomes larger, and hence the region of the disc that is accreted grows. For $T \to \infty$, all the disc mass is accreted and an infinitesimally small part of it migrates to infinity.

Figure 2.3 shows surface density, disc mass, radial velocity and accretion rate of the self similar solution as a function of radius and for different T.

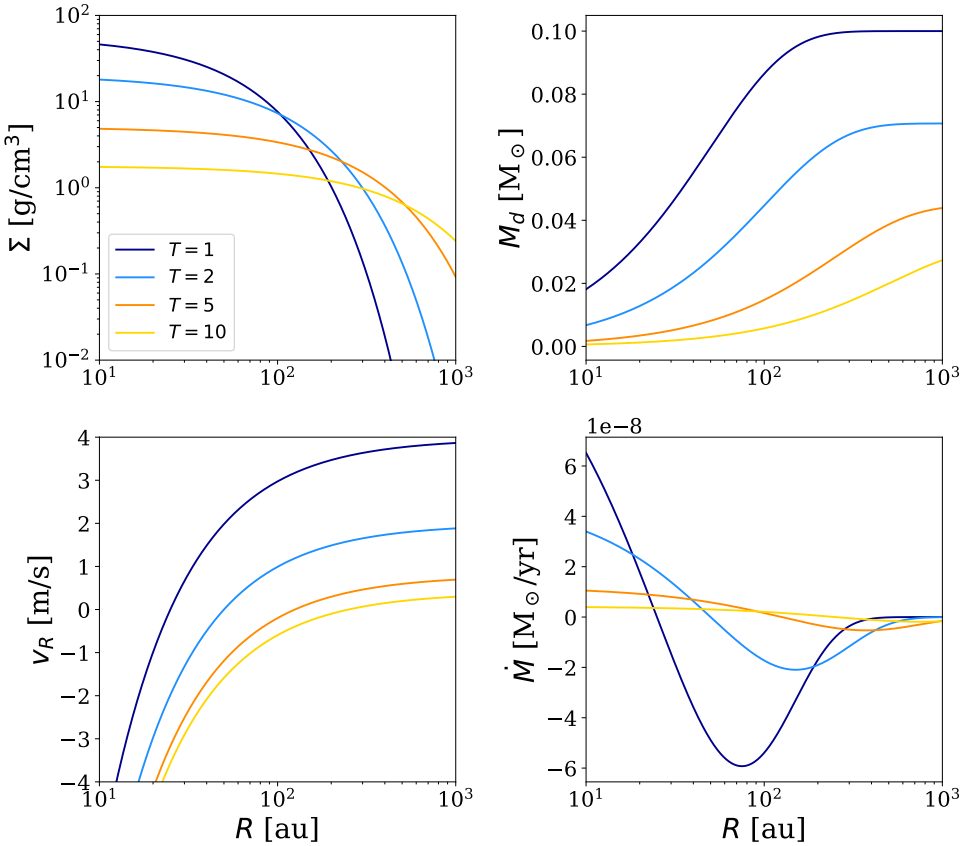

Figure 2.3: Surface density, disc mass, radial velocity and accretion rate of the self-similar solution for a disc with an initial mass $M_{d,0} = 0.1\mathrm{M}_\odot$, $\gamma = 1$, $R_c = 50$au, $\nu_c = 500\mathrm{km}^2/\mathrm{yr}$. The value of ν_c has been chosen in order to reproduce a disc around a solar mass star with an aspect ratio of 0.1 at 50au and an α-viscosity of 0.005. The meaning of α viscosity will be explained in the next subsection. The different curves, from top to bottom, show the solutions for different dimensionless time $T = [1, 2, 5, 10]$.

Stationary solution

Another solution of astrophysical interest is the stationary solution, which supposes that the fluid maintain a steady accretion rate. Mathematically speaking, we set the time derivative of the surface density to zero and, from the continuity equation, we obtain that

$$R\Sigma v_R = C_1, \tag{2.52}$$

where C_1 is a constant. This condition correspond to the steady accretion rate hypothesis. Indeed, since $\dot{M} = -2\pi R\Sigma v_R$, it follows that

$$C_1 = -\frac{\dot{M}}{2\pi}. \tag{2.53}$$

Then, setting the time dependent part equal to zero in eq. (2.30) gives that

$$R^2\Sigma v_R\Omega - \nu R^3\Sigma\frac{\mathrm{d}\Omega}{\mathrm{d}R} = C_2, \tag{2.54}$$

where C_2 is a constant. In order to determine C_2, we need to consider an inner boundary condition. We suppose that the inner radius of the disc is connected to the radius of the star $R_\star$. In a realistic case, the star is rotating with an angular frequency $\Omega_\star$, that is smaller compared to the Keplerian frequency at this radius $\Omega_k(R_\star)$. We hence suppose that the angular velocity of gas particles connect to the angular velocity of the star, meaning that exists a radius $R_\star + b$ where $\Omega' = 0$. In the limit of $b << R_\star$, we can suppose that $\Omega'(R_\star) = 0$; combining this request with eq. (2.54) and (2.53), we obtain

$$C_2 = -\frac{\dot{M}}{2\pi}\sqrt{GM_\star R_\star}. \tag{2.55}$$

Hence, we have the two equations

$$R\Sigma v_R = -\frac{\dot{M}}{2\pi}, \tag{2.56}$$

and

$$R^3\Sigma v_R\Omega - \nu R^3\Sigma\frac{\mathrm{d}\Omega}{\mathrm{d}R} = -\frac{\dot{M}}{2\pi}\sqrt{GM_\star R_\star};, \tag{2.57}$$

and, by substituting the first into the second one, we obtain

$$\nu\Sigma = \frac{\dot{M}}{3\pi}\left[1 - \left(\frac{R_\star}{R}\right)^{1/2}\right]. \tag{2.58}$$

If we consider the limit $R >> R_\star$, equation (2.58) becomes

$$\nu\Sigma = \frac{\dot{M}}{3\pi}. \tag{2.59}$$

The last expression shows that the mass infall rate and the viscosity depend linearly on each other for a fixed surface density profile. It is also possible to write the radial velocity for a steady disc, that is

$$v_R = -\frac{\dot{M}}{2\pi R\Sigma} = -\frac{3\nu}{2R}\left[1 - \left(\frac{R_\star}{R}\right)^{1/2}\right]^{-1}. \tag{2.60}$$

2.3 Radiation from steady thin discs

Viscous forces are dissipating energy in accretion discs. This is the mechanism that characterize an active disc. It is possible to obtain the energy dissipated per unit area by viscous forces (Clarke & Carswell 2014), and it reads

$$D(R) = \frac{G\Omega'}{2\pi R} = \nu\Sigma(R\Omega')^2 = \frac{9}{4}\nu\Sigma\Omega^2, \tag{2.61}$$

where the last identity is valid for a Keplerian disc. Combining the above equation with (2.58), we obtain the energy dissipated per unit area for a steady thin disc

$$D(R) = \frac{3}{4\pi}\frac{GM_\star\dot{M}}{R^3}\left(1 - \sqrt{\frac{R_\star}{R}}\right). \tag{2.62}$$

We can now evaluate the total power emitted by the disc, by integrating the above equation

$$L_{\rm acc} = \int_{R_\star}^{\infty} {\rm d}R 2\pi R D(R) = \frac{1}{2}\frac{GM_\star\dot{M}}{R_\star}, \tag{2.63}$$

and we obtain the accretion luminosity presented in eq. (2.1). It is interesting to note that the luminosity of the disc is equal to the gravitational energy needed to bring a mass element from infinity to $R_\star$ times the accretion rate, that is the mass flow rate. The $1/2$ factor comes from the virial theorem, since along a circular orbit the kinetic energy is half the gravitational one.

Now we want to compute the temperature profile of such a disc. By assuming that each annulus of the disc radiates as a black body with temperature $T_{\rm eff}(R)$, such that the emitted flux balances the viscous dissipation $D(R)$, we require

$$2\sigma_B T_{\rm eff}^4(R) = \frac{3}{4\pi}\frac{GM_\star\dot{M}}{R^3}\left(1 - \sqrt{\frac{R_\star}{R}}\right). \tag{2.64}$$

For $R >> R_\star$, the temperature of an active accretion disc scales as $T \propto R^{-3/4}$. Interestingly, this is the same behaviour of a passive thin disc, however here the reason is different, and it can be understood by considering the Kepler's laws. Indeed, the 3 factor derives from Ω_k^2, while the $1/4$ factor from the Stefan-Boltzmann law.

In general, we assume that the temperature of an accretion disc scales as

$$T(R) \propto R^{-q}, \tag{2.65}$$

with $1/2 < q < 3/4$, where the limits are for a flared passive and an active disc, respectively. The spectral energy distribution of such disc is obtained by summing black body spectra over annuli at the appropriate temperature, weighting their contribution according to their area. The SED is then

$$\nu F_\nu = \int_{R_\star}^{R_{\rm out}} {\rm d}R 2\pi R\nu B_\nu(T(R)), \tag{2.66}$$

with

$$B_\nu(T) = \frac{2h}{c^2}\frac{\nu^3}{\exp\left[\frac{h\nu}{k_B T}\right] - 1}, \tag{2.67}$$

where c is the speed of light, h the Planck constant and k_B the Boltzmann one. This spectrum is usually referred to as multicolour black body spectrum. For low frequency ($h\nu << k_B T_{\rm out}$), the Rayleigh Jeans limit is recovered

$$\nu F_\nu \propto \nu^3; \tag{2.68}$$

for high frequencies ($h\nu >> k_B T_{\rm in}$), the spectrum follows the Wien form with the exponential cut-off

$$\nu F_\nu \propto \nu^4 \exp[-h\nu/k_B T_{\rm in}]. \tag{2.69}$$

For intermediate wavelengths, it is possible to show (Hartmann 2009) that

$$\nu F_\nu \propto \nu^{4-2/q}. \tag{2.70}$$

Thus, the final profile of the SED is given by the composition of these three regions. By evaluating the spectral index in the intermediate region for typical values of q, we obtain that

$$s = \begin{cases} 4/3, & q = 3/4 \\ 0, & q = 1/2 \end{cases} \tag{2.71}$$

where the first case is for a Keplerian active disc, and the second one for a passive flared disc. The presence of a disc makes $s \in [0, 4/3]$, that is the typical range of spectral indexes of Class II discs.

2.3.1 Timescale for thermal processes

In this paragraph, we obtain the thermal timescale, i.e. the propagation timescale of a thermal perturbation. This quantity is defined as the ratio between the thermal energy e and the energy dissipation rate.

The thermal energy per unit mass e can be obtained from the first principle of thermodynamics

$$\mathrm{d}e = p\mathrm{d}(\rho^{-1}), \tag{2.72}$$

where P is the pressure per unit mass and ρ is the density. Assuming a polytropic equation of state $p = k\rho^\gamma$ and integrating the above equation, we obtain

$$e = \frac{c_s^2}{\gamma(\gamma - 1)}. \tag{2.73}$$

The thermal timescale is hence the thermal energy per unit surface Σe over the dissipation rate per unit surface given by eq. (2.61)

$$t_{\rm th} = \frac{\Sigma c_s^2}{\gamma(\gamma-1)} \frac{1}{\nu\Sigma(R\Omega')^2} = \frac{4}{9\gamma(\gamma-1)\alpha}\Omega^{-1}, \tag{2.74}$$

where in the last identity is valid for a Keplerian disc.

2.4 The nature of the viscosity

So far, we have avoided a discussion about the physical nature of the viscosity and what is its strength. It is instructive to check if standard collisional viscosity provides enough

transport of angular momentum in protoplanetary discs. In the standard collisional scenario, the kinematic viscosity ν is the sound speed (i.e. the average velocity of gas particles) times the collisional mean free path $\lambda_{\rm coll}$. The latter quantity depends on the particle density and cross-section according to

$$\lambda_{\rm coll} = \frac{1}{n\sigma_{\rm coll}} = \frac{\mu m_{\rm p}}{\rho\sigma_{\rm coll}} = \left(\frac{\mu m_{\rm p}}{\Sigma\sigma_{\rm coll}}\right) H, \tag{2.75}$$

where $\sigma_{\rm coll}$ is the molecular hydrogen cross-section and μ is the mean molecular weight, that is assumed to be 2.1 in protoplanetary discs. Hence, the collisional kinematic viscosity is

$$\nu_{\rm coll} = \frac{\mu m_p}{\Sigma\sigma_{\rm coll}} c_s H. \tag{2.76}$$

In order to understand its magnitude, we evaluate its viscous timescale for a typical protostellar system, that is

$$t_\nu = \frac{R^2}{\nu} = \frac{\Omega R^2}{\nu}\Omega^{-1} = \Omega^{-1}{\rm Re}, \tag{2.77}$$

where ${\rm Re} = \Omega R^2/\nu$ is the Reynolds number of the fluid at radius R and Ω^{-1} is the dynamical time, i.e. the orbital time at a radius R. Hence, the Reynolds number is the factor of proportionality between the viscous time and the dynamical one. For collisional viscosity, the Reynolds number is

$${\rm Re} \simeq 10^{12}\left(\frac{\Sigma}{20{\rm g/cm}^2}\right)\left(\frac{H/R}{0.1}\right)^{-2}. \tag{2.78}$$

Since the dynamical timescale is of the order of several years, it implies that the viscous time is longer than the Hubble time. Clearly, the collisional viscosity is not able to explain the angular momentum transport needed in protoplanetary discs.

It is worth highlighting that the ratio between the viscous and the dynamical timescale, which is of the order of 10^{12}, indicates an incredibly high Reynolds number for the flow. It implies that the fluid is subject to develop turbulent motions. In this scenario, viscosity can be higher because angular momentum is exchanged by the mixing of fluid elements, because of turbulence. To better understand the problem, we rewrite the Euler equation separating the mean flow motions $\mathbf{v}$ from the fluctuating quantities $\delta\mathbf{v}$

$$\frac{\partial}{\partial t}\left(\Sigma R v_\varphi\right)\frac{1}{R}\frac{\partial}{\partial R}\left(R v_R \Sigma R v_\varphi\right) = -\sum_i \frac{1}{R}\frac{\partial}{\partial R}\left(R^2\Sigma\left\langle \delta v_R^{(i)}\delta v_\varphi^{(i)}\right\rangle\right), \tag{2.79}$$

where the angle brackets indicate a vertical and azimuthal average and the summation is over the fluctuating fields. For example, we can have proper velocity field fluctuations ($\mathbf{v}+\delta\mathbf{v}$), magnetic field fluctuations ($\mathbf{B}_0+\delta\mathbf{B}$) or gravitational field fluctuations ($\mathbf{g}_0+\delta\mathbf{g}$), where $\mathbf{g}$ is the gravitational field. In the simplest case of a purely hydrodynamic flow, the only relevant field is the velocity, and its contribution to the stress tensor is called Reynolds stress

$$T_{R\phi}^{\rm Re} = -\Sigma\left\langle v_R^{\rm Re} v_\phi^{\rm Re}\right\rangle, \tag{2.80}$$

where $v^{\rm Re}$ is the velocity fluctuation. If the disc is magnetized, the magnetic field fluctuations provide another source of transport

$$T_{R\phi}^{\rm M} = \Sigma\left\langle v_R^{\rm A} v_\phi^{\rm A}\right\rangle, \tag{2.81}$$

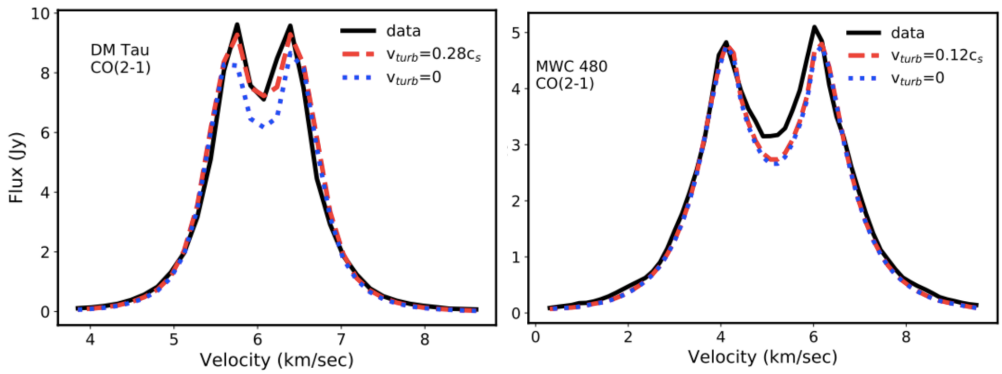

Figure 2.4: Detection (left panel) and non detection (right panel) of non-thermal motions in DM Tau and MWC 480 from Flaherty et al. (2020).

where $v^{\rm A} = B/\sqrt{4\pi\rho}$ is the Alfvén velocity. Finally, if the disc is self-gravitating, the perturbations of the gravitational field generate another source of angular momentum transport in the form

$$T^{\Phi}_{R\phi} = -\Sigma \left\langle v^{\Phi}_R v^{\Phi}_\phi \right\rangle , \tag{2.82}$$

where $v^{\Phi} = \Phi/\sqrt{4\pi G\rho}$ (Lynden-Bell & Kalnajs 1972). Turbulence is supposed to arise as a consequence of the development of disc instabilities such as hydrodynamic, gravitational or magneto-hydrodynamic. While it is a matter of debate whether pure hydrodynamic disc could produce instabilities, it is commonly thought that in the earliest phases of star formation, gravitational instabilities can produce enough transport of angular momentum (Kratter & Lodato 2016). As far as MHD instabilities are concerned, Balbus & Hawley (1991) studied the so-called "Magneto Rotational Instability" (MRI) that, under appropriate conditions, could explain the angular momentum transport in protostellar discs. However, this is still an open problem called "angular momentum problem".

In any case, the stress generated by turbulent motions plays exactly the same role as a viscous stress in the Navier Stokes equation; how can we estimate the magnitude of such viscosity? A simple estimate has been provided by (Shakura & Sunyaev 1973), based on a dimensional analysis: the stress tensor is a pressure, that is a density times the square of a velocity. The simplest assumption is to consider the stress tensor to be proportional to the vertically integrated pressure $P = \Sigma c_s^2$

$$T_{R\phi} = \frac{{\rm d}\log\Omega}{{\rm d}\log R}\alpha\Sigma c_s^2, \tag{2.83}$$

where ${\rm d}\ln\Omega/{\rm d}\log R$ is just a number and α is the proportionality factor. If we consider the kinematic viscosity, we can express the Shakura & Sunyaev prescription in the usual form

$$\nu = \alpha c_s H. \tag{2.84}$$

It is important to underline that the α prescription is not a theory of viscosity, but it is just a simple parameterisation based on dimensional analysis; it simply moves the unknown from ν to α.

Under an observational point of view, several ways to quantify α have been proposed. A first approach consists in measuring statistical properties of protoplanetary discs at different ages (i.e. in different star forming regions), and comparing them with viscous evolution theory (Andrews & Williams 2007; Lodato et al. 2017; Ansdell et al. 2018). The results indicate that the range of α is wide, ranging from 10^{-4} to 0.1. Another method consists in directly measuring non-thermal motions in high resolution gas observations (Flaherty et al. 2020). Figure 2.4 shows two estimates of α from CO $J = 2 - 1$ observations. The left panels show a detection of turbulent motions in the disc DM Tau, while the right panel a non detection in MWC 480. For DM Tau, the estimate is $\alpha \simeq 0.08$, while for MWC 480 the upper limit is $\alpha < 0.006$. To conclude, the value of α obtained so far is still extremely uncertain, and some more steps need to be done in order to understand the actual amount and the physical origin of turbulence in protostellar discs.

CHAPTER 3

Self-gravity and gravitational instability in protostellar discs

Self-gravitation is the process through which the components of a body are held together by their own gravity. This mechanism is fundamental in astrophysics, from cosmic structures to stars and planetary rings. In the context of protoplanetary discs, self-gravity is particularly important in the early stages of the disc lifetime. Indeed, there is observational evidence that younger protostars host more massive discs: Tobin et al. (2020) within the VANDAM survey found that the dust mass of protoplanetary discs in younger star forming region, as Orion, is higher compared to older regions, as Lupus Taurus or Upper Sco. Physically speaking, this can be easily understood: indeed, younger systems are expected to be more massive, since most of their mass has not yet been accreted by the central object.

A crucial consequence of the disc self-gravity in discs is the development of gravitational instability. This mechanism is characterized by the formation of large scale spiral structure, transporting angular momentum throughout the disc. The foundations of our understanding of self-gravity and gravitational instability in discs comes from the field of galactic dynamics. Indeed, during the second half of the last century, the so-called "density wave theory" was developed to explain the origin of spiral structure in galaxies (Lin & Shu 1964; Toomre 1964). Besides spiral galaxies, in protoplanetary discs several spiral structures have been observed with ALMA, and some of them are attributed to gravitational instability. A well-known example of a very young system (approximately 1.5×10^5 years old, class 0) where gravitational instability is at play is L1448 IRS3B (Tobin et al. 2016). Furthermore, in class II systems, there is substantial evidence supporting the idea that the spectacular spiral arms observed in Elias 2-27 result from gravitational instability (Meru et al. 2017; Cadman et al. 2020; Veronesi et al. 2021; Paneque-Carreño et al. 2021) (see also chapter 8). Figure 3.1 displays the dust continuum emission from both sources, clearly showing the presence of spiral arms. As for other class II sources such as IM Lup (Cadman et al. 2020; Lodato et al. 2023), GM Aur (Schwarz et al. 2021; Lodato et al. 2023), AB Aur (Cadman et al. 2021) and WaOph6 (Cadman et al. 2020), there is ongoing research exploring the potential influence of gravitational instability on their evolutionary processes.

3.1 Self-gravitating discs : equilibrium state

In this section, we will present the relevant dynamical equations for a self-gravitating discs. As for chapter 2, we make the thin disc hypothesis, whose consequences are the same as before. The equations that govern gas dynamics are the continuity and the Navier Stokes equations. The difference compared to the non-self-gravitating case is

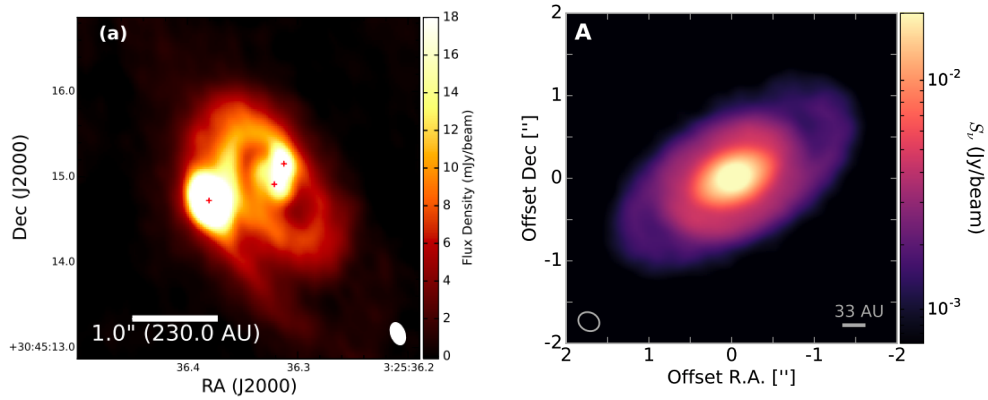

Figure 3.1: Left panel: ALMA 1.3mm image of the L1448 IRS3B disc showing a large scale spiral structure (Tobin et al. 2016). Right panel: ALMA 1.3mm image of the Elias 2-27 disc, showing two prominent spiral arms (Pérez et al. 2016).

that the gravitational potential Φ is given by the sum of the stellar contribution and the disc self-gravity.

Gravitational potential of a disc

In this paragraph, we go through the derivation of the disc self-gravity contribution to the gravitational potential, as done in (Bertin & Lodato 1999). We consider a distribution of matter infinitesimally thin and axisymmetric, with a surface density given by $\Sigma(R)$, where (R, ϕ) are radial and azimuthal coordinates. The gravitational potential associated to this matter distribution on the midplane is given by

$$\Phi(R) = -2G \int_0^{\pi} d\phi \int_0^{\infty} dR' \frac{\Sigma\left(R'\right) R'}{\left(R^2 + R'^2 - 2RR' \cos\phi\right)^{1/2}}. \tag{3.1}$$

The denominator of the last expression can be rewritten as $(R^2 + r'^2 - 2RR' \cos\phi)^{1/2} = [R + R'(1 + \zeta^2 \cos(\phi/2))]$, where $\zeta = 4R'/(R + R')^2$. The potential is thus

$$\Phi(R) = -4G \int_0^{\infty} K(\zeta) \frac{\Sigma\left(R'\right) R' dR'}{(R + R')}, \tag{3.2}$$

where

$$K(\zeta) = \int_0^{\pi/2} \frac{dt}{1 + \zeta^2 \cos^2 t} \tag{3.3}$$

is a complete elliptic integral of the first kind. We now define

$$K^{(0)}(R, R') = \frac{1}{\pi} \sqrt{\frac{R'}{R}} \zeta K(\zeta), \tag{3.4}$$

thus equation (3.2) reads

$$\Phi(R) = -2\pi G \int_0^{\infty} dR' K^{(0)}\left(R, R'\right) \Sigma\left(R'\right). \tag{3.5}$$

The last equation diverges for $\zeta \to 1$, that corresponds to $R \to R'$: this kind of divergence is typical of infinitesimally thin disc, although the potential Φ is finite. Actually, by integrating the expression, the divergence disappears. Mathematically, to avoid this problem, we compute the gravitational potential at a finite vertical distance $z \neq 0$ and then take $z \to 0$. In a cylindrical system of coordinates (R, ϕ, z), we thus rewrite ζ as

$$\zeta^2 = \frac{4R'}{(R+R')^2 + z^2}. \tag{3.6}$$

In the context of fluid equations, it is useful to write the radial derivative of the gravitational potential, since it appears in the Navier Stokes equation. Differentiating equation (3.5) with respect to R, we get

$$\frac{\partial \Phi}{\partial R}(R,z) = \frac{G}{R}\int_0^\infty dR' \left[\zeta K - 2R\frac{d(\zeta K)}{d\zeta}\frac{\partial \zeta}{\partial R}\right]\Sigma(R')\sqrt{\frac{R'}{R}}. \tag{3.7}$$

The last expression can be simplified by using a property of elliptic integrals, that is

$$\frac{d(\zeta K)}{d\zeta} = \frac{E(\zeta)}{1-\zeta^2}, \tag{3.8}$$

where

$$E(\zeta) = \int_0^{\pi/2} dt \sqrt{1-\zeta^2\cos^2 t} \tag{3.9}$$

is another complete elliptic integral. The final equation is

$$\begin{aligned}\frac{\partial \Phi_d}{\partial R}(R,z) = \frac{G}{R}\int_0^\infty dR' \Bigg[K(\zeta) - \frac{1}{4}\left(\frac{\zeta^2}{1-\zeta^2}\right) \times \\ \times \left(\frac{R'}{R} - \frac{R}{R'} + \frac{z^2}{RR'}\right)E(\zeta)\Bigg]\sqrt{\frac{R'}{R}}\zeta\Sigma(R').\end{aligned} \tag{3.10}$$

The Mestel disc

One interesting case is the so-called Mestel disc (Mestel 1963), where the surface density of the disc scales as $\Sigma = \Sigma_0 R_0/R$ and the disc extends out to infinity. In this case, the gravitational potential is really simple, and reads

$$\Phi_d = 2\pi G\Sigma(R)R. \tag{3.11}$$

In the limit in which the central object is negligible, the rotation curve is determined only by the disc, and it is

$$v_\phi = 2\pi G\Sigma_0 R_0, \tag{3.12}$$

that is flat, and the angular frequency $\Omega \propto R^{-1}$.

3.1.1 Hydrostatic equilibrium : density structure

The hydrostatic balance for a self-gravitating disc differs from a star dominated one. Indeed, the hydrostatic equilibrium involves the total gravitational potential of the system that, in this case, is given by the sum of the star and disc contribution. Hence, the equation reads

$$\frac{1}{\rho}\frac{\partial P}{\partial z} = -\frac{\partial}{\partial z}(\Phi_\star + \Phi_d) \tag{3.13}$$

It is possible to analytically solve the hydrostatic equilibrium by neglecting the star term, namely for a completely self-gravitating object: this is known as self-gravitating isothermal slab of surface density Σ. Using the equation of state $P = c_s^2 \rho$ and neglecting the star contribution, the hydrostatic equilibrium becomes

$$\frac{c_s^2}{\rho}\frac{\partial \rho}{\partial z} = -2\pi G \Sigma, \tag{3.14}$$

with $\Sigma = \int_0^z \mathrm{d}z' \rho(z')$. As in chapter 2, we make the hypothesis that the sound speed does not depend on the z coordinate. We write the previous equation as a function of Σ rather than ρ, and we obtain

$$\frac{\partial^2 \Sigma}{\partial z^2} = -2\pi G \Sigma \frac{\partial \Sigma}{\partial z}. \tag{3.15}$$

We define dimensionless variables $\sigma = \Sigma/\Sigma_0$ and $\zeta = z/H_{\rm sg}$, where

$$H_{\rm sg} = \frac{c_s^2}{\pi G \Sigma_0}, \tag{3.16}$$

is the typical scale height of a self-gravitating slab. The dimensionless hydrostatic equilibrium reads

$$\frac{\partial^2 \sigma}{\partial \zeta^2} = -2\sigma \frac{\partial \sigma}{\partial z}, \tag{3.17}$$

with the boundary conditions $\rho(0) = \rho_0, \quad \sigma(0) = 0$ and $\sigma'(0) = 1$. The solution of the equation is

$$\Sigma = \Sigma_0 \tanh\left(\frac{z}{H_{\rm sg}}\right), \quad \rho = \rho_0 \cosh^{-2}\left(\frac{z}{H_{\rm sg}}\right). \tag{3.18}$$

Now, we can ask a question: how massive has to be the disc, in order for self-gravity to significantly affect its vertical structure? To answer, we compare the non-self-gravitating and the self-gravitating scale height

$$\frac{H_{\rm sg}}{H_{\rm nsg}} = \frac{c_s \Omega}{\pi G \Sigma}. \tag{3.19}$$

The two scale height are comparable when their ratio is one. The parameter on the right is akin to the Toomre Q parameter (Toomre 1964), that controls the development of gravitational instabilities in the disc. A thorough explanation of the onset of gravitational instability is given in the next section.

One could in principle try to solve the complete equation 3.13. A smart way to rewrite it is in terms of the typical scale heights of the self-gravitating and non self-gravitating limits. In particular, if we use $\sigma = \Sigma/\Sigma_0$ and $\zeta = z/H_{\rm nsg}$, the equation reads

$$\frac{\partial^2 \sigma}{\partial \zeta^2} = -\zeta \frac{\partial \sigma}{\partial \zeta} - \frac{2\sigma}{Q}\frac{\partial \sigma}{\partial \zeta}, \tag{3.20}$$

where Q is the Toomre parameter and the boundary conditions are $\sigma(0) = 0$ and $\sigma'(0) = 1$. This equation cannot be solved analytically, but a simple and accurate interpolation formula between the two regimes has been obtained by Bertin & Lodato (1999). They found that the typical scale height is

$$H = \frac{c_s^2}{\pi G \Sigma}\left(\frac{\pi}{4Q^2}\right)\left[\sqrt{1 + \frac{8Q^2}{\pi}} - 1\right], \tag{3.21}$$

where Q determines the transition between the self-gravitating and non-self-gravitating regime.

3.1.2 Centrifugal balance : the rotation curve

The disc self-gravity also impacts the centrifugal balance of an accretion disc, giving a super-Keplerian contribution to the azimuthal velocity. In section 2.1.1 we showed that the radial component of the Navier Stokes reads

$$v_\phi^2 = R\frac{\partial \Phi}{\partial R} + \frac{R}{\rho}\frac{\partial P}{\partial R}, \tag{3.22}$$

where $\Phi = \Phi_\star + \Phi_d$. The disc contribution to the rotation curve is given by eq. (3.10), and it reads

$$R\frac{\partial \Phi_{\rm d}}{\partial R}(R,z) = G\int_0^\infty \left[K(k) - \frac{1}{4}\left(\frac{k^2}{1-k^2}\right)\times \right. \tag{3.23}$$
$$\left.\left(\frac{R'}{R} - \frac{R}{R'} + \frac{z^2}{RR'}\right)E(k)\right]\sqrt{\frac{R'}{R}}k\Sigma\left(R'\right)dR'.$$

The self-gravitating contribution depends on the disc surface density, hence on the disc mass. In addition, this is a super-Keplerian contribution, unlike the pressure gradient. A comprehensive model of the rotation curve, taking into account both self-gravity and pressure gradient, is presented in chapter 4.

3.2 Linear theory of gravitational instability

To approach gravitational instability in protostellar discs, we must understand how to describe a perturbation in a disc. We consider a disc basic state characterized by a density ρ_0, and a perturbation $\rho_1 << \rho_0$ so that the total density is $\rho = \rho_0 + \rho_1$. The perturbation ρ_1 can be decomposed into an even and an odd part $\rho_1 = \rho_+ + \rho_-$ with respect to the disc midplane. Figure 3.2 shows the even and the odd part of a given perturbation on a disc. Even perturbations are called density waves, since they are able to locally modify the density. Conversely, an odd perturbation is a bending wave, that is simply distorting the geometry, without changing the density. Examples of density or bending waves are spirals and warps respectively. Figure 3.3 shows an actual example of this kind of waves in Saturn's A ring. Since spirals are density waves, because they change the background density, we will focus our attention on them.

How can we describe an $m-$armed spiral perturbation? Firstly, we consider a razor-thin disc, so that perturbations develop only in the radial R and azimuthal ϕ directions. Within this framework, a spiral disturbance can be described as

$$m\phi + \psi(R) = \text{const}, \quad \text{mod } 2\pi \tag{3.24}$$

where $\psi(R)$ is the so-called phase function and m is the number of spiral arms. The phase function is linked to the radial wavenumber, as

$$k = \frac{{\rm d}\psi}{{\rm d}R}, \tag{3.25}$$

while the azimuthal wavenumber is simply defined as m/R. The radial wavenumber is a function of radius, and its sign determines the class of the wave. In particular, if the disc rotates in the sense of increasing ϕ, $k < 0$ implies leading waves, whereas $k > 0$

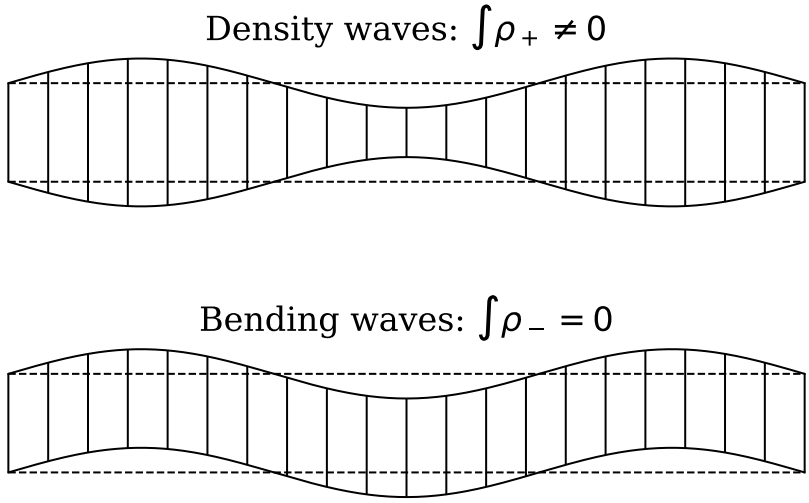

Figure 3.2: Even (top) and odd (bottom) perturbations on a disc. Even perturbations are density waves, and they are able to generate mass since the density changes. Odd perturbations do not create mass, and they just bend the disc.

implies trailing waves. Another significant quantity to mention is the opening angle of the spiral (pitch angle), that is given by

$$\tan \alpha_p = \frac{m}{rk}. \tag{3.26}$$

As an example, if the pitch angle is constant over the all radial extent of the disc, the shape function is a logarithm.

As for the time dependence, the location of the spiral arm $\phi(R,t)$ is described by

$$\phi(R,t) = \phi_0 + \Omega_p t, \tag{3.27}$$

where Ω_p is the spiral pattern speed.

The surface density of a disc with a spiral perturbation can simply be written as the sum of the unperturbed axisymmetric component $\Sigma_0(R)$ and the spiral perturbation $\Sigma_1(R,\phi)$. Supposing that the perturbation $\Sigma_1 \propto \exp[i(m\phi + kR)]$, it is possible to show (Binney & Tremaine 1987) that its gravitational potential is

$$\Phi_1 = -\frac{2\pi G}{k}\Sigma_1. \tag{3.28}$$

This result will be essential in the following paragraphs.

3.2.1 The quadratic dispersion relation

In section 3.1, we focused our attention on examining the effects of disc self-gravity on the equilibrium state, assuming the system to be stable. However, it is important to note that this assumption should not be taken for granted. Indeed, gravitational instability

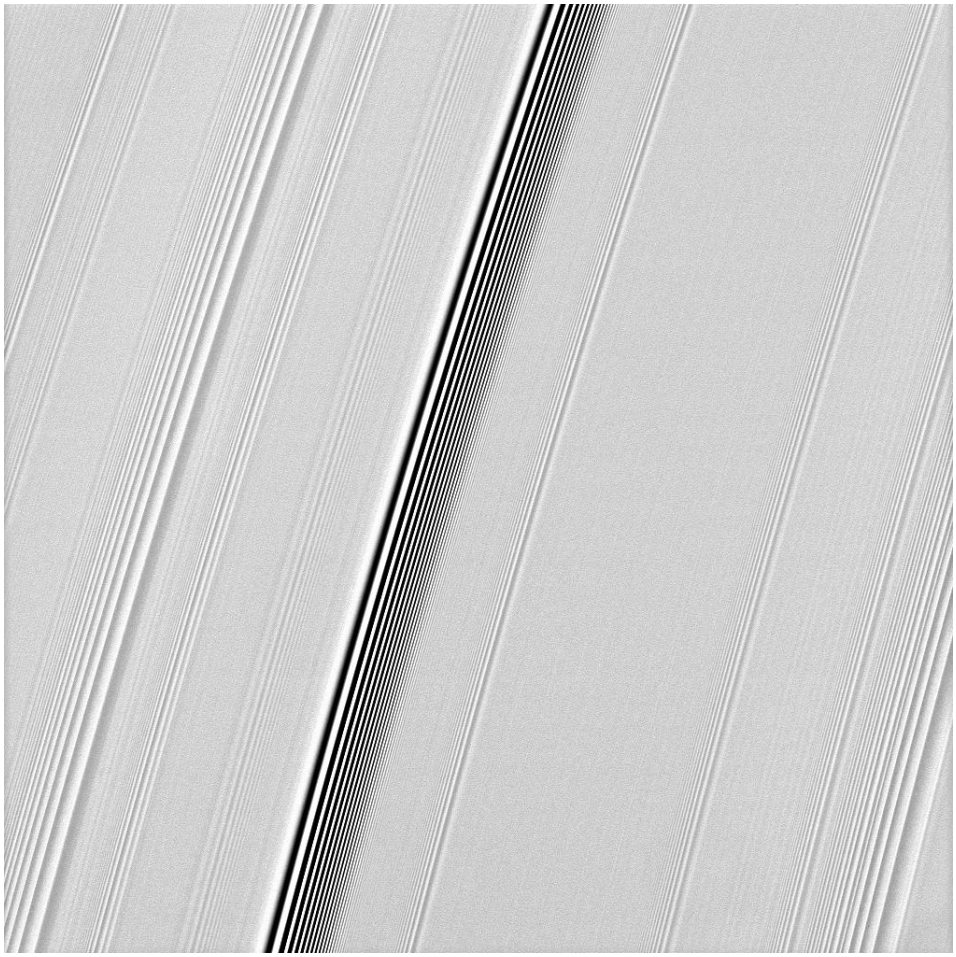

Figure 3.3: Cassini spacecraft image of two types of waves in Saturn's A ring: a spiral density wave on the left of the image and a more pronounced spiral bending wave near the middle.

occurs when the self-gravitating forces within the disc become dominant over the stabilizing effects of pressure and rotation. How can we quantify this behaviour? A first hint comes from the previous analysis regarding the structure of a self-gravitating disc. Indeed, in eq. (3.19) we showed that the height of a self-gravitating disc is comparable with the non-self-gravitating one when

$$Q \simeq \frac{c_s \Omega}{\pi G \Sigma} = 1, \tag{3.29}$$

where the ratio is akin to the Toomre parameter. This number is easy to interpret, since it basically represents the ratio between the stabilizing terms (pressure c_s and rotation Ω) and the destabilizing one (self-gravity Σ). However, to better understand the onset of gravitational instability in protoplanetary discs, it is necessary to set a perturbative analysis of the fluid equations, and obtain a dispersion relation. The theory was first developed in the context of galactic dynamics, and it is the foundation of the density wave theory for spiral galaxies (Safronov 1960; Lin & Shu 1964; Toomre 1964).

In cylindrical coordinates, the fluid equations for a thin axis disc are

$$\frac{\partial \Sigma}{\partial t} + \frac{1}{R}\frac{\partial}{\partial R}\left(\Sigma R v_R\right) + \frac{1}{R}\frac{\partial}{\partial \phi}\left(\Sigma v_\phi\right) = 0, \tag{3.30}$$

$$\frac{\partial v_R}{\partial t} + v_R \frac{\partial v_R}{\partial R} + \frac{v_\phi}{R}\frac{\partial v_R}{\partial \phi} - \frac{v_\phi^2}{R} = -\frac{\partial}{\partial R}\left(\Phi + h\right), \tag{3.31}$$

$$\frac{\partial v_\phi}{\partial t} + v_R \frac{\partial v_\phi}{\partial R} + \frac{v_\phi}{R}\frac{\partial v_\phi}{\partial \phi} = -\frac{1}{R}\frac{\partial}{\partial R}\left(\Phi + h\right), \tag{3.32}$$

$$\nabla^2 \Phi = 4\pi G \Sigma \delta(z), \tag{3.33}$$

$$dh = c_s^2 \frac{\mathrm{d}\Sigma}{\Sigma}, \tag{3.34}$$

where $h = c_s^2 \log \Sigma$ is the enthalpy. The basic equilibrium state is characterized by zero radial velocity $v_R = 0$, azimuthal velocity described in terms of angular velocity $v_\phi = R\Omega$ and, for the moment, we do not make any assumption on the form of c_s, Φ, h and Σ. We perturb the basic state quantities X_0 with a perturbation X_1 so that $X_1 << X_0$, and we linearize the equations. The first order expressions are

$$\frac{\partial \Sigma_1}{\partial t} + \frac{1}{R}\frac{\partial}{\partial R}\left(\Sigma_0 R v_{R1}\right) + \frac{1}{R}\frac{\partial}{\partial \phi}\left(\Sigma_0 v_{\phi 1} + \Sigma_1 v_{\phi 0}\right) = 0, \tag{3.35}$$

$$\frac{\partial v_{R1}}{\partial t} + \Omega \frac{\partial v_{R1}}{\partial \phi} - 2\Omega v_{\phi 1} = -\frac{\partial}{\partial R}(\Phi_1 + h_1), \tag{3.36}$$

$$\frac{\partial v_{\phi 1}}{\partial t} - 2B v_{R1} + \Omega \frac{\partial v_{\phi 1}}{\partial \phi} = -\frac{1}{R}\frac{\partial}{\partial \phi}(\Phi_1 + h_1), \tag{3.37}$$

$$h_1 = c_s^2 \frac{\Sigma_1}{\Sigma_0}, \tag{3.38}$$

$$\nabla^2 \Phi_1 = 4\pi G \Sigma_1 \delta(z), \tag{3.39}$$

where $B = -1/2\left[\Omega + (\Omega R)'\right]$ is the Oort constant (Oort 1927). Now, we make the assumption that the wave modes are determined by local effects only. With this is mind, we assume that the radial dependence of perturbed quantities has the form $\exp[ikR]$,

where k is the radial wavenumber. This is known as WKB approximation. As for the temporal and spatial dependence, we assume the perturbations to be proportional to $\exp[i(-\omega t + m\phi)]$. Within this assumption, the radial, temporal and azimuthal derivatives corresponds to $\partial_R \rightarrow ik$, $\partial_t \rightarrow -i\omega$ and $\partial_\phi \rightarrow im$. By using equation (3.28) for the gravitational potential, we end up with three equations for surface density Σ_1, radial and azimuthal velocity $v_{R1}, v_{\phi 1}$

$$-i(\omega - m\Omega)\Sigma_1 + ik\Sigma_0 v_{R1} + i\frac{m\Sigma_0}{R} = 0, \tag{3.40}$$

$$-i(\omega - m\Omega)v_{R1} - 2\Omega v_{R1} = ik\Sigma_1\left(\frac{2\pi G}{|k|} - \frac{c_s^2}{\Sigma_0}\right), \tag{3.41}$$

$$-i(\omega - m\Omega)v_{\phi 1} - 2Bv_{R1} = i\frac{m\Sigma_1}{R}\left(\frac{2\pi G}{|k|} - \frac{c_s^2}{\Sigma_0}\right). \tag{3.42}$$

In order to obtain the standard quadratic dispersion relation (Lin & Shu 1964; Toomre 1964), we consider only tightly wound perturbation (i.e. small opening angle), and hence we suppose that $m/Rk << 1$. This approximation allows us to simplify some terms in the previous equations, that become

$$-i(\omega - m\Omega)\Sigma_1 + ik\Sigma_0 v_{R1} = 0, \tag{3.43}$$

$$-i(\omega - m\Omega)v_{R1} - 2\Omega v_{R1} = ik\Sigma_1\left(\frac{2\pi G}{|k|} - \frac{c_s^2}{\Sigma_0}\right), \tag{3.44}$$

$$-i(\omega - m\Omega)v_{\phi 1} - 2Bv_{R1} = 0. \tag{3.45}$$

In order to obtain the dispersion relation $\omega(k)$, we write the coefficient matrix A so that $A\mathbf{x} = 0$, where $\mathbf{x} = [\Sigma_1, v_{R1}, v_{\phi 1}]$

$$A = \begin{pmatrix} -i(\omega - m\Omega) & ik\Sigma_0 & 0 \\ -ik\left(\frac{2\pi G}{|k|} - \frac{c_s^2}{\Sigma_0}\right) & -i(\omega - m\Omega) & -2\Omega \\ 0 & -2B & -i(\omega - m\Omega) \end{pmatrix}. \tag{3.46}$$

The dispersion relation is simply given by imposing the determinant of this matrix to be zero, and it reads

$$(\omega - m\Omega)^2 = c^2k^2 - 2\pi G\Sigma|k| + \kappa^2, \tag{3.47}$$

where $\kappa^2 = 2\Omega/R(R^2\Omega)'$ is the radial epicyclic frequency that, for a Keplerian potential, it is simply Ω_k. The last equation is a quadratic in k, and each term has a physical interpretation. The left side term is the Doppler shifted perturbation frequency, and can be re-written by underlying the spiral pattern frequency $\omega - m\Omega = m(\Omega_p - \Omega)$, where Ω_p is the spiral pattern frequency. The first term on the right side of eq. (3.47) is the stabilizing pressure contribution. It is quadratic in k and hence it is important for large wavenumbers - short wavelengths. The second term is the disc self-gravity, that is linear with the wavenumber. Its contribution is more significant at intermediate wavelengths, and its role is destabilizing. Finally, the third term is the disc rotation. It does not depend on k and hence its stabilizing effect is dominant at large wavelengths. The competition of these three effects determines the stability of the system.

Stability of axisymmetric perturbations

We now consider axisymmetric disturbances, for which $m = 0$. The instability threshold can be determined by studying the sign of ω^2: when $\omega^2 > 0$, a perturbation simply propagates as a wave; when $\omega^2 < 0$, an exponentially growing instability arises. Solving the dispersion relation for axisymmetric disturbances, the perturbation is unstable if

$$Q = \frac{c_s \kappa}{\pi G \Sigma} < 1, \tag{3.48}$$

where Q is the Toomre parameter. We recall that for a Keplerian disc $\kappa = \Omega$. In a protostellar disc, the sound speed and the surface density can be described as power laws with the radius. We usually assume that $c_s \propto R^{-q/2}$, and $\Sigma \propto R^{-\gamma}$: this implies that $Q \propto R^{\gamma - q/2 - 3/2}$. If $\gamma > (q+3)/2$, the Toomre parameter decreases with the radius, meaning that the outer part of the disc is more prone to be unstable. Conversely, if $\gamma > (q+3)/2$, the disc will be more likely gravitationally unstable in the inner regions. If we consider a standard power-law exponent for temperature ($q = 1/2$), it is likely that the condition will be met in the outer (inner) regions of the disc when $\gamma < 7/4$ ($\gamma > 7/4$). Observations of discs have typically yielded power-law exponents within the range of [0, 2] (Andrews & Williams 2007), making it more likely for the condition $Q < 1$ to be fulfilled in the outer regions of a disc.

For the case of an unstable disc, the most unstable wavenumber k_J (i.e. where the right-hand side of equation (3.47) is at its minimum) occurs at

$$k_J = \frac{\pi G \Sigma}{c_s^2}. \tag{3.49}$$

When the disc is marginally unstable ($Q = 1$), only modes close to $k_{\rm uns}$ are excited. If we evaluate eq. (3.47) for $Q = 1$ and $k = k_J$, we get the condition $\Omega_p = \Omega$, which means that all excited modes are expected to be close to co-rotation. It is worth noting that the most unstable wavenumber k_J is exactly the inverse of the disc thickness in the self-gravitating limit. Equivalently, it is possible to define the most unstable wavelength

$$\lambda_J = \frac{2\pi}{k_J} = \frac{2c_s^2}{G\Sigma} = 2\pi H_{\rm SG}. \tag{3.50}$$

k_J and λ_J are respectively the most unstable wavenumber and wavelength, often called Jeans wavenumber and wavelength.

Marginal stability curve

An alternative way of looking at the dispersion relation is by asking whether there are parameters for which $\mathrm{Im}(\omega) < 0$, meaning that the system is unstable. To do so, it is possible to derive the marginal stability curve, that depicts the threshold between stability and instability. Starting from the quadratic dispersion relation, we define the dimensionless quantities

$$\nu^2 = \frac{(\omega - m\Omega)^2}{\kappa^2}, \tag{3.51}$$

$$\hat{k} = 2\frac{k}{k_J}, \quad \hat{\lambda} = \hat{k}^{-1} \tag{3.52}$$

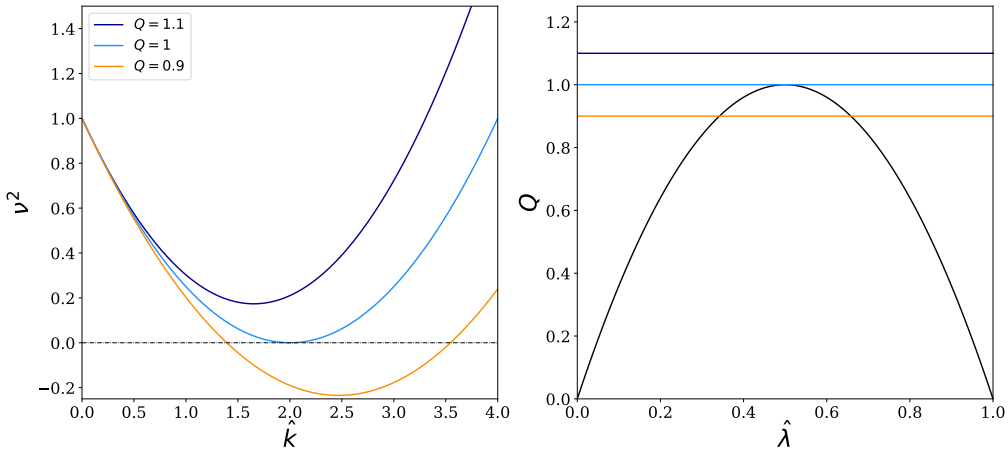

Figure 3.4: Left panel: dimensionless perturbation frequency ν^2 as a function of the dimensionless perturbation wavenumber $\hat{k}$ for different values of the Toomre parameter $Q = [0.9, 1, 1.1]$. Right panel: marginal stability curve for the quadratic dispersion relation (eq. (3.54)). The coloured lines corresponds to $Q = [0.9, 1, 1.1]$: for $Q > 1$, the line does not cross the marginal stability curve, and there are no unstable wavelengths, as shown in the left panel; for $Q = 1$, there is only an unstable wavelength, that is k_J^{-1}; for $Q < 1$, there is an interval of unstable wavelengths, as shown in the left panel.

so that eq. (3.2.1) can be rewritten as

$$\nu^2 = 1 + \frac{1}{4}Q^2\hat{k}^2 + |\hat{k}|. \tag{3.53}$$

The marginal stability condition corresponds to $\nu^2 = 0$: this curve in the space $(Q^2, \hat{\lambda})$ is the marginal stability curve. Hence, the region above the curve is stable, while the one below is unstable. For the quadratic dispersion relation, the marginal stability curve is simply a parabola, and it reads

$$Q^2 = 4\hat{\lambda}(1 - \hat{\lambda}). \tag{3.54}$$

The maximum of the curve correspond to the instability threshold $Q = 1$, and it occurs for $k = k_J$. Figure 3.4 displays a schematic view of the quadratic dispersion relation and the marginal stability curve, for different values of the Toomre parameter.

3.2.2 Finite thickness effect

The dispersion relation (3.47) has been derived under important approximations. Firstly, the equilibrium structure of the disc is assumed to be axisymmetric, and secondly (and more important) the disc is infinitesimally thin. As we have discussed in the previous chapter, protoplanetary discs have a finite vertical extent, and this is impacting the onset of gravitational instability. In particular, the finite thickness of the disc dilutes the gravitational field, giving an additional pressure like term. A simple way to take into account for this effect is by modifying the quadratic dispersion relation as follows (Vandervoort 1970)

$$(\omega - m\Omega)^2 = c_s^2k^2 - 2\pi G\Sigma|k|e^{-|kH|} + \kappa^2 \simeq (c_s^2 + 2\pi G\Sigma H)k^2 - 2\pi G\Sigma|k| + \kappa^2, \tag{3.55}$$

where we have expanded to first order to make it clear the additional pressure term. In this case, the marginal stability value decreases to $Q \simeq 0.6$ for a Keplerian disc.

3.2.3 Cubic dispersion relation

In the context of galactic dynamics, it was recognized (Ostriker & Peebles 1973; Hohl 1973) that discs that are locally stable according to the $Q-$criterion, might still generate large scale spiral waves. This behaviour is due to the fact that such global modes are not captured by the WKB tightly wound approximation, under which the quadratic dispersion relation has been obtained. As a matter of fact, the azimuthal wavenumber m/R enters only in the Doppler-shifted perturbation frequency. A WKB description can still be obtained under less restrictive conditions than the tightly wound approximation, as done in Lau & Bertin (1978). The resulting dispersion relation is a cubic, and contains a new dimensionless parameter $\mathcal{J}$

$$\mathcal{J} = m\frac{\pi G\Sigma}{R\kappa^2}\frac{4\Omega}{\kappa}\left|\frac{\mathrm{d}\log\Omega}{\mathrm{d}\log R}\right|^{1/2} \simeq \sqrt{6}m\frac{M_d}{M_\star}. \tag{3.56}$$

Also $\mathcal{J}$ has a physical interpretation: while Q balances rotation, pressure and self-gravity, $\mathcal{J}$ is essentially a measurement of the disc to star mass ratio. In the limit of $\mathcal{J} \to 0$, the cubic dispersion relation tends to the standard quadratic one. This happens for axisymmetric perturbation $(m = 0)$ or for low disc to star mass ratio. This parameter is suggesting us that high mass discs behave differently from low mass ones.

3.3 Non-linear evolution

In the previous section, we presented an analytical framework to linearly describe the gravitational instability. Now, we ask what is the non-linear evolution of such instability, and whether it can lead to transport of angular momentum. To tackle this question, it becomes imperative to employ numerical simulations of gravitationally unstable discs. Over the past two decades, this topic has gained considerable attention, employing various numerical techniques. These methods encompass local shearing sheet models (Gammie 2001; Booth & Clarke 2019; Baehr & Zhu 2021a,b; Baehr et al. 2022), global Eulerian grid-based models (Pickett et al. 2003; Mejía et al. 2005; Kratter & Matzner 2006; Kratter et al. 2008, 2010; Paardekooper 2012; Deng et al. 2017), global Lagrangian particle-based models (Rice et al. 2004; Lodato & Rice 2004; Rice et al. 2006; Meru & Bate 2010, 2011, 2012; Booth & Clarke 2016; Longarini et al. 2023a)). Remarkably, despite the diverse approaches, the results appear to converge into an essentially coherent picture.

3.3.1 Self-regulation

To describe the non-linear evolution of gravitational instability, we start with the definition of the stability parameter Q. It is proportional to the disc sound speed, hence to the temperature. This implies that colder discs are more likely to be unstable. We consider an initially stable hot disc $(Q >> 1)$. In the absence of external heating or cooling mechanisms, the disc will cool down through radiative cooling, eventually reaching the marginally stable condition $Q \sim 1$. At this point, gravitational instability turns on: the disc develops a spiral structure that, by means of compression and shocks, leads to an efficient energy dissipation, and the disc heats up again. Hence, the stability condition works as a thermostat, so that the heating turns on only when the disc becomes enough

cold. If this thermostat mechanism works (see sections 3.3.3 and 3.3.4), we expect the instability to self-regulate in such a way that the disc maintains $Q \simeq 1$.

It is possible to describe such a self-regulated state in terms of steady-state models of self-gravitating accretion discs. Firstly, the self-regulation condition is simply

$$Q \simeq 1. \tag{3.57}$$

As shown in chapter 2, at large radii the accretion rate for a steady state accretion disc can be written

$$\dot{M} = 2\pi\nu\Sigma \left| \frac{\mathrm{d}\log\Omega}{\mathrm{d}\log R} \right|, \tag{3.58}$$

where we have not assumed that the disc is Keplerian. An interesting consequence of the above relation arises when we use the $\alpha-$prescription, and we assume that the disc is self-gravitating $H = H_{\mathrm{SG}}$. In this case we obtain

$$\dot{M} = \frac{2\alpha c_s^3}{G} \left| \frac{\mathrm{d}\log\Omega}{\mathrm{d}\log R} \right|. \tag{3.59}$$

The last equation shows that for a self-gravitating disc, the accretion rate $\dot{M}$ depends only on α and the sound speed. In particular, if we assume a constant value of α, the disc must be approximately isothermal (Lodato 2008). If we assume a disc-dominated potential, it is possible to provide an analytical self-similar solution to the model. We consider a Mestel disc (see section 3.1) with $\Sigma \propto R^{-1}$, and we obtain

$$c_s = \left(\frac{G\dot{M}}{2\alpha} \right)^{1/3}, \tag{3.60}$$

$$v_\phi = \frac{2\sqrt{2}}{Q} \left(\frac{G\dot{M}}{2\alpha} \right)^{1/3}, \tag{3.61}$$

and

$$\Sigma = \frac{4}{\pi G Q^2 R} \left(\frac{G\dot{M}}{2\alpha} \right)^{2/3}. \tag{3.62}$$

This solution has very simple properties, having a flat profile of c_s, v_ϕ and Q. Clearly, this solution applies only at large radii, where the effect of the central point mass is negligible.

3.3.2 Accretion and angular momentum transport: local or non-local?

One of the most significant consequences of gravitational instability is its ability to transport angular momentum throughout the disc. This fact is well known since the '70s in the context of galactic dynamics (Lynden-Bell & Kalnajs 1972). As we have discussed in chapter 2, the ability of transporting angular momentum can be linked to viscous processes. Balbus & Papaloizou (1999) showed that it is possible to write the $R\phi$ component of the GI stress tensor as

$$T^{\mathrm{GI}}_{R\phi} = \int \left\langle \frac{g_R g_\phi}{4\pi G} \right\rangle \mathrm{d}z, \tag{3.63}$$

where g_R and g_ϕ are the radial and azimuthal component of the perturbed gravitational field of the disc. Equation (3.63) only accounts for the transport induced by the gravitational field itself. However, gravitational instability will also induce density and velocity perturbations, that contribute to the transport and should be included in the calculations. This contribution is enclosed in the Reynolds stress, that is simply

$$T_{R\phi}^{\text{Reynolds}} = \Sigma \langle \delta v_R \delta v_\phi \rangle, \tag{3.64}$$

where $\delta v_R, \delta v_\phi$ are the radial and azimuthal perturbations of the velocity field. Given the expression for the gravitational stress tensor, one could be tempted to use the α prescription, and to assume that $T_{R\phi}^{\text{GI}}$ is simply proportional to the local pressure. However, since viscosity is a local dissipation of energy, we need to verify whether GI stresses act locally or not. If the locality condition is respected, it is possible to describe gravitational instability within an $\alpha-$framework.

Now, we turn our attention to the transport of energy and angular momentum through the propagation of spiral density waves. From classical wave mechanics, the energy $\mathcal{E}$ and the angular momentum $\mathcal{L}$ of a wave can be expressed in terms of the wave action $\mathcal{A}$

$$\mathcal{E} = \omega \mathcal{A} = m \Omega_p \mathcal{A}, \tag{3.65}$$

$$\mathcal{L} = m \mathcal{A}. \tag{3.66}$$

Within the WKB approximation, the wave action can be written as (Toomre 1969; Shu 1970; Fan & Lou 1999)

$$\mathcal{A} = \frac{m(\Omega_p - \Omega)}{8\pi^2 G^2 \Sigma} |\delta\Phi|^2, \tag{3.67}$$

where $\delta\Phi$ is the perturbed gravitational potential, given by eq. (3.28). More explicitly, the energy of the wave is given by the sum of two components

$$\mathcal{E} = \frac{\Sigma}{2} \frac{m^2}{k^2} \Omega (\Omega_p - \Omega) \left(\frac{\delta\Sigma}{\Sigma} \right)^2 + \frac{\Sigma}{2} \frac{m^2}{k^2} (\Omega_p - \Omega)^2 \left(\frac{\delta\Sigma}{\Sigma} \right)^2. \tag{3.68}$$

The first component is exactly the wave angular momentum $\mathcal{L}$ times the local angular velocity Ω, and thus it represents a local viscous-like term. Conversely, the second term is an anomalous energy transport term, that acts globally rather than locally (Balbus & Papaloizou 1999). The ratio of the two terms measures the non-locality of the perturbation, and it is

$$\xi = \frac{|\Omega_p - \Omega|}{\Omega}. \tag{3.69}$$

Physically speaking, the transport of the angular momentum will be global if the waves are able to travel far from their co-rotation $(\Omega_p - \Omega)$, and this ability is measured by ξ. How does ξ relate to the disc properties? To answer this question, we examine the Doppler shifted Mach number of the dominant mode $\mathcal{M}$. Cossins et al. (2009) through numerical simulations showed that $\mathcal{M}$ is remarkably close to unity, regardless of the disc to star mass ratio of the disc

$$\mathcal{M} = \frac{|\Omega_p - \Omega| R}{c_s} \simeq 1, \tag{3.70}$$

as shown in the top panel of figure 3.5. The meaning of this condition is explained as follows. A spiral wave generates a shock as soon as it travels far from the co-rotation. The

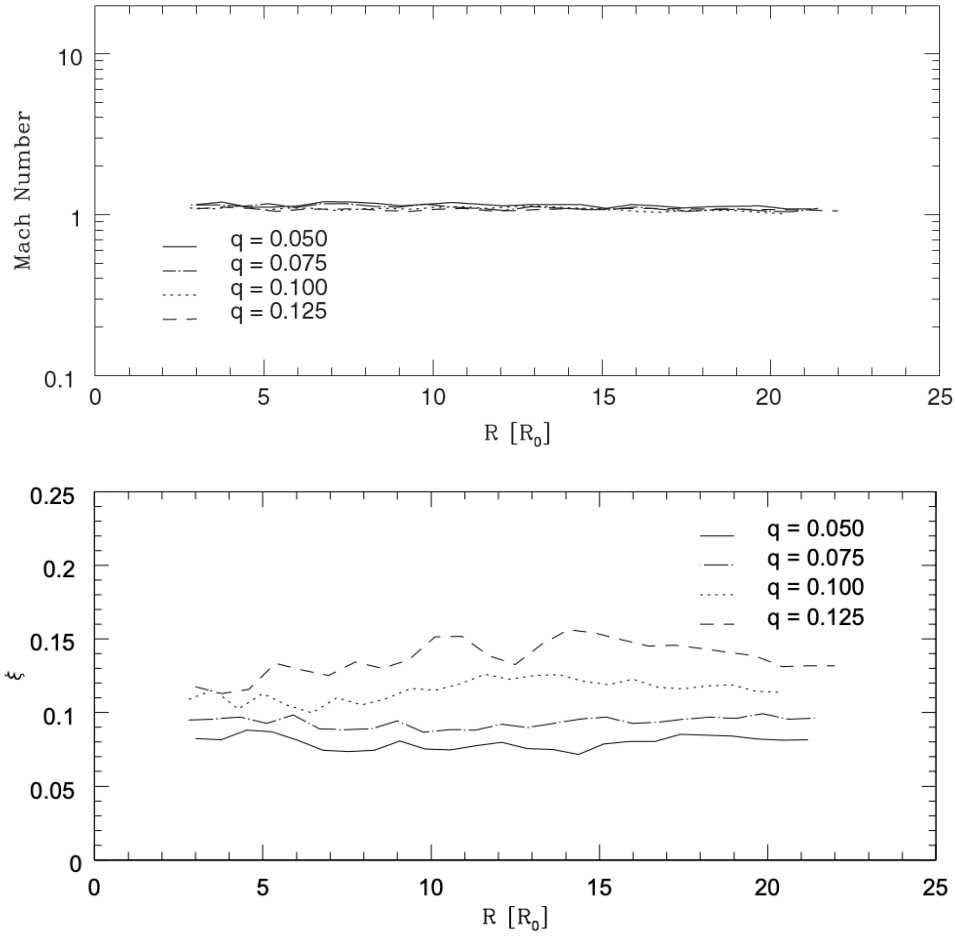

Figure 3.5: Top panel: Bottom panel: Locality parameter ξ for different disc to star mass ratio. As expected, the non locality parameter increases with the disc to star mass ratio, reaching $\sim 15\%$ for $M_d/M_\star = 0.125$. Image taken from Cossins et al. (2009).

sonic condition is telling us that this shock rapidly becomes sonic, dissipating the spiral wave. Thanks to the sonic condition, it is possible to re-write the "locality" parameter as

$$\xi = \frac{c_s}{R\Omega} = \frac{H}{R} \simeq \frac{M_d}{M_\star}, \tag{3.71}$$

where the last identity is true for a marginally stable disc $(Q = 1)$. This last expression is really important because it is telling us that the disc to star mass ratio determines the degree of non-locality of the perturbation, as shown in the bottom panel of figure 3.5.

The non-locality condition, together with the $\mathcal{J}$ parameter (see section (3.2.3)), suggest that low mass and high mass discs behave differently. Under a morphological point of view, Cossins et al. (2009) showed that the average mode number m varies inversely with the mass ratio: hence, high mass discs show fewer spiral arms compared to low mass ones, as depicted in figure 3.6, where we show the power spectrum of the spiral

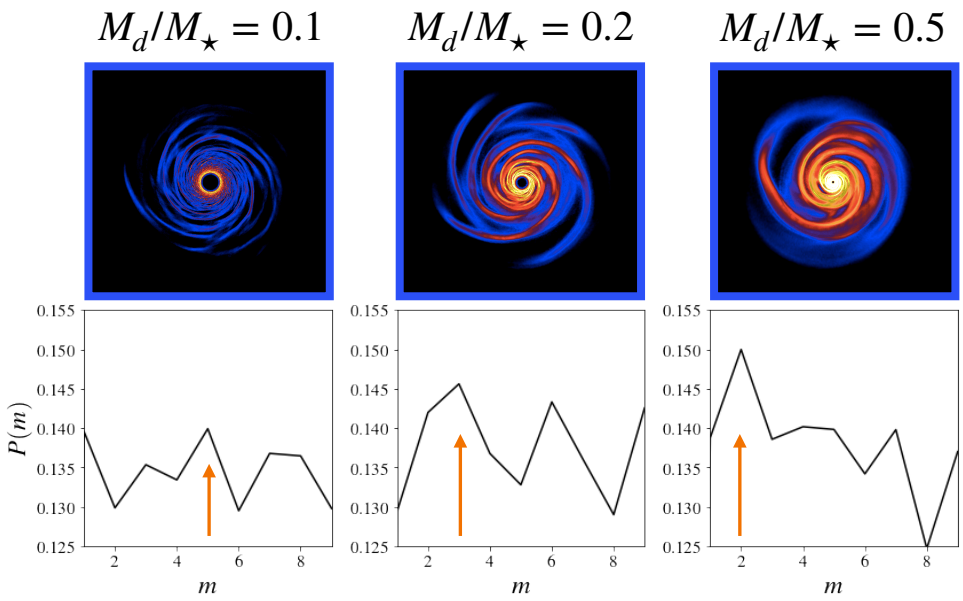

Figure 3.6: Top panel: Snapshots of three numerical SPH simulations of gravitationally unstable protostellar discs, with three different disc to star mass ratios $M_d/M_\star = (0.1, 0.2, 0.5)$. The simulations have been performed with the code PHANTOM and the disc extent is $[0.25, 25]$au. Bottom panel: power spectrum of the three snapshots at an intermediate radius of 10au. The orange arrow underline the dominant mode, that is decreasing with the disc to star mass ratio, as expected. The morphology of the spiral clearly changes with the disc to star mass ratio: more massive discs shows fewer spiral arms and their opening angle is bigger.

structure for different disc to star mass ratios. Additionally, the pitch angle of the spirals is also linked to the disc mass. In particular, there is a positive correlation between the two quantities: high mass discs show more open spiral arms. Moreover, under a dynamical point of view, we have shown that more massive discs tend to become more subject to non-local effects. In the scenario, the self-regulation can not be achieved, resulting in a recurring pattern of highly temporally variable instabilities within the disc (Lodato et al. 2017). During these episodes, the torques generated by self-gravity can attain significant magnitudes, redistributing very fast the gas material in the disc.

However, Lodato & Rice (2004) showed that for typical protostellar disc, $(M_d/M_\star < 0.2)$, the transport of angular momentum by GI is local, since ξ remains small. Hence, for such systems, GI acts as a viscous phenomenon.

3.3.3 Cooling driven GI

A key role in the evolution of self-gravitating protostellar disc is played by the cooling. Indeed, we will show that the balance between the disc cooling and the internal heating mechanisms allows the system to reach a self-regulated state. In addition, the cooling also determines the amount of the angular momentum that is transported.

Although recently a lot of effort has been put into the development of realistic cooling prescription (Stamatellos et al. 2007), for our purposes, a very simple cooling law can be adopted to explore the role of the cooling timescale in the outcome of the gravitational

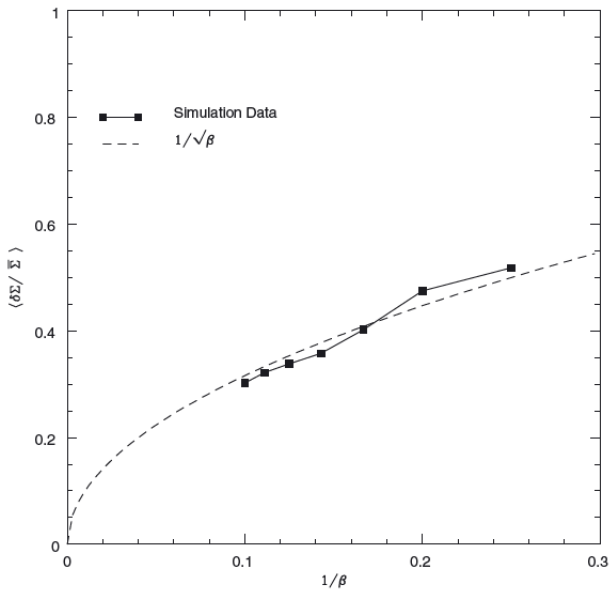

Figure 3.7: Relationship between the density contrast of the spiral perturbation $\delta\Sigma/\Sigma$ and cooling factor β (Cossins et al. 2009). As expected from the energy balance, in thermal saturation regime $\delta\Sigma/\Sigma \propto \beta^{-1/2}$

instability. It reads

$$\left.\frac{\mathrm{d}e}{\mathrm{d}t}\right|_{\mathrm{cool}} = -\frac{e}{t_{\mathrm{cool}}}, \tag{3.72}$$

where e is the internal energy of the fluid and t_{cool} is the cooling timescale. It is important to stress that the above description is not meant to reproduce any specific cooling process. In the following part, we will suppose that the cooling time is proportional to the dynamical time, and the constant of proportionality is called beta-cooling

$$\beta = \Omega t_{\mathrm{cool}}. \tag{3.73}$$

According to the value of β, there are two possible scenarios: a thermal saturation regime, where the instability saturates and angular momentum is efficiently transported, and the fragmentation of the spiral into gravitationally bounded objects.

Thermal saturation

When $\beta > 3$ (Gammie 2001; Deng et al. 2017), the heating provided by gravitational instability compensates the imposed cooling, and the system reaches a thermal saturated regime. This means that the amplitude of the spiral perturbation saturates at a given value and the system sets in a self regulated state characterized by a constant $Q = 1$ profile. In this sense, the $Q-$stability condition acts as a thermostat so that heating turns on only if the system is sufficiently cold, keeping it in a marginal stable state.

In terms of the heating, Cossins et al. (2009) obtained heating rate per unit mass due

to the gravitational instability as

$$q^+ = \epsilon \Omega c_s^2 \frac{\mathcal{M}\tilde{\mathcal{M}}}{2} \left(\frac{\delta\Sigma}{\Sigma} \right)^2, \tag{3.74}$$

where ϵ is the heating factor, defined as the cooling one and $\mathcal{M}$ and $\tilde{\mathcal{M}}$ are the phase and Doppler-shifted phase Mach numbers, defined as

$$\mathcal{M} = \frac{m\Omega_p}{kc_s}, \qquad \tilde{\mathcal{M}} = \frac{m|\Omega_p - \Omega|}{kc_s}. \tag{3.75}$$

Once the gravitational instability is saturated, we consider the disc to be in dynamic thermal equilibrium, such that the energy released through spiral shocks and compression heating is balanced by the imposed cooling, i.e $q^+ + q^- = 0$, where we recall the cooling rate per unit mass

$$q^- = -\frac{e}{t_{\text{cool}}} = -\frac{\Omega c_s^2}{\gamma(\gamma-1)\beta}, \tag{3.76}$$

where we have used $e = c_s^2/\gamma(\gamma-1)$ (eq. 2.73). Now, we can equate the heating and the cooling rate per unit mass, and determine the relationship between the amplitude of the spiral perturbation and the cooling factor

$$\left(\frac{\delta\Sigma}{\Sigma} \right)^2 = \frac{2}{\epsilon\beta} \frac{1}{\gamma(\gamma-1)} \left(\frac{1}{\mathcal{M}\tilde{\mathcal{M}}} \right) \propto \beta^{-1}. \tag{3.77}$$

This relationship is really important, since it tells us that the strength of the spiral perturbation is proportional to $\beta^{-1/2}$. This behaviour is confirmed by numerical simulations (Cossins et al. 2009), as shown in figure 3.7.

Thus, for a disc in thermal saturated regime, there are two important parameters that determines the morphology of the spiral. Firstly, the number of spiral arms and the pitch angle are determined by the disc to star mass ratio. In particular, more massive discs show fewer spiral arms, that are more open. Conversely, low mass discs show a high number of spiral arms, that are tightly wound. The second important parameter is the cooling factor, and it determines the amplitude of the spiral, according to eq. (3.77). A summary of the morphological properties of GI spiral is given in figure 3.8.

Finally, we compute the relationship between the viscosity and the cooling time in thermal equilibrium. Indeed, assuming that there is no other source of heating in the disc, in equilibrium the heating rate provided by viscosity should balance the cooling. Hence, by imposing $t_{\text{cool}} = t_{\text{th}}$ (equations 3.73 and 2.74 respectively), we obtain that the $\alpha-$coefficient associated to gravitational instability is

$$\alpha_{\text{GI}} = \frac{4}{9\gamma(\gamma-1)\beta}. \tag{3.78}$$

Fragmentation

If the cooling is too fast, the heating provided by gravitational instability can not balance it, resulting in the exponential growth of the spiral perturbation. In this regime, the thermal saturation is not reached, and the spiral fragments into gravitationally bounded objects.

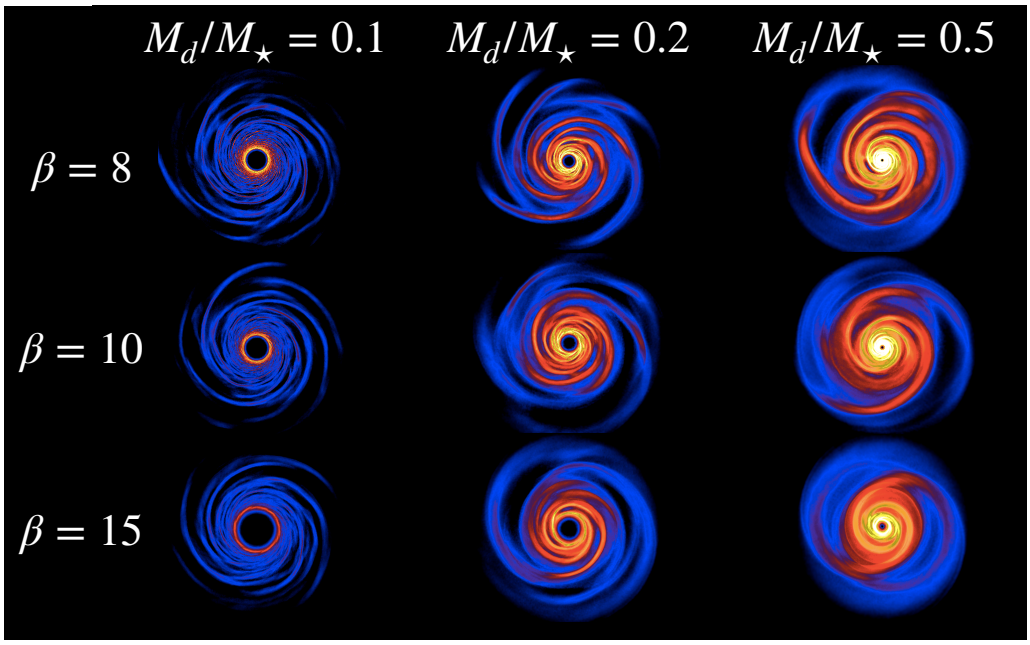

Figure 3.8: Morphology of GI spirals for different cooling factor β and disc to star mass ratio $M_d/M_\star$. All the simulations have been performed with the SPH code PHANTOM (Price et al. 2018b).

The critical value of beta has been a subject of extensive debate during the last twenty years. Firstly, Gammie (2001) performed shearing box simulations of gravitational instability using the $\beta-$cooling prescription. He found that if the cooling timescale is faster than approximately 3 times than the dynamical one, fragmentation occurs. Afterwards, Rice et al. (2005) tackled this problem through three-dimensional global SPH simulations. They found that, depending on the value of the γ coefficient, the critical value of β is between 6 and 10. Meru & Bate (2010) and Meru & Bate (2011) performed high resolution SPH simulations, and they did not find convergence in their results when using a different number of gas particles. Lodato & Clarke (2011) proposed that this behaviour could be driven by resolution effects. One year later, Meru & Bate (2012) obtained evidence that convergence with increasing resolution occurs with SPH, as long as the effects of numerical viscosity are taken into account[1]. Additionally, they also found convergence for grid based codes, however the results were in contrast with the particle based ones. From this analysis, they found that $\beta_{\rm crit}$ is larger than previously thought. In particular, for $\gamma = 5/3$, the critical β is higher than 20, implying that young discs are very likely to fragment. Finally, Deng et al. (2017) obtained convergence between SPH and grid based codes, and the value of β below which fragmentation occurs is

$$\beta_{\rm crit} = 3, \tag{3.79}$$

as firstly proposed by Gammie (2001). A minimum value of β implies a maximum value of α, i.e. the maximum amount of angular momentum that can be transported through

[1]In particular, the authors found that reducing the dissipation from the numerical viscosity leads to larger values of the critical cooling time at a given resolution. This happens because the numerical dissipation in SPH depends on the resolution.

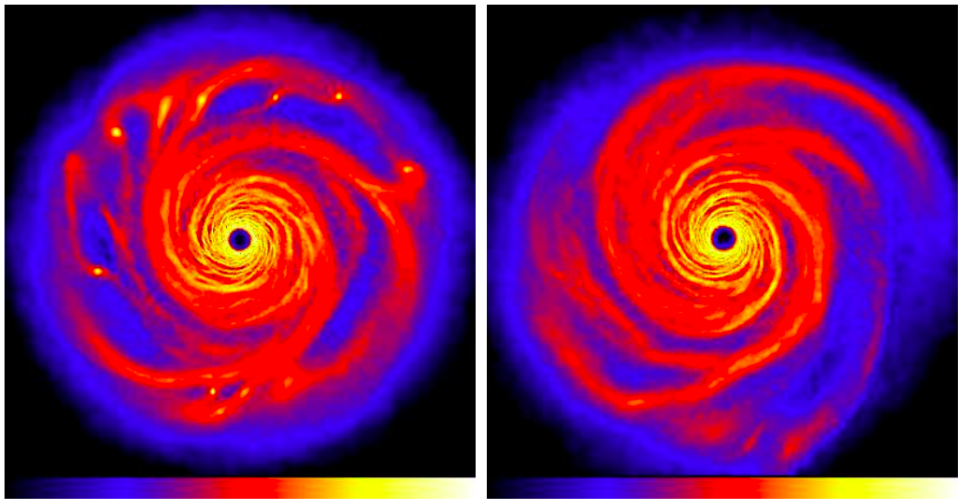

Figure 3.9: SPH simulation of a gravitationally unstable disc that shows fragmentation (left panel) and thermal saturation (right panel) from Rice et al. (2005).

GI. For $\beta_{\rm crit} = 3$, the maximum value of α is

$$\alpha_{\rm max} = 0.13, \tag{3.80}$$

for $\gamma = 5/3$. Figure 3.9 shows both the cases of fragmentation and thermal saturation.

3.3.4 Accretion driven GI

In this section, we briefly discuss a second path to trigger gravitational instability, that is the evolution of the disc surface density due to infall. We consider a disc with $Q >> 1$, that undergoes infall from the environment such that Q, eventually, reaches the unity. As the system reaches the marginal stability condition, gravitational instability turns on, and transports angular momentum. In discs undergoing infall at some rate $\dot{M}_{\rm inf}$, it exists a regulation mechanism akin to thermal saturation. We suppose that gravitational instability can provide accretion up to a maximum value $\dot{M}_{\rm max,GI}$. If $\dot{M}_{\rm inf} < \dot{M}_{\rm max,GI}$, the disc can transport material at the same rate it is being fed, and the disc mass acts as a regulator of the process (Kratter et al. 2010). Otherwise, if $\dot{M}_{\rm inf} > \dot{M}_{\rm max,GI}$, the disc will eventually fragment (Kratter et al. 2008). In order to predict what sets the maximum rate of accretion induced by GI, Kratter et al. (2010) introduced two dimensionless parameters that are strong predictors of fragmentation driven by accretion. The parameters are

$$\xi = \frac{\dot{M}_{\rm inf}}{c_s^3/G} \tag{3.81}$$

and

$$\Gamma = \frac{\dot{M}_{\rm inf}}{M_T \Omega}, \tag{3.82}$$

where M_T is the total system mass (disc + envelope). The first parameter refers to the isothermal sphere collapse rate, and the second one is the ratio between the dynamical

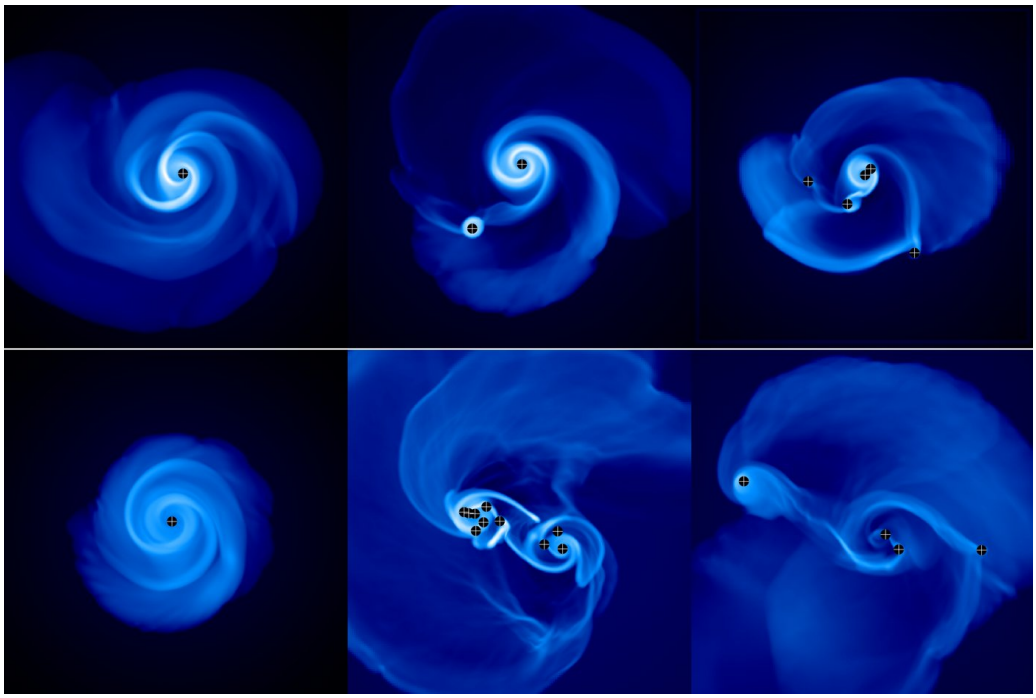

Figure 3.10: Isothermal simulation of accretion driven gravitational instability from Kratter et al. (2010). For different values of ξ and Γ, a steady configuration can be obtained (top left and bottom left panel), or fragmentation can occur.

timescale and the mass doubling one. Kratter et al. (2010) performed a suite of three-dimensional isothermal simulations of discs undergoing self-similar accretion (see figure 3.10), and found that fragmentation occurs when

$$\Gamma > \frac{\xi^{2.5}}{850}. \tag{3.83}$$

Afterwards, Offner et al. (2010) and Zhu et al. (2012) confirmed this results, using more realistic thermal physics.

3.4 Planet formation through gas fragmentation

In the '90s, the discovery of the first extrasolar giant planet (Mayor & Queloz 1995) presented a significant challenge to theorists, as the widely accepted core accretion model could not explain the formation of such a massive planet, because of the too long timescale. Boss (1997) proposed gravitational instability as an alternative paradigm for giant planet formation. For disc to star mass ratios of the order of $\gtrsim 0.1$, the outer part of the disc is likely to be marginally gravitationally unstable, according to the $Q-$criterion. If the thermal saturation is not reached, because of a too short cooling time, gas fragmentation can happen. Boss (1997) proposed gas fragmentation as a way to rapidly form planets in the outer disc. One natural question to ask is: what is the typical mass of a GI fragment? We expect that the mass of the fragment is of the order of the Jeans mass. In section 3.2.1

we showed that the Jeans length for the quadratic dispersion relation is $\lambda_J = 2\pi H_{\rm sg}$. Thus, the Jeans mass is

$$M_J = \Sigma\lambda_J^2 = 4\pi \left(\frac{H}{r}\right)^4 \frac{M_\star}{M_d} M_\star = 10^{-2} \left(\frac{H/r}{0.1}\right)^4 \left(\frac{M_d/M_\star}{0.1}\right)^{-1} M_\star; \tag{3.84}$$

this means that for a solar mass star, the typical Jeans mass is of the order of $\sim 10 M_{\rm jup}$, where $M_{\rm jup}$ is the Jupiter mass. It is important to note that this value is just an initial mass. Indeed, the GI fragment will start accreting material in the disc, that is dense because the disc is massive. This process will lead to runaway accretion, and to the formation of a stellar companion (Kratter & Matzner 2006; Kratter & Lodato 2016) rather than a planet. Indeed, the theoretical minimum mass a star must have to undergo fusion at the core, is estimated to be about $75 \mathrm{M_{jup}}$ (Prialnik 2009), and it can be rapidly reached in those conditions. Although it solves the timescale problem, the standard gravitational instability scenario is not likely to explain the formation of planets, without invoking *ad hoc* mechanisms, such as tidal downsizing Nayakshin (2017). However, there is ongoing research whether this could explain the formation of giant planets in early discs, such as AB Aur (Cadman et al. 2021).

CHAPTER 4

Gas kinematics in protostellar discs

Gas emission from planet-forming environments traces the kinematics of the disc, i.e. the observed velocity field. Kinematics is a powerful tool to investigate physical phenomena happening in protoplanetary discs, since it is possible to reach incredibly high spatial and spectral resolution with ALMA telescope. This offers a unique opportunity to map the velocity of these systems, investigating the physical conditions in which planets form. Recently, ALMA observational campaigns have been pushing the resolution to incredible limits: an example is the MAPS large program (PI: K. Öberg, Öberg et al. (2021)), whose aim was to map complex molecules' emission in five protoplanetary discs. The quality of these data is so high that velocities are measured with a precision of the order of 100 m/s. Another ongoing ALMA large program is exoALMA (PI: R. Teague), whose aim is to observe 15 protoplanetary discs at incredible high resolution to study the natal environment of protoplanets. Here, the velocity resolution will be almost 4 times better than in MAPS: these extraordinary data offer a unique opportunity to conduct high precision kinematical studies

4.1 Velocity field in protostellar discs

The vast majority of the gas mass in protoplanetary discs is molecular hydrogen (H_2) that, because of its chemical structure, can't be detected. This is primarily because the molecule lacks a dipole moment due to its symmetry, and all ro-vibrational transitions within the electronic ground state are quadrupolar, making them faintly observable in the near infrared. Luckily, other gas tracers are available in protoplanetary discs: the most abundant are isotopologues of carbon monoxide (CO). In particular, the most commonly used in kinematics are ^{12}CO, ^{13}CO and C^{18}O. The spatial distribution of these molecules depends on the disc characteristics and on the chemistry of these environments. In general, ^{12}CO, which is the most abundant isotopologue, is not a good tracer of the disc midplane, because its emission comes from the disc surface. On the contrary, the other two less abundant CO isotopologues, ^{13}CO and C^{18}O, traces better the disc midplane, since their emission is deeper. However, their spatial extent is smaller compared to the ^{12}CO. These molecules emit through rotational electromagnetic transitions at a given rest frequency: this is called line emission. If the molecule is moving towards the line of sight, the frequency of emission will be Doppler-shifted, according to its velocity. By knowing the rest frequency and measuring the Doppler-shift, it is possible to map the velocity field of protoplanetary discs.

What are the typical velocities in protostellar discs? Of course, the dominant motions are the azimuthal ones. As a first approximation, azimuthal motions are Keplerian, and

the magnitude is of the order of few km/s

$$v_k = \sqrt{\frac{GM_\star}{R}} = 2.97 \left(\frac{M_\star}{1\mathrm{M}_\odot}\right)^{1/2} \left(\frac{R}{100\mathrm{au}}\right)^{-1/2} \mathrm{km/s}. \tag{4.1}$$

In a pure viscous disc, radial motions are related to accretion processes; as shown in chapter 2, their magnitude is very small, since accretion takes place in secular timescale. A rough estimate of the radial velocity is

$$v_R \simeq \alpha \left(\frac{H}{R}\right)^2 v_k = 0.297 \left(\frac{\alpha}{0.01}\right) \left(\frac{H/R}{0.1}\right)^2 \mathrm{m/s}. \tag{4.2}$$

The molecular emission is set both by the global velocity and the local linewidth. In this context, a crucial velocity to take into account is the sound speed. As already mentioned at the beginning of chapter 2, the sound speed is smaller compared to the Keplerian motion, and its magnitude is of the order of $\sim 100\mathrm{m/s}$

$$c_s = \sqrt{\frac{k_B T}{\mu m_p}} = 281 \left(\frac{T}{20\mathrm{K}}\right)^{1/2} \mathrm{m/s}. \tag{4.3}$$

4.2 A detailed model for the rotation curve of a protostellar disc

As mentioned before, the dominant motion in protostellar discs is the rotation around the central object. Thanks to the incredibly high spatial and spectral resolution of ALMA telescope, it is possible to study in detail the azimuthal velocity profile. Hence, a detailed model for the rotation curve of a protostellar disc is needed. Here, we refer to the model presented by Lodato et al. (2023).

In centrifugal balance, the rotation curve of a disc is given by

$$v_\phi^2 = R\frac{\partial \Phi_\star}{\partial R}(R,z) + \frac{R}{\rho}\frac{\partial P}{\partial R}(R,z) + R\frac{\partial \Phi_\mathrm{d}}{\partial R}(R,z), \tag{4.4}$$

where the first term is the contribution of the stellar gravitational potential (see section 2.1.1)

$$R\frac{\partial \Phi_\star}{\partial R} = v_k^2 \left(1 + \frac{z^2}{R^2}\right)^{-3/2}, \tag{4.5}$$

the second is the pressure gradient (see section 2.1.1)

$$\frac{R}{\rho}\frac{\partial P}{\partial R} = v_k^2 \left(\frac{H}{R}\right)^2 \frac{\partial \log \rho}{\partial \log R}, \tag{4.6}$$

and the third term is the self-gravitating contribution of the disc (see section 3.1). We assume that the disc surface density is described by the self-similar solution (see eq. (2.44))

$$\Sigma(R) = \frac{(2-\gamma)M_\mathrm{d}}{2\pi R_\mathrm{c}^2} \left(\frac{R}{R_\mathrm{c}}\right)^{-\gamma} \exp\left[-\left(\frac{R}{R_\mathrm{c}}\right)^{2-\gamma}\right], \tag{4.7}$$

where M_d is the disc mass and R_c is the scale radius. For what concerns the vertical disc structure, we assume that the disc is vertically isothermal and that the density is given by (see section 2.1.1)

$$\rho(R,z) = \rho_{\rm mid}(R) \exp\left[-\frac{R^2}{H^2}\left(1 - \frac{1}{\sqrt{1+z^2/R^2}}\right)\right]. \tag{4.8}$$

Radially, we assume the temperature to be a power law

$$T(R) = T_c \left(\frac{R}{R_c}\right)^{-q}. \tag{4.9}$$

Neglecting for the moment the disc contribution to the gravitational potential, the rotation curve is given by

$$v_\phi^2 = v_k^2 \left\{1 - \left[\gamma' + (2-\gamma)\left(\frac{R}{R_{\rm c}}\right)^{2-\gamma}\right]\left(\frac{H}{R}\right)^2 - q\left(1 - \frac{1}{\sqrt{1+(z/R)^2}}\right)\right\}, \tag{4.10}$$

and this is valid for a tapered power law surface density, where $v_k^2 = GM_\star/R$ is the Keplerian velocity and $\gamma' = \gamma + 3/2 + q/2$. The disc contribution to the rotation curve is

$$v_d^2(R,z) = G\int_0^\infty \left[K(k) - \frac{1}{4}\left(\frac{k^2}{1-k^2}\right) \times \right. \tag{4.11}$$
$$\left.\left(\frac{r}{R} - \frac{R}{r} + \frac{z^2}{Rr}\right)E(k)\right]\sqrt{\frac{r}{R}}k\Sigma\left(r\right)dr,$$

and a discussion about this term is given in section 3.1. Since Σ scales as the disc mass, it is easy to see that the disc contribution to the rotation curve is order $O(M_{\rm d}/M_\star)$ with respect to the standard Keplerian term.

We see that there are three corrections to a pure Keplerian profile. The first one is due to the radial pressure gradient, it is sub-Keplerian (i.e. it is a negative contribution to v_ϕ^2 and is given by

$$\frac{\delta v_p^2}{v_k^2} = -\left[\gamma' + (2-\gamma)\left(\frac{R}{R_{\rm c}}\right)^{2-\gamma}\right]\left(\frac{H}{R}\right)^2, \tag{4.12}$$

where v_p^2 is the pressure gradient contribution to the rotation curve (i.e. the term proportional to $(H/R)^2$ in eq. (4.10). This term is generally of the order of $(H/R)^2$, and is important in the outer part of the disc, since it increases with the radius. For typical values of γ' and H/R, the correction due to the radial pressure gradient becomes important for $R \gtrsim 4R_c$.

The second one is due to the fact that we evaluate the rotation curve at a finite height z and is due to both the stellar gravitational field and the pressure gradient. It is also sub-Keplerian and is given by

$$\frac{\delta v_z^2}{v_k^2} = -q\left(1 - \frac{1}{\sqrt{1+(z/R)^2}}\right) \approx -\frac{q}{2}\left(\frac{z}{R}\right)^2, \tag{4.13}$$

where v_z^2 is given by the term proportional to q in eq. (4.10). Also this term is of order of $(H/R)^2$. Finally, the third correction is due to self-gravity, and it is a super-Keplerian

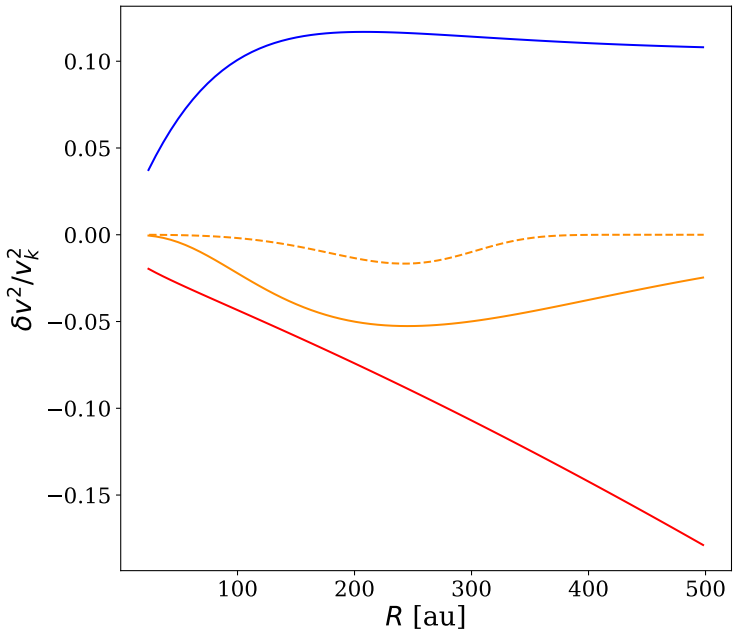

Figure 4.1: The three sources of non Keplerianity in IM Lup as resulting from Lodato et al. (2023) model. In blue, the self-gravitating term, in red the radial pressure gradient δv_p^2 and in orange the vertical height term δv_z^2 (solid line for ^{12}CO and dashed line for ^{13}CO), emphasising the effect of looking at the curve from an emission layer at a given height.

contribution. The relative importance of these three corrections to Keplerian rotation depends on the ordering of the two dimensionless parameters H/R and $M_{\rm d}/M_\star$. The self-gravity correction is negligible when $M_{\rm d}/M_\star \ll (H/R)^2 \approx 0.01$. On the other hand, for a marginally gravitationally unstable disc, for which $M_{\rm d}/M_\star \approx H/R$, the self-gravity correction dominates over the pressure one[1]. At the same time, there may well be a range of parameters such that $(H/R)^2 < M_{\rm d}/M_\star < H/R$, in which self-gravity gives a dominant contribution to the rotation curve, while the disc is gravitationally stable (Veronesi et al. 2021). Figure 4.1 shows the three sources of non Keplerianity for the disc IM Lup, from Lodato et al. (2023). The most important terms are the pressure gradient and the self-gravity, that contribute $\sim 5-10\%$ of the Keplerian velocity.

4.3 What we observe

The end product of molecular line observations is a *datacube* (see fig. 4.2). This object has three axes, two spatial (sky coordinates) and a frequency one. Knowing the rest frequency of the chosen molecular line and the systemic velocity of the system, the frequency axis can be eventually converted into a velocity axis. As already mentioned, most of the gas content of the disc is molecular hydrogen, that does not emit because of its symmetry. Therefore, one should rely on molecular tracer such as CO isotopologues. The emission of a molecule is spatially located in the region of the disc where it is most abundant. This enables us to probe different vertical and radial regions of the disc with different tracers. As an example, because of the different vertical distribution of the CO isotopologues, the abundant ^{12}CO traces a region that is about 3-4 times the hydrostatic scale height H, while ^{13}CO and C^{18}O about one.

To understand what a velocity map looks like, we consider a protoplanetary disc inclined towards the line of sight of an angle i. If we simply assume that gas particles move with a purely azimuthal velocity, the projected velocity towards the line of sight will be

$$v_{\rm obs} = v_\phi \sin i \cos\phi, \tag{4.14}$$

where v_ϕ is the azimuthal Keplerian velocity, ϕ is the azimuthal angle in the protoplanetary disc and i is the disc inclination (where $i = 0$ means a face-on disc). The observed velocity field is divided into two parts: a blue-shifted one, where the observed velocity is negative, and a red-shifted one, where it is positive. At a given frequency (velocity), molecular line emission is concentrated along an isovelocity curve, i.e. the region where the projected velocity is constant. Since the velocity field of protostellar discs is dominated by the Keplerian rotation, the isovelocity curves follow a *butterfly pattern*, as shown in figure 4.2. In general, if the disc has azimuthal, radial and vertical velocities, the observed velocity field will be

$$v_{\rm obs} = (v_\phi \cos\phi + v_R \sin\phi)\sin i + v_z \cos i + v_{\rm sys}. \tag{4.15}$$

While pre-ALMA observations were able to probe just the Keplerian velocity of protoplanetary discs (Sargent & Beckwith 1987; Dutrey et al. 2014), with ALMA it is possible to spatially resolve the emission, and disentangle the upper and lower surface contribution (Disk Dynamics Collaboration et al. 2020).

An alternative way to look into kinematic data is to spectrally collapse the datacube into moment maps. The most significant moment maps are the moment zero and the

[1] In the marginally unstable case $M_d/M_\star \approx H/R$, and this comes from the fact that the Toomre-Q parameter is equal to 1. Indeed, $Q = H/R/(M_d/M_\star)$.

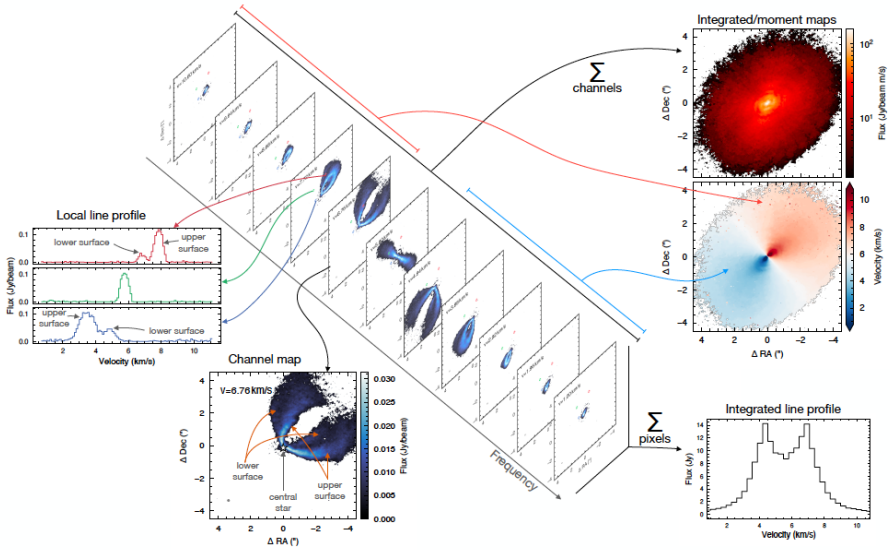

Figure 4.2: Graphical representation of a datacube, taken from Pinte et al. (2020).

moment one, and are computed as follows

$$M_0 = \sum_j^{N_{\rm ch}} I_j, \tag{4.16}$$

and

$$M_1 = \sum_j^{N_{\rm ch}} \frac{I_j v_j}{M_0}, \tag{4.17}$$

where the index j runs over the channels and I is the intensity. The zeroth moment displays the integrated intensity, hence it reveals the global morphology of the emission (top right panel of figure 4.2), while the first moment is the intensity weighted average velocity (central right panel of figure 4.2).

4.3.1 Extracting the height of the emitting layer

The combination of high spatial and spectral resolution and sensitivity offered by ALMA allows us to directly map the disc thermal and kinematic structure, by resolving the gas disc both radially and vertically. As a matter of fact, it is possible to locate gas emitting surfaces, directly reconstructing the position and velocity of each layer. In this context, discs at intermediate inclinations are ideal targets, as the Keplerian motion allows the separation of the upper and lower emitting surfaces. The left panel of figure 4.3 displays a schematic view of the various layers observed in the CO lines.

Pinte et al. (2018a) presented a simple geometrical method to reconstruct the position of the CO emitting layers. To apply this method, the inclination and position angle of the source should be known. Figure 4.3 displays the geometrical method. For a given

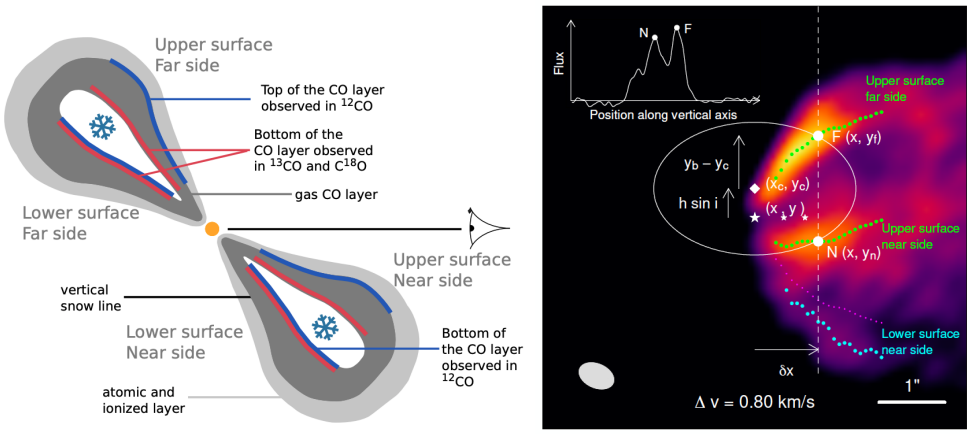

Figure 4.3: Left panel: sketch of the various layers observed in the CO lines (Pinte et al. 2018a). Right panel: schematic description of the geometrical method of Pinte et al. (2018a).

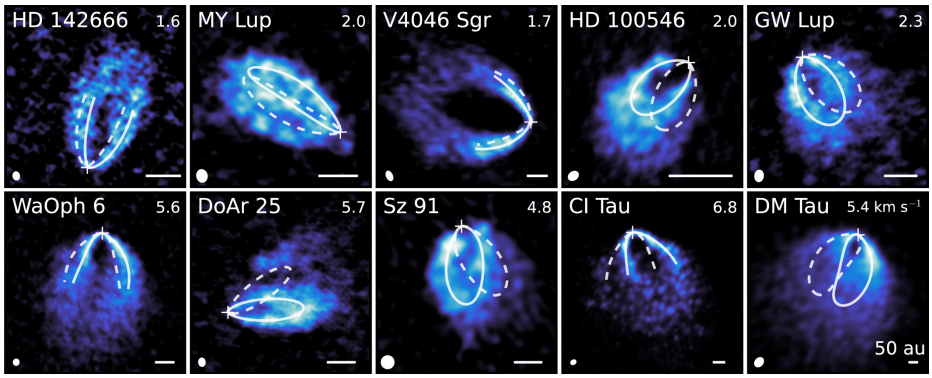

Figure 4.4: Upper and lower emission surfaces for 10 discs with mid-inclination, from Law et al. (2022).

channel, the image is rotated of an angle PA, in order to have the disc semi major axis parallel to the x axis. The position of the central object is marked by a star. For a given offset δx along the disc major axis, there are two maxima in the emission (N and F), that corresponds to the emission coming from the upper near and far side of the disc. These points belong to the same inclined circular orbit, that is the white ellipsis. In order to compute the ellipsis, the inclination of the disc is needed. At this point, the height of the emission is simply computed as the offset between the centre of the ellipse (x_c, y_c) and the star position $(x_\star, y_\star)$, according to

$$h = \frac{y_c - y_\star}{\sin i}. \tag{4.18}$$

In principle, if the data allows to, it is also possible to constrain the orientation of the lower emitting surface. Figure 4.4 shows the geometrical method successfully applied to a set of protostellar discs, where the two emission surfaces of CO are visible and disentangled.

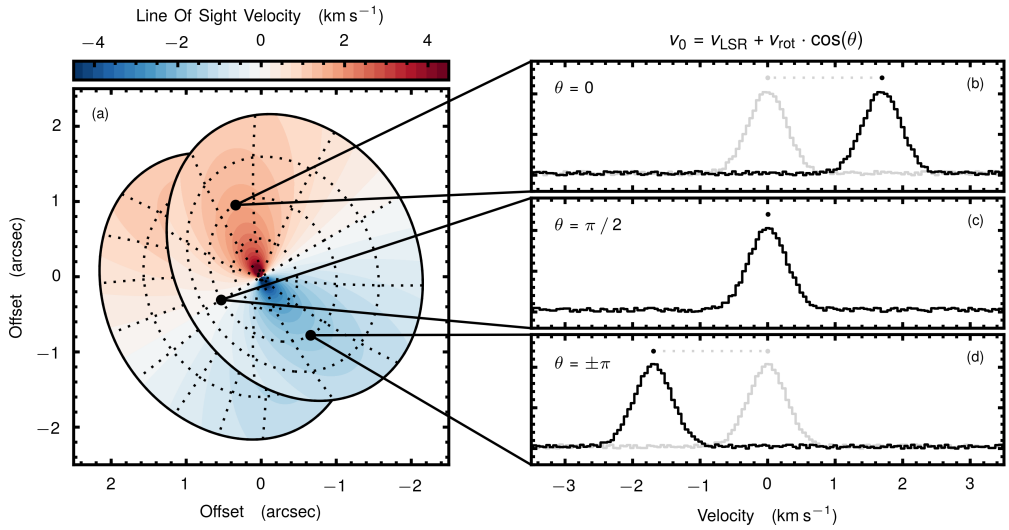

Figure 4.5: Schematic view of the simple harmonic oscillator method to extract the velocity profiles (Teague et al. 2018).

An important point to underline is that the geometrical method is valid if the emission originates from a vertically thin layer, so that the emitting layer is well-defined. Thus, in the case of diffuse emission, this method does not give accurate results, as it is not possible to define a proper emitting surface. A clear example of this is the outer region of the IM Lup disc (Pinte et al. 2018a; Izquierdo et al. 2023), where the surface can not be constrained. Another important assumption that has been made to derive this method is that the disc is axisymmetric.

4.3.2 Extracting the velocity profiles

Extracting a velocity profile may appear straightforward at first, but it is a task full of challenges. Several difficulties can emerge during the process, and there are instances where the initial working assumptions are not respected, making this job exceptionally demanding. Currently, there is significant ongoing research and effort to find the best method to extract rotation profiles (e.g. Izquierdo et al. (2023)). So far, there are several ways to do so: in this thesis we are not interested in characterizing each of them, and we will present the "Simple harmonic oscillator" (SHO) method as an illustrative case. We follow the explanation provided in Teague et al. (2018). Figure 4.5 gives a schematic view of the process.

The first assumption we make is that the system is axisymmetric. If we know the height of the emitting layer $z(R)$ and the disc geometry (inclination and position angle), we can associate the spectrum at any given (projected) location in the disc to its radial distance from the centre of the disc. Because of the axisymmetric hypothesis, we expect the spectra to have the same shape (i.e., peak and width), but to have their line centres shifted by the local velocity of the disc, projected along the line of sight ($v_{\rm obs}$). Under the assumption that the line profiles are the same, we can infer the underlying velocity structure. The easiest approach to take into account the velocity shift is to describe the line centroid as a harmonic oscillator. In the simplest case of only azimuthal motion, we

recall the observed velocity

$$v_{\rm obs}(R,\phi) = v_\phi(R)\sin i\cos\phi + v_{\rm sys}, \tag{4.19}$$

where v_ϕ is the azimuthal velocity, $v_{\rm sys}$ is the systemic velocity, i is the inclination of the disc, and ϕ is the azimuthal angle in the disc plane. Note that ϕ and R are retrieved from any projected location by assuming a thin emitting layer, with height $z(R)$. Then, there are different methods to fit the line centroids, as the Quadratic method and the Gaussian method, each of them showing pros and cons. In particular, the Quadratic fit is dependent on the velocity sampling, and it is also sensitive to the channel correlation. As for the Gaussian method, note that the selected velocity range may affect the result in case of skewed profiles. For a thorough explanation of these methods, see Teague et al. (2018). Within this framework, the value of the azimuthal velocity at a fixed radial location is the one that "aligns" the spectra (i.e. the location of their peak emission) in the annulus in a velocity-azimuth plot, after shifting the spectrum at each azimuth according to a cosine functional form. More generally, the Simple Harmonic Oscillator (SHO) method is able to also obtain the radial velocity by modelling the velocity shift as

$$v_{\rm obs}(R,\phi) = v_\phi(R)\sin i\cos\phi + v_R(R)\sin i\sin\phi + v_{\rm sys}. \tag{4.20}$$

Yet, there is another feature that needs to be accounted for. It is known that the impact of the disc lower emission surface on the observed velocities can be critical when it comes to kinematical analyses of high resolution observations of molecular lines in discs (see e.g. Izquierdo et al. (2021, 2022); Pinte et al. (2022); Izquierdo et al. (2023)). For instance, the lower surface can systematically shift the centroid of the observed intensity profile as a function of the disc coordinates, affecting the velocities derived via first moment maps or via parametric fits to the line profile (see e.g. Fig A2 of Izquierdo et al. (2021)). Alternatively, at the cost of velocity accuracy, some methods derive velocities around the peak of the line profile to approximately account for the contribution of the disc upper surface only (see e.g. Teague et al. (2018)). However, when the emission is optically thin, or even marginally optically thick, these methods struggle at distinguishing between the two surfaces as the intensity contrast between both can be very small. An alternative method to disentangle the signal coming from the upper and lower surface is implemented in the code DISCMINER (Izquierdo et al. 2021, 2022, 2023), and consists in using "double moment maps", i.e. moment maps that fit the spectra with a double-peak function. In this way, it is possible, in principle, to obtain the velocity field of both surfaces. While this method works well for mid-high inclination discs, and for optically thick tracers as the ^{12}CO, when the emission coming from the upper and lower surfaces can not be easily disentangled it fails. An example of this method working is shown in figure 4.6, where both the signal coming from the upper and lower surface of the ^{12}CO in the disc HD 163296 have been successfully reconstructed using a double moment map.

4.3.3 Extracting the 2D thermal structure

Combining the line emitting surfaces and the peak surface brightness, it is possible to extract the two-dimensional (R, z) temperature structure of protoplanetary discs. As a matter of fact, the pixels in the datacube contain information about the peak surface brightness that can be converted into gas temperature for optically thick lines. Hence, by knowing the radial and vertical position of the emitting material, the temperature structure at the emitting layer can be probed. Combining multimolecular and / or different transitions allows reconstructing the whole thermal structure of the disc. As already

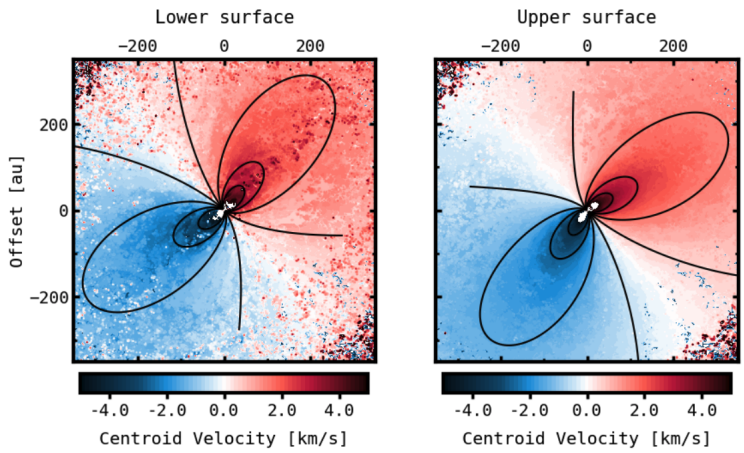

Figure 4.6: Reconstruction of centroid velocities from the lower and upper emitting surfaces of the HD 163296 disc as observed in ^{12}CO $J = 2 - 1$ (Izquierdo et al. 2022).

mentioned, this method can be applied only to optically thick tracers, where the gas brightness temperature is a good estimate of its temperature. At the typical densities and temperatures of protoplanetary discs, the CO, and the ^{13}CO $J = 2 - 1$ lines are optically thick and in local thermal equilibrium (Weaver et al. 2018), hence these tracers are perfect for this purpose. Each pixel of the datacube has the value of the peak surface brightness I_ν. Under the previous hypotheses, the associated gas temperature is

$$T_b = \frac{h\nu}{k_B} \left[\log \left(\frac{2h\nu^3}{c^2 I_\nu} \right) + 1 \right]. \tag{4.21}$$

An example of this method applied to the discs belonging to the MAPS sample (Öberg et al. 2021) is shown in figure 4.7 (Law et al. 2021).

4.4 Kinematic signatures

While the number of systems where kinematics studies can be performed is growing year by year, it seems that most if not all the sources display kinematic substructures on top of a smooth Keplerian rotation, when sufficient spatial and spectral resolution is available. This is not surprising, since we know from dust continuum and scattered light emission that protoplanetary discs are not flat, smooth and sub-structureless. In addition, inside these systems several physical phenomena take place, such as planet disc interaction, disc binary interaction, disc instabilities, and these influence the velocity field of gas particles. In figure 4.8 there is a collection of kinematic signatures, generated by the presence of an embedded planet, a central binary, gravitational instability and vertical shear instability. During the last few years, considerable attention has been devoted to the study of kinematic signatures in planet forming discs, in order to characterize the physical phenomena happening inside them.

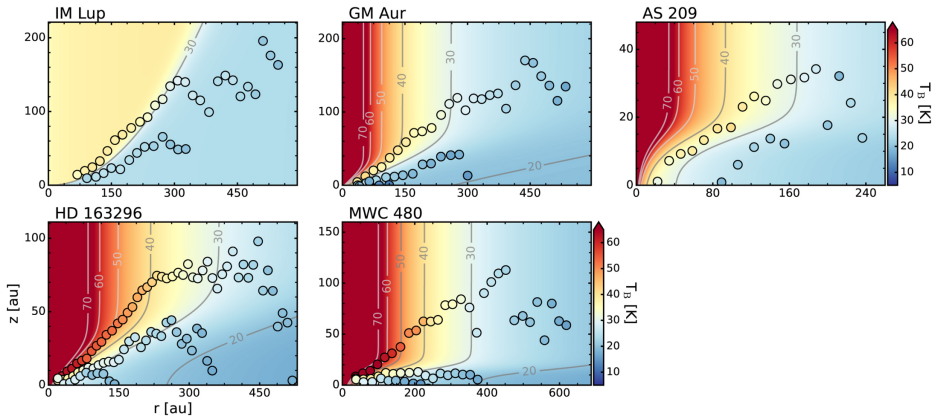

Figure 4.7: Two-dimensional temperature structure of the discs in the MAPS sample, from Law et al. (2021). The points correspond to the ^{12}CO and ^{13}CO emission, coming from different emitting layers (the upper one is the ^{12}CO, the lower one is the ^{13}CO).

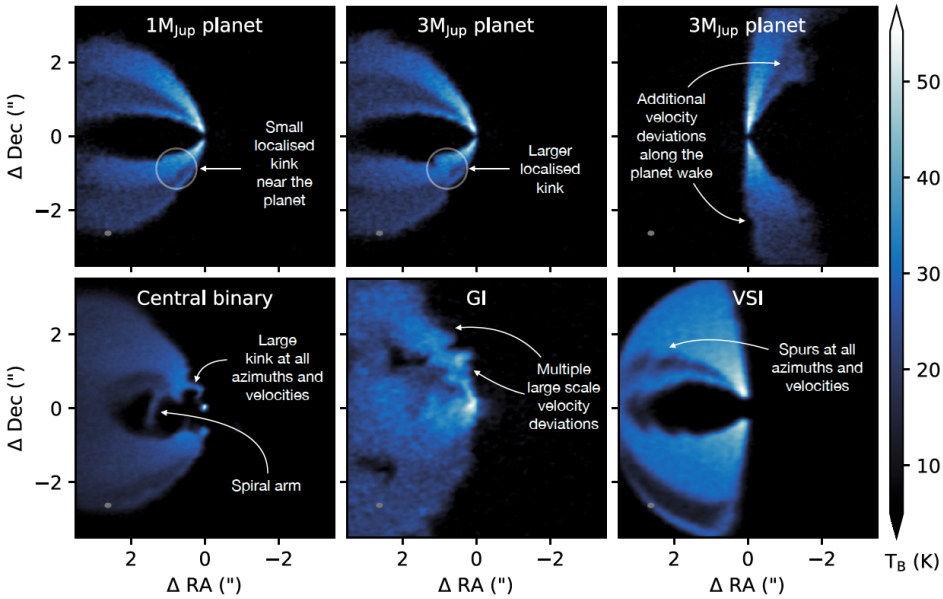

Figure 4.8: Collection of kinematic signatures in planet forming discs (Pinte et al. 2022).

4.4.1 Planet-disc interaction: the kink

Protoplanetary discs are the environments where planets form, but directly imaging the protoplanets is a hard job. The spectacular cases of PDS 70 Benisty et al. (2021); Facchini et al. (2021) and HD 169142 (Hammond et al. 2023) are the only cases in which we directly observe the emission coming from the planetary material, and these kinds of detections have proven to be very challenging. Therefore, it is often more feasible to investigate the effects that protoplanets exert on the accretion disc. One approach is to study dust continuum emission, since we expect protoplanets to create dust substructures. Nonetheless, multiple mechanisms can explain the observed substructures, not necessarily invoking the presence of an embedded planet (Bae et al. 2022; Paardekooper et al. 2022). In this context, kinematics offers an alternative and complementary window to investigate the presence of planets in protostellar discs (Disk Dynamics Collaboration et al. 2020).

An embedded protoplanet interacts with the surrounding disc, exerting a gravitational perturbation that leads to an exchange of energy and angular momentum. The theory of satellite-disc interaction was first studied by Goldreich & Tremaine (1979, 1980), who showed that a planet launches spiral density waves at the Lindblad resonances, inside and outside its orbit. These waves propagate away from the planet, disturbing the density and velocity structure of the disc. While most of the previous works were interested in the characterization of the density perturbations (Goodman & Rafikov 2001; Rafikov 2002), recently Bollati et al. (2021) described the associated velocity field. Near the planet, azimuthal disturbances prevail and are directly proportional to the planet's mass. In contrast, far away, radial motions dominate, and the deviations are proportional to the square root of the planet mass. These perturbations can be up to 10% of the Keplerian rotation. Under an observational point of view, the first kinematic evidence of an embedded protoplanet was claimed by Pinte et al. (2019). What is the observed kinematic feature associated to a planet? In a given channel map, the emission is concentrated along the isovelocity curve. In the presence of an embedded protoplanet, the flow is gravitationally perturbed, and an additional Doppler shift is induced. Hence, the isovelocity curve is distorted, and the emission shows a "kink", localized in the position of the planet. Hence, we expect to observe a strong non-Keplerian signature in the channel where the isovelocity curve crosses the embedded planet. Figure 4.9 from Pinte et al. (2020) displays the kink in the HD 97048 system, showing how the kink corresponds to the gap in dust continuum emission. Nevertheless, when enough spatial and spectral resolution are available, it is also possible to appreciate the kinematic effects of the planetary wake far from the position of the planet, as shown by Izquierdo et al. (2022); Calcino et al. (2022) in the case of HD 163296. Another spectacular case of velocity kink can be found in the system J 1604 (Stadler et al. 2023). Here, since the disc is almost face on, vertical motions dominate the kinematics, showing a strong red-shifted signal at the location of the planet.

4.4.2 Gravitational instability: the GI wiggle

As pointed out in the previous paragraph, the presence of a spiral density wave perturbs the azimuthal and radial velocity components. In addition to planets, gravitational instability also generates spiral density waves (Kratter & Lodato 2016).

Hall et al. (2020) demonstrated through numerical SPH simulations that a disc undergoing gravitational instability shows clear kinematic signatures in molecular line emission. These signatures are referred to as "GI wiggle", and they consist in a "zig-zag"-like

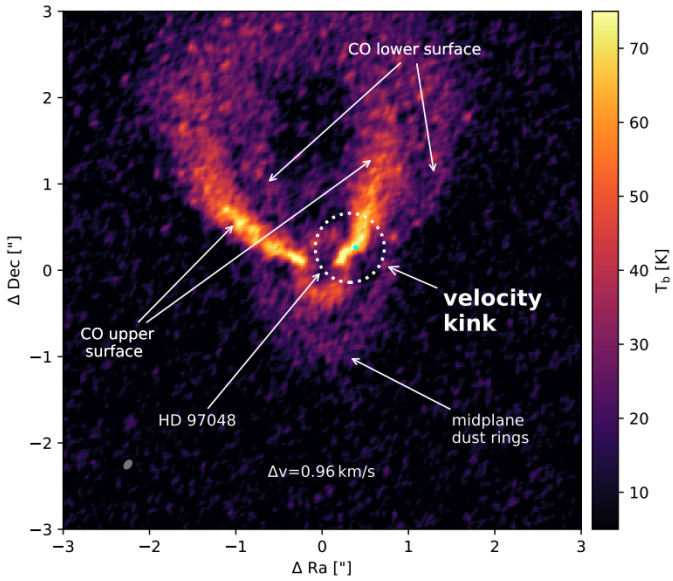

Figure 4.9: ALMA observations of the disc surrounding HD 97048, showing a kink in the 0.96km/s channel of the ^{13}CO $J = 3 - 2$.

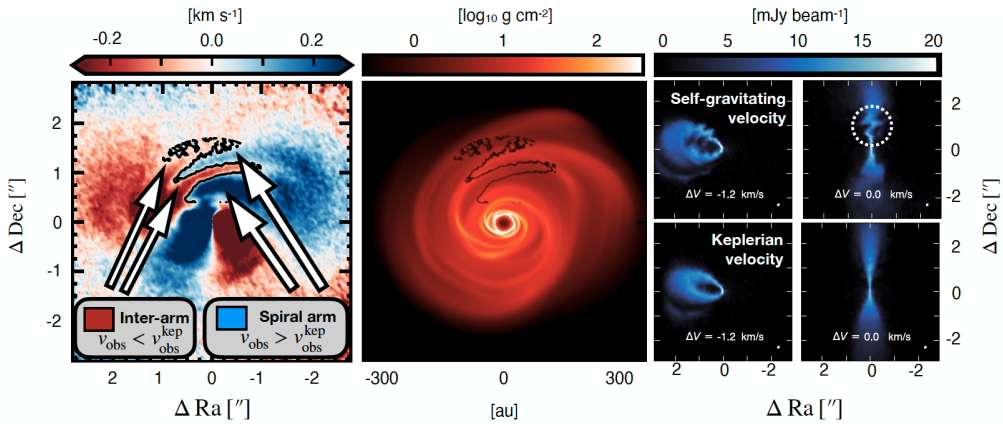

Figure 4.10: Left panel: observed velocity relative to Keplerian rotation, with the line $v_{\rm obs} - v_{\rm k,obs} = 0$ drawn in black. Central panel: surface density calculated by integrating along the line of sight at an observed inclination angle $i = 30°$. the line $v_{\rm obs} - v_{\rm k,obs} = 0$ is shown in black. Right panel: comparison between GI and Keplerian channels, showing the "zig-zag" like feature. Taken from (Hall et al. 2020).

feature over all the channels. As a matter of fact, opposed to the planetary driven spirals, these perturbations are global, rather than localized. Indeed, GI spirals continually perturb the disc velocity field of the disc, regardless of the position. When crossing a spiral arm, the velocity of the gas is perturbed. In particular, within the spiral arms, the velocity increases compared to the Keplerian background. Consequently, this causes emissions to shift towards the neighbouring channel associated with a higher velocity, as displayed in the right panel of figure 4.10. Conversely, in the areas between the arms, the opposite effect occurs. This leads to the emergence of the "interlocking finger" structure, as depicted in the left panel of figure 4.10.

Since the velocity perturbations are caused by spiral arms, understanding their morphology is crucial. As shown in chapter 3, the disc to star mass ratio and the cooling factor determines the spirals' properties. Hence, we expect these parameters to be related to the amplitude and the frequency of the wiggle. An analytical description of the velocity perturbation driven by gravitational instability is given in chapter 6.

CHAPTER 5

Dust in protostellar discs

Solid particles in protoplanetary discs are considered the fundamental building blocks for the planets. Specifically, according to the core accretion model, planets form sequentially from the solid component within these discs. For this reason, studying the dynamics of dust particles in protoplanetary discs is of paramount importance. Dust and gas in planet forming environments aerodynamically interact through drag forces. Because of their physical properties, the dynamical behaviour of the two components can be very different, sometimes questioning our understanding of the planet formation process. In addition, dust dominates the opacity of protoplanetary discs, determining the thermal structure and the millimetric emission observable with ALMA.

5.1 Aerodynamical coupling: drag force

Although protoplanetary discs are considered to be a mixture of gas and dust, we begin our description of dust dynamics by considering a system composed of a single solid particle embedded in a gas fluid. At this stage, we also assume that the dust does not affect the gas dynamics. This description can then be generalized to a two-fluid system.

We assume dust grains to be spherical with radius s, intrinsic density ρ_0 and mass $m_p = 4/3\pi\rho_0 s^3$. We will refer to dust velocity as $\mathbf{v}_d$, and for the gas $\mathbf{v}_g$. Since the drag force between gas and dust tends to damp the relative velocity $\Delta\mathbf{v} = \mathbf{v}_\mathrm{d} - \mathbf{v}_\mathrm{g}$, it is directly proportional to this velocity difference, and its expression is

$$|\mathbf{F}_\mathrm{d}| = \frac{1}{2} f C_\mathrm{D} \pi s^2 \rho |\Delta v|^2, \tag{5.1}$$

where C_D is a coefficient that depends on the drag regime, ρ is the total density[1] and f is a correction factor to take into account the case where the relative motion between the gas and dust in protoplanetary discs is supersonic. Its expression is given by (Kwok 1975)

$$f = \sqrt{1 + \frac{9\pi}{128}\left(\frac{|\Delta\mathbf{v}|}{c_s}\right)^2}. \tag{5.2}$$

The different aerodynamical coupling regimes depend upon the size of dust particles relative to the gas mean free path. It is possible to define a dimensionless parameter, called the Knudsen number (Paardekooper & Mellema 2006), that measures this property

$$\mathrm{Kn} = \frac{9\lambda_g}{4s}, \tag{5.3}$$

[1] In the case of a single dust grain embedded into a gas fluid, the total density is just the gas density. In the general case, the total density ρ is the sum of the gas and dust ones.

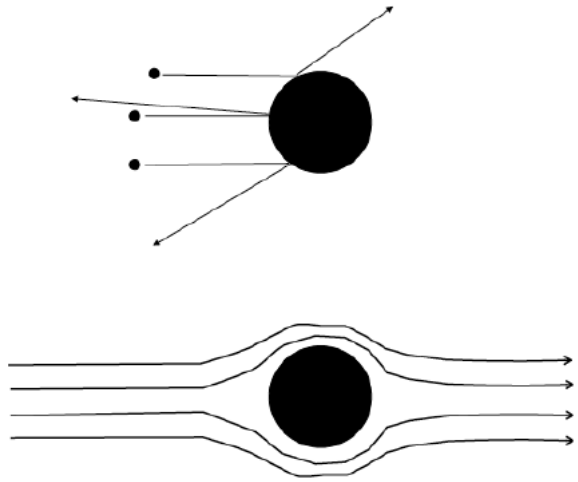

Figure 5.1: Dust particle in Epstein (top) and Stokes (bottom) regime, taken from G. Dipierro PhD Thesis.

where s is the dust particle size and $\lambda_{\rm g}$ is the gas particles' mean free path, given by

$$\lambda_{\rm g} = \frac{\mu m_p}{\rho_{\rm g}\sigma_{\rm coll}}, \tag{5.4}$$

where $\sigma_{\rm coll}$ is the cross-section of molecular hydrogen, $\mu = 2.1$ is the mean molecular weight, $\rho_{\rm g}$ is the gas density and m_p is the mass of the proton. Typically, in protoplanetary discs, Kn > 1, meaning that the dust particles' size is smaller than the gas mean free path: this is called the Epstein regime. However, when the disc is very massive, there is a transition between Epstein and Stokes regime (Kn < 1), since the gas density increases. The main impact of this transition is that in the inner denser region of the disc, where particles' size is comparable with the gas mean free path, the drag force is weaker compared to Epstein regime. The $C_{\rm D}$ coefficient is given by (Fassio & Probstein 1970)

$$C_{\rm D} = \begin{cases} \frac{8v_{\rm th}}{3|\Delta v|} & {\rm Kn} > 1 \\ 24{\rm Re}^{-1} & {\rm Kn} < 1, \quad {\rm Re} < 1 \\ 24{\rm Re}^{-0.6} & {\rm Kn} < 1, \quad 1 < {\rm Re} < 800 \\ 0.44 & {\rm Kn} < 1, \quad {\rm Re} > 800 \end{cases} \tag{5.5}$$

where c_g is the gas sound speed and the Reynolds number based upon the difference of velocity is given by

$${\rm Re} = \frac{2s|\Delta \mathbf{v}|}{\nu} = 4\frac{s|\Delta \mathbf{v}|}{\lambda_g c_s}, \tag{5.6}$$

and the last equivalence is true for collisional viscosity. Another important quantity to define is the stopping time, i.e. the time needed to modify the relative velocity between gas and dust. The longer it is, the less the particles are coupled. For spherical grains, it

is given by

$$t_{\rm s} = \frac{m_d |\Delta \mathbf{v}|}{|\mathbf{F}_D|} = \frac{8 \rho_0 s}{3 C_D \rho |\Delta \mathbf{v}|}. \tag{5.7}$$

In order to measure the strength of the aerodynamical coupling, it is very useful to define a dimensionless parameter as the ratio between the stopping time and the dynamical one. It is called Stokes number and, in general, its expression is

$$\mathrm{St} = t_{\rm s}\Omega = \frac{8}{3C_{\rm D}} \left(\frac{\rho_0}{\rho}\right) \left(\frac{v_{\rm k}}{|\Delta \mathbf{v}|}\right) \left(\frac{s}{R}\right). \tag{5.8}$$

As mentioned before, for typical protoplanetary discs, the gas mean free path is much larger than the dust particle size, hence the drag force is well described by the Epstein regime. Expanding eq. (5.8) in the Epstein regime, we obtain

$$\mathrm{St} = \gamma^{1/2} \frac{\pi}{2} \frac{\rho_0 s}{\Sigma(R)} \exp\left[\frac{z^2}{2H^2}\right] = \mathrm{St}_{\rm mid}(R) \exp\left[\frac{z^2}{2H^2}\right], \tag{5.9}$$

where we have used that $\rho = \Sigma/\sqrt{2\pi H^2} \exp\left[-\frac{z^2}{2H^2}\right]$. The Stokes number is a function of the position (R, z) in the disc, being inversely proportional to the density ρ. In general, solid particles are less coupled in low-density regions, hence in the outer disc and at $z > H$. We consider a protostellar disc with a mass of $0.01 \mathrm{M}_\odot$ and a radial extent of 100au, the typical Stokes number for mm-sized dust particles at the disc midplane is

$$\mathrm{St} \simeq 1 \left(\frac{\Sigma}{1.4 \mathrm{g/cm}^2}\right)^{-1} \left(\frac{\rho_0}{3 \mathrm{g/cm}^3}\right) \left(\frac{s}{1 \mathrm{mm}}\right). \tag{5.10}$$

The smaller the Stokes number is, the more tightly the particles are coupled: so, for $\mathrm{St} \to 0$, dust dynamics follows the gas one, while for $\mathrm{St} \to \infty$, the two fluids do not aerodynamically influence each other. Hence, the Stokes number refers to the degree of coupling of dust particles, since it compares the strength of the drag force with the ones that are acting on the particles, i.e. the gravitational attraction of the central object. However, this is not a general definition, since the main forces acting on particles can be different. As an example, in the case of a particle accreting onto a planetary core, the Stokes number should compare the stopping time with the free fall time, because the gravitational attraction of the planetary core is driving the particle evolution.

The dynamics of dust particles within protoplanetary discs is influenced by the aerodynamical interaction with the surrounding gas, and *vice-versa*. Because the gas-to-dust ratio is quite high during the formation of the disc, usually assumed to be 100, we can in general describe the coupling between dust and gas using the framework that has just been introduced. However, in some cases, the dynamical role of the dust is non-negligible, being its concentration so high to drive gas evolution. Some of these cases will be discussed at the end of this chapter.

So far, we have just described the dynamics of a single dust grain embedded into a gas flow. Now, we make a step forward in modelling the dynamics of solid particles, by considering dust as a continuum. This approach allows computing macroscopic fluid quantities, as density, velocity field, and describing the dynamics through the fluid equations. A physical assumption that is always made is to consider dust as a presureless fluid. This is justified because the rate of collision between dust particles is very low

compared to the one between particles and gas in protoplanetary discs. As a matter of fact, the collision timescale between two equally-sized dust grains is

$$t_{\rm coll} = \frac{\rho_0 s}{\rho_d v_{\rm coll}}, \tag{5.11}$$

where ρ_d is the dust volume density, ρ_0 is the intrinsic density of a dust grain and $v_{\rm coll}$ is the collisional velocity between two dust particles. To understand the importance of dust-dust collisions, we compare this timescale with the stopping time in the Epstein regime

$$\frac{t_{\rm coll}}{t_s} = \frac{\rho_g}{\rho_d}\frac{c_s}{v_{\rm coll}}. \tag{5.12}$$

This ratio depends on the gas-to-dust ratio, which typically is $>> 1$, and on the ratio between the sound speed and the collisional velocity. In a typical protoplanetary disc, the relative velocity between dust particles is always sub-sonic (Cuzzi & Hogan 2003; Ormel & Cuzzi 2007; Birnstiel et al. 2016), hence the ratio between the collision time and the stopping time is higher than 1, making the presureless fluid hypothesis well justified.

5.2 Dust dynamics

In this section, we study the effects of the aerodynamical coupling on the dust dynamics. The system we are going to analyse consists of a dust-gas mixture in a thin, axisymmetric, non-magnetic, non-self-graviting, viscous and vertically isothermal disc. We treat the dust phase as a pressureless and viscousless fluid of equally-sized solids. The fluid equations for this system are

$$\frac{\partial \Sigma_g}{\partial t} + \nabla \cdot (\Sigma_g \mathbf{v}_g) = 0, \tag{5.13}$$

$$\frac{\partial \Sigma_d}{\partial t} + \nabla \cdot (\Sigma_d \mathbf{v}_d) = 0 \tag{5.14}$$

$$\frac{\partial \mathbf{v}_g}{\partial t} + (\mathbf{v}_g \cdot \nabla)\mathbf{v}_g = -\frac{1}{\rho_g}(\nabla P - \nabla \cdot \sigma) - \nabla\Phi - \frac{1}{\rho_g}\mathbf{F}_{\rm d}^V, \tag{5.15}$$

$$\frac{\partial \mathbf{v}_d}{\partial t} + (\mathbf{v}_d \cdot \nabla)\mathbf{v}_d = -\nabla\Phi + \frac{1}{\rho_d}\mathbf{F}_{\rm d}^V, \tag{5.16}$$

where $\mathbf{F}_{\rm d}^V$ is the drag force per unit volume, defined as

$$\mathbf{F}_{\rm d}^V = \frac{\rho_d}{t_s}\Delta\mathbf{v}. \tag{5.17}$$

We note that eq. (5.15) is the Navier-Stokes equation already discussed in the previous chapter, with an additional force given by the dust backreaction. We underline that the effect of the drag force onto the gas component is weaker of a factor $\rho_d/\rho_g < 1$, that is the dust to gas ratio.

The main effects of the aerodynamical coupling between gas and dust in protoplanetary are the vertical settling and the radial drift of solid particles. These phenomena are crucial in the context of planet formation.

5.2.1 Vertical settling

Dust particles tend to settle into the midplane, and their behaviour depends on the coupling with the gaseous component. In order to study this phenomenon, we write the vertical equation of motion for the dust and we solve it. Writing eq. (5.16) in cylindrical coordinates and assuming the backreaction to be negligible, the vertical motion of dust grains is given by the Langevin equation (Youdin & Lithwick 2007)

$$\frac{\partial v_{d,z}}{\partial t} = -\Omega_k^2 z + \frac{v_{g,z} - v_{d,z}}{t_s}. \tag{5.18}$$

Supposing that the gas flow is stationary ($v_{g,z} = 0$), the equation of motion of dust grains is

$$\frac{\mathrm{d}^2 z}{\mathrm{d}t^2} + \frac{1}{t_\mathrm{s}}\frac{\mathrm{d}z}{\mathrm{d}t} + \Omega_k^2 z = 0, \tag{5.19}$$

that describes a damped harmonic oscillator. We re-scale the time t with respect to the dynamical time of the system, defining $\tau = \Omega_k t$, and the equation becomes

$$\frac{d^2 z}{d\tau^2} + \frac{1}{\mathrm{St}}\frac{dz}{d\tau} + z = 0, \tag{5.20}$$

where the Stokes number naturally appears. We solve the differential equation with the ansatz $z \propto \exp(\lambda\tau)$, and the characteristic polynomial is

$$\lambda^2 + \frac{\lambda}{\mathrm{St}} + 1 = 0, \tag{5.21}$$

which has the two solutions

$$\lambda_{1,2} = -\frac{1}{2\mathrm{St}}\left(1 \pm \sqrt{1 - (2\mathrm{St})^2}\right). \tag{5.22}$$

According to the sign of the discriminant $\Delta = 1 - (2\mathrm{St})^2$, there are two classes of solutions. For $\Delta > 0$ and $\mathrm{St} < 1/2$, $\lambda_{1,2}$ are real and $z(t)$ is an over damped oscillation; for $\Delta < 0$ and $\mathrm{St} > 1/2$, $\lambda_{1,2}$ are complex and $z(t)$ is an under damped oscillation. Before continuing, it is important to underline that we are considering the Stokes number to be constant with z, which is not true in general (see eq. (5.10)). Hence, the following arguments are valid only in the limit $z << H$, where H is the hydrostatic scale height of the gas.

Over damped oscillation, St $< 1/2$

If St$< 1/2$, dust particles are strongly coupled. The solution in this case is

$$z(t) = A\exp[\lambda_1\tau] + B\exp[\lambda_2\tau], \tag{5.23}$$

where A, B are set by the initial conditions, that are $z(0) = z_0$ and $\dot{z}(0) = 0$. We expand Δ for St$<< 1/2$

$$\lim_{\mathrm{St}<<1/2} \Delta = 1 - 2\mathrm{St}^2 \rightarrow \lambda_{1,2} = \{-\mathrm{St}, -1/\mathrm{St}\}, \tag{5.24}$$

and this allows to write the solution as

$$z(t) = A\exp[-\mathrm{St}\tau] + B\exp[-\tau/\mathrm{St}]. \tag{5.25}$$

Since second term goes to zero fast, the typical timescale for settling in this regime is

$$t_\mathrm{settle} = \frac{1}{\mathrm{St}\Omega_k} > t_\mathrm{dyn}. \tag{5.26}$$

Underdamped oscillation, St $> 1/2$

If St$> 1/2$, dust particles tend to be decoupled from the gas ones. In this case, the solutions of the characteristic polynomials are

$$\lambda_{1,2} = -\frac{1}{2\mathrm{St}} \mp i\frac{\sqrt{|\Delta|}}{2\mathrm{St}} = -\frac{1}{2\mathrm{St}} \mp i\gamma, \tag{5.27}$$

and the solution of the equation of motion is

$$z(t) = z_0 \exp\left[-\frac{\tau}{2\mathrm{St}}\right] \left(\sin(\gamma\tau) + \cos(\gamma\tau)\right). \tag{5.28}$$

The typical timescale for settling in this regime is given by

$$t_{\mathrm{settle}} = \frac{2\mathrm{St}}{\Omega_k} > \Omega_k^{-1} = t_{\mathrm{dyn}}. \tag{5.29}$$

We have just shown that if St $< 1/2$, the settling time grows like $1/\mathrm{St}$, while if St $> 1/2$, the settling time grows linearly with the Stokes number: this happens because highly coupled dust particles follow the gas vertical shape H, while uncoupled particles oscillates vertically with a small drag force.

In Figure 5.2, the two solutions are shown. The blue line represents the behaviour of strongly coupled dust particles, with the evolution of the variable z following an exponential-like function. Conversely, the orange line illustrates the behaviour of weakly coupled dust particles, characterized by oscillations around the midplane, gradually decreasing in amplitude.

5.2.2 Turbulent vertical settling

In the previous analysis, we assumed that the gas vertical motions are negligible compared to the dust ones, which is only valid in absence of sustained turbulent motions. However, the gas disc is expected to be highly turbulent, especially in the upper layers. The turbulence is expected to stir dust particles up to high altitude and prevent dust sedimentation.

We describe gas and dust as two different fluids, with density $\rho_g(R, z)$ and $\rho_d(R, z)$. The dust density evolution due to settling and diffusion can be computed for low dust-to-gas ratio $\epsilon = \rho_d/\rho_g << 1$, and it reads (Clarke & Pringle 1988)

$$\frac{\partial \rho_d}{\partial t} = \frac{\partial}{\partial z}\left[D_{d,z}\rho_g \frac{\partial}{\partial z}\left(\frac{\rho_d}{\rho_g}\right)\right] + \frac{\partial}{\partial z}(z\Omega\mathrm{St}\rho_d), \tag{5.30}$$

where $D_{d,z}$ is the vertical diffusion coefficient for dust particles. This equation is called advection diffusion equation, where the advective term is the first derivative (settling) and the diffusive term is the second derivative (turbulent diffusion). We look for steady solutions, and the equation becomes

$$\frac{1}{\epsilon}\frac{\mathrm{d}\epsilon}{\mathrm{d}z} = -\frac{\Omega\mathrm{St}_{\mathrm{mid}}}{D_{d,z}} z \exp\left[\frac{z^2}{2H_g^2}\right] \tag{5.31}$$

where we use eq. (5.9) for the Stokes number. In order to integrate the previous equation, the knowledge of $D_{d,z}$ is required. In general, it is a function of z and of the Stokes

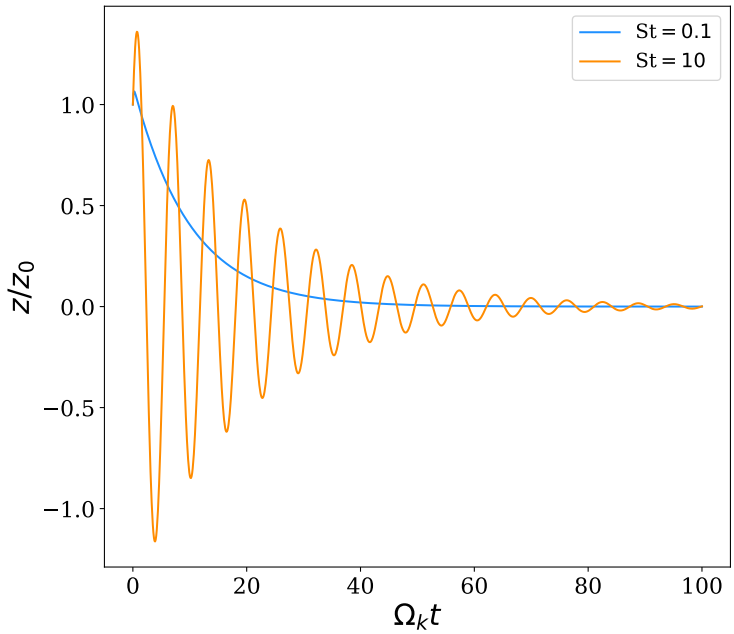

Figure 5.2: Dust settling for different Stokes number. The curves show the two different regimes

number, however its expression is unknown. We make the hypothesis that it is constant along the vertical direction, and that it can be approximated with the gas kinematic viscosity ν. Making this hypothesis, the solution for the advection diffusion equation is

$$\rho_d(R,z) = \rho_{d,0} \exp\left\{-\frac{z^2}{2H_g^2} - \frac{\mathrm{St}_{\mathrm{mid}}}{\alpha}\left[\exp\left(\frac{z^2}{2H_g^2}\right) - 1\right]\right\}, \tag{5.32}$$

where we have used the $\alpha-$prescription. Close to the midplane ($z < H_g$, and $\mathrm{St} \sim \mathrm{St}_{\mathrm{mid}}$), this profile approaches to a Gaussian with scale height

$$H_d = H_g \sqrt{\frac{\alpha}{\alpha + \mathrm{St}}}. \tag{5.33}$$

This equation clearly shows that dust settling towards the midplane is balanced by turbulent diffusion, which determines the thickness of the dust disc. Additionally, this result shows that the sedimentation of particles is more effective in the outer part of the disc, where the Stokes number is higher, the drag force is weaker and hence the turbulence can not stir up dust particles.

5.2.3 Radial drift

As mentioned earlier, the aerodynamic interaction between gas and dust imparts a radial motion to solid particles, which eventually prevents planet formation. The nature of this phenomenon can be ascribed to the different motions between the two phases, both in the radial and azimuthal direction. These kinematic differences are linked to the different nature of the two fluids. Indeed, the gas feels the pressure, that makes its azimuthal

velocity sub-Keplerian, and the viscosity, that generates a negative radial velocity. On the contrary, the dust is pressureless and inviscid, hence a freely orbiting dust particle feels only centrifugal forces and gravity, and should therefore be in a Keplerian orbit without any radial motion.

Hence, dust particles feel a continuous headwind in the azimuthal direction, and a crosswind towards the central object from the gas flow. The headwind causes dust particles to lose angular momentum, and spiral towards the central object. This behaviour is a direct consequence of the aerodynamical coupling between the two components, since the drag force tends to delete velocity differences. This is known as *radial drift*. On the other hand, the crosswind pushes dust particles towards inner radii, according to the viscous velocity of the gas. This is known as *drag*.

For simplicity, we write the gas azimuthal velocity as

$$v_{g,\phi} \simeq v_k(1-\eta), \tag{5.34}$$

where $\eta = n/2(H/R)^2$ from eq. (2.26). We write equations (5.15) and (5.16) in cylindrical coordinates, we rearrange them, and we obtain

$$\frac{\mathrm{d}v_{d,R}}{\mathrm{d}t} = \frac{1}{R}(v_{d,\phi}^2 - v_k^2) - \frac{1}{t_s}(v_{d,R} - v_{g,R}), \tag{5.35}$$

that is the centrifugal balance, and

$$\frac{\mathrm{d}}{\mathrm{d}t}(Rv_{d,\phi}) = -\frac{R}{t_s}(v_{d,\phi} - v_{g,\phi}), \tag{5.36}$$

that is the conservation of angular momentum. We suppose that the radial velocity is smaller compared to the azimuthal one, meaning that the solid particles spiral towards the central object through a succession of circular orbits. This allows us to re-write the temporal derivative of the angular momentum as

$$\frac{\mathrm{d}}{\mathrm{d}t}(Rv_{d,\phi}) = v_{d,R}\frac{\mathrm{d}}{\mathrm{d}R}(Rv_{d,\phi}) \simeq \frac{1}{2}v_{d,R}v_k, \tag{5.37}$$

where we have also assumed that the dust azimuthal velocity is Keplerian, at zeroth order. The dust radial velocity is hence

$$v_{d,R} = -\frac{2}{\mathrm{St}}(v_{d,\phi} - v_{g,\phi}). \tag{5.38}$$

We are interested in steady state solutions, hence we set the time derivative of eq. (5.35) to zero, and we obtain

$$\frac{1}{R}(v_{d,\phi} - v_k)(v_{d,\phi} + v_k) - \frac{1}{t_s}(v_{d,R} - v_{g,R}) \simeq \frac{2v_k}{R}(v_{d,\phi} - v_k) - \frac{1}{t_s}(v_{d,R} - v_{g,R}) = 0, \tag{5.39}$$

where we have used $v_{d,\phi} + v_k \simeq 2v_k$. After some algebra, we get the expression for the radial and azimuthal velocity of dust particles

$$v_{d,R} = -\frac{|v_{g,R}| + 2\eta v_k \mathrm{St}}{1+\mathrm{St}^2}, \tag{5.40}$$

$$v_{d,\phi} = \frac{\mathrm{St}^2}{1+\mathrm{St}^2}\left[v_k - v_{g,\phi}\left(1 - \frac{1+\mathrm{St}^2}{\mathrm{St}^2}\right)\right]. \tag{5.41}$$

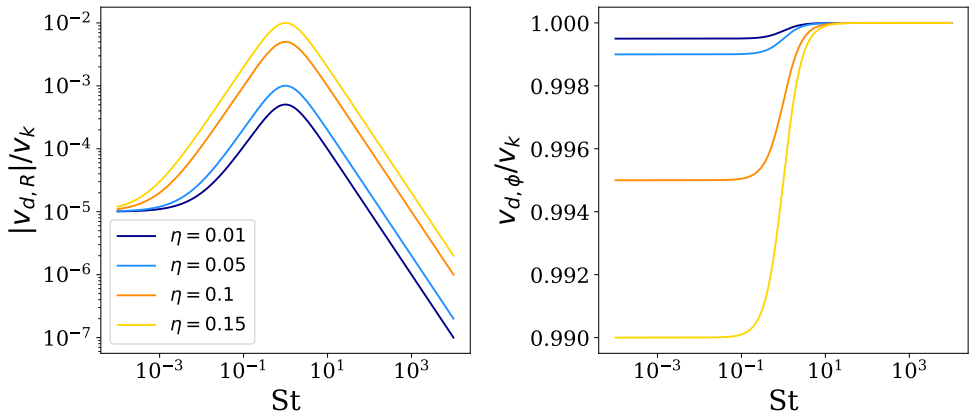

Figure 5.3: Radial and azimuthal velocity of solid particles for different value of the η parameter and for $v_{g,R} = 10^{-5} v_k$. The effect of the radial drift (left panel) is maximum for St$= 1$

The left panel of figure 5.3 shows the radial velocity of dust particles for different values of the η parameter (i.e. different gas pressure gradient). It is evident that the radial velocity of dust tends to the gas one for St $\to 0$, that is the standard viscous velocity. For St$= 1$, solid particles experiences the strongest radial drift, since $|v_{d,R}|$ is at its maximum. For St $\to \infty$, solid particles are decoupled from the gas and the role of the drag force becomes negligible, and their radial velocity is zero.

It is useful to evaluate the radial drift timescale for St $= 1$ particles, to understand the strength of this process. For St $= 1$, the dust radial velocity is $v_{d,R} \simeq 2\eta v_k \simeq (H/R)^2 v_k$, and so

$$t_{\rm drift} = \frac{R}{v_{d,R}} \simeq \left(\frac{H}{R}\right)^{-2} \Omega^{-1} = 100 \left(\frac{H/R}{0.1}\right)^{-2} \left(\frac{R}{1{\rm au}}\right)^{3/2} {\rm yr}. \tag{5.42}$$

At 1au the radial drift timescale is of the order of ~ 100yr, that is incredibly small compared to the disc lifetime. Hence, as soon as the Stokes number of dust particles reaches 1, they inevitably drift towards the central object in a very small timescale. In a typical protoplanetary disc, this occurs for mm-sized dust particles (see eq. (5.10)). Hence, we expect that millimetre dust grains rapidly drift towards the central object, preventing the formation of planetary objects. This is known as *radial drift barrier* to planet formation (Weidenschilling 1977).

5.2.4 Dust trapping

Under an observational perspective, there is evidence of millimetre dust grains in protostellar environments, even though we would expect them to be drifted towards the central object because of the radial drift. To explain the retention of marginally coupled solid particles in protostellar discs, a mechanism that slows down the radial drift is needed, usually referred to as "dust traps". Several ideas have been proposed, such as planet-disc interaction, spiral arms, vortices, snowlines, magnetic winds (Pinilla et al. 2012; Rice et al. 2004; Dipierro et al. 2015a; Gonzalez et al. 2017; Suriano et al. 2018). These are just a handful of examples, and the common feature of these effects is a radial and/or azimuthal inhomogeneity in the gas density that traps dust particles in the

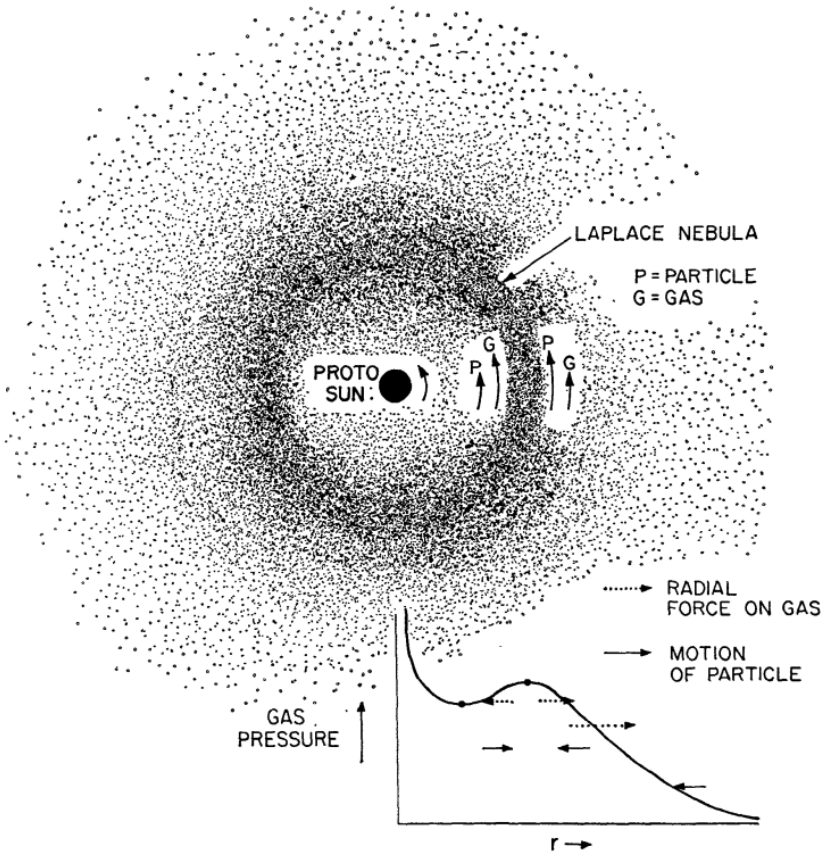

Figure 5.4: Illustration of the dust trapping mechanism, from Whipple (1972). Since the gas pressure gradient changes from positive to negative on one side of the inhomogeneity to negative on the other, the gas orbital velocity changes from super- to sub-Keplerian causing dust grains to drift toward the density/pressure maxima.

over-pressure region. As a matter of fact, as a consequence of the barotropic hypothesis ($P = c_s^2 \rho$), the pressure is proportional to the density, and hence a density maximum corresponds to a pressure maximum. Since the gas pressure gradient changes sign when crossing the inhomogeneity, the gas azimuthal velocity changes from sub-Keplerian to super-Keplerian, causing dust grains to drift towards the density/pressure maximum. This mechanism is generally referred to as *dust trap*, and it is able to prevent radial drift of solid particles. A schematic view of the dust trapping mechanism is shown in figure 5.4 taken from Whipple (1972).

Observationally speaking, there are several evidences of dust trapping. One remarkable example is given by Rosotti et al. (2020). They compared the dust brightness temperature profile with the rotation curve of gas, after subtracting a Keplerian background. This quantity is tracing the non-Keplerian component of the rotation curve that, in the case of negligible disc self-gravity, is the pressure gradient. This term, as shown in chapter 4, is proportional to the derivative of the pressure profile. In figure 5.5 it is possible to see that the maxima of the dust brightness temperature (i.e. dust rings) correspond

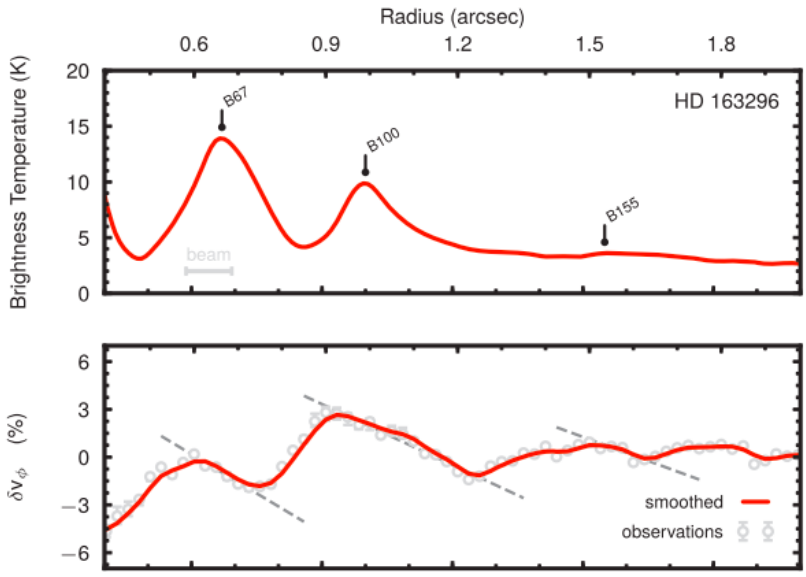

Figure 5.5: Dust continuum emission profile (top panel) where the location of the continuum peaks are marked, and rotation curve (bottom panel) of HD 163296 (Rosotti et al. 2020). The continuum peaks corresponds to the location where the rotation curve transitions from super-Keplerian to sub-Keplerian. This is an indication that dust trapping in gas pressure maxima is the origin of dust substructures.

to the zero velocity shift, indicating that dust overdensities are caused by trapping in pressure maxima.

5.3 Planet formation: core accretion theory

Studying dust dynamics is essential to understand planet formation. As a matter of fact, the classical theory of planet formation is the Core Accretion model (Safronov 1969; Goldreich & Ward 1973) (hereafter CA), and it is completely focused on dust dynamics. Four stages can be identified, according to the grains' size and Stokes number: (i) *dust growth*, (ii) *planetesimal formation*, (iii) *collisional growth* and (iv) *core accretion*.

Dust growth

The first stage is called "dust growth" (Drążkowska & Dullemond 2014) as dust coagulates from micron-size to centimetre-size through microphysical mechanisms. The way in which dust can grow up to cm-size is fostered by the vertical settling of the dust disc, and in general it is very well understood, both theoretically and observationally (Testi et al. 2014). At this stage, the Stokes number is below unity, and it increases according to the dust grains' size. The problem arises when $\mathrm{St} = 1$ is reached: indeed, at this point, radial drift is maximum, stopping the process of dust growth. In addition, when $\mathrm{St} = 1$, the critical dust size s_{crit} is proportional to the surface density Σ according to 5.10. As the disc evolves, the surface density decreases because of accretion, and the critical dust size does so. This fact goes against planet formation, since the radial drift barrier occurs

sooner.

Planetesimal formation

The second stage is called "planetesimal formation" and it has not yet been completely understood. As a matter of fact, it is not clear how dust grows from centimetre to kilometre size, forming the so-called planetesimals. Indeed, during this stage the Stokes number is ~ 1 and thus radial drift effect is maximum. For this reason, the presence of a mechanism that stops radial drift is fundamental for planet formation, otherwise dust growth would stop (Weidenschilling 1977).

Collisional growth

The third step is called "collisional growth". Through scattering and collisions, planetesimals grow, eventually reaching planetary cores sizes. Collisions between planetesimals are fostered by the so-called "gravitational focusing". According to this mechanism, the geometrical cross-section increases because of gravitational attraction, making planetesimal collisions more likely to happen. Through classic Newtonian physics, it is possible to show that for two planetesimals with mass $m_{\rm pl}$, radius $R_{\rm pl}$ and relative velocity $\sigma_{\rm pl}$, the effective cross-section is

$$\Gamma_{\rm eff} = \Gamma_g \left(1 + \frac{v_{\rm esc}^2}{\sigma_{\rm pl}^2} \right), \tag{5.43}$$

where $\Gamma_g = \pi R_{\rm pl}^2$ is the standard geometrical cross-section and $v_{\rm esc}^2 = 4Gm_{\rm pl}/R_{\rm pl}$ is the escape velocity. Hence, the effect of gravitational focusing is significant if the escape velocity is higher compared to the relative velocity of the planetesimals. This latter quantity can be interpreted as a dispersion velocity of the dust planetesimal layer. Since the planetesimal mass scales as $m_{\rm pl} \propto R_{\rm pl}^3$, the escape velocity is proportional to $v_{\rm esc}^2 \propto R_{\rm pl}^2 \propto m_{\rm pl}^{2/3}$. In terms of cross-section, it reads

$$\Gamma_{\rm eff} \propto \begin{cases} m_{\rm pl}^{2/3}, & v_{\rm esc} < \sigma_{\rm pl} \\ m_{\rm pl}^{4/3}, & v_{\rm esc} > \sigma_{\rm pl} \end{cases} \tag{5.44}$$

This means that the higher is the mass of the planetesimals, the bigger is the effect of gravitational focusing. This effect promotes the growth of bigger planetesimals and for this reason it is called "oligarchic growth" (Kokubo & Ida 1998).

Core accretion

The last stage is "core accretion", in which planetary cores accrete gas forming their atmospheres and, under certain conditions, become gaseous giants (Stevenson 1982). By imposing the hydrostatic equilibrium for the planetary core and its atmosphere[2], it is possible to show that there is a critical core mass, above which the atmosphere is unstable. This corresponds to the formation of a gaseous giant planet. The value of the critical mass is

$$M_{\rm cr} = 12 \left(\frac{\dot{M}_c}{10^{-6} {\rm M}_\oplus/{\rm yr}} \right)^{1/4} \left(\frac{k_R}{1 {\rm cm}^2/{\rm g}} \right)^{1/4} {\rm M}_\oplus. \tag{5.45}$$

[2]To do so, it is necessary to specify the core accretion rate $\dot{M}_c$ and the atmosphere opacity k_R.

It is not easy to reach the critical mass since the required accretion rate is high. In particular, in the outer disc, where the surface density is low, the accretion onto the core is less efficient.

Although this model currently provides the most popular explanation for the formation of planets, it has been shown that formation timescales may be anywhere up to ~ 10Myr, exceeding typical disc lifetimes (Haisch et al. 2001), specifically in the case of giant planets in the outer disc. For example, the formation of systems as HD100546 (Fedele et al. 2021) or CIDA 1 (Pinilla et al. 2021; Curone et al. 2022) is particularly challenging for CA theory.

Table 5.1: Table that resumes size of dust grains and Stokes number of different stages in Core Accretion theory.

Stage	Grain size	St
Dust growth	μm $\rightarrow$ m	< 1
Planetesimal formation	m$\rightarrow 10$km	~ 1
Collisional growth	Planetary cores	> 1
Core accretion	Planets	-

5.4 Dust and self-gravity

So far, we have just studied situations in which the dust density is so low that it is negligible in terms of global evolution of the disc. However, this condition may be violated due to interplay between vertical settling, radial drift and dust trapping. In particular, if dust concentration is high enough, the role of its self-gravity becomes dynamically important, and new physical effects may occur. In this section, we present the so-called "Goldreich-Ward" mechanism, we discuss how gravitational instability works in a two phases fluid and how dust is trapped inside gas spiral arms.

5.4.1 Goldreich-Ward mechanism

Safronov (1969) and, independently, Goldreich & Ward (1973) proposed that a thin dust layer located at the disc midplane may be gravitational unstable, and such instability might result in the prompt for planetesimal formation. The basic idea is illustrated in figure 5.6, and it involves three stages

1. Initially, dust particles are well mixed with the gas. The degree of solid particles concentration is too low to be dynamically important.

2. Over the time, dust grows and settles to the midplane, forming a dense thin layer around the $z = 0$ plane. Also radial drift can play an important role in increasing dust concentration.

3. The combination of high surface density and low dispersion velocity makes the dust layer gravitationally unstable, and this may lead to the formation of bound clumps of particles, which rapidly agglomerate to form planetesimals.

Although this mechanism might seem a possible way to solve the conundrum of planetesimal formation, there are some caveats that we should point out. Firstly, we

assume that the dust possess a dispersion velocity c_d, and that it is related to its scale height H_d according to the hydrostatic equilibrium

$$c_d = H_d \Omega. \tag{5.46}$$

At zeroth order, the stability of a particle layer can be determined according to the Toomre criterion, defining the Toomre parameter for the dust

$$Q_d = \frac{c_d \Omega}{\pi G \Sigma_d} = Q_g \frac{H_d}{H_g} \epsilon^{-1}, \tag{5.47}$$

where ϵ is the dust to gas ratio. The $Q_d = 1$ condition can be translated into

$$H_d = \frac{\epsilon H_g}{Q_g} \simeq \frac{H_g}{100 Q_g}, \tag{5.48}$$

where we took a dust-to-gas ratio of $1/100$. Hence, the thickness of the dust layer must be, at least, two order of magnitude smaller compared to the gas one. Such a razor-thin disc is not implausible, indeed the vertical thickness of Saturn's rings, for example, is of the order of only 10 m. However, in a gas-rich environment such a protoplanetary disc, we need to verify whether turbulence will preclude the particle layer from ever becoming so thin. Using eq. (5.33) for the dust scale height, it is clear that the Goldreich-Ward mechanism can not work for small dust particles (low Stokes number), unless α is very small. Additionally, since the Stokes number is higher at large radii, it is likely that Goldreich-Ward mechanism works in that region of the outer disc.

Cuzzi et al. (1993) introduced the concept of self-induced turbulence, that can prevent the dust particle layer to settle to the point of being unstable. If we consider a thin dust layer settled at the midplane, the gas is sub-dominant and the orbital velocity of the flow is determined by solid particles, being then Keplerian. Just above the particle layer, the gas becomes dominant and hence the velocity of the flow is comparable with the gas one, being sub-Keplerian. As a consequence, there is a vertical shear that can, in principle, be unstable to the development of Kelvin-Helmholtz instability. This self-excited turbulence can prevent the particle layer from ever settling to the point where self-gravity could set in.

5.4.2 Two-fluid instability

It is possible to move toward a more realistic description of the gravitational stability of a two phases fluid. The stability for a multi-phase fluid is, in general, different from the single-fluid case. This topic first captured interest within the context of galactic dynamics. In galaxies, the two components are stars and gas. Stars are the most abundant and the "hot" component, where hot refers to the dispersion velocity of the fluid. As for the gas, it is less abundant and cold. In protoplanetary discs, the situation is similar: here, the hot (cold) and most abundant (less abundant) component is the gas (dust). The two components can be described as two different fluids with surface density Σ_h, Σ_c and sound speed[3] c_h and c_c, where the subscript h refers to the hot component (stars in galaxies, gas in protostellar discs) and c to the cold one (gas in galaxies and dust in protostellar discs.). In both galaxies and protoplanetary discs, the hot component is more abundant

[3] In protoplanetary discs, the gas possesses a sound speed that is generated by thermal processes ($c_g^2 \propto T$). As for the dust, this quantity is a dispersion velocity, that is not related to thermal processes, assuming that the dust is a collisonless fluid.

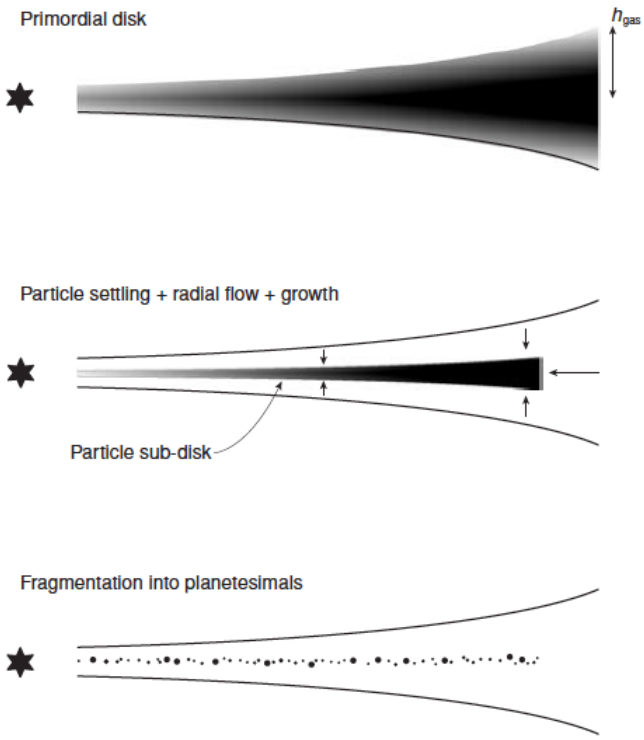

Figure 5.6: Sketch of the Goldreich & Ward mechanism for planetesimal formation taken from Armitage (2013).

$\Sigma_h > \Sigma_c$ and, clearly, hotter $c_h > c_c$. It is possible to define two parameters that measure these properties: the first one is the relative abundance of the cold component

$$\epsilon = \frac{\Sigma_c}{\Sigma_h}, \tag{5.49}$$

that, in the context of protoplanetary disc, is the dust-to-gas ratio; the second one is the relative temperature

$$\xi = \left(\frac{c_c}{c_h}\right)^2. \tag{5.50}$$

The one-component fluid limit is given by the condition $\epsilon \to 0$.

Kato (1972) first proposed that the presence of a second cold component can trigger gravitational instability at small scales. Jog & Solomon (1984) first tackled the problem of a galactic disc of stars and gas, by treating the disc as a two-fluid system. In this model, the two components are coupled to each other only through the common gravitational field. They derived the dispersion relation, that reads

$$\omega^4 - \omega^2(\alpha_h + \alpha_c) + (\alpha_h\alpha_c - \beta_h\beta_c) = 0, \tag{5.51}$$

with $\alpha_i = \kappa^2 + c_i^2k^2 - 2\pi G\Sigma_i|k|$ and $\beta_i = 2\pi G\Sigma_i|k|$. Bertin & Romeo (1988) then determined a global stability criteria for a two-fluid disc, defining a marginal stability curve given by

$$\begin{aligned} Q_h^2 = \tfrac{2\hat{\lambda}}{\xi}\Big[&(\epsilon+\xi) - \hat{\lambda}(1+\xi) + \\ &\sqrt{\hat{\lambda}^2(1-\xi)^2 - 2\hat{\lambda}(1-\xi)(\epsilon-\xi) + (\epsilon+\xi)^2}\Big], \end{aligned} \tag{5.52}$$

where the parameter Q_h is the Toomre parameter of the hot component, and $\hat{\lambda}$ is the dimensionless wavelength, defined as

$$\hat{\lambda} = \frac{k_J}{2k} = \frac{\pi G\Sigma}{2c_g^2k}, \tag{5.53}$$

as in chapter 3. A comparison between the marginal stability curve of the one-component fluid model and the two-component one is shown in figure 5.7. The profile of Q_h may exhibit two peaks, one arising from instability in the hot component, at intermediate wavelengths, and one at smaller wavelengths, dominated by the cold component. This second peak emerges when the second component is sufficiently abundant and cold: Bertin & Romeo (1988) found that there is a transition from hot to cold driven instability when $\epsilon > \sqrt{\xi}$.

In the two-component fluid model, the Jeans length is defined as the wavelength at which Q_h^2 has its maximum, so when instability is *cold-driven*, the Jeans length is smaller compared to the hot-driven case. A peculiar characteristic of the *cold-driven* gravitational instability is that it occurs at higher values of the Toomre parameter Q (Bertin & Romeo 1988). An application to protoplanetary discs, generalized taking into account the drag force, is given in chapter 9.

5.4.3 Dust trapping and collapse in gas spiral arms

How dust grows beyond cm-sizes remains one of the biggest problems in the planet formation scenario. As a matter of fact, as shown in section 5.3, a mechanism that traps

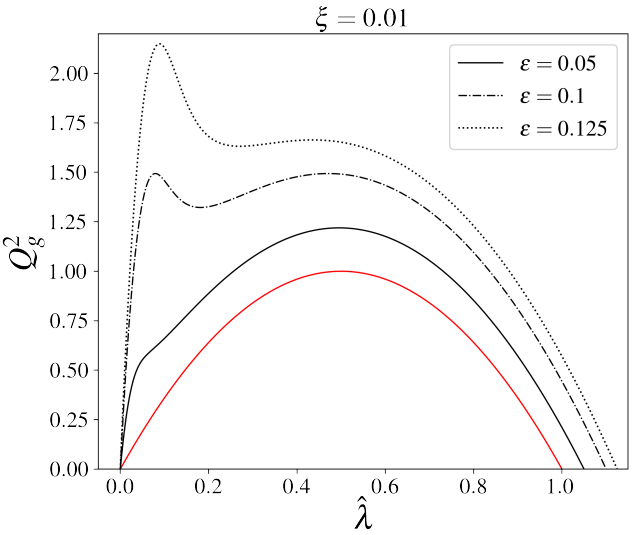

Figure 5.7: Marginal stability curve of the one-component fluid model (red line) and of the two-component fluid one (black lines) for $\xi = 0.01$ and different values of ϵ. It can be seen that for $\epsilon < \sqrt{\xi}$ the "hot" peak is dominant, while for $\epsilon > \sqrt{\xi}$ the "cold" peak at smaller wavelengths is higher.

dust is needed in order to overcome the St$= 1$ barrier. As mentioned previously, dust is trapped in pressure maxima, and GI spiral arms are so. As a matter of fact, a spiral density wave creates both an azimuthal and radial gradient of pressure, efficiently collecting dust particles (Dipierro et al. 2015a).

The interplay between dust trapping and dust self-gravity has been proposed as a path to solve the conundrum of planetesimal formation in protostellar discs (Rice et al. 2004, 2006). According to this model, solid cores can form rapidly in the outer disc from dust concentration in the spiral structure of a non-fragmenting gravitationally unstable disc. Inside gas spiral arms, the dust to gas ratio can reach unity, making the dust unstable itself. Rice et al. (2006) found that, if the dust self-gravity is taken into account, the solid component fragments, forming clumps of the order of the Earth mass. Clearly, the degree of concentration of dust particles is determined by the Stokes number. This effect is at its maximum for St $= 1$ particles (Rice et al. 2004; Dipierro et al. 2015a). After those works, the topic of dust dynamics in gas spiral arms gained interest. Walmswell et al. (2013) studied the dynamics of weakly coupled solid particles in gravitoturbulent discs, showing that it is well described by a series of perturbations through gravitational scattering by the spiral arm. As a matter of fact, the spiral arm is "kicking" dust particles, exciting them and potentially preventing the collapse. Booth & Clarke (2016) tackled this problem through two-dimensional SPH simulations. The level of dust particle excitation relies on the strength of the spiral perturbation and its aerodynamical interaction with gas. Notably, they determined that the dust dispersion velocity grows as the amplitude of the spiral perturbation increases. Specifically, when the spiral density contrast $\delta\Sigma/\Sigma$ is higher, the kick becomes more powerful, leading to greater particle dispersion velocity. It is worth noting, as discussed in Chapter 3, that $\delta\Sigma/\Sigma$ is proportional to $\beta^{-1/2}$. This implies that if cooling is more rapid (low β), dust becomes more efficiently excited. As far

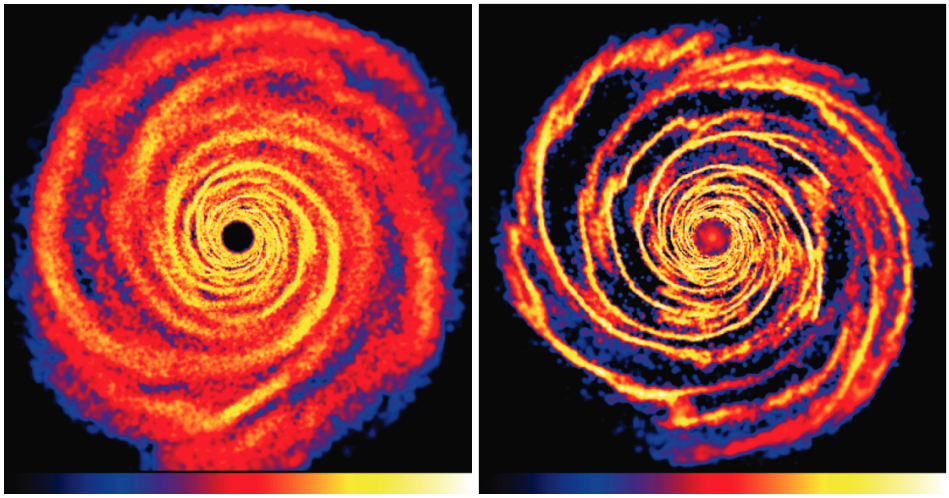

Figure 5.8: Snapshot of a numerical SPH simulation (Rice et al. 2006) of a gravitationally unstable disc showing the surface density of gas (left) and dust (right) component.

as the aerodynamical coupling is concerned, the drag force has the role of damping the kick: indeed, if a solid particle is strongly coupled, it is excited less effectively. Hence, they found that for $\mathrm{St} > 1$, the excitation of dust particles scales as $\mathrm{St}^{1/2}$. The interplay between dust concentration and excitation determines the possibility of collapse inside spiral arms.

Part II

Kinematics of self-gravitating protostellar discs

CHAPTER 6

Kinematic signatures of gravitational instability

*This chapter is based on the paper "Investigating protoplanetary disc cooling through kinematics: analytical GI Wiggle" by **Cristiano Longarini**, Giuseppe Lodato, Claudia Toci, Benedetta Veronesi, Cassandra Hall, Ruobing Dong and Jason P. Terry, published in Astrophysical Journal in October 2021.*

For cold massive discs, the role of the disc self-gravity becomes dynamically important, affecting the vertical and radial structure of the system (Kratter & Lodato 2016; Bertin & Lodato 1999). In this context, gravitational instabilities often arise, determining the evolution of the system and playing a fundamental role in the transport of angular momentum. On the one hand, a possible outcome of GI in protostellar environments is the fragmentation of the disc: this phenomenon can potentially lead to the formation of low-mass stellar companions (Kratter & Matzner 2006; Stamatellos et al. 2007; Cadman et al. 2020), because the initial clump mass is of the order of several Jupiter masses, too high to form a planet (Kratter & Lodato 2016). On the other hand, GI is a very effective way to transport angular momentum within the disc, by means of a global spiral perturbation (Lodato & Rice 2004; Rice et al. 2004).

High resolution observations with ALMA have revealed that most of the observed protostellar discs possess substructures as rings or spirals. The origin of rings is often explained by planets (Dipierro et al. 2015a, 2018; Toci et al. 2020a; Veronesi et al. 2020), however what causes the spirals is still ambiguous. Indeed, super-Jupiter objects can excite spiral density waves with azimuthal wavenumber $m \sim 1-2$, that match with good agreement the observed structures in scattered light (Dong et al. 2015; Dong & Fung 2017; Veronesi et al. 2019). In addition, some spirals may also be induced by an inner or outer stellar companion (Price et al. 2018a), or by a flyby (Cuello et al. 2019, 2020). At the same time, large scale spiral perturbations also characterize self-gravitating discs, with a typical $m \sim M_\star/M_d$, where M_d is the disc mass and $M_\star$ is the mass of the star (Cossins et al. 2009). Distinguishing the origin of a spiral is difficult, but recent high resolution observations of protostellar environments allow us to conduct kinematic studies that might shed some light on this issue. It is well known that the presence of a perturber inside the disc creates a localized deviation from the Keplerian observed velocity, called "kink" (Pinte et al. 2018b; Teague et al. 2018): when the perturber is a planet, the kink can be used as a proxy for its mass (Bollati et al. 2021). As far as GI is concerned, Hall et al. (2020) showed, based on hydrodynamical simulations, that the spiral perturbation deeply affects the gas kinematic: in particular, it creates a global (rather than a localized) deviation from Keplerian observed velocity - a "global kink" - dubbed GI wiggle by Hall et al. (2020), that is apparent in the observed velocity field (Paneque-Carreño et al. 2021).

In this chapter, we present an analytical study of the response of a self-gravitating protostellar disc to a spiral density wave in WKB regime. We focus our attention on the velocity perturbations (hereafter referred as VPs). We show that unstable discs have clear kinematic imprints into the gas component across the entire disc extent, due to the GI spiral wave perturbation, resulting in deviations from Keplerian rotation. The VPs are related to the disc structure, in particular, they are determined by the disc mass and the strength of GI (described in terms of cooling factor). By detecting these features, we can put constraints on protoplanetary discs cooling and hence on the transport of angular momentum. The analytical theory enables us to compute the observed velocity field, and then to make a connection to observations.

6.1 Velocity perturbations

In this paragraph we obtain the velocity perturbations induced by gravitational instability. To do so, we start with the fluid equations for a thin self-gravitating axisymmetric gas disc, we perturb them, and we keep only the first order terms. We basically follow the same procedure of section 3.2.1, but here, we are interested into the first order velocity perturbations. We solve for them and we obtain

$$\begin{aligned} v_{R1} &= \frac{i}{\Delta}\left[(\omega - m\Omega)\frac{\partial}{\partial R}(\Phi_1 + h_1) - \frac{2m\Omega}{R}(\Phi_1 + h_1)\right], \\ v_{\phi 1} &= -\frac{1}{\Delta}\left[2B\frac{\partial}{\partial R}(\Phi_1 + h_1) + \frac{m(\omega - m\Omega)}{R}(\Phi_1 + h_1)\right], \end{aligned} \tag{6.1}$$

where $B(r) = -\frac{1}{2}\frac{\mathrm{d}(\Omega r)}{\mathrm{d}r} + \Omega$ is one of the Oort parameter (Oort 1927), Φ_1 is given by (3.28), $h_1 = c_s^2\Sigma_1/\Sigma_0$ and $\Delta = \kappa^2 - (\omega - m\Omega)^2$. These equations are well known in literature (Binney & Tremaine 1987).

Now we make some assumptions: firstly, we write the perturbation as

$$X_1(R, \phi, t) = \mathrm{Re}\left[\delta X(R) e^{i(m\phi - \omega t + \psi)}\right], \tag{6.2}$$

where δX is exclusively a function of the radius. Secondly, we consider a marginally stable accretion disc with $Q = 1$, meaning that $\Delta = \kappa^2$ and $k = k_{\mathrm{uns}}$. Thirdly, both the potential ($\delta\Phi$) and the enthalpy (δh) perturbations are linked to the density one that, for a self regulate state, is connected to the basic state through the cooling rate. Hence, the perturbed potential and enthalpy are just a function of the basic state quantities and the cooling β

$$\delta\Phi = -\frac{2\pi G}{|k|}\delta\Sigma = -2c_s^2\beta^{-1/2}, \tag{6.3}$$

$$\delta h = c_s^2\frac{\delta\Sigma}{\Sigma_0} = c_s^2\beta^{-1/2} = -\frac{1}{2}\delta\Phi. \tag{6.4}$$

Finally, the VPs are

$$\begin{aligned} \delta v_R &= \frac{2im\Omega}{R\kappa^2}\beta^{-1/2}c_s^2, \\ \delta v_\phi &= \frac{2iB}{\kappa^2}\frac{\mathrm{d}\psi}{\mathrm{d}R}\beta^{-1/2}c_s^2. \end{aligned} \tag{6.5}$$

6.1.1 Nearly Keplerian disc

Now, we make the hypothesis of nearly Keplerian disc. This enables us to write the VPs as a function of the Keplerian speed and Keplerian frequency. This regime is identified by the conditions that

$$\frac{\kappa - \Omega_k}{\Omega_k} < 1, \quad \frac{\Omega - \Omega_k}{\Omega_k} < 1. \tag{6.6}$$

This assumption allows us to write $\kappa \simeq \Omega \simeq \Omega_k \propto R^{-3/2}$ and $B \simeq -\Omega/4$. With these assumptions, the equations for the VPs are

$$\begin{aligned} \delta v_R &= 2im\beta^{-1/2} \left(\frac{M_d(R)}{M_\star}\right)^2 v_k \\ \delta v_\phi &= -\frac{i\beta^{-1/2}}{2} \left(\frac{M_d(R)}{M_\star}\right) v_k, \end{aligned} \tag{6.7}$$

where v_k is the Keplerian speed. Finally, the velocity field is given by

$$v_R = \mathrm{Re}\left[\delta v_R e^{i(m\phi - \omega t + \psi)}\right], \tag{6.8}$$

$$v_\phi = R\Omega + \mathrm{Re}\left[\delta v_\phi e^{i(m\phi - \omega t + \psi)}\right]. \tag{6.9}$$

To obtain these expressions we used that $Q = 1$ and that $\mathrm{d}\psi/\mathrm{d}R = k = k_{\mathrm{uns}}$. Note that $\delta v_R/\delta v_\phi \simeq 4mM_d/M_\star$: for example, when $m = 2$, a relatively light disc having $M_d = 0.125M_\star$ has $\delta v_R = \delta v_\phi$.

In the analysis above, we have neglected the effect of pressure gradients. This is for two main reasons: firstly, it influences only the basic state of the system, not the perturbations, at least to first order. Secondly, when we consider a marginally unstable self-gravitating disc ($Q = 1$), we expect the contribution of the pressure gradient to the velocity field to be sub-dominant with respect to the self-gravity one. Indeed, for such a disc, the self-gravitating contribution is of the order of H/R, while the pressure term is $O(H^2/R^2)$ (Kratter & Lodato 2016; Veronesi et al. 2021). The effects of pressure gradients are stronger when considering much lower disc to star mass ratios (e.g., see Rosenfeld et al. 2013). For the massive discs that we consider in this work, the pressure gradient can thus be neglected. In the light of this, while considering the pressure gradient is critical when one wants to explore the basic state, as done in Veronesi et al. (2021); Lodato et al. (2023), this is not strictly necessary in our perturbation theory.

6.1.2 Not constant cooling factor

So far we have considered only the case of constant $\beta-$cooling. However, self-consistent models of GI discs (Clarke 2009; Rice & Armitage 2009) show that β varies with the radius (Hall et al. 2016). This happens because these models give a realistic cooling prescription, i.e. radiative cooling, and its rate depends on the temperature of the disc at the midplane and on the Rosseland opacity (Bell & Lin 1994). If one sets the density profile to be a power law with radius, the cooling prescription can be written as a collection of power laws with indices n_i, depending on the density and the temperature.

In general, we can choose any cooling law $\beta(R, \rho(R), T(R))$ and then obtain the VPs thorugh equations (6.5).

6.2 Connection with observations: observed velocity field

In this paragraph, we want to connect what we have found to observations: what are the observational imprints of these perturbations? The observed velocity field of the gas is obtained by calculating the intensity weighted average velocity of the emission line profile, i.e. the "moment-1" map. In this work, we do not take into account line emission processes, and instead we simply compute the projected velocity field along the line of sight and we study the impact of velocity perturbations that we have just obtained.

We assume two-dimensional polar system of coordinates (R, ϕ) centred upon the star, so that the velocity vector can be written as $\mathbf{v} = (v_R, v_\phi)$. We consider the disc inclined with an angle θ, that in the following we take equal to $\pi/6$. Within this framework, the projected velocity field can be written as

$$v_{\rm obs} = v_R \sin\phi \sin\theta + v_\phi \cos\phi \sin\theta + v_{\rm syst}, \tag{6.10}$$

where $v_{\rm syst}$ is the velocity of the system projected towards the line of sight. A channel map is defined as the iso-velocity contours for a chosen observed velocity.

Hence, by knowing the radial and the azimuthal components of the perturbed velocity field (equations 6.7), we can sketch the projected velocity field (moment-1 equivalent) and the channel maps, as shown in the top and central panels of figure 6.1. As already noted in Hall et al. (2020), the VPs due to gravitational instability appear throughout the whole extent of the disc, rather than being localised in position and velocity, as occurs for the kink produced by an embedded protoplanet. This is clearly shown in the bottom panel of figure 6.1, where we subtract the Keplerian field to the perturbed one: an "interlocking fingers" structure is present, as already pointed out in Hall et al. (2020). If we look at the central channel, the deviations from the Keplerian behaviour exactly match with the fingers pattern.

We want to underline that in this work we are only considering the projection of the velocity field along the line of sight, without making any assumptions about the gas emission processes. In order to convert velocities to fluxes, it is necessary to include the physics of the gas, specifying the selected tracer and the emission lines observed and considering also the effect of the beam size and the possible presence of observational noise.

6.3 Constraining the cooling factor - mock test

So far, we have seen that the cooling factor deeply influences the shape of the channel maps. Thanks to this property, we propose a method with which we can constrain effectively the cooling factor of observed systems. In order to verify the accuracy of the calculations we have made, we apply the method just described to a numerical simulation. We perform an SPH simulation using the code PHANTOM (Price et al. 2018b). This code is widely used in astrophysical community to study gas and dust dynamics in accretion discs (Toci et al. 2020b; Ragusa et al. 2020; Veronesi et al. 2020); in this work, we used the so-called "one fluid" method and we simulated a gas only disc, neglecting the dust component. The initial conditions of the disc are $R_{\rm in} = 1$au, $R_{\rm out} = 50$au, $\Sigma \propto R^{-1}$, $M_d = 0.5\mathrm{M}_\star$, $M_\star = 1\mathrm{M}_\odot$. The cooling factor β has been set to $\beta = 8$ and the two parameters that control the artificial viscosity to $\alpha^{AV} = 0.1$, $\beta^{AV} = 0.2$, in order to reduce as much as possible the effects of artificial dissipation (Lodato & Rice 2004). The initial sound speed profile follows a simple power law $c_s \propto R^{-0.25}$. However, this profile is

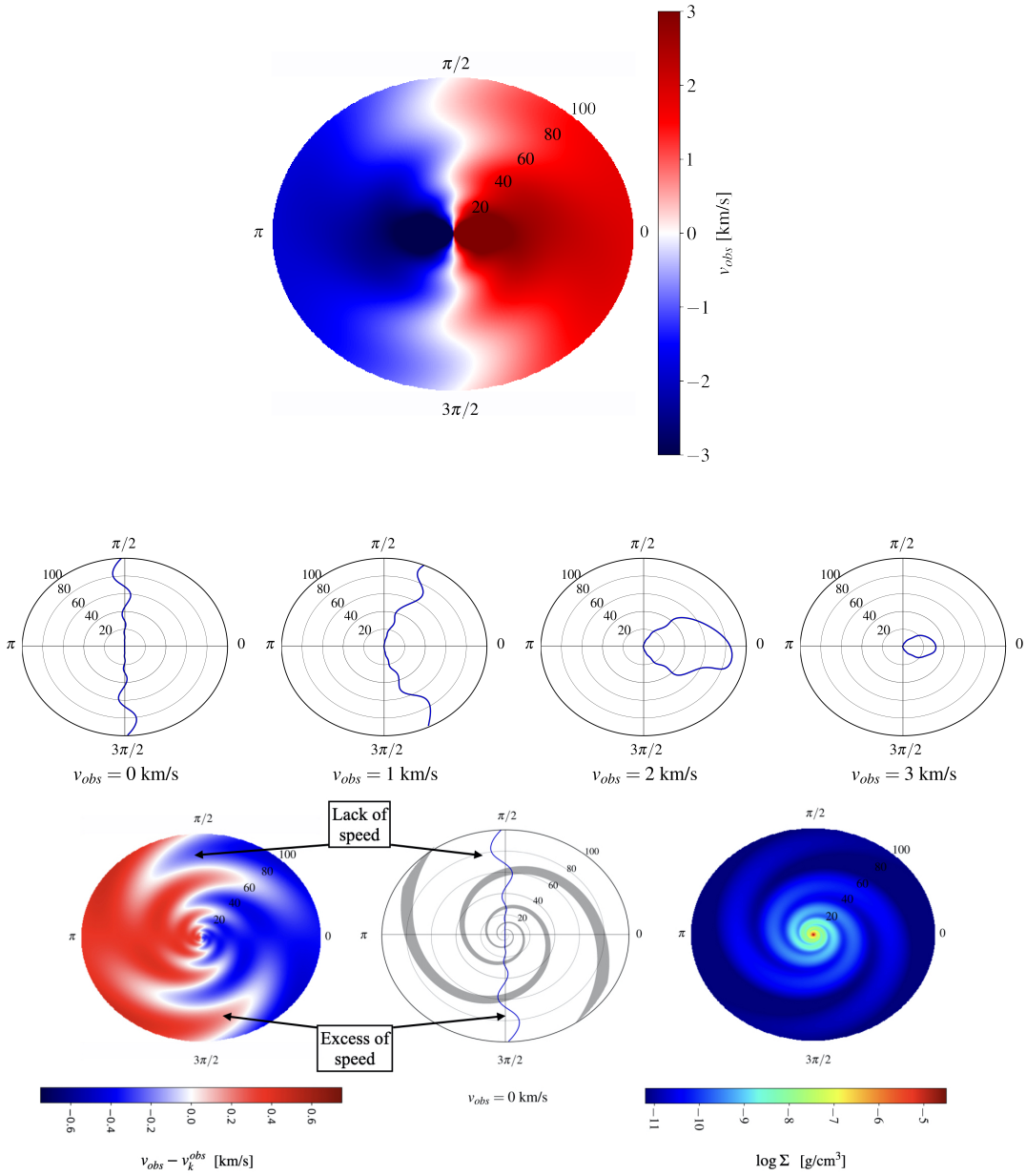

Figure 6.1: Moment one map (top panel) and channel maps (middle panel) for a self-gravitating accretion disc seen with an inclination angle of $\pi/6$ and with a systemic velocity $v_{\rm syst} = 0$. (Bottom panel) Left side: projected map of the velocity perturbation, after subtraction of the Keplerian field. A system of interlocking fingers is clearly visible, as already noted by Hall et al. (2020). Central side: the $v_{\rm obs} = 0$ contour (blue line) overlaid with the spiral shape (grey line). The deviations from the Keplerian channel (that is simply a straight line) perfectly match with the spiral pattern. Right side: surface density of the disc. The parameters of the disc are the following: $r_{\rm in} = 1$au, $r_{\rm out} = 100$au, $M_\star = 1{\rm M}_\odot$, $M_d = 0.3{\rm M}_\star$, $p = -1$, $\beta = 5$, $\alpha_p = 15^\circ$ and $m = 2$.

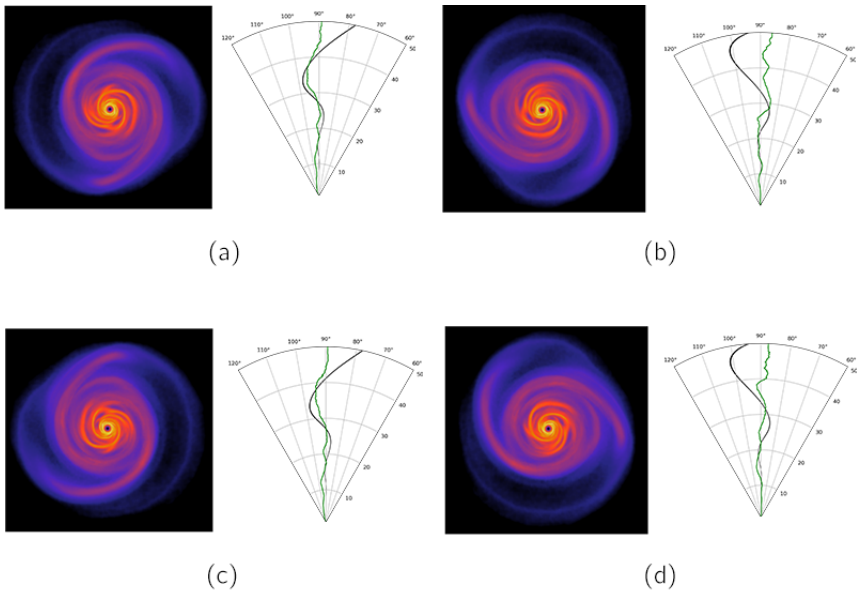

Figure 6.2: Comparison between analyical (black line) and numerical (green line) perturbation for different viewing angle of the simulated GI disc. Each picture is rotated along the z-axis of an angle of $\pi/2$.

rapidly modified by the cooling. For this simulation, we used $N = 5 \times 10^5$ particles of gas. the simulation shows a predominance of the $m = 2$ azimuthal mode and the computed pitch angle is $\alpha_p \sim 13°$.

We now constrain the cooling factor using the method described previously, and make a comparison with the actual value set in the simulation. First of all we compute the rotation curve, azimuthally averaging $u_\phi(R, \phi)$. Then, we find the value of the disc mass that best describe the curve using equation (4.10): the best value corresponds to $M_d = 0.5\mathrm{M}_\star$, as expected. We have broken the degeneracy between the mass and the cooling: thus, we are now able to constrain the cooling β through the wiggle amplitude. Figure 6.2 shows the central channel of the projected velocity field of the simulation compared with the one from the analytical model, for different spiral angles: as expected, a wiggle is present. The amplitude of the simulated wiggle is $\mathcal{A}_{\mathrm{sim}} = 0.11\mathrm{rad}$. The amplitude of the wiggle as a function of the cooling factor, for the parameters previously reported, is described by $\mathcal{A}(\beta) = \mathcal{A}_{\mathrm{in}}\beta^{-0.5}$, where $\mathcal{A}_{\mathrm{in}} = 0.33\mathrm{rad}$. The estimated cooling factor is then $\beta_{\mathrm{sim}} = (\mathcal{A}_{\mathrm{sim}}/\mathcal{A}_{\mathrm{in}})^{-2} \simeq 9$, that is in good agreement with the real value $\beta = 8$. The overestimated value of β can actually be interpreted by the lack of viscosity in our analytical model. Indeed, because of its dissipative nature, we expect it to damp GI-driven perturbations, resulting in a less pronounced wiggle. This behaviour is visible in the comparison with the numerical simulations, hence the simulated perturbation appears less wide than the analytical one.

Figure 6.2 shows a comparison between the analytical and the numerical wiggle, for different viewing angle of the spiral structure (the observer is assumed to be along a vertical line on the bottom of the images). There is a very good agreement in the top left panel and bottom left for which the line of sight intercept the largest extent of the spiral, while the perturbation is overestimated in panel top right and bottom right in which

the prominent spiral structure lies on a line perpendicular to the line of sight. For the former case, the agreement between our model and the simulation is remarkable. For the two other orientations, while there is good agreement in the inner disc (where the perturbation is however smaller), our model overestimates the perturbation in the outer disc, where in the simulation the spiral structure vanishes. This suggests that in actual observations, our analysis is most reliable when a density spiral (for example traced by the dust continuum) is also visible superimposed to the kinematical wiggle.

6.4 Discussion

6.4.1 Shape of the wiggle

So far, we have seen that deviations from the Keplerian behaviour are visible in every channel map, however we now focus on the central velocity channel that, in a case where $v_{\rm syst} = 0$, corresponds to $v_{\rm obs} = 0$. This channel is particularly interesting since in the Keplerian case it is simply a straight line, because the radial velocity is zero. In the GI case, the central channel shows oscillation around the Keplerian value (i.e. the wiggle): this happens because the spiral wave perturbs both the azimuthal and the radial component. The amplitude and the radial frequency of the wiggle depend on the strength of the spiral wave (that is related to the cooling factor β), the opening angle α_p and the number of arms m (figure 6.4), and on the structure of the underlying disc, in particular its mass.

It is possible to quantify the amplitude of the VPs by considering the integrated geometrical distance between the perturbed and the unperturbed channel. Mathematically, a channel map C_v is a 2D curve defined parametrically from a one-dimensional interval $\mathcal{I}$ to a two-dimensional space $\mathcal{R}^2$. In our case, the two-dimensional space is the cylindrical space (R, ϕ) and the interval $\mathcal{I}$ depends on the parameterization we choose: for simplicity, we take $\mathcal{I} = [0, 1]$. For a given channel velocity v, we call the Keplerian channel map C_v^k and the perturbed one C_v^p. Mathematically speaking, the two channel maps can be written parametrically as

$$C_v^k(s) = \begin{pmatrix} f_R^k(s) \\ f_\phi^k(s) \end{pmatrix}, \quad C_v^p(s) = \begin{pmatrix} f_R^p(s) \\ f_\phi^p(s) \end{pmatrix}, \tag{6.11}$$

where s is a parameter in the interval $\mathcal{I}$, in our case $s \in [0, 1]$. The amplitude of the perturbation is then computed as

$$\mathcal{A}_v = \left[\int_0^1 \mathrm{d}s ||C_v^p - C_v^k||^2 \right]^{1/2}, \tag{6.12}$$

that is the length of the curve $C_v^p - C_v^k$. The top panel of figure 6.3 schematically shows the quantities involved in equation (6.12). The amplitude is determined by both the cooling factor and the disc mass: a smaller β generates a bigger deviation from the Keplerian case, because the amplitude of the spiral is inversely proportional to β. On the bottom panel of figure 6.3 we show the amplitude of the wiggle ($v_{\rm obs} = 0$) as a function of the cooling parameter β: it is possible to describe the relation between $\mathcal{A}$ and β as a power law, with an index of $-1/2$, and this can be easily seen from equations (6.7). The role of the cooling factor acts as the planet mass in the case of planetary kinks: indeed, the amplitude of the kink is determined by the mass of the embedded protoplanet, and it follows the relation $\mathcal{A} \propto M_p^{1/2}$ (Bollati et al. 2021). In addition, the amplitude of the wiggle is also determined by the disc mass: in particular, it affects the perturbed velocities

because it is related to the sound speed. Indeed, with the hypothesis of $Q \simeq 1$ we get $c_s = v_k H/R \simeq v_k M_d/M_\star$. The disc mass is directly proportional to the sound speed, and then bigger c_s means faster propagation of density waves. The bottom panel of figure 6.3 shows how the amplitude of the wiggle depends on the disc mass. The trend is easily explained by looking at the equations of the VPs (6.7): in the radial perturbation, the disc mass appears with a quadratic dependence, while in the azimuthal one, it appears linearly. The amplitude of the channel (6.12) is proportional to the root sum of squares, thus $\mathcal{A} \propto \sqrt{c_1 M_d^2 + c_2 M_d^4}$, where c_1, c_2 are two constants that depend on the other parameters, as the cooling.

The mass of the disc and the cooling β are degenerate parameters when we consider the shape of the wiggle: as a matter of fact, they both contribute to its amplitude. Is it possible to break the degeneracy? This can be done if an independent method to measure M_d is available. For example, using again the gas kinematics, one could measure the disc mass through rotation curve (Veronesi et al. 2021; Lodato et al. 2023). Conversely, when an approach like this is not possible, we can give a rough estimate of the disc mass through dust emission. Indeed, from dust thermal emission it is possible to measure the dust mass of the disc and then, assuming a dust to gas ratio, we can estimate also the total mass of the disc.

Interestingly, if we look at the perturbed velocity field, there could also be a purely kinematical way to break the degeneracy between disc mass and cooling. Indeed if we write the observed velocity field for $\phi = \pi/2$ (semi-minor axis of the disc) we get

$$v_{\rm obs} = v_R \sin\theta = \mathrm{Re}\left[\delta v_R(R) e^{i(m\pi/2+\psi)}\right] \sin\theta = f_1(R)\beta^{-1/2}\left(\frac{M_d}{M_\star}\right)^2 v_k, \tag{6.13}$$

where f_1 is a known function of radius; conversely, for $\phi = 0$ (semi-major axis of the disc) we get

$$v_{\rm obs} = v_\phi \sin i = \left(R\Omega + \mathrm{Re}\left[\delta v_\phi(R) e^{i\psi}\right]\right) \sin i = f_2(R)\beta^{-1/2}\frac{M_d}{M_\star} v_k + R\Omega \sin i, \tag{6.14}$$

where f_2 is a known function of the radius. Since the perturbed velocities scale differently with disc mass, if we could measure accurately the ratio of the two components of the perturbed velocity, we could in principle directly obtain a measurement of the disc mass. However, we note that it is challenging to extract these information from an actual observation.

Breaking the degeneracy allows us to constrain the cooling parameter β, which gives important information about the physical processes that are happening in the protoplanetary environment, and on the tendency of the disc to fragment into bound clumps and the amount of angular momentum transported by the GI.

So far we have described what determines the amplitude of the wiggle: as far as its frequency is concerned, it is determined by the pitch angle and by the number of spiral arms. In figure 6.4 we show the shape of the wiggle for different values of α_p and m. We clearly see that the frequency of the wiggle is bigger when decreasing α_p and increasing m.

6.4.2 Limitations

As can be seen in figure 6.4, the number of spiral arms slightly influences the amplitude of the wiggle: all the calculations have been made under the WKB assumption, that requires $m/rk << 1$. Thus, for high m, this assumption is not valid anymore: in fact,

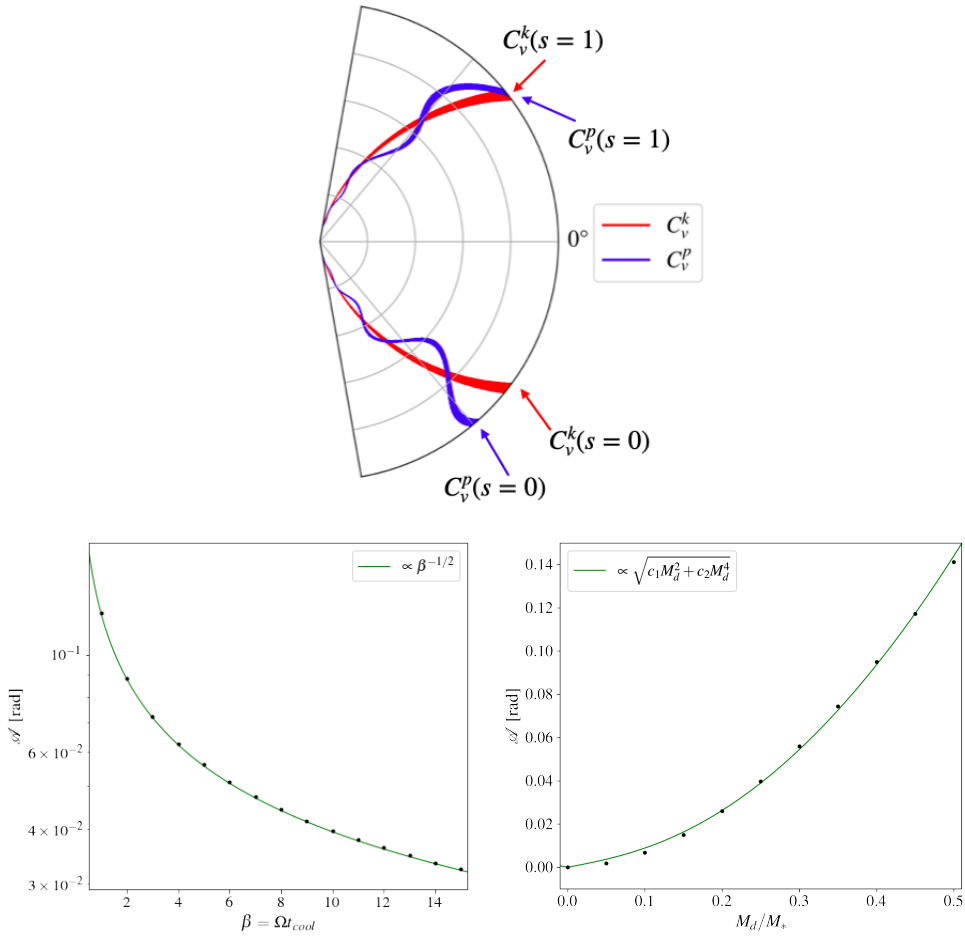

Figure 6.3: Schematic view of how the amplitude of the wiggle is computed. Top panel: the red line is the Keplerian channel map, while the blue line is the perturbed one. The amplitude of the perturbation is computed using equation 6.12. Amplitude of the perturbation in the central channel as a function of the cooling parameter β (bottom left panel) for a disc mass $M_d/M_\star = 0.3$ and of the mass of the disc (bottom right panel) for a cooling parameter $\beta = 5$. The black dots are the results of the analytical model so far described.

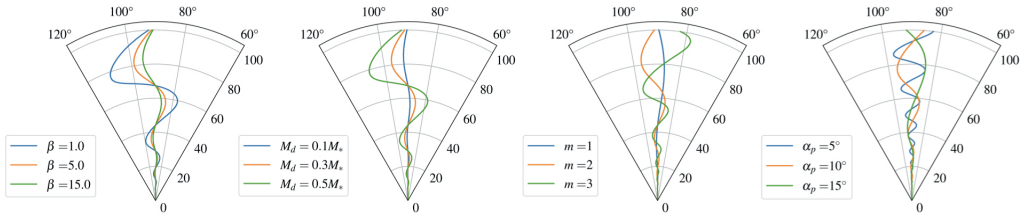

Figure 6.4: Shape of the wiggle varying (from left to right) the cooling factor β, the mass of the disc M_d, the pitch angle α_p in degrees and the azimuthal wavenumber m. The reference disc parameters are $r_{\text{in}} = 1\text{au}$, $r_{\text{out}} = 50\text{au}$, $M_\star = 1\text{M}_\odot$, $M_d = 0.3\text{M}_\star$, $p = -1$, $\beta = 5$, $\alpha_p = 15°$ and $m = 2$.

we are not considering the relations between the number of spiral arms and the mass of the disc, or its thickness; the only way to take into account these non-linear effects is by means of numerical simulations (Terry et al. 2022). This argument is better understood when looking at the quadratic dispersion relation (eq. (3.2.1)): in the tight winding approximation (WKB), m does not enter explicitly in the dispersion relation (except in the Doppler-shifted frequency), thus both axisymmetric ($m = 0$) and non-axisymmetric ($m \neq 0$) perturbations have the same instability threshold. However, it is well known (Ostriker & Peebles 1973) that massive discs are subject to large scale non-axisymmetric instabilities even though $Q > 1$. Indeed, a local dispersion relation can also be obtained in the case of open spiral structures (see sect. 3.2.3).

Another important point to stress is that we built a 2D model of the disc, neglecting its height. Thus, we are considering only what happens in the disc midplane. The main effect of the disc thickness is to "dilute" the gravity field, and this can be incorporated into the quadratic dispersion relation (see section 3.2.2). Observationally speaking, the disc thickness is important when we take into account the molecular line emission of CO isotopologues. As a matter of fact, ^{12}CO, that is the most abundant isotopologue, is not a good tracer of the disc midplane, because it becomes optically thick at the disc surface. On the contrary, other less abundant CO isotopologues as ^{13}CO or C^{18}O have more optically thin lines and as a consequence they trace better the disc midplane (Miotello et al. 2014).

Finally our analysis takes into account a single spiral mode m, while it is well known that for small disc -to-star mass ratio, there could be a superposition of modes. However this is not an actual problem: indeed, we know that after filtering out through the ALMA response (that we do not do in this paper), as shown in Dipierro et al. (2014), only the dominant mode appears. This makes our single-mode analysis still valid.

6.5 Conclusion

In this chapter, we have analytically studied the velocity perturbations in a self-gravitating disc caused by the presence of a spiral density wave in the WKB regime. We then applied this result to obtain the projected velocity field (moment one equivalent) and the channel maps, studying their deviations from the Keplerian case. We found what Hall et al. (2020) have already seen from numerical simulations, that deviations from Keplerian rotation are a global phenomenon, resulting in velocity "kinks" across the entire radial and azimuthal extent of the disc. The kinematics deviations, called GI wiggles, depend on the structure of the spiral density wave, namely its amplitude (connected to

the cooling and to the disc mass) and its radial frequency (connected to the pitch angle and to the azimuthal wavenumber).

Pinte et al. (2020) found nine deviations from Keplerian rotation pattern in the DSHARP circumstellar discs: three of them, Elias 2-27 (Pérez et al. 2016; Paneque-Carreño et al. 2021), IM Lup and WaOph6 show also spiral structures in the millimetric continuum emission. These three systems are believed to be self-gravitating (Huang et al. 2018a), thus their deviations from Keplerian rotation may be interpreted as wiggles. In addition, Veronesi et al. (2021) have shown that the rotation curve of Elias 2-27 is better described adding the contribution of the disc gravitational potential, meaning that the effects of disc self-gravity are not negligible.

Higher resolution observations of systems like those will make it possible to investigate the cooling of protoplanetary discs: indeed, the degeneracy between mass and cooling can be broken by means of the rotation curve, and thus the cooling parameter β can be constrained effectively through the wiggle's amplitude, as we have shown in section 6.3. Knowing more about the cooling will give us insights about the gravitational instability process.

CHAPTER 7

Weighing and sizing protoplanetary discs with gravity

*This chapter is based on the papers "Weighing protoplanetary discs with kinematics: physical model, method and benchmark" by Benedetta Veronesi, **Cristiano Longarini**, Giuseppe Lodato, Guillaume Laibe, Cassandra Hall, Stefano Facchini and Leonardo Testi, submitted to Astronomy & Astrophysics, and "Rotation curves in protoplanetary discs with thermal stratification" by Paola Martire, **Cristiano Longarini**, Giuseppe Lodato, Giovanni Rosotti, Andrew Winter, Stefano Facchini, Caitlyn Hardimann, Myriam Benisty, Jochen Stadler, Andrés Felipe Izquierdo and Leonardo Testi, submitted to Astronomy & Astrophysics.*

The mass of protoplanetary discs sets the amount of material available for planet formation, determines the level of coupling between gas and dust, and possibly sets the onset of gravitational instabilities. Measuring mass of discs is challenging, since it is not possible to directly detect H_2, and CO-based estimates remain poorly constrained. An alternative method, that does not rely on tracers-to-H_2 ratios, consists in dynamically measure the disc mass, together with star mass and scale radius, by looking at deviations from Keplerian rotation induced by the self-gravity of the disc. This method rely on results of Bertin & Lodato (1999), and it has been used for the first time in the context of protoplanetary discs by Veronesi et al. (2021), and then improved by Lodato et al. (2023). In this chapter, we benchmark through numerical simulations the vertically isothermal model, as presented in chapter 4, and then we generalize it by including thermal stratification. The benchmarking of the vertically isothermal model (section 7.1) is based on the paper *Veronesi, Longarini et al.* and the modelling of the thermal stratification (sections 7.2, 7.3) on *Martire, Longarini et al.*

7.1 Benchmarking the isothermal model

The aim of this work is to benchmark the vertically isothermal model, assessing the minimum measurable disc mass and the accuracy of the measurement. The vertical isothermal model we refer to is the one in section 4.2. For completeness, we write the equation for the azimuthal velocity

$$v_\phi^2 = v_\mathrm{k}^2 \left\{ 1 - \left[\gamma' + (2-\gamma) \left(\frac{R}{R_\mathrm{c}} \right)^{2-\gamma} \right] \left(\frac{H}{R} \right)^2 - q \left(1 - \frac{1}{\sqrt{1+(z/R)^2}} \right) \right\} + v_d^2 \,, \tag{7.1}$$

where $\gamma' = \gamma + 3/2 + q/2$, $v_k^2 = GM_\star/R$ and

$$v_{\rm d}^2 = G\int_0^\infty \left[K(k) - \frac{1}{4}\left(\frac{k^2}{1-k^2}\right) \times \left(\frac{r}{R} - \frac{R}{r} + \frac{z^2}{Rr}\right) E(k)\right] \sqrt{\frac{r}{R}} k\Sigma\left(r\right) {\rm d}r \,. \tag{7.2}$$

$K(k)$ and $E(k)$ are complete elliptic integrals and $k^2 = 4Rr/[(R+r)^2+z^2]$. To benchmark the model, we follow this pipeline

- **Hydrodynamical simulations:** we perform a set of hydrodynamical simulations of vertically isothermal protostellar discs with the code PHANTOM (Price et al. 2018b), varying the disc to star mass ration in the range $[0.01, 0.15]$;
- **Radiative transfer simulations:** we post-process the hydrodynamical simulations with the code MCFOST (Pinte et al. 2006, 2009), simulating the ^{12}CO and ^{13}CO J=2-1 line emission;
- **Spatial and spectral convolution:** we spatially and spectrally convolve the synthetic datacube to simulate the effect of a spatial and spectral beam, as in actual observations;
- **Emitting surface and rotation curve extraction:** we extract the height of the emitting layer with the geometrical method of Pinte et al. (2018a) using the code DISKSURF (Teague et al. 2021) and then we retrieve the azimuthal velocity using the simple harmonic oscillator method (Teague et al. 2018), implemented in EDDY (Teague 2019);
- **Fitting procedure:** we fit for disc mass, star mass and scale radius with the vertically isothermal model, and we assess the accuracy of the method. The parameters we fix are the disc inclination, the height of the emitting layer, and the disc temperature.

7.1.1 Hydrodynamical simulations

We perform a suite of 3D Smoothed Particle Hydrodynamics (SPH) simulations of gaseous protoplanetary discs, using the code PHANTOM (Price et al. 2018b). The system consists of a central star of mass $M_\star = 1\,M_\odot$ surrounded by a gas disc with mass $M_d = [0.01, 0.025, 0.05, 0.1, 0.15]\,M_\odot$. These simulations can be rescaled in terms of disc-to-star mass ratio. The disc extends from $R_{\rm in}$ = 10 au to $R_{\rm out}$ = 300 au, and is simulated with 10^6 SPH particles. The initial profile of surface density is a relaxed exponential tapered power law, with $R_{\rm c} = 100$ au and $\gamma = 1$. Simulations include the disc self-gravity as described in Price et al. (2018b), adopting a locally isothermal equation of state $P = c_{\rm s}^2\rho_{\rm g}$ with $q = 0.5$ for the power-law index of the temperature radial profile. Despite the non-negligible disc to star mass ratio, all the discs are gravitationally stable according to the Toomre criterion ($Q > 1$), hence the discs appear smooth and sub-structureless.

The disc is vertically extended by initially setting up an initial disc aspect ratio of $(H/R)_{\rm c} = 0.075$ with a Gaussian profile for the volume density, ensuring nearly vertical hydrostatic equilibrium. We model the angular momentum transport throughout the disc using the SPH shock capturing viscosity (Price et al. 2018b, see Sec. 2.6) with $\alpha_{\rm AV} \simeq 0.19$, which results in a Shakura & Sunyaev (1973) viscous parameter $\alpha_{\rm SS} \approx 0.005$.

7.1.2 Radiative transfer and synthetic observations

We compute the 3D thermal structure and we simulate the emission of the hydrodynamical discs using code MCFOST (Pinte et al. 2006, 2009). We use a Voronoi tesselation where each MCFOST cell corresponds to a gas SPH particle. The goal is to generate mock ^{12}CO and ^{13}CO isotopologue channel maps, from which we will extract disc rotation curves.

The main inputs for the radiative transfer modelling are the source of luminosity, i.e. the star, the gas density profile extracted from the simulations, and models for dust opacities and densities. Self-gravitating isothermal discs do not present any kind of substructures, and the underlying dust density profile can therefore assumed to be smooth. We do not account for an eventual dust drift, since Stokes numbers are expected to be small in these discs, and we consider short-enough disc evolutions. The dust contribution to the gravitational potential of the disc is also negligible. As such, we adopt a constant dust-to-gas ratio of $\sim 10^{-2}$ that corresponds to a standard averaged ISM (Draine 2011).

The thermal structure of the disc is computed with the following assumptions. At first, emission is at local thermal equilibrium and $T_{\rm gas} = T_{\rm dust}$. This assumption is valid for rotational transitions of CO isotopologues, as dust and gas a thermally coupled (Facchini et al. 2017; Bae et al. 2021). Dust is treated as a mixture of silicates (70%) and carbon (30%) (Draine & Lee 1984), and the optical properties are calculated using Mie theory for spheres (Andrews et al. 2009). Opacities are computed following the procedure described in the DIANA model (Woitke et al. 2016; Min et al. 2016). We assume an ISM-like grain size distribution ($dn/ds \propto s^{-3.5}$), with $s_{\rm min} = 0.01\,\mu$m and $s_{\rm max} = 1$ mm. The disc is heated passively, i.e. the source of radiation is only the central star, which is assumed to radiate isotropically with a Kurucz spectrum at 4000 K. The expected channel maps are computed via ray-tracing, using 10^8 photon packets to sample the radiation field. The disc inclination with respect to the line of sight is $i = 30°$, and the system is simulated to be located at 140 pc, which corresponds to a typical protostellar discs in a star-forming region such as Taurus. For ^{12}CO and ^{13}CO, we consider the J=2-1 transition and assume abundances of 10^{-4} and 1.4×10^{-6} respectively. MCFOST simulations are post-processed with PYMCFOST [1], by simulating a velocity resolution of $0.1\,{\rm km/s}$. We then spatially convolve the channels with a Gaussian beam of 0.1 arcsec, similarly to the value of the MAPS survey (Öberg et al. 2021). We finally introduce Gaussian noise with an RMS of 5mJy/beam.

7.1.3 Extracting the emitting layer and the rotation curve

From the synthetic datacubes, we first extract the height of the emitting layer with DISKSURF (Teague et al. 2021). The emitting layer is defined as the region where the emission we observe originates. Since different molecules have specific optical depth and column density, the location of the emitting layer changes accordingly. Having a precise estimate of the height of the emitting layer is crucial to correctly deproject azimuthal velocities and to evaluate the model.

We then use EDDY (Teague 2019) to extract the rotation curves with the simple harmonic oscillator method (Teague et al. 2018). Two methods have currently been developed to fit the line centroids: the quadratic and the Gaussian methods, as outlined in section 4.3.2. To perform our analysis we chose the quadratic method, and we will briefly discuss this choice in Sec. 7.1.3.

[1] `https://github.com/cpinte/pymcfost`

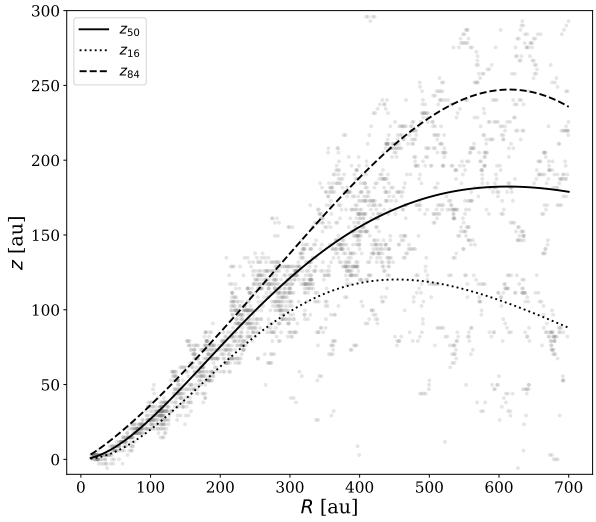

Figure 7.1: Example (^{12}CO, $M_{\rm d} = 0.1\,M_{\odot}$) of one of the emitting layer derived with DISKSURF (grey dots) and then fitted with an exponentially tapered power-law (solid line). We also show the 16th (dotted line) and the 84th (dashed line) percentiles, which we take into account to compute the rotation curve errors.

Retrieving the height of the emitting layer

We use the code DISKSURF (Teague et al. 2021) to extract the height of the emitting layer $z^n\,(r_i)$ of the i-th radial bin for the n-th channel. DISKSURF implements the method presented in Pinte et al. (2018a). Briefly, this is a geometrical method that allow to trace the emission maxima of each velocity channel and reconstruct the position of the CO layers. For each bin, we determine the heights $z^n_{16}\,(r_i)$, $z^n_{50}\,(r_i)$ and $z^n_{84}\,(r_i)$ that corresponds to the 16-th, 50-th and 84-th percentile of the emitting layer distribution respectively. We then use the tapered power-law

$$z(R) = z_0\,[\text{arcsec}] \left(\frac{R}{1\text{arcsec}}\right)^{\psi} \exp\left[-\left(\frac{R}{R_t}\right)^{q_t}\right], \tag{7.3}$$

to parametrize continuously the emitting surfaces $z_{16}(R)$, $z_{50}(R)$ and $z_{84}(R)$. We choose to extract three emitting layers to estimate the uncertainties associated to the extraction procedure.

Table 7.1 presents the results obtained for $z_{\rm em}\,(r)$ that will be used as reference surface through the following analysis. As an example, Fig. 7.1 shows the emission surface (grey markers) obtained with DISKSURF for the ^{12}CO datacube, from mock observations generated by a simulation with $M_{\rm disc} = 0.1\,M_{\odot}$. The three lines are the fits of the data points, namely z_{50} (solid line), as well as z_{16} (dotted line) and z_{84} (dashed line).

Extracting the rotation curve

We extract the azimuthal velocity with EDDY (Teague 2019) using the harmonic oscillator method, following Teague et al. (2018)

Table 7.1: ^{12}CO and ^{13}CO fit results for the disc emitting layer relevant parameters (z_0, ψ, R_t, q_t) obtained with DISKSURF from the 50th percentiles of the particle vertical distribution.

	md0.01	md0.025	md0.05	md0.1	md0.15
^{12}CO					
z_0	0.83	0.24	0.38	0.45	0.33
ψ	3.06	1.88	1.66	1.85	1.13
R_t	0.49	3.7	3.54	2.76	5.1
q_t	0.69	1.77	1.46	1.11	9.47
^{13}CO					
z_0	0.078	0.09	0.097	0.09	0.09
ψ	1.25	1.52	1.72	1.82	2.04
R_t	3.01	3.25	3.35	3.46	3.38
q_t	6.27	5.39	4.22	3.54	2.83

For each emitting layers $z_{16}, z_\mathrm{em} = z_{50}$ and z_{84}, we compute three rotation curves v_{16}, v_{50} and v_{84}. We then assume the azimuthal velocity of the system to be $v_\phi = v_{50}$, with an uncertainty σ_v estimated as

$$\sigma_v = \sqrt{|v_{84} - v_{16}|^2 + \sigma^2_\mathrm{eddy}}\,, \tag{7.4}$$

where σ_eddy is the numerical error obtained with EDDY. This procedure refines the approach of Lodato et al. (2023), since it includes uncertainties associated to estimate of the height the emitting layer.

Since we fixed the inclination of the disc to be $i = 30°$, we use the Quadratic method to extract the rotation curve, that fits only the peak of emission, which is less sensitive to the lower surface. Indeed, using instead the Gaussian method provides the following bias: the emission coming from the lower surface systematically shifts the position of the line centroids, resulting in a systematic error for the velocity estimate. Fig. 7.2 shows a comparison between the quadratic and the Gaussian methods. Interestingly, despite being smoother, the curve obtained with the Gaussian method underestimates the velocity in the inner disc and overestimates it in the outer disc. This happens because the method tries to fit a double-peaked spectrum with a single Gaussian.

Fig. 7.3 shows the rotation curves obtained with the quadratic method following the procedure above, for both CO isotopologues (^{12}CO in the left panel, ^{13}CO in the right panel). We compare them with the analytical rotation curve obtained assuming a disc of zero mass (black dashed-dot line).

7.1.4 Fitting procedure and uncertainties estimate

For every simulation, we obtain two rotation curves: one for ^{12}CO and another for ^{13}CO. These curves are then fitted using the self-gravitating model of Eq. 7.1. The free parameters are the star and disc mass, and the disc scale radius R_c. The fits are performed with an MCMC algorithm as implemented in EMCEE (Foreman-Mackey et al. 2013) using the code DySc `https://github.com/crislong/DySc`. We choose a simple Gaussian likelihood, and flat priors respectively $[0, 5]\mathrm{M}_\odot$ for the star mass, $[50, 300]$au for the scale radius and $[0, 0.5]\mathrm{M}_\odot$ for the disc mass. We choose 250 walkers and 1000 steps (having verified that convergence is reached). We fit the two isotopologues both individually, and then simultaneously.

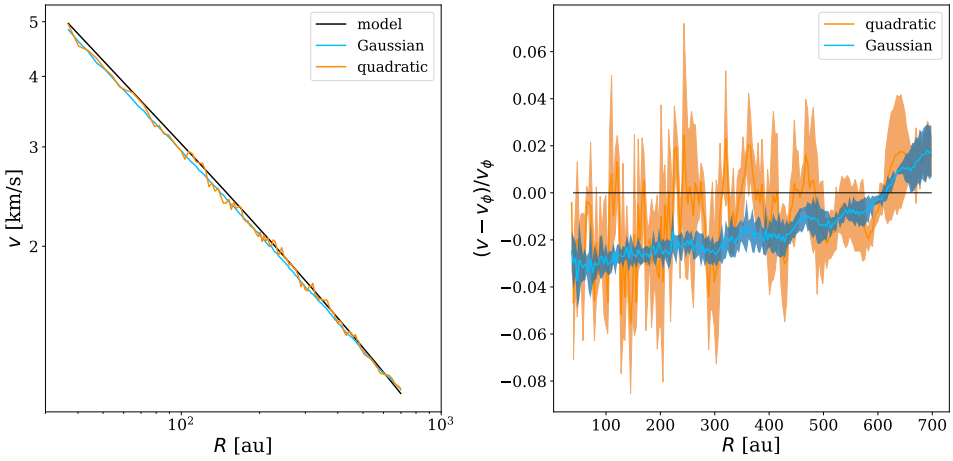

Figure 7.2: Differences between rotation curves obtained with the Gaussian and quadratic methods. Left panel: comparison between the rotation curves from the model (black line, Eq. 7.1 with a disc mass $M_{\rm d} = 0.1\,M_\odot$), the Gaussian method (blue line) and the quadratic method (orange line). We observe that the Gaussian curve is systematically shifted with respect to the model. Right panel: difference between the extracted rotation curve (Gaussian method in blue, quadratic method in orange) and the model v_ϕ from Eq. 7.1). Gaussian extraction is biased by the lower surface, shifting the curve towards lower velocity in most of the radial extent of the disc. Conversely, the quadratic method, although noisier, better reproduces the theoretical model.

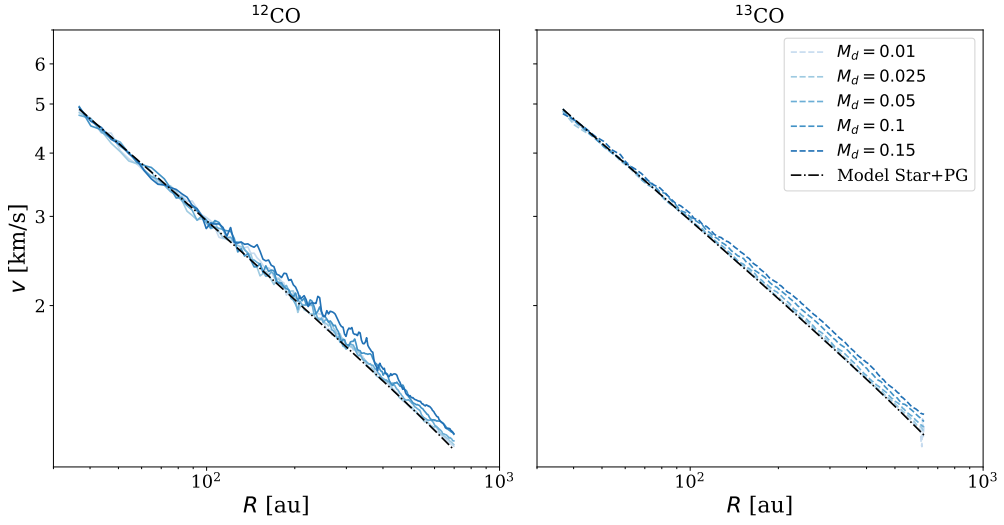

Figure 7.3: Quadratic rotation curves obtained for all the disc masses simulation (from $M_{\rm disc} = 0.01\,M_\odot$ to $M_{\rm disc} = 0.15\,M_\odot$) for the ^{12}CO isotopologue (solid lines in the left panel) and the ^{13}CO isotopologue (dashed lines in the right panel). The black dashed-dot line shows the analytical rotation curve obtained by only considering the star and pressure gradient contribution.

Table 7.2: Results for the ^{12}CO, ^{13}CO and the combined fit procedure. True values are: $M_\star = 1\,M_\odot$, $M_\mathrm{d} = [0.01, 0.025, 0.05, 0.1, 0.15]\,M_\odot$, $R_\mathrm{c} = 100$ au.

	^{12}CO	$\Delta X/X_{12}$	^{13}CO	$\Delta X/X_{13}$	Combined	$\Delta X/X$
	$M_\star = 1.02$	0.02	$M_\star = 0.99$	0.01	$M_\star = 0.99$	0.01
md0.01	$M_d = 0.03$	1.99	$M_d = 0.00$	1.0	$M_d = 0.00$	1.0
	$R_c = 80.00$	0.2	$R_c = 105.15$	0.05	$R_c = 103.7$	0.037
	$M_\star = 0.99$	0.01	$M_\star = 0.99$	0.01	$M_\star = 0.99$	0.01
md0.025	$M_d = 0.04$	0.6	$M_d = 0.00$	1.0	$M_d = 0.00$	1.0
	$R_c = 92.17$	0.078	$R_c = 115.55$	0.15	$R_c = 115.2$	0.15
	$M_\star = 0.99$	0.01	$M_\star = 0.97$	0.03	$M_\star = 0.98$	0.02
md0.05	$M_d = 0.044$	0.12	$M_d = 0.07$	0.4	$M_d = 0.055$	0.099
	$R_c = 102.78$	0.028	$R_c = 94.27$	0.057	$R_c = 97.8$	0.022
	$M_\star = 1.04$	0.04	$M_\star = 0.97$	0.03	$M_\star = 0.97$	0.03
md0.1	$M_d = 0.09$	0.10	$M_d = 0.12$	0.20	$M_d = 0.12$	0.19
	$R_c = 88.33$	0.117	$R_c = 90.8$	0.09	$R_c = 91.2$	0.088
	$M_\star = 1.00$	0.0	$M_\star = 1.00$	0.0	$M_\star = 1.00$	0.0
md0.15	$M_d = 0.18$	0.2	$M_d = 0.15$	0.0	$M_d = 0.15$	0.0
	$R_c = 86.00$	0.14	$R_c = 87.5$	0.125	$R_c = 88.114$	0.12

Table 7.2 collects the best fit values for the star mass $M_\star$, the disc mass M_d and the disc scale radius R_c. The disc-to-star mass ratio threshold below which the disc mass can not be recovered is 0.05.

Uncertainties

When analysing actual data, the three main sources of uncertainties are the height of the emitting layer, the aspect ratio of the disc and its inclination. Uncertainties on $z\,(R)$ have been estimated through the extraction of z_{16} and z_{84}. As for the aspect ratio and the inclination, so far in the fitting procedure we have enforced their value to the *true* one from the numerical simulations. To estimate the uncertainties associated to those parameters, we perform again the fitting procedure over the same synthetic channel maps, by using different values of H/R and i. For H/R, we simply perform new fits over the rotation curves previously extracted. For a set up value of $H/R = 0.075$, we test H/R = [0.05, 0.07, 0.08, 0.1]. For the inclination, the estimate of the uncertainty requires the extraction of new disc emitting layers and rotation curves. For a set up value of $i = 30°$, we test i = [27, 29, 31, 33]°. The values of the uncertainties obtained by this procedure are summarized in Table. 7.2. Fig. 7.4 shows how the value of the disc mass changes according to H/R and i. A key result of this study is that disc masses of self-gravitating discs can be estimated from channel maps with averaged systematic uncertainties of order $\sim 25\%$. The three parameters H/R, i and z have similar contributions as sources of errors. No clear trend appears when varying H/R and z. Values that differ from the expected one still provide a mass estimates with a same level of uncertainty. On the other hand, precise values of i provide uncertainties of order $5 - 10\%$ whereas an error of a few degrees provide uncertainties of order $20 - 30\%$. Hence, the ability to accurately determine disc masses by our procedure is quite reliable. For instance, when recovering a disc mass of $0.1\,M_\odot$, the estimated range spans from 0.075 to 0.125.

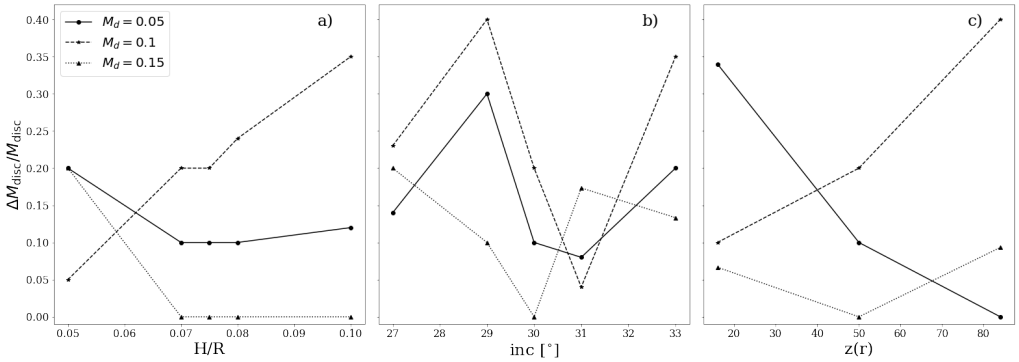

Figure 7.4: Uncertainties related to the fitting procedure for the disc mass $M_{\rm d}$. Estimates are given as functions of the aspect ratio of the disc H/R (left column), the disc inclination (middle column) and the disc emitting layer $z(R)$ (right column). Different markers and lines styles represent results obtained for simulations with different disc masses.

7.2 Thermal stratification: model and testing

In recent years the gas kinematics probed by molecular lines detected with ALMA has opened a new window to study protoplanetary discs. High spatial and spectral resolution observations have revealed the complexity of protoplanetary disc structure and correctly interpreting these data allow us to gain a better comprehension of the planet formation process. In this work, we make a step forward and we investigate the impact of thermal stratification on the azimuthal velocity of protoplanetary discs. High resolution gas observations are showing velocity differences between CO isotopologues, which cannot be adequately explained with vertically isothermal models. We analytically solve the hydrostatic equilibrium for a stratified disc, and we derive the azimuthal velocity. We test the model with SPH numerical simulations, and then we use it to fit for star mass, disc mass and scale radius of the sources in the MAPS sample. In particular, we use ^{12}CO and ^{13}CO datacubes.

7.2.1 Assumptions

In our analytical calculations, we do not make any assumption on the surface density Σ, considering it as arbitrary. However, in order to apply the model to observations, we are forced to choose a parameterisation for the surface density and we assume that it is described by the self-similar solution of Lynden-Bell & Pringle (1974)

$$\Sigma = \frac{(2-\gamma)M_{\rm d}}{2\pi R_{\rm c}^2}\left(\frac{R}{R_{\rm c}}\right)^{-\gamma}\exp\left[-\left(\frac{R}{R_{\rm c}}\right)^{2-\gamma}\right], \tag{7.5}$$

where $M_{\rm d}$ and $R_{\rm c}$ are the disc mass and the scale radius respectively, R is the cylindrical radius and γ is a free parameter describing the steepness of the surface density. The disc density at the midplane $\rho_{\rm mid}$ is

$$\rho_{\rm mid} = \frac{\Sigma}{\sqrt{2\pi}H_{\rm mid}} \propto R^{-(\gamma+(3-q)/2)}\exp\left[-\left(\frac{R}{R_{\rm c}}\right)^{2-\gamma}\right], \tag{7.6}$$

where $H_{\rm mid} = c_{\rm s,mid}/\Omega_{\rm k}$ is the typical scale height of the disc at the midplane, $c_{\rm s,mid} = \sqrt{k_{\rm b}T_{\rm mid}/(\mu m_{\rm p})} \propto R^{-q/2}$ is the sound speed at the disc midplane, $k_{\rm b}$ is the Boltzmann constant, $T_{\rm mid} = T_{\rm mid,100}(R/100{\rm au})^{-q}$ is the temperature at midplane, μ is the mean molecular weight (usually assumed to be 2.1), $m_{\rm p}$ is the proton mass and $\Omega_{\rm k} = \sqrt{GM_\star/R^3}$ is the Keplerian angular velocity (G is the gravitational constant and $M_\star$ is the stellar mass).

From literature (Chiang & Goldreich 1997; Dullemond et al. 2020) and observational data (Rosenfeld et al. 2013; Pinte et al. 2018a; Law et al. 2021), we know that protoplanetary discs are thermally stratified. We take this into account by defining a function f that describes the dependency of the temperature T on height such that

$$T(R,z) = T_{\rm mid}(R)f(R,z), \tag{7.7}$$

$$c_{\rm s}^2(R,z) = c_{\rm s,mid}^2(R)f(R,z). \tag{7.8}$$

We underline that the isothermal case can be obtained considering $f \equiv 1$, thus $T = T_{\rm mid}(R)$. As for the density, we assume that

$$\rho = \rho(R,z) = \rho_{\rm mid}(R)g(R,z), \tag{7.9}$$

where g describes how the density changes vertically. Note that in order to smoothly connect the functions above to their value at midplane it is necessary that $f(z=0) = 1 = g(z=0)$. Assuming a barotropic fluid, the pressure P is given by

$$P(R,z) = P_{\rm mid}(R)fg(R,z) = c_{\rm s,mid}^2(R)\rho_{\rm mid}(R)fg(R,z). \tag{7.10}$$

While the profile of f is arbitrary, this does not hold for g, whose value is set by solving the vertical hydrostatic equilibrium.

7.2.2 Hydrostatic equilibrium and rotation curve

To compute the vertical density profile we assume a non-self-gravitating disc under the condition of hydrostatic equilibrium in the vertical direction:

$$\frac{1}{\rho}\frac{dP}{dz} = -\frac{d\Phi_\star}{dz}, \tag{7.11}$$

where $\Phi_\star = -GM_\star/r$ is the stellar potential ($r = \sqrt{R^2+z^2}$ is the spherical radius). Equation (7.11) can be written as:

$$c_{\rm s,mid}^2 f\frac{d\log(fg)}{dz} = -\Omega_{\rm k}^2 z\left[1+\left(\frac{z}{R}\right)^2\right]^{-3/2}. \tag{7.12}$$

Solving for $\log(fg)$, we find

$$\log(fg) = -\frac{1}{H_{\rm mid}^2}\int_0^z \frac{z'}{f}\left[1+\left(\frac{z'}{R}\right)^2\right]^{-3/2} dz' \tag{7.13}$$

and hence the density is given by

$$\rho(R,z) = \frac{\rho_{\rm mid}(R)}{f(R,z)}\exp\left\{-\frac{1}{H_{\rm mid}^2}\int_0^z \frac{z'}{f(R,z')}\left[1+\left(\frac{z'}{R}\right)^2\right]^{-3/2} dz'\right\}. \tag{7.14}$$

Assuming the condition of centrifugal balance, the rotation curve is given by the radial component of Navier-Stokes equation

$$v_\phi^2(R,z) = \frac{R}{\rho}\frac{dP}{dR}(R,z) + R\frac{d\Phi_\star}{dR}(R,z), \tag{7.15}$$

where we are neglecting the self-gravitating contribution. The first term in eq.(7.15) can be written as

$$\frac{R}{\rho}\frac{dP}{dR} = c_{\rm s,mid}^2 f\left[\frac{d\log P_{\rm mid}}{d\log R} + \frac{d\log(fg)}{d\log R}\right], \tag{7.16}$$

and the second one as

$$R\frac{d\Phi_\star}{dR}(R,z) = v_{\rm k}^2\left[1+\left(\frac{z}{R}\right)^2\right]^{-3/2}, \tag{7.17}$$

where $v_{\rm k} = \sqrt{GM_\star/R}$ is the Keplerian velocity. Therefore, the rotation curve is

$$\begin{aligned} v_\phi^2(R,z) = v_{\rm k}^2\Bigg\{&\left[1+\left(\frac{z}{R}\right)^2\right]^{-3/2} + \left[\frac{d\log P_{\rm mid}}{d\log R} + \right. \\ &\left. + \frac{{\rm d}\log(fg)}{{\rm d}\log R}\right]\left(\frac{H}{R}\right)^2_{\rm mid} f(R,z)\Bigg\}, \end{aligned} \tag{7.18}$$

which in the self-similar case becomes

$$\begin{aligned} v_\phi^2(R,z) = v_{\rm k}^2\Bigg\{&\left[1+\left(\frac{z}{R}\right)^2\right]^{-3/2} - \left[\gamma' + (2-\gamma)\left(\frac{R}{R_c}\right)^{2-\gamma} - \right. \\ &\left. - \frac{{\rm d}\log(fg)}{{\rm d}\log R}\right]\left(\frac{H}{R}\right)^2_{\rm mid} f(R,z)\Bigg\}, \end{aligned} \tag{7.19}$$

where $\gamma' = \gamma + (3+q)/2$. Each term of equation (7.19) can be easily interpreted: $[1 + (z/R)^2]^{-3/2}$ is the star contribution at the height z, γ' is the effect of the power law scaling of the pressure, $(2-\gamma)(R/R_c)^{2-\gamma}$ is the effect of the exponential truncation and the logarithmic term is the effect of the vertical stratification. Since the latter is the derivative of a product, we do not know a priori its sign and thus if the rotation is accelerated or slowed down by thermal stratification. In any case, in all our attempts this term never dominates over the variation of gravity with z. Thus, we found rotation to slow down with z and this effect is more pronounced as compared to the isothermal case when considering the parameters of the MAPS sample.

We underline that for the isothermal case ($f \equiv 1$), this expression reduces to the one derived and analysed by Lodato et al. (2023), while Eq. (7.13) simplifies as

$$\log g = -\frac{1}{H_{\rm mid}^2}\int_0^z \frac{z'dz'}{[1+(z'/R)^2]^{3/2}} = -\frac{R^2}{H_{\rm mid}^2}\left(1 - \frac{1}{\sqrt{1+z^2/R^2}}\right). \tag{7.20}$$

Therefore, the density in the isothermal case is given by

$$\rho(R,z) = \rho_{\rm mid}(R)\exp\left[\frac{R^2}{H_{\rm mid}^2}\left(\frac{1}{\sqrt{1+z^2/R^2}} - 1\right)\right]. \tag{7.21}$$

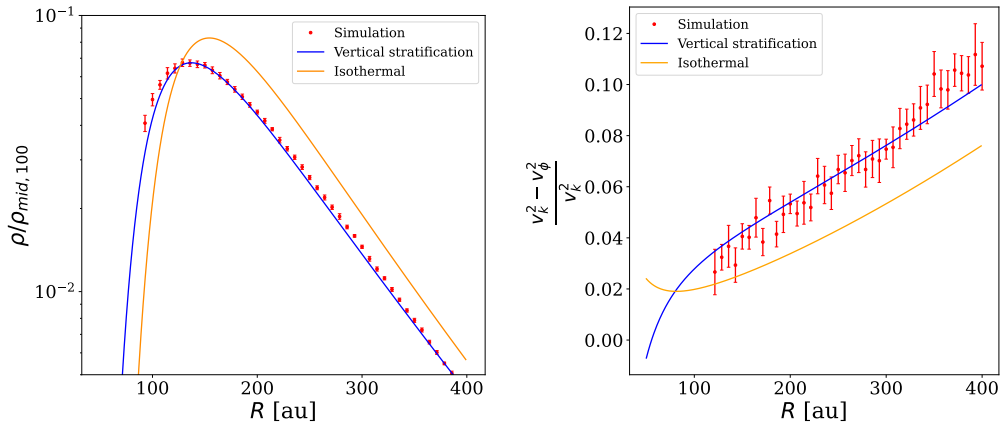

Figure 7.5: Comparison between the analytical models and the simulation after 8 outer orbits and at $z = 20$au. Left panel: density field. The red dots represent the data of the simulation, while the blue and orange line show the thermally stratified model and the isothermal one respectively. Right panel: pressure gradient term of the rotation curve. The red dots represent the simulation data, while the blue and orange line show the thermally stratified model and the isothermal one respectively. The model with thermal stratification matches very well the simulation.

7.2.3 Temperature prescriptions

The two parametrisations of the vertical temperature more often used are given by Dartois et al. (2003) and Dullemond et al. (2020). In this work we will use the one by Dullemond et al. (2020), which is given by:

$$T(R,z)^4 = T_\epsilon^4(R) + \frac{1}{2}T_{\rm atm}^4(R)\left[1 + \tanh\left(\frac{z}{Z_q(R)} - \alpha\right)\right] \tag{7.22}$$

and thus

$$f(R,z) = \left\{\left(\frac{T_\epsilon}{T_{\rm mid}}\right)^4 + \frac{1}{2}\left(\frac{T_{\rm atm}}{T_{\rm mid}}\right)^4(R)\left[1 + \tanh\left(\frac{z}{Z_q(R)} - \alpha\right)\right]\right\}^{1/4}, \tag{7.23}$$

where the atmospheric temperature is parameterised as $T_{\rm atm}(R) = T_{\rm atm,100}(R/100{\rm au})^{-q_{\rm atm}}$, T_ϵ is considered as an approximation of the temperature at midplane $T_\epsilon \simeq T_{\rm mid}$, $Z_q(R)$ is defined as $Z_q(R) = \zeta_{100}(R/100{\rm au})^\beta$ and α is a parameter that describes where the transition from midplane to atmospheric temperature occurs in the vertical direction. We note that in this case $f(R, z = 0) \neq 1$ and thus the temperature does not smoothly connect to its value at midplane. We underline that Eq. (7.22) is a good approximation for the five discs within the MAPS large program in most of the radial extent of the disc.

Once the function f is defined, Eq.(7.14) and (7.18) can be solved semi-analytically and completely specify the rotation curve. We have implemented this calculation in DYSC[2].

[2]The code is publicly available at `https://github.com/crislong/DySc`

7.2.4 Comparison with numerical simulations

In this work, we performed numerical Smoothed Particle Hydrodynamics (SPH) simulations of protostellar discs using the code PHANTOM (Price et al. 2018b). This code is widely used in the astrophysical community to study gas and dust dynamics in accretion discs (Dipierro et al. 2015b; Ragusa et al. 2017; Curone et al. 2022) and recently it has also been employed for kinematical studies (Pinte et al. 2018b; Hall et al. 2020; Terry et al. 2022; Verrios et al. 2022). The aim of this simulation is to test the model before applying it to actual data.

To test the analytical model, we simulated a thermally stratified disc using the parameters of MWC 480 presented in Law et al. (2021). The simulation has been performed with $N = 10^6$ gas particles, initially distributed as a tapered power law density profile, smoothed at inner radius, with $\gamma = 1$ and $R_c = 150$au, between $R_{\rm in} = 10$au and $R_{\rm out} = 400$au. The mass of the star is $2.1 M_\odot$. For the temperature structure we used the Dullemond prescription (Eq. (7.22)), with $\zeta_0 = 7$au$, \alpha = 2.78, \beta = -0.05, T_{\rm mid,100} = 27$K, $q = 0.23$, $T_{\rm atm,100} = 69$K, $q_{\rm atm} = 0.7$. The $\alpha_{\rm SS}$ Shakura & Sunyaev (Shakura & Sunyaev 1973) viscosity coefficient has been set to 0.005. No self-gravity or dust have been included in the simulation.

We let the system evolve and reach hydrostatic equilibrium. We observed that after a couple of orbits the system reaches a relaxed state. We decided to analyse the output of the simulation after 8 outer orbits (~ 45kyr). In figure 7.5 we show a comparison between the density and the velocity of the simulations (red dots) at $z = 20$au and both the isothermal and stratified model predictions. The red dots represent the azimuthal average of the respective quantity computed by averaging over all SPH particles within each of the 50 radial bins and the error bar is the corresponding standard deviation. The stratified model perfectly describes the density and the velocity field of the simulation and is a significant improvement over the isothermal one. In particular, in the right panel of figure 7.5 we see that the difference between the azimuthal velocity and the Keplerian velocity $(v_{\rm k}^2 - v_\phi^2)/v_{\rm k}^2$ reaches the $10-12\%$ and only the stratified model is able to reproduce it.

7.3 Kinematic evidence of thermal stratification in MAPS discs

In this section, we applied the model to the entire sample of discs from the MAPS ALMA Large Program (Öberg et al. 2021). We performed our fits under the assumption of vertically isothermal or stratified disc in order to compare the results. For the vertically isothermal model, the thermal structure is defined by the hydrostatic height of the disc at $R = 100$au and the power law coefficient of the temperature profile q. These parameters are taken by Zhang et al. (2021). As for the stratified model, Law et al. (2021) obtained the two-dimensional temperature structure of the MAPS discs, using the Dullemond et al. (2020) prescription (Eq. 7.22). Note that the rotation curve traced by a specific molecule is defined by

$$v_{\rm rot}^2(R) = v_\phi^2(R, z(R)), \tag{7.24}$$

where $z(R)$ is the height of the emitting layer of the considered molecule. For the emitting layer, we use

$$z(R) = z_0 \left(\frac{R}{100\text{au}}\right)^{\psi} \exp\left[-\left(\frac{R}{R_t}\right)^{q_t}\right], \tag{7.25}$$

where the best fit parameters have been obtained by Izquierdo et al. (2022).

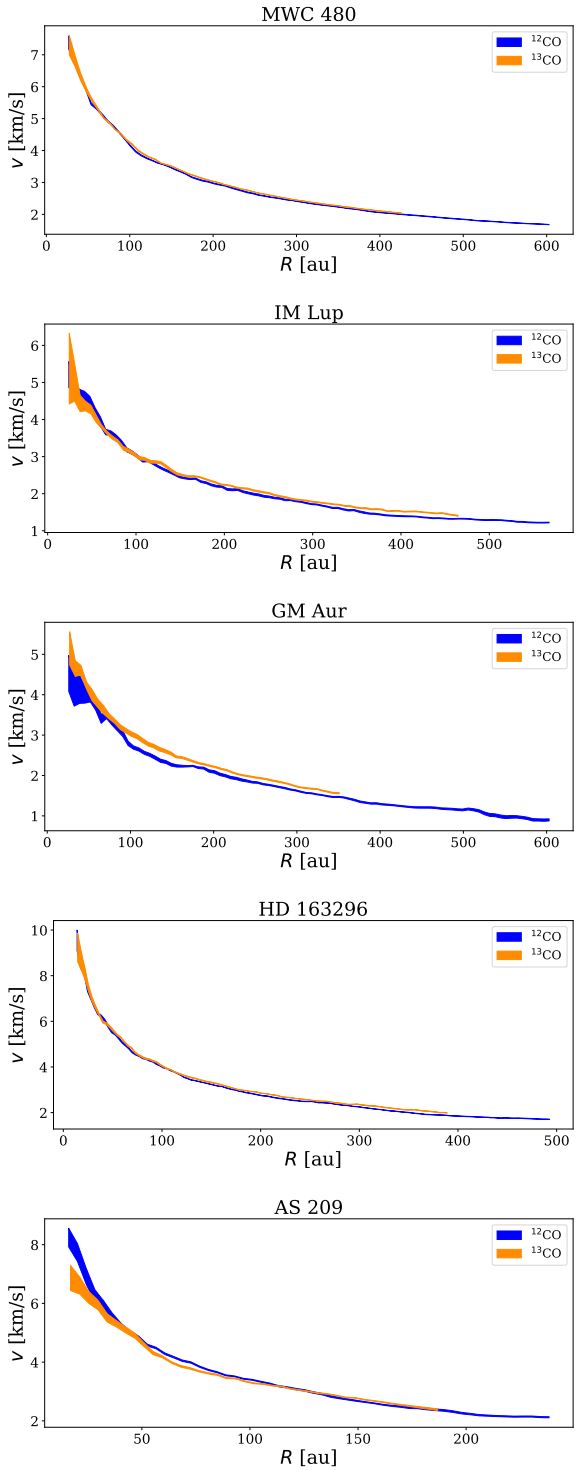

Figure 7.6: ^{12}CO and ^{13}CO rotation curves of the MAPS discs extracted with DISCMINER.

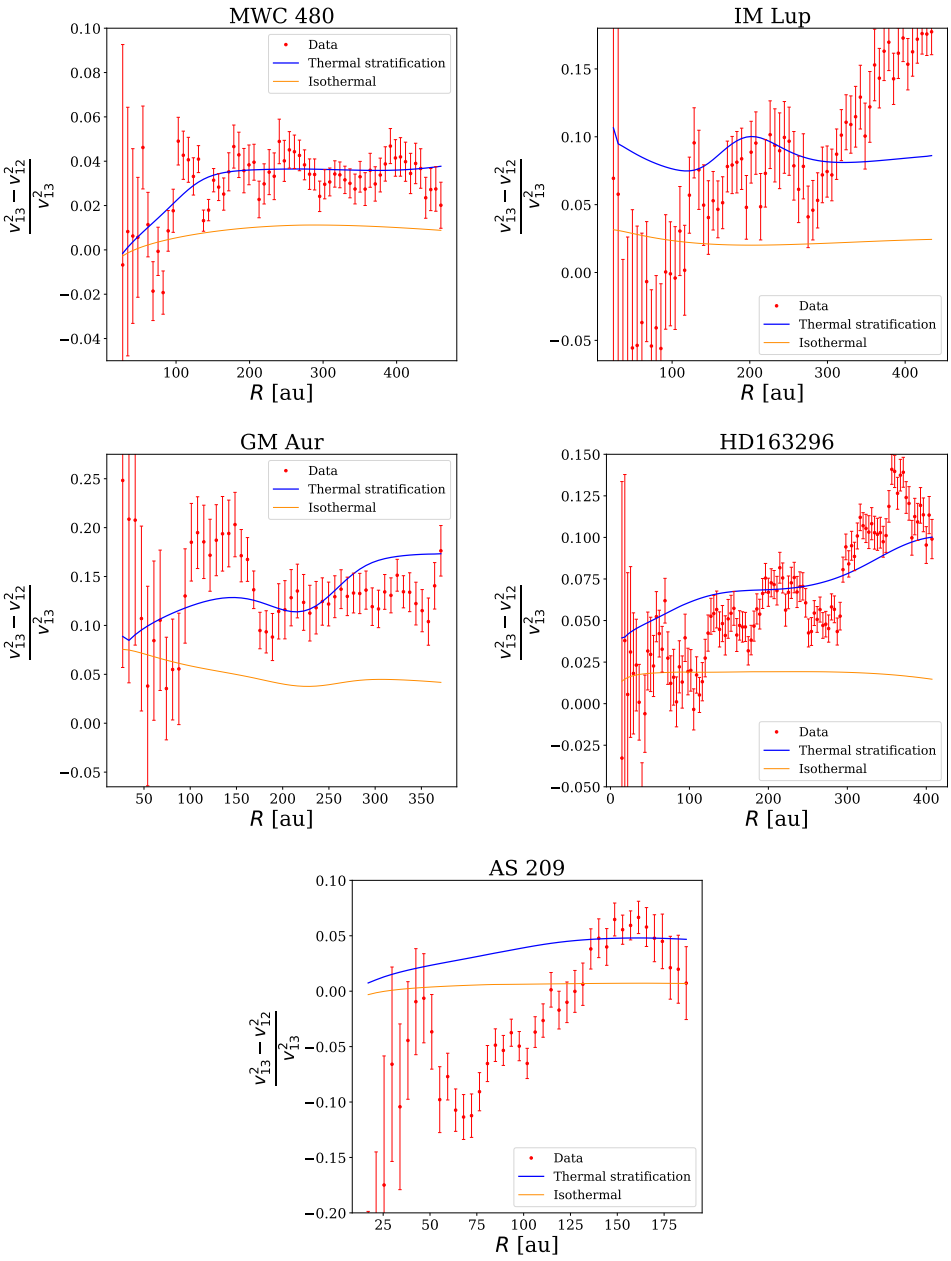

Figure 7.7: Relative difference between the squares of observed ^{12}CO and ^{13}CO rotation curves predicted by the thermally stratified model (blue line), the isothermal model (orange line) and the data (red dots). Except for AS 209, where this quantity is negative in the inner part, it is clearly visible that data are well reproduced by the stratified model. Indeed, the difference of speed between the two curves cannot be explained just in terms of different height.

Table 7.3: Velocity extraction method, orientation parameters, thermal parameters and emitting surfaces for ^{12}CO and ^{13}CO data of the MAPS discs. The orientation parameters and the emitting surfaces are taken from Izquierdo et al. (2023), the thermal parameters for the isothermal model are taken from Zhang et al. (2021), for the stratified model from Law et al. (2021).

	MWC 480	**IM Lup**	**GM Aur**	**HD 163296**	**AS 209**
Orientation					
i [deg]	-37.00	-47.50	53.20	46.69	-39.95
PA [deg]	58.15	54.50	-36.02	42.75	-4.80
Isothermal					
H_{100}[au]	10	10	7.5	8.4	6
q	0.82	0.66	0.3	0.84	0.5
Stratified					
$T_{\rm mid}$[K]	27	25	20	24	25
$T_{\rm atm}$[K]	69	36	48	63	37
q	0.23	0.02	0.01	0.18	0.18
$q_{\rm atm}$	0.7	-0.03	0.55	0.61	0.59
ζ_0[au]	7	3	13	9	5
α	2.78	4.91	2.57	3.01	3.31
β	-0.05	2.07	0.54	0.42	0.02
^{12}CO Surface					
z_0[au]	17.04	34.13	32.00	27.14	16.47
ψ	1.35	0.99	0.97	1.07	1.24
R_t[au]	579.43	889.40	729.91	534.00	327.52
q_t	1.63	3.18	3.22	2.99	3.01
^{13}CO Surface					
z_0[au]	11.52	22.84	18.21	16.09	4.13
ψ	1.09	1.27	1.14	1.12	0.96
R_t[au]	402.77	529.06	512.13	392.75	180.22
q_t	1.87	1.65	2.73	3.43	3.59

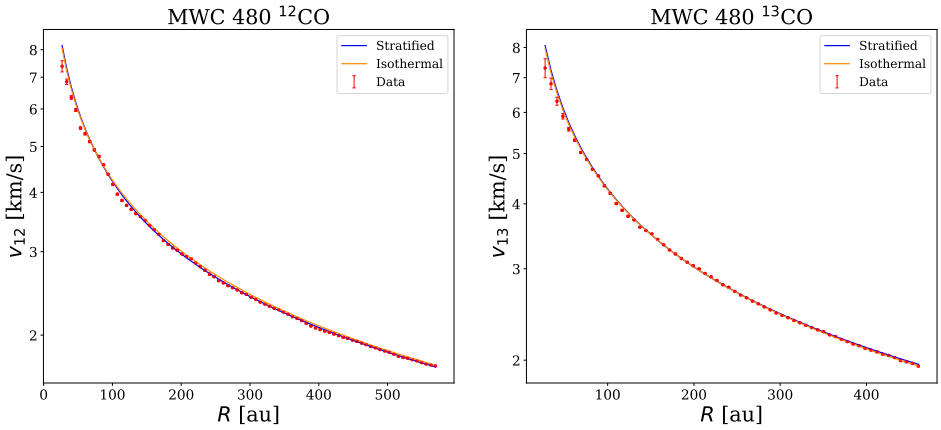

Figure 7.8: Left panel: rotation curve of MWC 480 obtained from ^{12}CO data (red points), along with our best fitting curve for the stratified model (blue line) and the isothermal one (orange line). Right panel: same for the ^{13}CO data.

Rotation curves (Fig. 7.6) can be obtained through different moment maps, according to the disc emission (Izquierdo et al. in prep). All the parameters used are summarised in table 7.3.

7.3.1 Results

We fitted simultaneously the ^{12}CO and ^{13}CO data with both the isothermal and stratified model including the self-gravitating contribution. The results are shown in figures 7.8, 7.9, 7.10, 7.11 and 7.12, and the best fitting parameters are reported in table 7.4.

In order to quantify the importance of thermal stratification, we computed the relative difference between the squares of ^{12}CO and ^{13}CO rotation curves, as shown in figure 7.7. According to the vertical isothermal model, this quantity is

$$\left(v_{13}^2 - v_{12}^2\right)_{\rm iso} = v_{\rm k}^2 q \frac{\sqrt{1+z_{12}^2/R^2} - \sqrt{1+z_{13}^2/R^2}}{\sqrt{\left(1+z_{13}^2/R^2\right)\left(1+z_{12}^2/R^2\right)}}, \tag{7.26}$$

which solely depends on the different height of the tracer, since it is assumed that the temperature does not change vertically. As for the stratified model, the expression is more complex, since it involves the evaluation of the term (7.13) at different heights. In this case, we expect to observe larger differences between the two isotopologues' velocity, since there is an additional shift caused by the different emission temperature. In order to determine the importance of vertical stratification, we quantify the maximum value of the velocity shift between ^{12}CO and ^{13}CO that can be predicted in the isothermal case:

$$\frac{\left(v_{13}^2 - v_{12}^2\right)_{\rm iso}}{v_{\rm k}^2} \approx q\frac{\Delta z^2}{2R^2} < 5\%, \tag{7.27}$$

where we used that typically $z/R < 0.5$. Hence, if the quantity $(v_{13}^2 - v_{12}^2)/v_{\rm k}^2$ is higher than 5%, the system cannot be described by an isothermal model, while it is likely that vertical stratification plays a significant role. It is important to note that the eq. (7.27) depends on the star mass through v_k^2. However, when dealing with data, it is useful

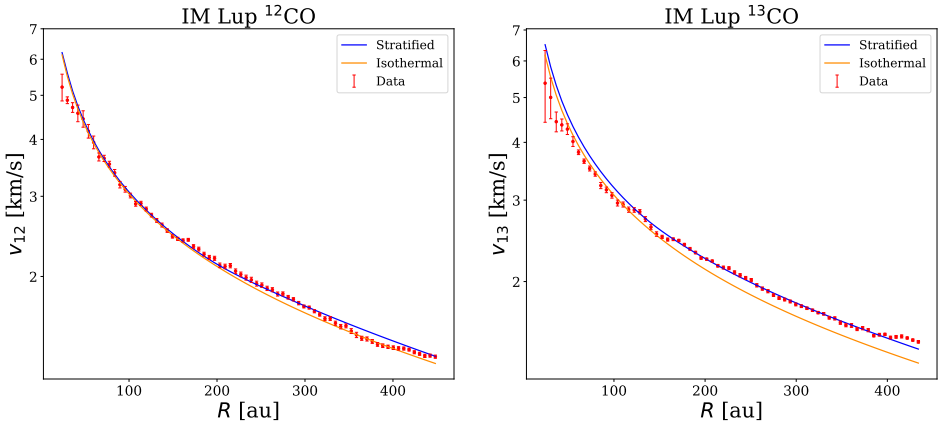

Figure 7.9: Same as figure 7.8 but for IM Lup.

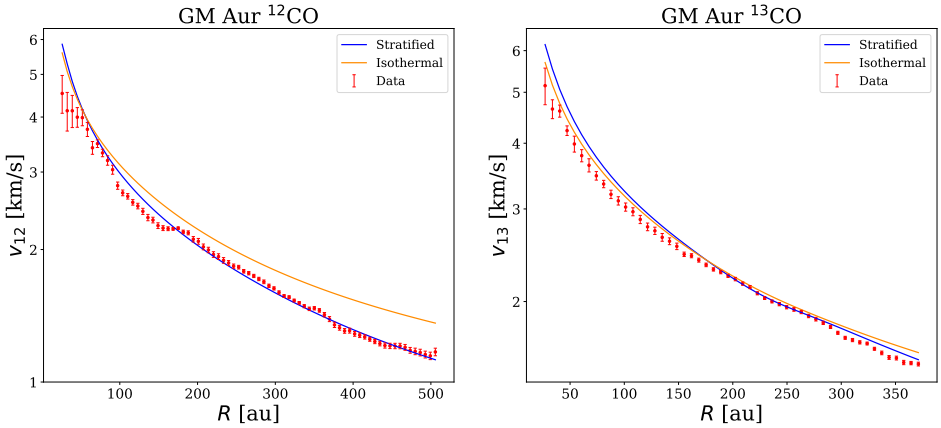

Figure 7.10: Same as figure 7.8 but for GM Aur.

to normalize the squared difference by the velocity of the ^{13}CO, since this quantity relies only on the data, without any assumption on the star mass. Figure 7.7 shows this quantity for the studied systems.

In the next paragraphs, we will present the results of each disc, discussing the importance of thermal stratification. In order to compare the results, we performed our fits for both the vertically isothermal and stratified case. In addition, we computed the dust mass from millimetric emission at 283GHz, using (Hildebrand 1983)

$$M_{\rm dust} = \frac{d^2 F_\nu}{\kappa_\nu B_\nu(T)}, \tag{7.28}$$

where d is the distance, F_ν is the flux density in Jy, $\kappa_\nu = 2.3(\nu/230{\rm GHz})^{0.4}{\rm cm}^2{\rm g}^{-1}$ is the dust opacity and B_ν is the blackbody spectrum. In our analysis, we assumed $T = 20$K and $\nu = 283$GHz, while the flux densities have been extracted from MAPS data. We remind that this equation implies that dust emission is optically thin. The results are reported in table 7.5.

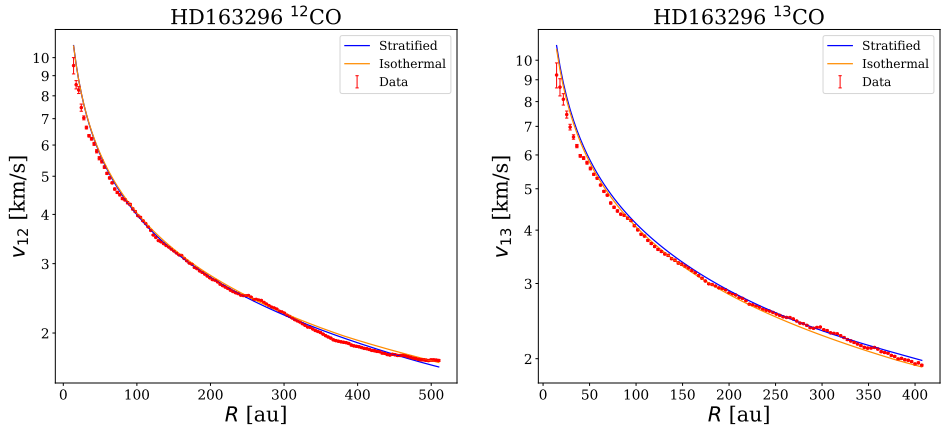

Figure 7.11: Same as figure 7.8 but for HD 163296.

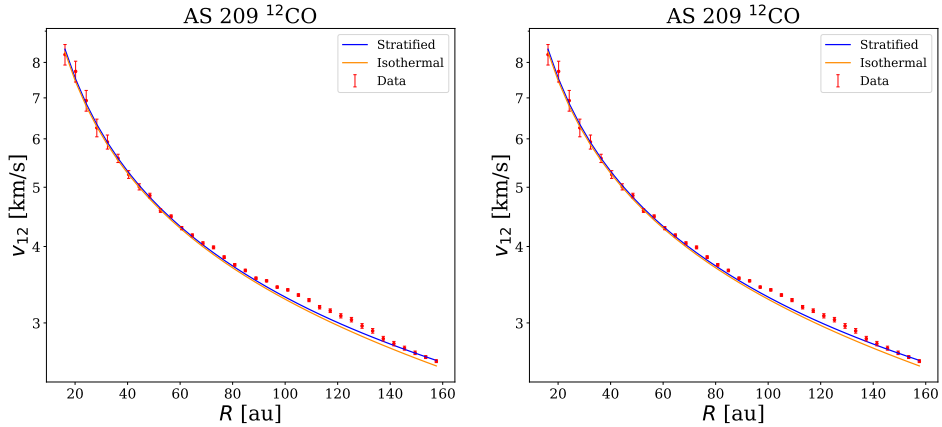

Figure 7.12: Same as figure 7.8 but for AS 209.

MWC 480

MWC 480 is a $\sim$ 7Myr Herbig Ae star located in the Taurus-Aurigae star forming region at a distance of $d = 162$pc (Montesinos et al. 2009). The most recent value of the stellar mass has been derived dynamically by Teague et al. (2021) to be $M_\star = 2.1\mathrm{M}_\odot$, which is the one adopted in the MAPS papers (Öberg et al. 2021). Zhang et al. (2021) through 2D thermochemical models computed disc mass and scale radius of the MAPS discs. For MWC 480, these values are $M_d = 0.16\mathrm{M}_\odot$ and $R_c = 200$au.

By inspecting the ^{12}CO and ^{13}CO rotation curves (fig. 7.6), no evident sign of thermal stratification is visible, since the two curves do not differ significantly. Figure 7.8 shows that the two models are nearly indistinguishable, but in figure 7.7 we see that the stratified model better reproduces data. When we assume an isothermal model, we obtain $M_\star = 1.969 \pm 0.002\mathrm{M}_\odot$, $M_d = 0.201 \pm 0.002\mathrm{M}_\odot$ and $R_c = 80 \pm 1$au, while for the stratified model $M_\star = 2.027 \pm 0.002\mathrm{M}_\odot$, $M_d = 0.150 \pm 0.002\mathrm{M}_\odot$ and $R_c = 128 \pm 1$au. The disc mass obtained with the stratified model is in agreement with the literature value (Zhang

et al. 2021). Since the reduced chi-squared $\chi^2_{\rm red}$ is smaller in the stratified case (see table 7.4), we adopt it as the best fit model.

IM Lup

IM Lup is a young pre-main sequence star ($\sim$ 1Myr) located in the Lupus star forming region at a distance of 158pc (Gaia Collaboration et al. 2018). The dynamical stellar mass is estimated to be $1.1{\rm M}_\odot$ (Teague et al. 2021), and it hosts an unusually large disc, extending out to ≈ 300 au in the dust continuum and out to ≈ 1000 au in the gas (Cleeves et al. 2016). The dust continuum emission shows clear evidence of a spiral morphology, which may be triggered by gravitational instability (Huang et al. 2018a). Cleeves et al. (2016) firstly estimated the disc mass from mm visibilities and found a massive disc of $0.2{\rm M}_\odot$. Verrios et al. (2022) claimed that the spiral structure of IM Lup could be generated by an embedded protoplanet. They performed numerical SPH simulations of planet-disc interaction and then post-processed them to compare their results with CO, dust and scattered light emission. Interestingly, a high disc mass ($\sim 0.1{\rm M}_\odot$) is required to match the scattered light image, in order for sub-micron sized grains to remain well coupled in the top layers of the disc. Cleeves et al. (2016) first estimated the disc scale radius $R_c = 100$au by comparing SED to a simple tapered power-law density profile. Afterwards, Pinte et al. (2018a) analysed CO data and found that a tapered power law density profile with $R_c = 284$au better reproduces the data. They also analysed the rotation curve of the disc and found that while the inner disc is in good agreement with Keplerian rotation around a $1 \pm 0.1{\rm M}_\odot$ star, both the ^{12}CO and the ^{13}CO rotation curves become sub-Keplerian in the outer disc. The authors attributed this effect to the pressure gradient. Lodato et al. (2023) analysed ^{12}CO and ^{13}CO rotation curves and fitted for star mass, disc mass and scale radius with an isothermal model[3].

Figure 7.9 shows both the isothermal and stratified fit. While for ^{12}CO both models describe well the rotation curve, for ^{13}CO the isothermal model fails, since the velocity shift is so high that cannot be explained just in terms of emitting surface. This difference is clearly visible when considering the $\chi^2_{\rm red}$, which for the stratified model is considerably smaller. The best fit parameters for the isothermal model are $M_\star = 1.055 \pm 0.002{\rm M}_\odot$, $M_d = 0.200 \pm 0.003{\rm M}_\odot$ and $R_c = 55 \pm 1$au, while for the stratified model are $M_\star = 1.1994 \pm 0.002{\rm M}_\odot$, $M_d = 0.106 \pm 0.002{\rm M}_\odot$ and $R_c = 115 \pm 1$au. The effects of thermal stratification are visible in figure 7.7. At $R \sim 250$au, the difference in the data between ^{12}CO and ^{13} CO is of the order of $\sim 10\%$, and it significantly increases in the outer part. There, neither the stratified model is able to explain that difference. Izquierdo et al. (2023) pointed out that the emission from the outer disc is so diffuse that the retrieval of the emitting surface, as well as the velocity extraction, needs to be taken with care. This is possibly an effect of external photoevaporation. Indeed, despite the very weak external radiation field irradiating IM Lup, Haworth et al. (2017) showed that the disc is sufficiently large that the outer part, which is weakly gravitationally bounded, can undergo photoevaporation.

GM Aur

GM Aur is a T-Tauri star in the Taurus-Auriga star-forming region, hosting a transition disc. The stellar mass has been estimated dynamically to be $M_\star = 1.1{\rm M}_\odot$ by Teague et al.

[3]In particular, the authors found that for the rotation curves extracted with EDDY the best fit are $M_\star = 1.012 \pm 0.003 M_\odot, M_{\rm d} = 0.096 \pm 0.003 M_\odot, R_c = 89 \pm 1$au and DISCMINER are $M_\star = 1.02 \pm 0.02, M_{\rm d} = 0.10 \pm 0.01 M_\odot, R_c = 66 \pm 1$au.

(2021), in agreement with previous measurements (Macías et al. 2018). Its CO morphology is very complex, showing spiral arms, tails and interactions with the environments (Huang et al. 2021). From thermochemical models of MAPS data, Schwarz et al. (2021) obtained a disc mass of $M_d = 0.2\mathrm{M}_\odot$ and a scale radius of $R_c = 111$au, making GM Aur a possibly gravitationally unstable disc. Lodato et al. (2023) fitted for star mass, disc mass and scale radius using an isothermal model and found that for GM Aur the two CO lines provide inconsistent rotation curves, which cannot be attributed only to a difference in the height of the emitting layer. In addition, the authors provided a simple order of magnitude estimate of the expected velocity shift due to thermal stratification concluding that the difference between the two rotation curves could not be explained by this effect. They drew this conclusion by taking into account the different temperature of the two molecules at their emission height $z_i(R)$ given by Law et al. (2021). However, what matters in the azimuthal velocity is not only the temperature at (R, z), but also its radial and vertical gradient at that location.

By analysing the rotation curves of the two CO isotopologues (fig. 7.6), a systematic shift between ^{12}CO and ^{13}CO curves is clearly visible, possibly attributed to thermal stratification. When we fit with the isothermal model, we obtain as the best fit parameters $M_\star = 0.872 \pm 0.003\mathrm{M}_\odot$, $M_d = 0.312 \pm 0.003\mathrm{M}_\odot$ and $R_c = 56 \pm 1$au, in agreement with Lodato et al. (2023), which lead to a high χ^2_{red}(see table 7.4). As a matter of fact, figure 7.10 shows that an isothermal model is not able to reproduce both ^{12}CO and ^{13}CO rotation curves. Conversely, when thermal stratification is taken into account, the two rotation curves are compatible and are in agreement with data, especially for $R > 180$au. In this case, the best fit value for the star mass is $M_\star = 1.128 \pm 0.002\mathrm{M}_\odot$, which is in line with the literature values (Teague et al. 2021; Macías et al. 2018). As for the disc mass, the best fit value is $M_d = 0.118 \pm 0.002\mathrm{M}_\odot$. Finally, the best fit value for the scale radius is $R_c = 96 \pm 1$au, almost twice the value obtained with the isothermal model and in good agreement with Schwarz et al. (2021). A stratified model reproduces very well the difference between ^{12}CO and ^{13}CO rotation curves, as shown in fig. 7.7 and leads to a significant decrease of the χ^2_{red}.

HD 163296

HD 163296 is one of the most well-studied Herbig Ae star system at millimetre wavelengths due to its relative close distance ($d = 101$pc) and bright disc. The disc presents several features that suggest ongoing planet formation, as dust rings, deviations from Keplerian velocities due to gas pressure variations, 'kinks' in the CO emission, and meridional flows (Isella et al. 2016, 2018; Pinte et al. 2018b; Teague et al. 2018; Pinte et al. 2020; Calcino et al. 2022; Izquierdo et al. 2022, 2023). This system has also been extensively studied because there are evidences of a massive disc. Powell et al. (2019) through modelling of dust lines found that the disc mass is $M_d = 0.21\mathrm{M}_\odot$. Booth & Clarke (2019) observed the ^{13}C^{17}O in HD 163296, a very rare CO isotoplogue that allows to give precise disc mass measurement. They found that the disc mass that better reproduces observations is $M_d = 0.31\mathrm{M}_\odot$. As for the scale radius, de Gregorio-Monsalvo et al. (2013) through radiative transfer modelling found that $R_c = 125$au is the value that better reproduces dust and CO ALMA observations. Guidi et al. (2016) presented a multiwavelength ALMA and VLA study of the disc and through visibilities modelling found that the best fit value of the scale radius is $R_c = 118$au, in agreement with de Gregorio-Monsalvo et al. (2013).

When we fit data with a vertical isothermal model, we obtain as the best fit parameters $M_\star = 1.842 \pm 0.002\mathrm{M}_\odot$, $M_d = 0.124 \pm 0.001\mathrm{M}_\odot$ and $R_c = 38 \pm 1$au. While

the star mass is realistic, the scale radius is unrealistically small compared to the gas emission extent of the order of 400au (Law et al. 2021). Additionally, the isothermal model is not able to reproduce the difference between the rotation curves of the two CO isotopologues (see fig. 7.7), resulting in a relatively poor fit with a large $\chi^2_{\rm red}$. If we include the 2D thermal structure, the quality of the fit increases (see $\chi^2_{\rm red}$ in table 7.4). In this case, the best fit for stellar mass and disc mass does not change significantly ($M_\star = 1.948 \pm 0.002 M_\odot, M_{\rm d} = 0.134 \pm 0.001 M_\odot$), while the scale radius does to $R_c = 91 \pm 1$au. Comparing our result for the disc mass to the literature values, we observe that our fit gives a value that is roughly half. Figure 7.11 shows that both the isothermal and the stratified model describe well the rotation curve of ^{12}CO and ^{13}CO. However, the shift between them, presented in figure 7.7, is well recovered only by the stratified model, which partially managed to explain the significant increase of the plotted quantity. The presence of pressure modulated substructures in the rotation curves (Izquierdo et al. 2023) impacts the quality of the fit and they are clearly visible in figure 7.7. A possible development would be to model them, including them in the fitting model.

AS 209

AS 209 is a young T-Tauri star in the Ophiucus star forming region ($d \sim 121$pc). The most recent stellar mass estimate is $M_\star = 1.2 {\rm M}_\odot$ (Teague et al. 2021). Fedele et al. (2018) gave an estimate for the scale radius $R_c = 80$au through mm visibilities modelling. Afterwards, through thermochemical modelling, they found a dust mass of $M_{\rm dust} = 3.5 \times 10^{-4} {\rm M}_\odot$ that, with a gas-to-dust ratio of 100, translates into $M_d = 0.0035 {\rm M}_\odot$, in agreement with the recent value $M_d = 0.0045 {\rm M}_\odot$ of Zhang et al. (2021). Interestingly, when inspecting the rotation curves of AS 209 (fig. 7.6), the ^{13}CO is slower compared to the ^{12}CO, despite it being closer to the midplane. This trend is observed up to ~ 125au. A possible explanation for this is that the inclination of the disc is low, and hence the emitting surfaces should be taken with care. When we fit with the isothermal model, we obtain as the best fit parameters $M_\star = 1.272 \pm 0.003 {\rm M}_\odot$, $M_d = 0.042 \pm 0.003 {\rm M}_\odot$ and $R_c = 45 \pm 1$au. When we fit with the stratified model, we obtain as the best fit parameters $M_\star = 1.311 \pm 0.001 {\rm M}_\odot$, and $R_c = 126 \pm 2$au, while for the disc mass we report a $3-\sigma$ upper limit of $M_d = 0.00025 \pm 0.00025 {\rm M}_\odot$, since the best fit parameter is compatible with zero. In figure 7.12 both models are shown. As for ^{12}CO, the two models behave in the same way, showing little difference in the outer edge. Conversely, for ^{13}CO the isothermal model works better in the inner part, where ^{13}CO is slower, while in the outer part the stratified model describes well the rotation curve. According to the $\chi^2_{\rm red}$, the stratified model describes better the data (see table 7.4).

7.3.2 Thermal stratification in MAPS discs

Table 7.4 presents a summary of the findings of this study, comparing the isothermal model with the stratified one. It is evident from the results that the reduced χ^2 value consistently decreases when employing the stratified model. This indicates that the inclusion of thermal stratification provides a more effective way of describing the observed data. In this context, MWC 480 is particularly interesting. Despite the small kinematic signatures of thermal stratification, as depicted in figure 7.7, the quality of the stratified fit is higher and it yields more reliable values for star mass, disc mass, and scale radius. On the opposite side, GM Aur is the system that shows the strongest effects of thermal stratification, being the ^{12}CO and ^{13}CO systematically shifted over all the radial extent of

Table 7.4: Results of the fitting procedure and reduced chi-squared for the two different models: isothermal and stratified.

	$M_\star$ [$\mathrm{M}_\odot$]	M_d [$\mathrm{M}_\odot$]	R_c [au]	χ^2_{red}
MWC 480				
Isothermal	1.969 ± 0.002	0.201 ± 0.002	80 ± 1	11.21
Stratified	2.027 ± 0.002	0.150 ± 0.002	128 ± 1	6.14
IM Lup				
Isothermal	1.055 ± 0.002	0.200 ± 0.003	55 ± 1	35.68
Stratified	1.194 ± 0.002	0.106 ± 0.002	115 ± 1	6.29
GM Aur				
Isothermal	0.872 ± 0.003	0.312 ± 0.003	56 ± 1	90.84
Stratified	1.128 ± 0.002	0.118 ± 0.002	96 ± 1	8.48
HD 163296				
Isothermal	1.842 ± 0.002	0.124 ± 0.001	38 ± 1	29.60
Stratified	1.948 ± 0.002	0.134 ± 0.001	91 ± 1	19.74
AS 209				
Isothermal	1.272 ± 0.003	0.042 ± 0.003	45 ± 1	25.13
Stratified	1.311 ± 0.001	0.0002 ± 0.0002	126 ± 2	10.55

Table 7.5: Continuum fluxes at 283 GHz, dust masses from eq. (7.28) and gas-to-dust ratio using the best fit value of the disc mass of the stratified model.

	F_{283} [mJy]	$M_{\rm dust}$ [$M_\odot$]	Gas-to-dust ratio
MWC 480	943.51	0.00138	108
IM Lup	536.25	0.00075	134
GM Aur	347.95	0.00049	240
HD 163296	1127.97	0.00064	202
AS 209	414.83	0.00034	< 192

the disc. The introduction of thermal stratification is able to reconcile these differences, reducing by an order of magnitude the $\chi^2_{\rm red}$. The only case where the stratified model encounters challenges in accurately describing both curves is AS 209. This system is peculiar because the CO emission is more compact compared to the other ones (see fig. 7.6). In addition, the low inclination of AS 209 influences the extraction of emission surfaces. Consequently, contrary to what expected, we observe that the ^{13}CO rotates slower than the ^{12}CO in the inner part. Despite that, the $\chi^2_{\rm red}$ is smaller when thermal stratification is taken into account.

7.3.3 Gas-to-dust ratio

With the knowledge of the disc mass, it is possible to evaluate the gas-to-dust ratio, using eq. (7.28) for the dust mass. The results are shown in table 7.5, and we found values between $100 - 250$, within only a factor of 2 from the usually assumed valued of 100. This is surprisingly, due to the several assumptions we made to obtain the dust mass. Indeed, as we have already mentioned, the optically thin hypothesis for dust emission could lead to a difference of a more than a factor 2 in the dust mass calculation (Guidi et al. 2016), underestimating it. In addition, the dust opacity could also vary of a factor ~ 10 depending on the grain size and composition. Hence, overall, it is significant that the inferred gas-to-dust ratio is so close to the standard value. As for AS 209, we estimate an upper limit for this quantity. Indeed, according to Veronesi et al. (in prep), the minimum measurable mass with the rotation curve is 5% of the star mass. Taking this value as an upper limit for AS 209 disc mass, it is possible to give an upper limit for the gas-to-dust ratio.

7.3.4 Toomre Q

In order to investigate the presence of gravitational instability we use our best fit parameters for the stratified model to compute the Toomre parameter (Toomre 1964) which, in the hypothesis of nearly Keplerian disc ($\kappa \simeq \Omega$), is

$$Q \simeq \frac{c_{\rm s}\Omega}{\pi G \Sigma} = 2 \left.\frac{H}{R}\right|_{\rm mid} \frac{M_\star}{M_d} \left(\frac{R}{R_c}\right)^{-1} \exp\left[\frac{R}{R_c}\right], \tag{7.29}$$

where we used eq. (7.5) for the surface density. According to the WKB quadratic dispersion relation (Lin & Shu 1964; Toomre 1964), the onset of the instability happens when $Q \sim 1$. Figure 7.13 shows the profile of the Q parameter for the MAPS sample, except for AS209, since its disc mass estimate is compatible with zero. Every disc is gravitationally stable, according to the Toomre criterion, since $Q > 1$. Interestingly, the two discs

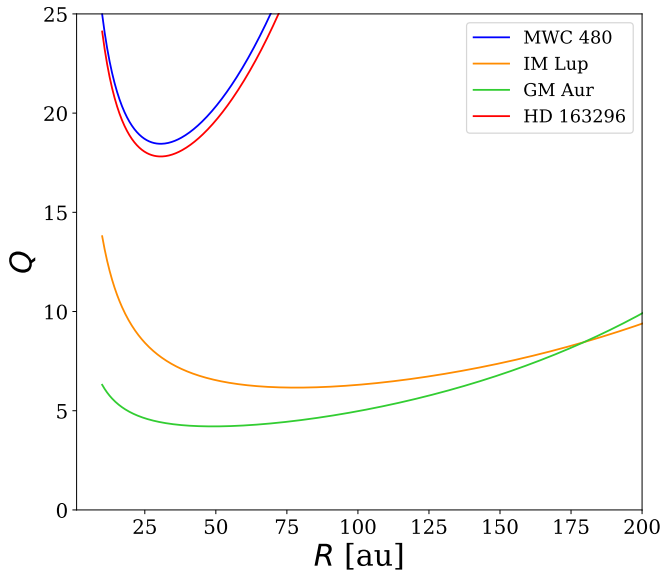

Figure 7.13: Toomre Q parameter of the MAPS discs with the best fit parameters of the stratified model. We excluded AS 209 because its best fit disc mass is compatible with zero.

that shows spiral structures (IM Lup and GM Aur), have the Toomre profile lower compared to the others, with a minimum value of ~ 4 for GM Aur and ~ 6 for IM Lup. Lau & Bertin (1978) showed that a WKB description of gravitational instability can still be obtained under less restrictive conditions compared to the quadratic relation and they showed that discs that are locally stable according to the Q criterion might still generate large scale spiral waves. In general, other mechanisms could increase the critical value of the Toomre parameter, such as external irradiation (Lin & Kratter 2016; Löhnert et al. 2020) or dust driven gravitational instability (Longarini et al. 2023a,b). Hence, we do not exclude that gravitational instability is at play in GM Aur and IM Lup.

7.3.5 Conclusions

Kinematic data of protoplanetary discs show velocity differences between ^{12}CO and ^{13}CO that cannot be explained through a vertically isothermal model, given the systematic shift between rotation curves of CO isotopologues. In this work, we predict how thermal stratification affects the density and the velocity field of a protoplanetary disc. We use SPH simulations to test our model, finding excellent agreement, and then we apply it to the MAPS sample. We extract rotation curve of CO isotopologues (^{12}CO and ^{13}CO) and we fit for star mass, disc mass and scale radius both with a vertically isothermal and a stratified model. The quality of the fit significantly improves when thermal stratification is taken into account and the best fit parameter are more realistic and aligned with literature. All the results are summarised in table 7.4.

Typically, when thermal stratification is considered, the best fit value for the star mass tends to rise. This can be intuitively understood, as an isothermal model would favour a star mass that lies between that of ^{13}CO and ^{12}CO, in this way underestimating it due to the slower rotation of ^{12}CO. Conversely, the stratified model encapsulates the

difference between the two curves, mitigating the underestimation issue and resulting in a more accurate mass estimate. While an isothermal model provides a satisfactory fit at small radii, the fit worsens at large radii where the difference between ^{12}CO and ^{13}CO is larger. The fit tries to compensate for this by increasing the disc mass, most of which resides at large radii, thereby changing the predicted curve only in the outer parts of the disc. Ultimately, a more accurate description of the thermal structure through a stratified model leads to a realistic estimate of the scale radius.

We note that the inclusion of thermal stratification into our model enhances our comprehension of the observed data within protoplanetary discs. This addition leads to more accurate estimate of disc properties, resulting in improved χ^2 values across all systems under examination.

CHAPTER 8

Kinematic study of a gravitational unstable disc : Elias 2-27

This chapter is based on the paper "Angular momentum transport through gravitational instability in Elias 2-27" by ***Cristiano Longarini*** *et al., in preparation.*

Gravitational instability is thought to be the main driver of angular momentum transport in young protoplanetary discs. Elias 2-27 offers a unique example of gravitational instability at play, being massive, showing two prominent spiral arms in dust continuum emission and global kinematic signatures in molecular line emission. In this work, we measure the angular momentum transport in this system using kinematical perturbations generated by gravitational instability. The $\alpha-$viscosity coefficient we find is $\alpha_{\rm GI} = 0.038$, that describes very well the observed accretion rate onto the protostar. The excellent agreement with the observed value is a further proof that gravitational instability is at play in this system.

8.1 The source: Elias 2-27

Elias 2-27 is a young (~ 0.5Myr) M0 star located at a distance of 116 pc (Gaia Collaboration et al. 2018) in the $\rho-$Oph star forming region. The star hosts a circumstellar disc, where two large-scale trailing spiral arms in dust continuum emission have been detected (Pérez et al. 2016), whose origin was first imputed to gravitational instability, due to the high dust mass. Later, Meru et al. (2017) performed three-dimensional numerical SPH simulations to investigate the origin of the spiral structure: by comparing gravitational instability, internal and external companion scenarios, they found that GI best reproduces the observed morphology. Similar results have also been found by Hall et al. (2018). In addition, due to its high brightness, Elias 2-27 became part of the DSHARP sample (Andrews et al. 2018), allowing more thorough studies of its dust morphology (Huang et al. 2018b). Even though the main focus of DSHARP program was dust emission, also kinematic data of CO isotopologues were collected. Pinte et al. (2020) found complex kinematic features in Elias 2-27 system, showing global perturbation to the velocity field. However, due to the low resolution of the data, a detailed analysis could not be possible. Paneque-Carreño et al. (2021) presented new data of this system, and conducted a detailed analysis of the morphology and the kinematics. Global perturbations in the velocity field of ^{13}CO and C^{18}O were found, and their morphology follows the shape of the spiral, possibly being GI Wiggles (Hall et al. 2020; Longarini et al. 2021b; Terry et al. 2022). From the same dataset, Veronesi et al. (2021) extracted the rotation curve and obtained a disc mass estimate of $M_d = 0.08$M$_\odot$, by measuring the super-Keplerian contribution of the disc self-gravity. The estimated disc to star mass ratio is $\sim 17\%$, making the role of the disc self-gravity non-negligible in this system.

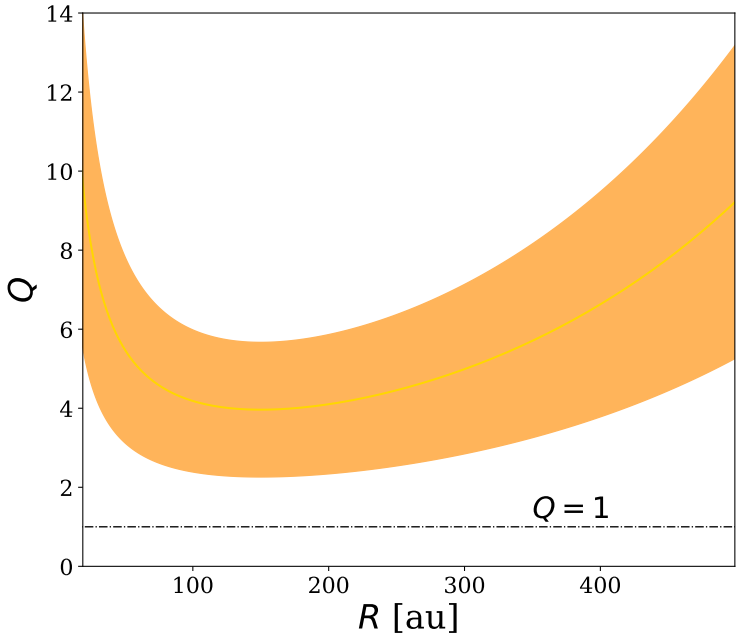

Figure 8.1: Toomre profile of Elias 2-27, where the shaded region indicates the uncertainties on the disc and star mass from Veronesi et al. (2021).

In this work, we use the ^{13}CO and C^{18}O $J = 3 - 2$ datacubes presented in Paneque-Carreño et al. (2021). The images have been obtained with a robust parameter of 0.5, resulting in a beam size of $0.26'' \times 0.25''$ for the ^{13}CO and $0.31'' \times 0.29''$ for the C^{18}O, and a spectral resolution of $\Delta v = 111$m/s.

8.2 Evidence of gravitational instability at play in Elias 2-27

8.2.1 Toomre parameter

Veronesi et al. (2021) estimated the dynamical mass of Elias 2-27 from ^{13}CO and C^{18}O rotation curves, and they found $M_\star = 0.46 \mathrm{M}_\odot \pm 0.03$ and $M_d = 0.08 \pm 0.04 \mathrm{M}_\odot$. They fixed the scale radius to $R_c = 200$au and the thermal structure $T(60\mathrm{au}) = 20$K from Pérez et al. (2016). With this information, it is possible to compute the Toomre parameter profile for Elias 2-27, as displayed in figure 8.1. Despite not being exactly $Q = 1$, the Toomre profile is enough close to the critical threshold to consider gravitational instability to be significant. In addition, we are not considering uncertainties on the thermal structure, that could impact on the $Q-$parameter estimate.

8.2.2 Location of the perturbations

A GI spiral density wave induces perturbations in the velocity field that are apparent in molecular line emission (Hall et al. 2020). Longarini et al. (2021b) have determined both the amplitude and phase of these velocity perturbations, establishing their correlation with the characteristics of the spiral. Specifically, the mathematical description of a spiral

wave involves three key parameters. The first parameter is the number of spiral arms m. The second one is the phase function $\psi(R)$ and it indicates how the shape of the spiral changes radially. The shape function is related to the opening angle α_p according to

$$\frac{\mathrm{d}\psi}{\mathrm{d}R} = \frac{m}{R\tan\alpha_p}, \tag{8.1}$$

and for a constant pitch angle, the shape function is logarithmic. The third parameter is the amplitude of the perturbation. For a GI spiral wave in thermal saturation regime, the amplitude of the perturbation $\delta\Sigma$ is linked to the cooling factor β according to

$$\delta\Sigma \propto \Sigma\beta^{-1/2}. \tag{8.2}$$

We underline that the amplitude of the density perturbation is a real quantity. As for the velocity perturbations, their amplitude are

$$\delta v_R = 2im\beta^{-1/2}\left(\frac{M_d}{M_\star}\right)^2 v_k, \tag{8.3}$$

$$\delta v_\phi = \frac{i\beta^{-1/2}}{2}\left(\frac{M_d}{M_\star}\right) v_k. \tag{8.4}$$

Conversely to the density perturbation, the amplitude of the velocity ones is an imaginary quantity.

The perturbed fields can be written by summing the basic unperturbed state with the real part of the amplitude times the exponential term $\exp[im\phi + i\psi]$. Hence, the surface density of a GI disc is

$$\Sigma(R,\phi) = \Sigma_0(R) + \mathrm{Re}\left[\delta\Sigma(R)\exp(im\phi + i\psi)\right] = \Sigma_0(R) + \cos(m\phi + \psi), \tag{8.5}$$

and the velocity components are

$$v_R(R,\phi) = \mathrm{Re}\left[\delta v_R(R)\exp(im\phi + i\psi)\right] = -|\delta v_R(R)|\sin(m\phi + \psi), \tag{8.6}$$

$$v_\phi(R,\phi) = R\Omega + \mathrm{Re}\left[\delta v_\phi(R)\exp(im\phi + i\psi)\right] = R\Omega - |\delta v_\phi(R)|\sin(m\phi + \psi), \tag{8.7}$$

where we took as axisymmetric basic state $\Sigma_0(R)$ for the surface density, $R\Omega$ for the azimuthal velocity and zero radial velocity. Interestingly, the density and velocity perturbations are shifted of a factor $\pi/2$. This means that the maximum of the density perturbation corresponds to the zero velocity shift. Conversely, the maximum/minimum of the velocity perturbation is co-located with the zero density perturbation, where $\Sigma = \Sigma_0$. Hence, we expect to observe the maximum velocity shift between two spiral arms. This is exactly what we observe in Elias 2-27 ^{13}CO data. Indeed, figure 8.2 shows two channels of the ^{13}CO and C^{18}O datacube at 1.88km/s (the central channel) and 1.55km/s, where the kinematic structures are located between two spiral arms, as expected. While these offsets are more prominent in ^{13}CO, we see that also C^{18}O emission traces them. To produce those figures, we used the spiral parameters of Paneque-Carreño et al. (2021): we assume a logarithmic spiral with pitch angle $\alpha_p = 13°$, the solid lines trace the continuum spirals, the dashed lines represent how the spiral would continue in the outer part of the disc.

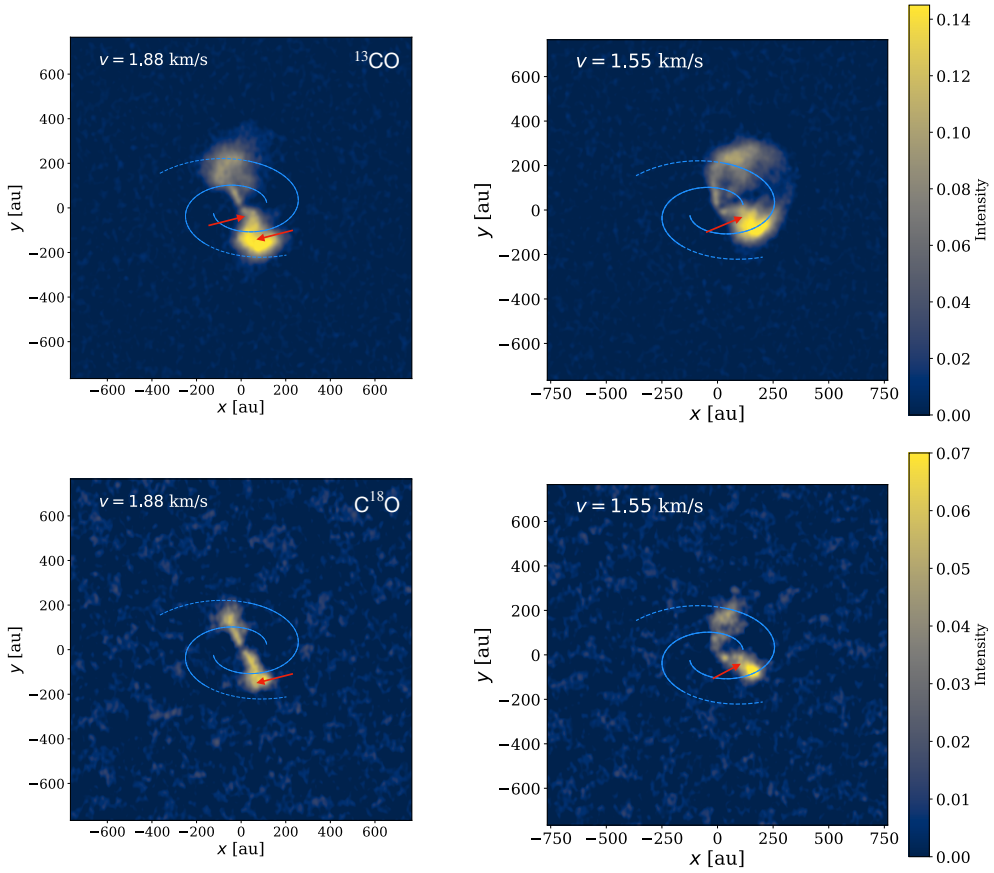

Figure 8.2: ^{13}CO and C^{18}O channels at 1.88km/s and 1.55km/s of Elias 2-27. The blue lines are the two spiral arms from dust continuum emission and the arrows indicate the regions of the emission that are perturbed by the spiral arms. As expected, the perturbed emission is between the spiral arms, and not co-located with them. While these offsets are more prominent in ^{13}CO, we see that also C^{18}O emission traces them.

8.3 Model of the GI Wiggle of Elias 2-27

In the analytical model for the GI wiggle of Longarini et al. (2021b), the amplitude of the velocity perturbations is determined by the disc to star mass ratio and the cooling factor. There is a degeneracy between the two quantities, however in the case of Elias 2-27 the value of the disc to star mass ratio is known (Veronesi et al. 2021). We extract the isovelocity curve relative to the central channel by using Gaussian moment maps, and the value of β that reproduces the amplitude of the perturbation is $\beta = 10.5$, having fixed $M_d/M_\star = 0.17$, $m = 2$ and $\alpha_p = 13°$. To obtain this result, we made the usual hypothesis that β is constant over the radial extent of the disc, meaning that the cooling timescale is proportional to the dynamical one with β as a proportionality factor.

8.3.1 Angular momentum transport

Under the hypothesis of thermally saturated gravitational instability, the cooling factor determines the amount of angular momentum that is transported throughout the disc. As a matter of fact, as shown in Cossins et al. (2009), the effective $\alpha-$viscosity generated by gravitational instability is

$$\alpha_{\rm GI} = \frac{4}{9\gamma(\gamma-1)\beta}, \tag{8.8}$$

where γ is the adiabatic index $\gamma = 5/3$. For Elias 2-27, the amount of angular momentum transported through gravitational instability is $\alpha_{\rm GI} = 0.038$. In this way, kinematics offers a unique opportunity to quantify the transport of angular momentum of a gravitationally unstable disc. In Longarini et al. (2021b), the authors showed that the amplitude of the GI wiggle is proportional to $\beta^{-1/2}$: however, the true quantity that contributes to the perturbation is $\alpha_{\rm GI}$, not β. As a matter of fact, the quantity we are constraining is the surface density perturbation $\delta\Sigma$, that is linked to the amount of the angular momentum that is transported. The $\beta-$cooling prescription is just a simple way in which we describe the strength of the gravitational instability. Thus, regardless of the origin of the gravitational instability, the actual parameter we are constraining with the GI wiggle is the amount of angular momentum that the spiral transports, that is $\alpha_{\rm GI}$.

8.3.2 Accretion rate

Measuring the $\alpha-$viscosity of a disc is a unique opportunity to investigate the angular momentum transport within it. In particular, since the viscosity is responsible for the accretion process, it is useful to predict the expected accretion rate onto the central object, and compare it with the observed one.

According to the self-similar solution, the surface density and the accretion rate of the disc can be written as

$$\Sigma = \frac{M_d}{2\pi R_c^2}\left(\frac{R}{R_c}\right)^{-1}\exp\left[-\frac{R}{R_c}\right], \tag{8.9}$$

$$\dot{M} = \frac{3M_d\nu_c}{2R_c^2}\exp\left[-\frac{R}{R_c}\right]\left(1-\frac{2R}{R_c}\right), \tag{8.10}$$

where we have supposed that $\nu = \nu_c(R/R_c)$. Within a $\alpha-$viscosity framework, the kinematic viscosity ν is

$$\nu = \alpha_{\rm GI}c_s H = \alpha_{\rm GI}\left(\frac{H}{R}\right)^2 v_k R. \tag{8.11}$$

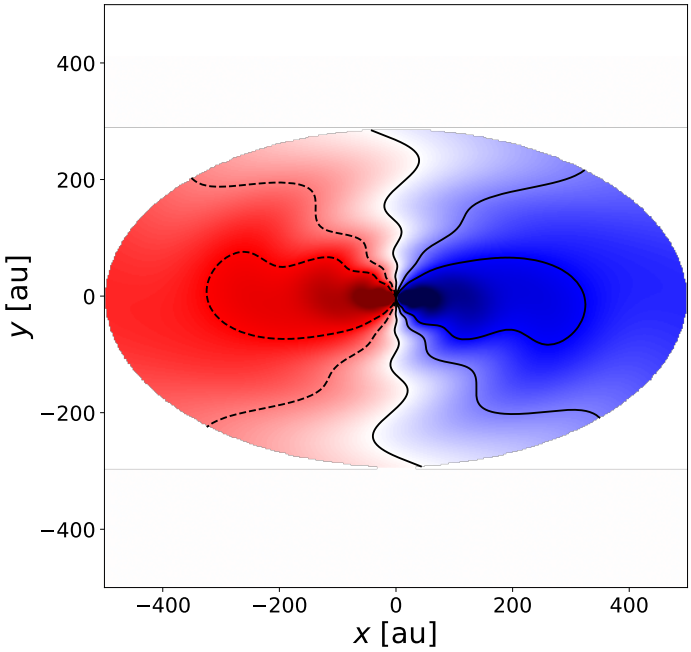

Figure 8.3: Analytical model of the observed velocity field of Elias 2-27, with $M_\star = 0.46\mathrm{M}_\odot$, $M_d = 0.08\mathrm{M}_\odot$, $R_c = 200$au for the disc, $m = 2$, $\alpha_p = 13°$, $\alpha_{\mathrm{GI}} = 0.038$ for the spiral and $i = 56.2°$.

In this way, we can write the accretion rate onto the central object as the limit for $R \to 0$ of eq. (8.10)

$$\dot{M}_\star = -\frac{3\alpha_{\mathrm{GI}}}{2}\left(\frac{H}{R}\right)^2_{R_c} M_d \Omega_c, \tag{8.12}$$

where $\Omega_c = \Omega(R_c) = \sqrt{GM_\star/R_c^3}$.

Using $\alpha_{\mathrm{GI}} = 0.038$, it is possible to compute the accretion rate onto the central object by using Eq. (8.12), and we obtain

$$\log_{10} \dot{M}_\star[\mathrm{M}_\odot/\mathrm{yr}] = -6.92 \pm 0.16, \tag{8.13}$$

where the error has been computed through propagation from the disc and star mass ones. The model for the accretion rate of Elias 2-27 reproduces very well the one measured by Natta et al. (2006) that is $\log_{10} \dot{M}_\star[\mathrm{M}_\odot/\mathrm{yr}] = -7.2 \pm 0.5$.

8.4 Discussion

The ability of our model to correctly reproduce the observed accretion rate points to the fact that gravitational instability is responsible for angular momentum transport in this system. As a matter of fact, the value of the $\alpha-$viscosity we get from the GI wiggle is the one required to explain the observed accretion rate onto the central object, having fixed Elias 2-27 density structure. In addition, the strong hypothesis we made is that viscous

processes are responsible for accretion. The inferred value for the $\alpha-$viscosity is higher than the usually assumed ($\sim 10^{-3} - 10^{-4}$). This is not surprisingly, since the strength of the viscosity generated by turbulent motions is higher.

8.4.1 Infall and interaction with the environment

Elias 2-27 is a young system, and its interactions with the surrounding environment are possibly perturbing the disc. Specifically, the disc is partially embedded within the molecular cloud, which absorbs both ^{12}CO and a portion of the ^{13}CO emissions Pérez et al. (2016); Paneque-Carreño et al. (2021). Moreover, the interaction with the cloud may influence the dynamics and morphology of the disc. In particular, simulations of infall predict the formation of spiral structures in the surface density (Kratter & Matzner 2006; Kratter et al. 2008; Lesur et al. 2015; Hennebelle et al. 2017), and the detection of infall-driven spirals has been asserted in a Class I disk (Lee et al. 2020).

In the CO datacubes of Elias 2-27 there is evidence of infall and interaction with the molecular cloud. Paneque-Carreño et al. (2021) found a striped pattern in the channel maps, that is possibly caused by stream of materials moving at the same velocity. However, the data lacks appropriate uv-coverage to accurately sample the whole field of view, that extends more than $20''$.

Even though the spiral structure is generated by infall, our $\alpha-$viscosity argument remains valid. As a matter of fact, as commented before, we are directly measuring the amplitude of the density perturbation $\delta\Sigma$ from the wiggle, and it is linked to the amount of angular momentum that is transferred. An interesting thing to investigate would be to link the $\delta\Sigma$ to the infall rate from the cloud, and hence constraining it from the wiggle.

8.4.2 Planet formation in Elias 2-27

Longarini et al. (2023a,b) investigated the possibility of forming planetary cores in gravitationally unstable discs through dust collapse. They found that for sufficiently long cooling time $\beta > 10$ and high disc to star mass ratio $M_d/M_\star \sim 0.2$, dust efficiently collects inside spiral arms, and its dispersion velocity is so low to directly collapse into bounded objects with mass $\sim 10\mathrm{M}_\oplus$. The inferred disc to star mass ratio (Veronesi et al. 2021) and the cooling time for Elias 2-27 make it a perfect candidate for planet formation through dust collapse.

Huang et al. (2018a) characterized annular substructures in the discs within the DSHARP sample, and found that Elias 2-27 has a gap at $R_g = 69.1 \pm 0.4$au with a width of $\Delta = 14.3 \pm 1.1$au. Although several mechanisms can explain the origin of gaps in protoplanetary discs, a common explanation is planet disc interaction. Under the planetary interpretation, the width of the gap scales as the Hill radius of the planet, defined as

$$R_h = \left(\frac{M_p}{3M_\star}\right)^{1/3} R_g, \tag{8.14}$$

where M_p is the mas of the protoplanet. Following Lodato et al. (2019), the relation between the gap width and the Hill radius is

$$\Delta = 5.5 R_h, \tag{8.15}$$

that translates into

$$M_p = 3\left(\frac{\Delta}{5.5 R_g}\right)^3 M_\star. \tag{8.16}$$

Using the gap width and location of Huang et al. (2018a), and the star mass of Veronesi et al. (2021), the inferred mass of the protoplanet is $M_p = 24 \pm 6 \mathrm{M}_\oplus$. This result is in good agreement with the mass range of Longarini et al. (2023a,b). Another element that points towards the dust collapse is the value of the Toomre parameter. As shown in Longarini et al. (2023a), when the gravitational instability is driven by the cold component (dust in this case), the critical value of the Toomre parameter is > 1, as observed in Elias.

8.5 Conclusion

In this chapter, we investigated the kinematic signatures of gravitational instability in the protoplanetary disc Elias 2-27. It is well known that gravitational instability leaves clear kinematic perturbations in molecular line emission (Hall et al. 2020), and their characteristics are related to the spiral density wave (Longarini et al. 2021b). We verified that the shape and the position of the velocity perturbations is compatible with the GI expectations, and we extract their amplitude. Under the hypothesis that angular momentum is transported through the GI spiral, we estimated the effective $\alpha-$viscosity of the system (Cossins et al. 2009), and linked it to the accretion onto the central object. We found very good agreement between the observed accretion rate and the one estimated from our model, pointing to the fact that gravitational instability is at play in this system. The range of disc mass and cooling factor inferred by our model makes Elias 2-27 a perfect candidate for dust collapse and planetary cores formation in spiral arms. The gap present in dust continuum emission at ~ 70au points to the presence of a $\sim 20 \mathrm{M}_\oplus$ protoplanet, in agreement with the planetary cores characteristics of Longarini et al. (2023b).

Part III

Dynamics of self-gravitating protostellar discs

CHAPTER 9

The interplay between drag force and gravitational instability

*This chapter is based on the paper "The role of the drag force in the gravitational stability of dusty planet forming disc - I. Analytical theory" by **Cristiano Longarini**, Giuseppe Lodato, Giuseppe Bertin and Philip J. Armitage, published in Monthly Notices of the Royal Astronomical Society in February 2023.*

Recent observations show that planet formation is already underway in young systems, when the protostar is still embedded into the molecular cloud and the accretion disc is massive. In such environments, the role of self-gravity (SG) and gravitational instability (GI) is crucial in determining the dynamical evolution of the disc. In this work, we study the dynamical role of drag force in self-gravitating discs as a way to form planetesimals in early protoplanetary stages. We obtain the dispersion relation for density-wave perturbations on a fluid composed of two phases (gas and dust) interacting through the common gravitation field and the mutual drag force, and we find that the stability threshold is determined by three parameters: the local dust-to-gas density ratio, the dust relative temperature and the relevant Stokes number. In a region of parameters space, where young protoplanetary discs are likely to be found, the instability can be *dust driven*, occurring at small wavelengths. In this regime, the Jeans mass is much smaller than the one predicted by the standard gravitational instability model. This mechanism can be a viable way to form planetary cores in protostellar discs, since their predicted mass is about $\sim 10\mathrm{M}_{\oplus}$.

9.1 Gravitational and aerodynamical coupling between gas and dust

In this analysis, we consider a gas and dust disc, where the two components are coupled through both gravitational and drag force. The gravitational interaction is described by the Poisson equation, that for this system is

$$\nabla^2\Phi = 4\pi G\delta(z)(\Sigma_g + \Sigma_d), \tag{9.1}$$

where Φ is the total gravitational potential, Σ_g, Σ_d are the surface densities of gas and dust respectively and $\delta(z)$ is the Dirac Delta function. Equation (9.1) is telling us that both gas and dust contribute to the total gravitational potential. As for the aerodynamical coupling, it appears in the Euler equations

$$\partial_t \mathbf{v}_g + (\mathbf{v}_g \cdot \nabla)\mathbf{v}_g = -\nabla(\Phi + h_g) + \frac{1}{\Sigma_g}\mathbf{F}_d, \tag{9.2}$$

$$\partial_t \mathbf{v}_d + (\mathbf{v}_d \cdot \nabla)\mathbf{v}_d = -\nabla(\Phi + h_d) - \frac{1}{\Sigma_d}\mathbf{F}_d, \tag{9.3}$$

where $\mathbf{v}_g, \mathbf{v}_d$ are gas and dust velocity vectors, h_g, h_d are gas and dust enthalpies[1] and $\mathbf{F}_d$ is the drag force per unit surface, defined as

$$\mathbf{F}_d = \frac{\Sigma_d}{t_s}(\mathbf{v}_d - \mathbf{v}_g), \tag{9.4}$$

where t_s is the stopping time of dust particles, i.e. the time in which drag modifies the relative velocity significantly. By these definitions, it is evident that the effect of the drag onto the gas component is smaller than the dust one of a factor $\epsilon = \Sigma_d/\Sigma_g$, the so-called "dust to gas ratio", that is considered to be $\epsilon \sim 0.01$ from ISM abundances (Draine 2011). Because of the small value of ϵ, we firstly neglect the effect of the backreaction (i.e. we neglect the last term in Eq. 9.2): this allows us to deal with simpler algebra; then, we add it, and we evaluate its effect.

9.1.1 Instability without backreaction

Here, we record the dispersion relation $D_{\rm nbr}(\omega, k)$ without taking into account the backreaction. To do so, we perform a first order perturbation analysis of the fluid equations (for an outline of the derivation, see Appendix B). We find a fifth order equation with complex coefficients, that reads

$$\begin{aligned} &D_{\rm nbr}(\omega,k) = -i\omega^5 + \tfrac{2\omega^4}{t_s} + i\omega^3\left(\alpha_g + \alpha_d + \tfrac{1}{t_s^2}\right) + \\ &-\tfrac{\omega^2}{t_s}\left(2\alpha_g + \alpha_d - \beta_d - \kappa^2\right) + \\ &-i\omega\left[\alpha_g\alpha_d - \beta_g\beta_d + \tfrac{1}{t_s^2}(\alpha_g - \beta_d)\right] + \\ &+\tfrac{1}{t_s}\left[\alpha_g\alpha_d - \beta_g\beta_d - \kappa^2(\alpha_g - \beta_d)\right] = 0, \end{aligned} \tag{9.5}$$

where $\alpha_i = \kappa^2 + c_i^2k^2 - 2\pi G\Sigma_i|k|$ and $\beta_i = 2\pi G\Sigma_i|k|$, in which the subscript i takes on the values g or d to denote which species the various quantities refer to. The dispersion relation can be divided into two parts, one that contains the drag coupling and one "drag-free", that corresponds to the two-component fluid model one

$$D_{\rm nbr}(\omega,k) = -i\omega D_{\rm 2f}(\omega,k) + \frac{1}{t_s}D_{\rm drag}(\omega,k), \tag{9.6}$$

with $D_{\rm 2f}$ does not contain drag terms, as the one obtained by Jog & Solomon (1984), and

$$\begin{aligned} &D_{\rm drag}(\omega,k) = 2\omega^4 + \tfrac{i\omega^3}{t_s} - \omega^2(2\alpha_g + \alpha_d - \beta_d - \kappa^2) + \\ &-\tfrac{i\omega}{t_s}(\alpha_g - \beta_d) + \left[\alpha_g\alpha_d - \beta_g\beta_d - \kappa^2(\alpha_g - \beta_d)\right]. \end{aligned} \tag{9.7}$$

One should note that in the limit of weak aerodynamical coupling, $t_s >> \kappa^{-1}$, where $\kappa^{-1} \simeq \Omega^{-1}$ is the dynamical time of the system, the dispersion relation reduces to the two-component fluid model one.

In order to compare this result with one and two-component fluid model, we compute the marginal stability curve. In this case, there are three parameters that determine the instability: ϵ and ξ, defined as before, and the Stokes number $\mathrm{St} = t_s\kappa$, that measures the strength of the aerodynamical coupling. Since the dispersion relation has complex coefficients, the instability threshold is given by $\mathrm{Im}(\omega) = 0$.

[1] The enthalpy is related to the sound speed: $\mathrm{d}h = c^2\mathrm{d}\Sigma/\Sigma$.

We first study the high drag limit $\mathrm{St} = t_s\kappa << 1$: in this case, Eq. 9.7 is dominated by the two imaginary terms and we neglect the others, so we can get analytically the marginal stability curve. As for the general case, we obtain numerically the marginal stability curve by imposing the imaginary part of the roots of Eq. (9.5) to be zero, and we find that it is well reproduced by the high drag approximation; this is also true when we take into account the backreaction.

In the high drag regime, the dispersion relation has the following form

$$\omega^4 - \omega^2\left(\alpha_g + \alpha_d + \frac{1}{t_s^2}\right) + \left[\alpha_g\alpha_d - \beta_g\beta_d + \frac{1}{t_s^2}(\alpha_g - \beta_d)\right] = 0. \tag{9.8}$$

To write the marginal stability curve, we set $\omega = 0$ in Eq. 9.8, we write it in a dimensionless form, and we solve for Q_g^2, obtaining

$$\begin{aligned} Q_g^2 = \tfrac{2\hat{\lambda}}{\xi}\Big\{&(\epsilon+\xi) - \hat{\lambda}(1+\xi+\mathrm{St}^{-2}) + \\ &+\sqrt{\left[\hat{\lambda}(1+\xi+\mathrm{St}^{-2}) - (\epsilon+\xi)\right]^2 + \\ &-4\xi\left[\hat{\lambda}^2\left(1+\mathrm{St}^{-2}\right) - \hat{\lambda}\left(1+\epsilon+(1+\epsilon)\mathrm{St}^{-2}\right)\right]}\Big\}. \end{aligned} \tag{9.9}$$

It is important to note that for $\mathrm{St} \to \infty$, Eq. (9.9) reduces to (5.52) since drag force is negligible. On the contrary, when $\mathrm{St} \to 0$, the system behaves as a single-component fluid with $\Sigma = \Sigma_g + \Sigma_d$ Figure 9.1 shows marginal stability curves for different values of ϵ, ξ and St compared to the one and two-component fluid models. The role of the drag force is to connect with continuity the one and two fluid instability. We define $Q_{1\mathrm{f}}^2$, $Q_{2\mathrm{f}}^2$ and Q_{D}^2 as the marginal stability curve of the one-component fluid model[2], of the two-component fluid model and of the drag model; once we fix ϵ and ξ, the following condition is always respected

$$Q_{1\mathrm{f}}^2 \leq Q_{\mathrm{D}}^2(\mathrm{St}) \leq Q_{2\mathrm{f}}^2. \tag{9.10}$$

As we have already pointed out, Bertin & Romeo (1988) found that the transition from gas to dust driven instability happens when $\epsilon > \sqrt{\xi}$: when we take into account the drag force, this relation changes. Indeed, when $\mathrm{St} \to 0$, gas and dust are strongly coupled, and they can be considered as one fluid: in this case, physically speaking, we expect that the velocity dispersion is the same ($\xi = 1$), and thus the instability is gas driven. This is just an approximation: in general, the thermal velocity of small dust particles is set by Brownian motions. Modelling this phenomenon is not the purpose of this work, hence we make the approximation that for $\mathrm{St} \to 0$, $c_d = c_g$. Under a mathematical point of view, even though $\mathrm{St} \to 0$, if $\epsilon \neq 0$, there is always a value of ξ under which the instability becomes dust driven. Conversely, when $\mathrm{St} \to \infty$, the system tends to the two-component fluid model, where the drag interaction is not taken into account, and thus the transition condition is the same of Bertin & Romeo (1988). Now, we want to generalize the transition condition taking into account the role of the drag force: we argue that the value of ϵ at which the transition from gas to dust driven instability occurs can be written as

$$\epsilon_{\mathrm{tr}} = f(\mathrm{St})\sqrt{\xi}, \tag{9.11}$$

[2]In the one-component fluid model, the surface density is given by $\Sigma = \Sigma_g + \Sigma_d$

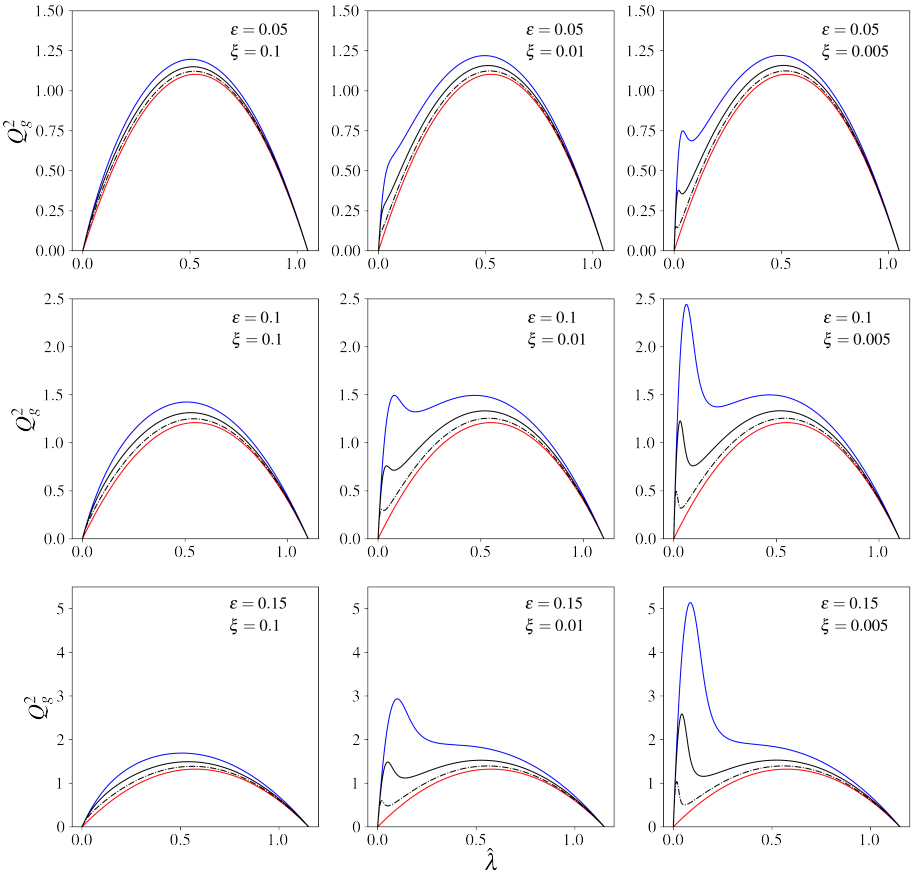

Figure 9.1: Examples of marginal stability curves for different values of ϵ, ξ and St. The blue line is the two-component fluid model without drag force, the red line is one-component fluid model and the black lines represents the two-component fluid model with drag force, without taking into account the backreaction; the solid line corresponds to $\mathrm{St} = 1$ and the dashed line $\mathrm{St} = 0.5$.

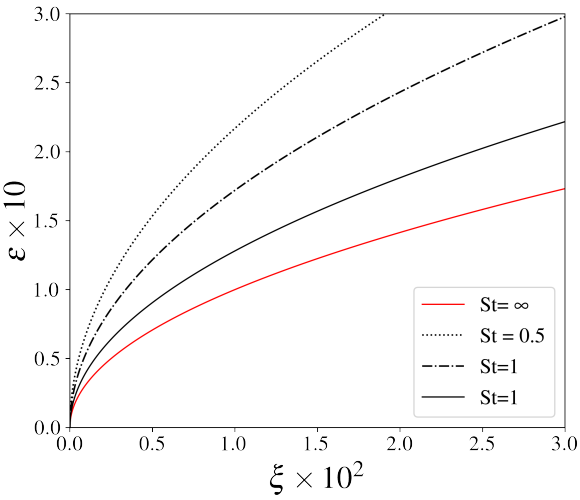

Figure 9.2: Transition curves for different Stokes number in the (ξ, ϵ) diagram obtained by Eq. (9.13). For a chosen Stokes number, in the region above the transition curve the instability is dust-driven, while below is gas-driven. The $\mathrm{St} \to \infty$ case recovers the well known result $\epsilon = \sqrt{\xi}$.

where f is a function for the Stokes number. This function must respect two conditions

$$\lim_{\mathrm{St}\to\infty} f(\mathrm{St}) = 1, \quad \lim_{\mathrm{St}\to 0} f(\mathrm{St}) = \infty, \tag{9.12}$$

in order to recover one and two fluid limits. For simplicity, we hypothesize that f has the following form

$$f(\mathrm{St}) = 1 + a\mathrm{St}^b, \tag{9.13}$$

and we found that the two best fit coefficients are $a = 0.72$, $b = -1.36$. Figure 9.2 shows the transition curves for different values of the Stokes number in the (ξ, ϵ) diagram: for a chosen St, in the region above the curve the instability is dust-driven, while below is gas-driven.

9.1.2 Instability with backreaction

Now we follow the same path as before, but taking into account the backreaction. We start from the same hypotheses of section 9.1.1, and we get the dispersion relation $D_{\mathrm{br}}(\omega, k)$ (an outline of the derivation is given in Appendix B)

$$\begin{aligned}
&-i\omega^5 + \tfrac{2\omega^4}{t_s}(1+\epsilon) + i\omega^3\left[\alpha_g + \alpha_d + \tfrac{1}{t_s^2}(1+2\epsilon+\epsilon^2)\right] + \\
&-\tfrac{\omega^2}{t_s}\left[(2\alpha_g + \alpha_d - \kappa^2)(1+\epsilon) - \beta_d\right] + \\
&-i\omega\left[\alpha_g\alpha_d - \beta_g\beta_d + \tfrac{1}{t_s^2}(\alpha_g - \beta_d + \right. \\
&\left.+\epsilon(\alpha_g + \alpha_d - \beta_g - \beta_d) + \epsilon^2(\alpha_d - \beta_g))\right] + \\
&+\tfrac{1}{t_s}\left[(\alpha_g\alpha_d - \beta_g\beta_d)(1+\epsilon) - \kappa^2\left(\alpha_g - \beta_d - \epsilon(\alpha_d - \beta_g)\right)\right] = 0.
\end{aligned} \tag{9.14}$$

As before, we write the dispersion relation in the high drag regime, given by the condition $\mathrm{St} = t_s\kappa << 1$

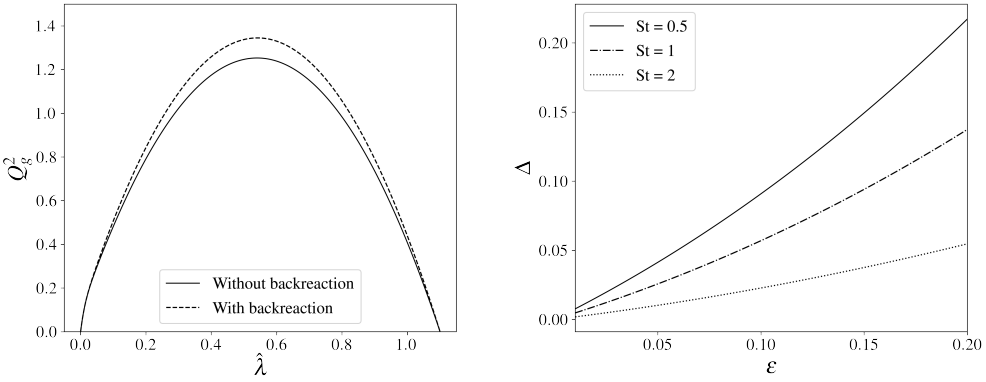

Figure 9.3: The effect of the backreaction onto the marginal stability curve. Left panel: marginal stability curve with and without backreaction, for $\epsilon = 0.1$, $\xi = 0.05$ and $\mathrm{St} = 0.5$. The effect of the backreaction is maximum in correspondence to the gaseous peak. Right panel: the quantity Δ that quantifies the effect of the backreaction as a function of dust-to-gas ratio, for different values of Stokes number and for $\xi = 0.05$.

$$\begin{aligned}\omega^4 - \omega^2\left[\alpha_g + \alpha_d + \tfrac{1}{t_s^2}(1+2\epsilon+\epsilon^2)\right] + [\alpha_g\alpha_d - \beta_g\beta_d + \\ + \tfrac{1}{t_s^2}(\alpha_g - \beta_d + \epsilon(\alpha_g + \alpha_d - \beta_g - \beta_d) + \epsilon^2(\alpha_d - \beta_g))\Big].\end{aligned} \tag{9.15}$$

We obtain the marginal stability curve by setting $\omega = 0$ in the last equation

$$\begin{aligned}Q_g^2 = \tfrac{2\hat{\lambda}}{\xi}\Big\{(\epsilon+\xi) - \hat{\lambda}(1+\xi+\mathrm{St}^{-2}+f_1) + \\ + \sqrt{\left[\hat{\lambda}(1+\xi+\mathrm{St}^{-2}+f_1) - (\epsilon+\xi)\right]^2 + \\ -4\xi\left[\hat{\lambda}^2\left(1+\mathrm{St}^{-2}+f_2\right) - \hat{\lambda}\left(1+\epsilon+(1+\epsilon)\mathrm{St}^{-2}+f_3\right)\right]}\Big\},\end{aligned} \tag{9.16}$$

where

$$f_1(\epsilon, \mathrm{St}) = \frac{\epsilon}{\mathrm{St}^2}(1+\xi+\epsilon\xi), \tag{9.17}$$

$$f_2(\epsilon, \mathrm{St}) = \frac{\epsilon}{\mathrm{St}^2}(2+\epsilon), \tag{9.18}$$

$$f_3(\epsilon, \mathrm{St}) = \frac{\epsilon}{\mathrm{St}^2}[2(1+\epsilon)+\epsilon(\epsilon+1)], \tag{9.19}$$

are three correction factors.

Physically speaking, the backreaction is the effect of the drag force onto the gas component: hence we expect to see differences at intermediate wavelengths, where the instability is gas-driven. The left panel of figure 9.3 shows a comparison between the marginal stability curve with and without the backreaction: as expected, the height of the gaseous peak is different. In particular, when we take into account the backreaction, the system is more unstable i.e. the gaseous peak is higher. This is in agreement with what found in secular GI: backreaction makes the secular GI operational at intermediate wavelengths (Takahashi & Inutsuka 2014). In addition, the effect of the backreaction is

stronger when the dust-to-gas ratio is bigger and the Stokes number is smaller: in order to measure the effects of the backreaction, we define a new quantity

$$\Delta = \text{Max}\left[\left|Q^2_{\text{br}} - Q^2_{\text{nbr}}\right|\right], \tag{9.20}$$

shown in right panel of figure 9.3. It can be clearly seen that the effect of the backreaction is small, even for extreme cases (high dust-to-gas ratio and low Stokes number): from now on, we will use the dispersion relation without backreaction, for computational convenience.

9.2 Application to protostellar discs

In the previous section we showed that the instability threshold is determined by three parameters, $\epsilon = \Sigma_d/\Sigma_g$, $\xi = (c_d/c_g)^2$ and $\text{St} = t_s\kappa$. Here, we aim at understanding instability conditions in protostellar discs: to do so, we need to choose realistic values of these parameters.

Firstly, the value of ϵ in protostellar discs is usually chosen $\epsilon \sim 0.01$. However, the gas disc is usually larger than the dust one, because of the radial drift: for this reason, locally, ϵ can reach higher values.

Secondly, the value of ξ is more complex to determine: indeed, dust particles stirring in protoplanetary discs is due to gravitational, aerodynamical and turbulent effects. In this work, we neglect turbulent phenomena since their magnitude is smaller in these systems. A simple relation between the two parameters, taking into account only the role of drag force, can be easily found Youdin & Lithwick (2007), and it reads

$$\xi = \frac{\alpha_{SS}}{1+\text{St}}, \tag{9.21}$$

where α_{SS} is the $\alpha-$viscosity (Shakura & Sunyaev 1973). The relative temperature is of course related to the viscosity of the disc: indeed, the threshold below which dust particles behave the same as gas ones is given by $\text{St} < \alpha_{SS}$.

Thirdly, the Stokes number of dust particles is essentially determined by the gas surface density and the dust particles' size. There are two main regimes of drag coupling, according to the value of the so-called Knudsen number

$$\text{Kn} = \frac{9\lambda_g}{4s}, \tag{9.22}$$

where λ_g is the gas mean free path and s is the dust particles' size. Epstein regime occurs when $\text{Kn} > 1$, whereas Stokes regime when $\text{Kn} < 1$. Although typical protoplanetary discs are well described by the Epstein regime, self-gravitating systems are between the two regimes (Rice et al. 2006). It means that, for the same particles' size, the Stokes number tends to be higher in self-gravitating discs[3].

9.2.1 Small dust particles

Small dust particles are strongly coupled to the gas ($\text{St} \to 0$), thus they can be considered as a single fluid with a unique sound speed. The condition $\xi = 1$ means that $c_d = c_g$, thus drag force has no effects because of the basic state we choose: indeed, $u_{d0} = u_{g0}$, and if

[3]This is particularly true in the inner part of the disc, where the Knudsen number is lower since the gas density increases.

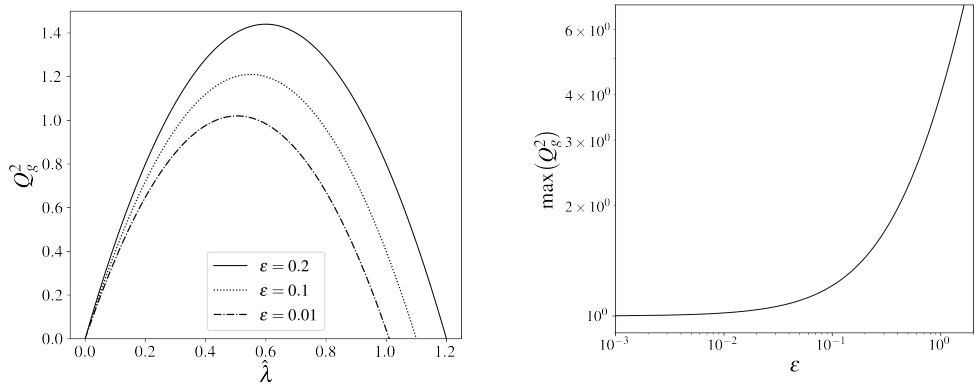

Figure 9.4: Stability for small dust particles. Left panel: marginal stability curve in the high drag regime with $\xi = 1$ and St $\to 0$. The parameter that controls the stability is ϵ. Right panel: maximum of Q_g^2 as a function of the dust-to-gas ratio with $\xi = 1$ and St $\to 0$. For increasing dust-to-gas ratio, the system is more unstable.

the dispersion velocities are the same, the response of the two fluids to the perturbations is equal ($u_{g1} = u_{d1}$), and drag force does not act since it depends on the difference of speed. Actually, the basic velocity of gas and dust is different because of the gas pressure gradient, that is the cause of the radial drift: this issue will be discussed in the following paragraphs.

Hence, in this regime, the stability threshold is determined only by ϵ and we recover the one fluid limit with $\Sigma_{\text{tot}} = \Sigma_g + \Sigma_d = \Sigma_g(1+\epsilon)$, as also shown in the context of secular GI (Takahashi & Inutsuka 2014). In this case, the cold component has a destabilizing role, since it increases the surface density of a factor $1+\epsilon$. Figure 9.4 shows the situation described so far: the left panel illustrates the marginal stability curve for different values of the dust-to-gas ratio, and the right panel shows the maximum of the curve as a function of ϵ. This value represents the critical Toomre parameter, and it increases for higher dust concentration.

9.2.2 Large dust particles

Large dust particles are less coupled, and in general their sound speed is different from the gas one. As we have shown the Stokes number and ξ are linked through Eq. (9.21), so we can study the instability threshold as a function of the Stokes number alone, for different values of dust-to-gas ratio and $\alpha-$viscosity.

Figure 9.5 shows how the maximum of the marginal stability curve (i.e. the squared critical Toomre parameter) changes as a function of the Stokes number for different values of ϵ and α_{SS}. For low Stokes number (St $< \alpha_{SS}$), $\xi \to 1$ and, we recover the previous case: the instability threshold is determined by the parameter ϵ. Increasing the Stokes number, the maximum of Q_g^2 remains essentially constant until St ~ 1 and then it starts rising: this happens because for St > 1 the relation between ξ and St is decreasing. When St $\in [10, 1000]$, depending on ϵ and α_{SS}, the curve rises exponentially: this happens because there is a transition from gas-driven instability (gaseous peak) to dust-driven instability (dusty peak). Additionally, the lower the $\alpha-$viscosity is, the sooner the transition between gas to dust driven GI happens. In general, for a disc in gravito-turbulent

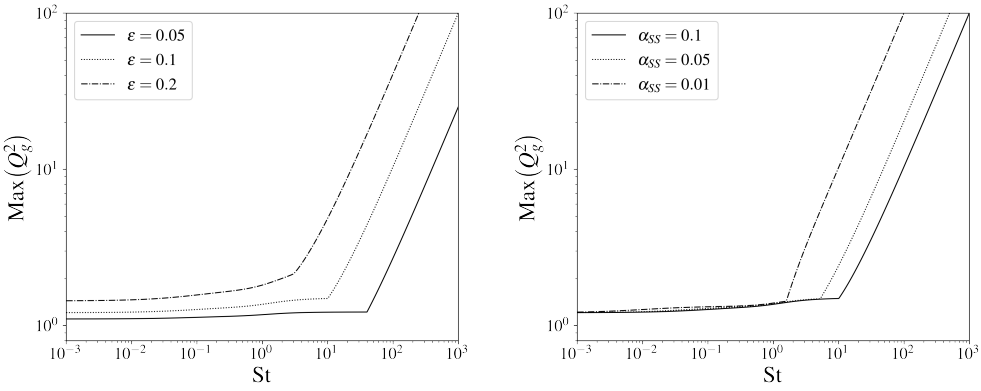

Figure 9.5: Marginal stability curve for large dust particles, where we assumed the relation between ξ and St to be equation (9.21), for different values of dust to gas ratio (left panel, $\alpha_{SS} = 0.1$) and the $\alpha-$viscosity (right panel, $\epsilon = 0.1$). The curve start rising for $\mathrm{St} > 1$, and it has an exponential growth when $\mathrm{St} \gtrsim \epsilon^{-2}\alpha_{SS}$.

regime, the value of α_{SS} can be relatively high $\alpha_{SS} \sim 0.05 - 0.1$ (Kratter & Lodato 2016), being GI an effective way to transfer angular momentum.

It is possible to find an approximate relation between the critical Stokes number for which the instability is driven by the dust and ϵ parameter, that reads

$$\mathrm{St}_{\mathrm{crit}} \simeq \epsilon^{-2}\alpha_{SS}, \tag{9.23}$$

where the last relation is obtained through a fit. Hence, systems with smaller dust-to-gas ratio and higher $\alpha-$viscosity show the transition at higher Stokes number, being more stable.

9.2.3 Planetesimal formation through gravitational instability

Now that we have obtained a general relation between ξ and St, we can study the Jeans length and Jeans mass of the perturbation. The left panel of figure 9.6 shows the Jeans length of our model $\lambda_J^{\mathrm{drag}}$ normalized to the one-component fluid model one $\lambda_{\mathrm{J}}^{\mathrm{1f}}$, and, as expected, for $\mathrm{St} > \epsilon^{-2}$ the value of $\lambda_{\mathrm{J}}^{\mathrm{drag}}$ decreases because the instability becomes dust-driven. The right panel of figure 9.6 shows the Jeans mass of our model $M_{\mathrm{J}}^{\mathrm{drag}}$ normalized to the one fluid one $M_{\mathrm{J}}^{\mathrm{1f}}$. As for the Jeans wavelength, $M_{\mathrm{J}}^{\mathrm{drag}}$ decreases when $\mathrm{St} > \epsilon^{-2}$, reaching values of $\sim 10^{-3}$.

The classical framework[4] of gravitational instability (for a review see Kratter & Lodato (2016)) can not explain the formation of planets, since the value of the Jeans mass is too high.

Within our model, it is possible to obtain Earth-like bodies through gravitational instability when it is dust-driven: as a matter of fact, the right panel of figure 9.6 shows that $M_{\mathrm{J}}^{\mathrm{drag}} \sim 10^{-2/-3} M_{\mathrm{J}}^{\mathrm{1f}}$, leading to a clump mass of the order of several Earth masses.

[4]With "classical framework" we refer to the case of a gas-only disc, with Jeans length computed from one-component fluid model.

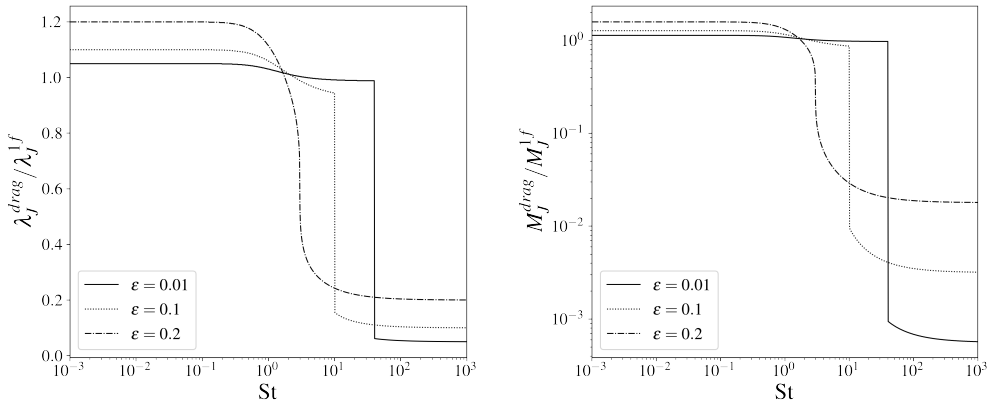

Figure 9.6: Jeans length (left panel) and Jeans mass (right panel) normalized to the LS one as a function of the Stokes number, for varying dust to gas ratio and $\alpha_{SS} = 0.1$. For typical protoplanetary disc parameters, the Jeans mass $\mu_J \sim 1 M_j$, meaning that dust-triggered instability could potentially lead to fragments of several Earth masses.

A mechanism that may allow the formation of Earth-like bodies as a consequence of Gravitational Instability (GI) was proposed by Rice et al. (2006). Concentration of solid particles in spiral arms, together with vertical settling, can lead to gravitational collapse in the solid component. Our findings are in agreement with the work Rice et al. (2006), however, higher resolution is needed in order to properly assess the mass of the fragments. In addition, it is known that gas spiral arms act as dust traps, since they are pressure maxima (Shi et al. 2016). Solid particles collect inside them (Dipierro et al. 2015b), reaching dust to gas ratio that can be of the order of unity. Conversely, the interaction between gas spiral arms and dust particles can excite them, imparting random motions that reduce the peak density and potential for collapse (Riols et al. 2020). Walmswell et al. (2013) found that large dust particles experience gravitational scattering by the spiral arms, while Booth & Clarke (2016) related the level of excitation of solid particles with the aerodynamical coupling and the cooling factor. Marginally coupled solid particles are less excited by spiral arms, while, in rapidly cooled discs, the level of dust excitation is higher. Baehr & Zhu (2021a) confirmed that trend through 3D shearing box simulations.

A possible scenario in which dust driven GI can be promoted is during stellar flybys (Cuello et al. 2023). Indeed, a flyby can rip away the external part of a protostellar disc that, because of radial drift, is low in dust (Cuello et al. 2019). Hence, after the interaction with the perturber, the dust to gas ratio in the inner part is significantly higher, fostering dust driven GI and, possibly, formation of planetesimals.

9.2.4 Comparison with previous works

In protoplanetary discs literature, the interplay between drag force and gravitational instability has been studied in the context of "Secular gravitational instability" (Youdin 2011; Takahashi & Inutsuka 2014; Tominaga et al. 2020), hereafter SGI. The general formulation of SGI is presented in Youdin (2011). In this model, dust particles are subject to turbulent diffusion (Eq. 11a of Youdin (2011)), dust self-gravity, drag force, and they are characterized by random velocities. The gas background is stable, and the role of its self-

gravity is negligible (i.e. $Q_g \to \infty$). The results are that there is a low frequency mode instability, that corresponds to a secular time instability, responsible for the creation of dust overdensities in a gravitationally stable gas disc ($Q_g >> 1$). More refined models have been presented in the following years (Takahashi & Inutsuka 2014; Tominaga et al. 2020), however the crucial difference between SGI and the model we propose here is that drag force is essential for SGI to arise, while in our model the instability already exists in the limit of St $\to \infty$ (Jog & Solomon 1984; Bertin & Romeo 1988). Moreover, our model investigates the gravitational stability of a two fluid system, and we are interested in understanding how the presence of dust destabilizes the system. In this work, the two components have different sound speed and are coupled through gravitational and drag force, without turbulent diffusion. The origin of gas and dust sound speed is different: as for the gas, it is generated by collision of particles (thermal origin), while for the dust, it is caused by stirring processes. In addition, the instability described in our model happens on a dynamical timescale, not in a secular one as for SGI. We decided not to include diffusive terms due to gas turbulence since, in the hydrodynamic equations the gas is considered as an inviscid fluid. As we have mentioned in section 3.1, the instability threshold in the limit of St $\to 0$ obtained within our model is in good agreement with what secular GI predicts, when diffusion is negligible.

9.2.5 The role of the asymmetric drift

As we have pointed out in paragraph 9.2.1, in this analysis we are not considering the difference of velocity in the basic state between gas and dust due to the pressure gradient. In the context of protostellar discs, this is particularly important since it is the main cause of the radial drift of solid particles.

Bertin & Cava (2006) obtained the dispersion relation for a self-gravitating disc made of two components in relative motion, without any coupling between them. In a rotating self-gravitating axisymmetric fluid disc at equilibrium, the radial gravitational force is balanced by rotation, with a contribution from the pressure gradient

$$\Omega^2 = \frac{1}{R\Sigma}\frac{\mathrm{d}P}{\mathrm{d}R} + \frac{1}{R}\frac{\mathrm{d}\Phi}{\mathrm{d}R}, \tag{9.24}$$

where P is the pressure. Since the pressure is connected to the sound speed, two fluids with different temperature have different angular frequency ($\Omega_g \neq \Omega_d$ in protostellar case). For cool fluids, the pressure gradient is negligible, and this is the case of dust in protostellar discs, whereas it is important for hotter fluids, i.e. the gas. Bertin & Cava (2006) showed that there are two new parameters that determine the stability of the system, that are

$$\delta = \frac{\Omega_d}{\Omega_g}, \tag{9.25}$$

$$\eta = m(\delta - 1)(\Omega_g/\kappa_g). \tag{9.26}$$

In the case of axisymmetric disturbances, $\eta = 0$ and so the only important parameter is δ. Since the hot component moves slower than the cool one because of the pressure gradient, usually $\delta > 1$. It is possible to show that in this regime the instability conditions are the same as the two fluid component model (Jog & Solomon 1984), with an appropriate rescaling[5] of ϵ and ξ.

[5] $\epsilon \to \epsilon/\delta^2$ and $\xi \to \xi/\delta^2$. Formally, for axisymmetric perturbations, the required rescaling indicates that a two-component model in which the presence of asymmetric drift is recognized explicitly is more stable than

In turn, for $m \neq 0$ a two-component disk in which the presence of asymmetric drift is recognized explicitly, taken to be marginally stable with respect to m = 0 perturbations, may be unstable even for small values of η. This fact is particularly interesting in protostellar discs: indeed, the number of spiral arms generated by gravitational instability m is inversely proportional to the disc-to-star mass ratio q (Cossins et al. 2009), and thus we expect to find $m >> 1$ for relatively light discs.

In protoplanetary discs, we are able to exactly determine the asymmetric drift, and thus the value of δ and η. To do so, we neglect the dust pressure gradient, and we consider the two components to be coupled through the drag force. It is possible to show (Armitage 2013) that, in absence of gas radial motion, the azimuthal velocities are

$$u_{g0} = u_k \left(1 - \gamma\right)^{1/2}, \tag{9.27}$$

$$u_{d0} = \frac{\mathrm{St}^2}{1 + \mathrm{St}^2} \left[u_k - u_{g0} \left(1 - \frac{1 + \mathrm{St}^2}{\mathrm{St}^2} \right) \right], \tag{9.28}$$

where $u_k = \sqrt{GM_\star/R}$, and γ is proportional to the disc temperature, and it is a positive quantity. Hence, the strength of the asymmetric drift is connected to the Stokes number: when gas and dust are strongly coupled (St $<< 1$), they move with the same velocity, and thus the asymmetric drift is zero ($\delta = 1, \eta = 0$), conversely when they are uncoupled (St $>> 1$), the asymmetric drift is maximum. Hence, the value of δ in protostellar discs is simply

$$\delta = \frac{u_{d0}}{u_{g0}}. \tag{9.29}$$

Figure 9.7 shows δ and η parameters for a protoplanetary disc as a function of the Stokes number. Even if we take extreme values of $\delta = 1.05$ and $\eta = 0.25$ and we use the dispersion relation without drag[6] obtained by Bertin & Cava (2006), the marginal stability curve does not change significantly. Thus, even though the asymmetric drift is crucial in protoplanetary disc evolution, since it causes the radial drift, in terms of gravitational instability it can be neglected, at a linear level.

9.2.6 Non-linear evolution

If we consider a perturbed disc, the value of ϵ and ξ significantly changes because of the spiral density wave. As for the gas-to-dust ratio, it increases inside the spirals for two reasons: firstly, because the perturbation is a minimum of gravitational potential and secondly since it is a gas pressure maximum, and thus the dust experiences trapping. In addition, as pointed out by Rice et al. (2004), dust growth is accelerated inside GI spirals, since its density is enhanced (the dust-to-gas ratio ϵ can reach values of the order of unity) and because of the effect of gravitational focusing. As for ξ, Booth & Clarke (2016) computed the dust dispersion velocity for gravito-turbulent discs[7] as a function of the Stokes number, and they found that the gravitational potential perturbation is effective only for St $\gtrsim 1$, and in this regime $\xi \propto \mathrm{St}^{1/2}$. The minimum ξ is reached for

a model without such drift and with the same values of surface densities, temperatures, and rotation curve (because the corresponding value of the effective Q which determines marginal stability is lower for the model with the drift).

[6] By what we have shown in this work, if we do not take into account drag interaction, the system will always be more unstable compared to the drag case. Hence, by evaluating the instability threshold with Bertin & Cava (2006), we give an upper limit to the instability boundary.

[7] In this work, the authors considered a marginally unstable disc with a constant cooling rate $\beta_{\mathrm{cool}} = \Omega t_{\mathrm{cool}}$.

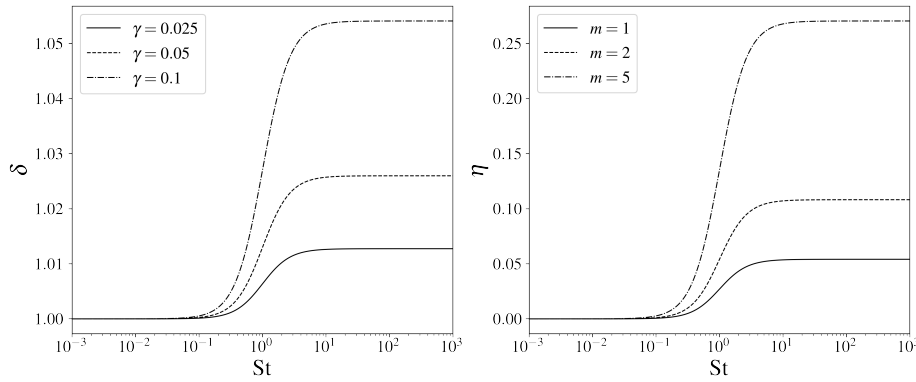

Figure 9.7: δ and η parameters for a protostellar disc. Left panel: ratio between dust and gas azimuthal velocity in the steady state, i.e. δ, for different values of γ, i.e. pressure gradient, as a function of the Stokes number. For St$\rightarrow 0$, the dust velocity is equal to the gas one, since the two components are strongly coupled. Conversely, for St$\rightarrow \infty$, dust velocity is higher than the gaseous one, and it tends to the Keplerian speed u_k and the asymmetric drift is maximum. Right panel: η parameter as a function for the Stokes number for different values of the azimuthal wavenumber m, for $\gamma = 0.1$ and $\Omega_g/\kappa_g = 1$.

St ~ 1, because dust particles are forced to stay into the spiral arms by both the effect of the gravitational potential and drag force. There, the dust to gas ratio is of the order of unity, and the median dispersion velocity of dust particles is $c_d \simeq 10^{-1} c_g$.

One can think to locally apply our linear theory with the parameters of the perturbed disc, using $\epsilon = 1, \xi = 0.01$ and St $= 1$. In this regime, the instability is dust driven and the most unstable wavelength is $\hat{\lambda} \simeq 0.2$ where the critical value of $Q_{\mathrm{g,cr}} \simeq 6$; the Jeans mass is between 2 and 3 order of magnitude lower than the one fluid one, that corresponds approximately to $M_J \sim 10 M_\oplus$.

However, we should be cautious with these results, since we are using a linear theory to describe the non-linear evolution of the system. To properly investigate the non-linear evolution of the system, numerical simulations of gas and dust discs are needed.

9.2.7 Drag force in the context of galactic dynamics

A natural comparison can be made in the context of galactic dynamics. In disc galaxies, drag force is connected to the phenomenon of dynamical friction (Chandrasekhar 1943). Ostriker (1999) evaluated this effect on a star travelling at a velocity $v_\star$ through a uniform gaseous medium with sound speed c_g: gaseous drag is generally more efficient when $\mathcal{M}_\star = v_\star/c_g > 1$, meaning that the star motion is supersonic. This is a particularly interesting case, since gas sound speed in the Milky Way is $c_g \simeq 10 km/s$ (Fux 1999) and the typical star velocity is $v_\star \simeq 30 km/s$. Although drag force in galactic environments is less relevant than in protostellar ones, it would be worth to evaluate its impact on global spiral modes.

9.3 Conclusions

In this work, we study the dynamical role of drag force in gravitational instability, and we propose a path to form planetesimals in early protoplanetary stages. The problem of the classical Gravitational Instability scenario of planet formation (Boss 1997) is that the Jeans mass is too large to form a planet, conversely it is an effective way to form low mass stellar companions.

The classical GI consider the system composed of one fluid, however, protoplanetary discs are made up of two components, gas and dust. When we consider the dynamical role of the second component, GI outcome can significantly change. Indeed, the instability threshold is always higher, and the presence of the second cold component can trigger instability at very short wavelengths, reducing of several order of magnitudes the Jeans length and mass.

Nevertheless, a step forward can be made: indeed, gas and dust in protoplanetary discs are aerodynamically coupled, and the role of drag force is crucial in determining their dynamical evolution. When we take into account the coupling between the two components (section 6.1), gravitational instability threshold is determined by three parameters, that are the relative concentration of the two fluids ϵ, the relative temperature ξ and the Stokes number, that measures the strength of the aerodynamical coupling. The effect of drag force in terms of gravitational instability is to connect one-component fluid model and two-component fluid model: in particular, if drag coupling is strong, the system behaves as a one fluid, conversely, if the two components are poorly coupled, the system behaves as two-component fluid.

We then applied this model to investigate gravitational instability in protoplanetary discs (section 9.2). We first hypothesize that dust velocity dispersion is completely determined by stirring processes, so that it can be written as a function of the Stokes number. Within this hypothesis, we found that instability is dust driven when $\mathrm{St} > \epsilon^{-2}$: hence, the Jeans mass is 3-4 order of magnitude smaller; thus, dust driven gravitational instability can be a viable way to form planetesimals in massive protostellar systems.

In addition, we studied the role of the asymmetric drift, that in protostellar discs is significant: we quantified its effect, and we stated that it does not impact on the value of the most unstable wavelength, but only on the critical Q_g. Then, we discussed the nonlinear evolution of the system, showing that GI spirals significantly modify the value of the stability parameters. We made a comparison between our model and numerical simulations of Rice et al. (2006); Booth & Clarke (2016) and we found good agreement. However, we should pay attention to this because our theory describes the linear behaviour of the system.

To conclude, we briefly discussed a possible application of this work in the context of galactic dynamics.

CHAPTER 10

Planetary cores formation through dust collapse in gravitationally unstable discs

*This chapter is based on the paper "The role of the drag force in the gravitational stability of dusty planet forming disc - II. Numerical simulations" by **Cristiano Longarini**, Philip J. Armitage, Giuseppe Lodato, Daniel J. Price and Simone Ceppi, published in Monthly Notices of the Royal Astronomical Society in July 2023.*

Young protostellar discs are likely to be both self-gravitating, and to support grain growth to sizes where the particles decouple from the gas. This combination could lead to short-wavelength fragmentation of the solid component in otherwise non-fragmenting gas discs, forming Earth-mass solid cores during the Class 0 / I stages of Young Stellar Object evolution, as presented in Longarini et al. (2023b). In this chapter, we use three-dimensional smoothed particle hydrodynamics simulations of two-fluid discs, in the regime where the Stokes number of the particles $\mathrm{St} > 1$, to study how the formation of solid clumps depends on the disc-to-star mass ratio, the strength of gravitational instability, and the Stokes number. Gravitational instability of the simulated discs is sustained by local cooling. We find that the ability of the spiral structures to concentrate solids increases with the cooling time, and decreases with the Stokes number, while the relative dynamical temperature between gas and dust of the particles decreases with the cooling time and the disc-to-star mass ratio, and increases with the Stokes number. Dust collapse occurs in a subset of high disc mass simulations, yielding clumps whose mass is close to linear theory estimates, namely 1–10 $\mathrm{M}_\oplus$. Our results suggest that if planet formation occurs via this mechanism, the best conditions correspond to near the end of the self-gravitating phase, when the cooling time is long and the Stokes number close to unity. This mechanism could possibly solve the conundrum of planetesimal formation, directly forming planetary cores in young systems.

10.1 Numerical simulations

In this work, we perform numerical SPH simulations of gas and dust protostellar discs using the code PHANTOM (Price et al. 2018b). This code is widely used in the astrophysical community to study gas and dust dynamics in accretion discs (Dipierro et al. 2015b; Ragusa et al. 2020), both in a single fluid mixture (Veronesi et al. 2019) or dust-as-particles approach (Longarini et al. 2021a). In this work, we use the dust-as-particles formulation.

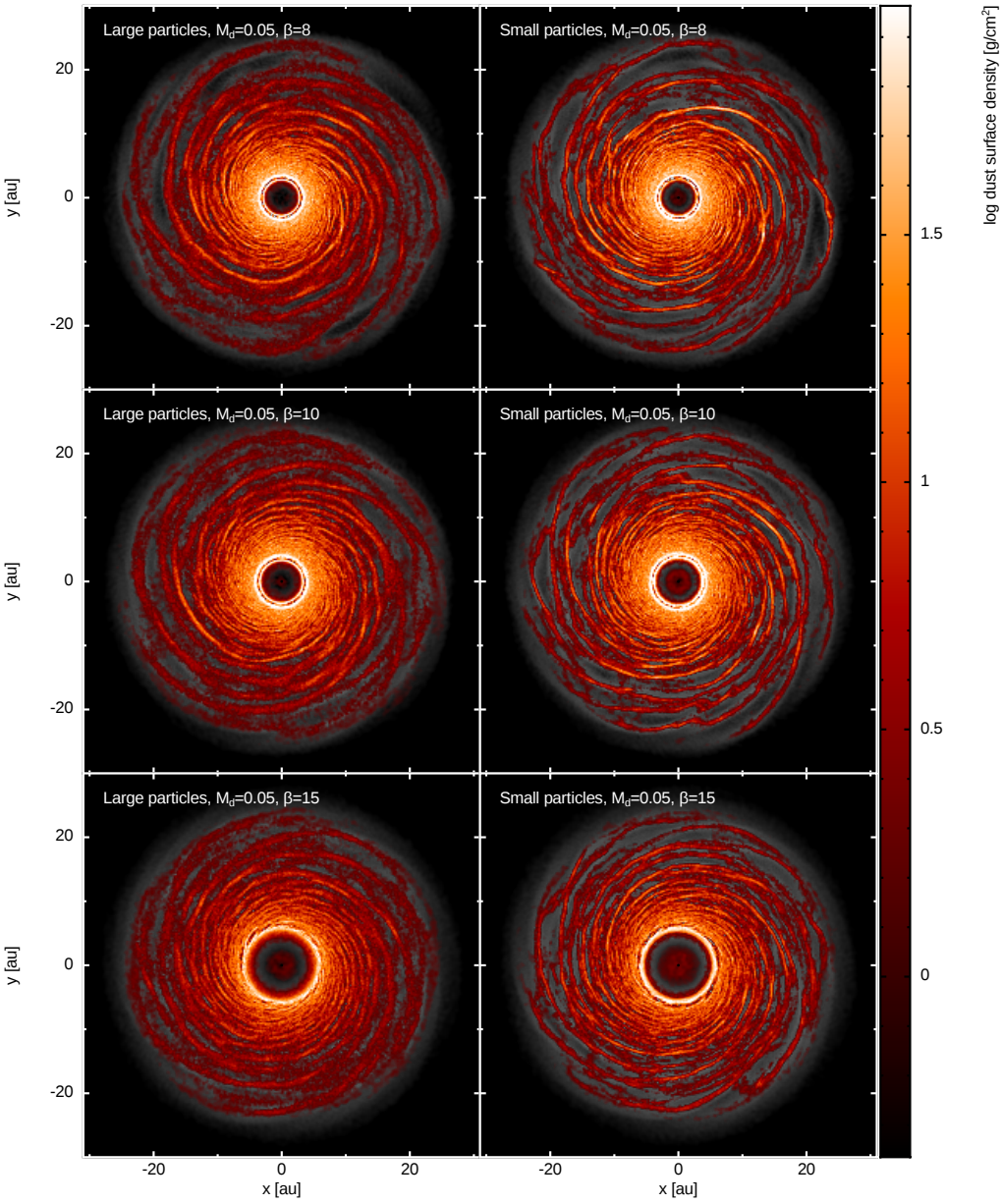

Figure 10.1: Dust dynamics in gas spiral arms: large and small dust particles surface density for different cooling factor and $M_d/M_\star = 0.05$.

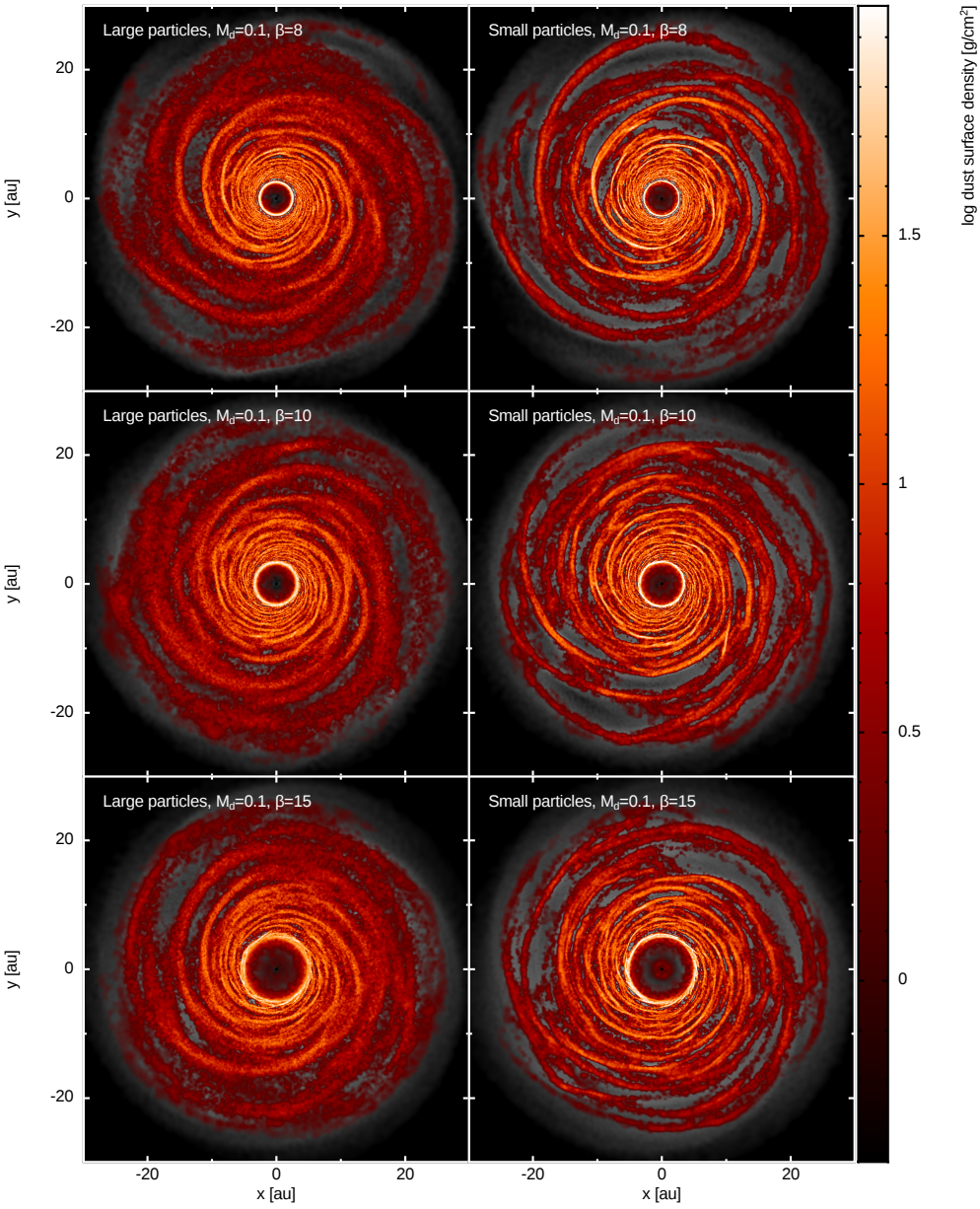

Figure 10.2: Dust dynamics in gas spiral arms: large and small dust particles surface density for different cooling factor and $M_d/M_\star = 0.1$.

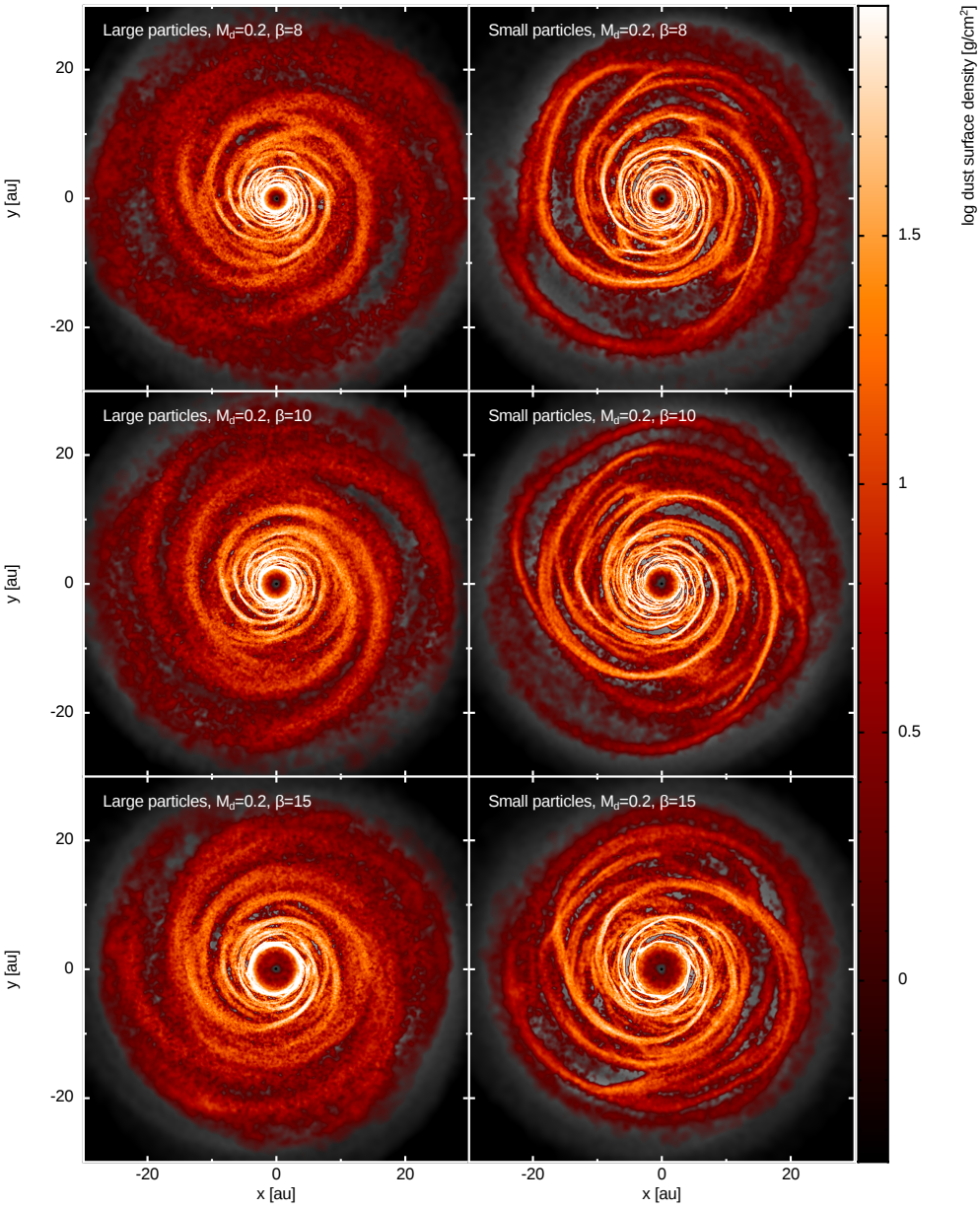

Figure 10.3: Dust dynamics in gas spiral arms: large and small dust particles surface density for different cooling factor and $M_d/M_\star = 0.2$.

10.1.1 Numerical setup

We perform simulations with three different disc-to-star mass ratios $M_d/M_\star = \{0.05, 0.1, 0.2\}$, three different cooling times $\beta_{\rm cool} = \{8, 10, 15\}$ and two different dust particle sizes, for a total of 18 simulations. See below for further details. We first initialize a gas-only disc around a solar mass star, with $R_{\rm in} = 0.25$au, $R_{\rm out} = 25$au, and $\Sigma_g \propto R^{-1}$. We set the aspect ratio so that $Q_{\rm ext} = 2$ initially and because of the cooling, it decreases, eventually reaching $Q = 1$. The shock viscosity coefficients $\alpha^{\rm AV} = 0.1$, $\beta^{\rm AV} = 0.2$ as in Rice et al. (2005). As a test, we performed a simulation with $\beta^{\rm AV} = 2$, and we did not find any differences in terms of the relevant quantities in this work. The self-gravity of both gas and dust is taken into account, as well as the dust back-reaction. We performed simulations at two different numerical resolutions: the standard runs are performed with $N_g = 10^6$ and the high resolution ones with $N_g = 2 \times 10^6$. In both cases, $N_d = N_g/5$, where N_g and N_d are the number of gas and dust particles respectively. We verify that the results are consistent with the different resolutions.

We let the system evolve for an outer thermal time ($\beta_{\rm cool}\Omega^{-1}$ at the outer radius), and then we add dust particles and evolve for a further 5 outer dynamical times (i.e. 5×10^3 inner dynamical times). The dust particles are added proportional to the gas distribution.[1] Distributing dust particles proportional to the gas is a valid assumption only for St < 10. Zhu et al. (2012) showed that for uncoupled particles gravitational interactions and stirring become quite relevant, and hence dust distribution is closer to a uniform one. This is particularly clear for St ~ 100. In our simulations of large dust grains, although the initial distribution is proportional to the gas one, we observe that the spiral is less prominent compared to smaller grains.

Dust back-reaction and dust self-gravity are always taken into account. Since the aim of the work is to study the effect of the drag force in GI, we use two different dust sizes: a larger one, to reproduce weakly coupled solid particles, and a smaller one, to study marginally coupled particles. Since the disc mass is different across our set of simulation, we chose to adapt the particles' size in order to obtain the same Stokes number distribution. To do so, we computed the radially averaged Stokes number as a function of the particle size for different disc-to-star mass ratio, starting from the initial conditions of the gas disc, taking into account the transition between Epstein and Stokes regime. We decided to choose the small particles' size so that the radially averaged Stokes number $\langle {\rm St} \rangle = 8$, and for the large ones $\langle {\rm St} \rangle = 40$: in this way we effectively cover a Stokes number range from 1 to 10 with smaller grains, and from 10 to 100 for larger ones. One exception is that the small dust particles for the highest disc-to-star mass ratio simulations are chosen to have $\langle {\rm St} \rangle = 16$ for computational reasons. In addition, as we will show in the next section, a higher disc-to-star mass ratio makes the dust unstable, and collapse can happen: for that reason, dust in simulations **S16, S17** and **S18** is evolved only for an outer dynamical time. In every simulation, dust intrinsic density is fixed $\rho_0 = 5{\rm g/cm}^3$.

Self-gravitating discs may be more radially extended than our models, which can be rescaled. If we rescale the outer radius of a factor λ, how does the dust particles' size need to be rescaled? Since ${\rm St} \propto s/\Sigma \propto sR_{\rm out}^2$, if we change the outer radius according to $R'_{\rm out} = \lambda R_{\rm out}$, in order to maintain the same Stokes number, the corresponding rescaling for dust particles size should be $s' = \lambda^{-2}s$. Hence, if we consider a larger disc

[1] We benchmarked our simulations with the ones of Rice et al. (2004), as they started with an initial uniform dust distribution, with a fixed thickness. We obtained the same results, since dust trapping is very efficient in these systems. Something that should be pointed out is that Rice et al. (2004) did not account for self-gravity acting on the solid particles.

Table 10.1: Parameters of simulations: disc-to-star mass ratio $M_d/M_\star$, cooling factor $\beta_{\rm cool}$, size of dust particles s, average Stokes number $\langle {\rm St} \rangle$ and corresponding dust particles size in a 10 times bigger disc s_{10}.

Simulation	$M_d/M_\star$	$\beta_{\rm cool}$	s [cm]	$\langle {\rm St} \rangle$	s_{10} [cm]
S1	0.05	8	300	40	3
S2	0.05	10	300	40	3
S3	0.05	15	300	40	3
S4	0.05	8	60	8	0.6
S5	0.05	10	60	8	0.6
S6	0.05	15	60	8	0.6
S7	0.1	8	600	40	6
S8	0.1	10	600	40	6
S9	0.1	15	600	40	6
S10	0.1	8	120	8	1.2
S11	0.1	10	120	8	1.2
S12	0.1	15	120	8	1.2
S13	0.2	8	1500	40	15
S14	0.2	10	1500	40	15
S15	0.2	15	1500	40	15
S16	0.2	8	600	16	6
S17	0.2	10	600	16	6
S18	0.2	15	600	16	6

with $R'_{\rm out} = 10 R_{\rm out} = 250$ au, the corresponding particle sizes should be rescaled as $s' = s/100$. Dust properties are summarized in Table 10.1, where we also include the rescaled dust particles' size. Snapshots of the hydrodynamical simulations are shown in Figures 10.1, 10.2, 10.3.

10.2 Analysis and Results

In this section, we present the analysis of the numerical simulations. Since the simulations use a two-fluid approach (Laibe & Price 2012a,b), gas and dust particles are treated as two different sets of particles, thus they occupy different locations and carry their own physical information. In order to obtain properties that depend on both gas and dust, such as dust to gas ratio, or Stokes number, we interpolate gas properties to the location of dust particles. In addition, since dust is modelled as a pressureless fluid, it has no internal energy and no thermal sound speed. However, stirring phenomena induce a velocity dispersion onto dust particles (Youdin & Lithwick 2007): to obtain this quantity, we compute it with an SPH interpolation over neighbouring dust particles, via

$$c_{d,i}^2 = \sum_{j=1}^{N_{\rm neigh}} m_j \frac{\left(v_{d,i} - v_{d,j}\right)^2}{\rho_j} W_{ij}\left(h_i\right). \tag{10.1}$$

For our analysis, we will mainly focus our attention on the dust to gas ratio ϵ, the relative temperature between gas and dust $\xi = (c_d/c_g)^2$, the Stokes number St, the cooling factor $\beta_{\rm cool}$ and the disc-to-star mass ratio $M_d/M_\star$. These parameters are related to different physical phenomena: the dust to gas ratio and the relative temperature trace dust

trapping and dust excitation respectively, the cooling factor is linked to the gas spiral amplitude (and hence to the strength of GI), the Stokes number determines the power of the aerodynamical coupling and the disc-to-star mass ratio is connected to the spiral morphology.

10.2.1 Dust trapping: the ϵ parameter

GI spiral arms trap dust particles (Dipierro et al. 2015a), since they are both pressure maxima and gravitational potential minima. We use the simulations to quantify how this phenomenon depends on the model parameters. Figure 10.4 shows the distribution of the dust to gas ratio for different $\beta_{\rm cool}$ and $M_d/M_\star$, for a set of simulations with large dust particles. The initial value of the dust to gas ratio is 10^{-2}. In Figure 10.4 the higher tail of the distributions reaches values of $\gtrsim 10^{-1}$, implying that dust concentration by up to approximately an order of magnitude is happening. Figure 10.5 shows a comparison between the dust to gas ratio distributions of large and small particles. As expected, dust concentration in spiral arms is stronger for smaller particles, and it can approach values of the order of unity, since their aerodynamical coupling with gas is stronger. The strength of dust trapping is determined by both the aerodynamic coupling between gas and dust and the gravitational potential of gas spiral arms. The combined effect of gravitational and drag interaction is maximised when St $\simeq Q \simeq 1$ (Baehr & Zhu 2021a), thus, in our simulations, smaller particles reach higher values of the dust to gas ratio. No particular correlations are found between ϵ and the disc to star mass ratio, while there is a slight dependence on the cooling factor. In order to understand this relationship, Figure 10.6 shows the quantity $\delta\Sigma/\Sigma_0$ for gas (orange dots) and dust (large particles - blue dots, small particles - green dots) as a function of the cooling factor $\beta_{\rm cool}$. The quantity Σ_0 is the azimuthally averaged surface density at a fiducial radius of 10 au, and the quantity $\delta\Sigma$ is its standard deviation. For the gas, it is known that $\delta\Sigma_g/\Sigma_{g0} \propto \beta_{\rm cool}^{-1/2}$ (Cossins et al. 2009), and we recover this behaviour in our simulations. For the dust, the situation is different. We do not find any evident correlation between the density contrast and the cooling factor. So, if we assume that

$$\frac{\delta\Sigma_g}{\Sigma_{g0}} \propto \beta_{\rm cool}^{-1/2}, \quad \frac{\delta\Sigma_d}{\Sigma_{d0}} = \text{const}, \tag{10.2}$$

the ratio between these two quantities is

$$\frac{\delta\Sigma_g}{\Sigma_{g0}}\frac{\Sigma_{d0}}{\delta\Sigma_d} = 0.01\epsilon^{-1} \propto \beta_{\rm cool}^{-1/2}, \tag{10.3}$$

where $\Sigma_{d0}/\Sigma_{g0} = 1/100$, meaning that $\epsilon \propto \beta_{\rm cool}^{1/2}$. This is the positive correlation we found before. Why do we not find any evident correlation between the dust density contrast and the cooling factor? Physically, the dust experiences the effect of the gas cooling through gravitational and drag forces. When St $\ll 1$, dust and gas particles are indistinguishable, and so $\delta\Sigma_g/\Sigma_{g0} = \delta\Sigma_d/\Sigma_{d0} \propto \beta_{\rm cool}^{-1/2}$. For higher Stokes number, the drag force is weaker, and the dust is less influenced by the gas cooling. In this case, we expect the relationship between $\delta\Sigma_d/\Sigma_{d0}$ and $\beta_{\rm cool}$ to be flatter than $\beta_{\rm cool}^{-1/2}$: if this condition is respected, the correlation between ϵ and $\beta_{\rm cool}$ will be positive. In general, $\delta\Sigma_d/\Sigma_{d0}$ is a function of both the cooling factor and the Stokes number.

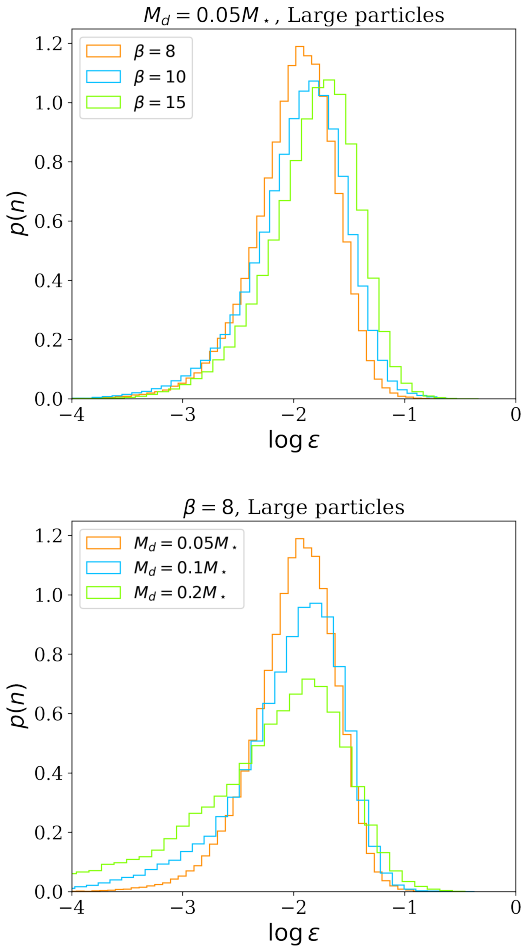

Figure 10.4: Distribution of the dust to gas ratio for different values of cooling factor (top panel) and disc to star mass ratio (bottom panel). The simulations shown in these plots are **S1,S2,S3,S7,S13**.

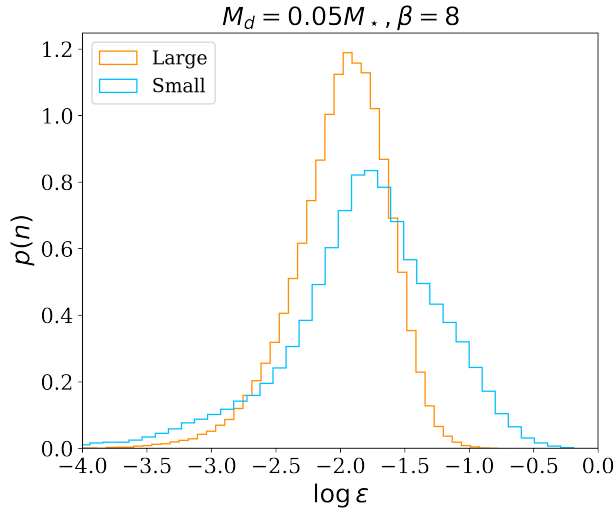

Figure 10.5: Comparison of the distribution of dust to gas ratio of large (orange line) and small (blue line) dust particles. The simulations shown in this plot are **S1** and **S4**.

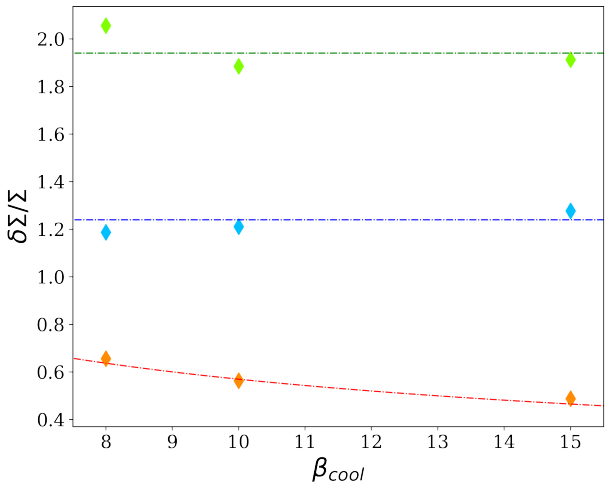

Figure 10.6: Density contrast $\delta\Sigma/\Sigma_0$ of gas (orange), large dust grains (blue) and small dust grains (green) as a function of the cooling factor, for $M_d/M_\star = 0.05$.

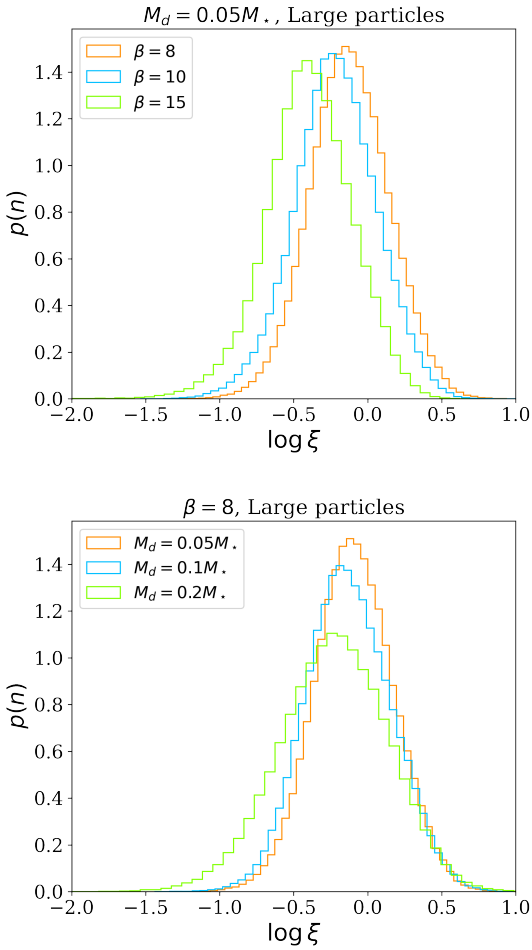

Figure 10.7: Distribution of the relative temperature for different values of cooling factor (top panel) and disc to star mass ratio (bottom panel). The simulations shown in these plots are **S1,S2,S3,S7,S13**.

10.2.2 Dust excitation: the ξ parameter

To investigate dust excitation by spiral arms, we study how the relative temperature $\xi = (c_d/c_g)^2$ varies as a function of the simulation parameters. Figure 10.7 shows the distribution of the dust relative temperature ξ for different values of $\beta_{\rm cool}$ and $M_d/M_\star$ for a set of simulations with large dust particles. We observe that for the simulations in which dust collapse is not happening, the dust dispersion velocity reaches very quickly (< 1 outer orbital time) a steady value. The relative temperature shows a negative correlation with both the disc-to-star mass ratio and the cooling factor. For the disc-to-star mass ratio, this can be understood by considering the relationship with the spiral morphology: $M_d/M_\star$ is inversely proportional to the azimuthal wavenumber m (Cossins et al. 2009), hence massive discs have fewer spiral arms. Since dust is excited because of "spiral kicks" (Walmswell et al. 2013), the lower the number of spiral arms, the less the dust is excited. For the cooling factor, the negative correlation can be understood in two ways. First, the cooling rate $\beta_{\rm cool}$ is linked to the amplitude of the spiral perturbation according to eq. 10.2. Since gas spiral arms excite dust particles by kicking them every passage, the higher is the perturbation, the stronger is the kick, and so the excitation. Second, in gravito-turbulent regime, transport of angular momentum is driven by the spiral perturbation, and it is possible to define an $\alpha-$viscosity coefficient related to the cooling rate (eq. 3.78). The height of a dust layer is determined by the interaction with the gas and by the vertical diffusion. In the hypothesis that the vertical diffusion coefficient is equal to the azimuthal one, we can obtain the height of the dust layer as

$$H_d = H_g \sqrt{\frac{\alpha}{\alpha + \mathrm{St}}}. \tag{10.4}$$

If we assume that $\alpha = \alpha_{\rm GI}$, the dust layer height, and thus the dust dispersion velocity, is inversely proportional to $\beta_{\rm cool}$.

Figure 10.8 compares the relative temperature distributions of large and small dust particles. Small particles are colder than the large ones, and their relative temperature is almost completely enclosed in the interval $\xi_{\rm small} \in [10^{-2}, 1]$, meaning that their random motions are subsonic. On average, the distribution of $\xi_{\rm small}$ is shifted by one order of magnitude compared to $\xi_{\rm large}$. This behaviour is in agreement with what Booth & Clarke (2016) found: larger particles tend to be dynamically hotter, because the kicks of the gas spiral are more effective, while if the coupling with the gas is stronger, the kicks are damped because of the drag force.

In principle, the observed trend would imply that increasing $\beta_{\rm cool}$ would lead to an arbitrarily thin dust layer, eventually causing gravitational collapse. This would be a direct analogue of the classical Goldreich & Ward (1973) mechanism for planetesimal formation in a (weakly) self-gravitating context, and in a more realistic model it likely be limited in a similar way by the excitation of shear turbulence (Cuzzi et al. 1993). However, there is an upper limit for $\beta_{\rm cool}$ set by the value above which the transfer of angular momentum would be driven by some process other than gravitational instability. To compute an estimate of the maximum cooling time, we require $\alpha_{\rm GI}$ to be larger than 10^{-3}. Observations of protoplanetary discs that are not expected to be self-gravitating suggest that this is a reasonable upper limit to the strength of turbulence (Flaherty et al. 2017). Thus, we obtain

$$\beta_{\rm cool}^{\rm max} = 400 \left(\frac{\alpha}{10^{-3}} \right)^{-1}, \tag{10.5}$$

Table 10.2: Table that summarizes the correlations between ϵ, ξ and $\beta_{\rm cool}$, $M_d/M_\star$ and St.

	$\beta_{\rm cool}$	$M_d/M_\star$	St
ϵ	Positive	None	Negative
ξ	Negative	Negative	Positive

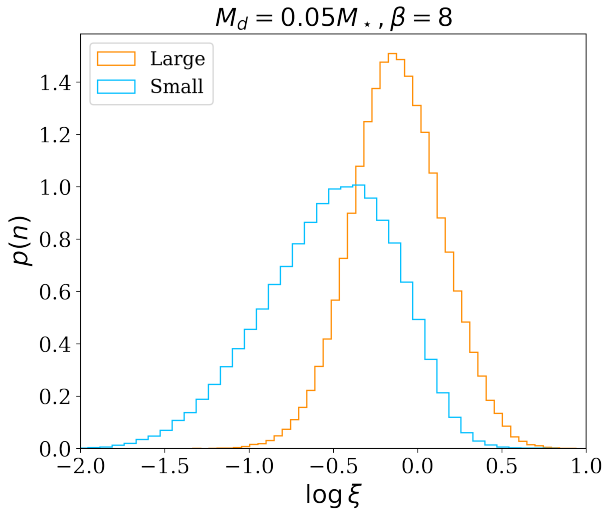

Figure 10.8: Comparison of the distribution of relative temperature of large (orange line) and small (blue line) dust particles. The simulations shown in this plot are **S1** and **S4**.

that corresponds to a minimum density perturbation

$$\left.\frac{\delta\Sigma_g}{\Sigma_{g0}}\right|_{\rm min} = 0.05\left(\frac{\alpha}{10^{-3}}\right)^{1/2}. \tag{10.6}$$

Table 10.2 summarizes the relationships we have discussed in these paragraphs.

Booth & Clarke (2016) studied the relationship between the dust excitation and both the cooling and the Stokes number. They found that $c_d \propto \beta^{-1/2}{\rm St}^{1/2}v_k$, where v_k is the Keplerian speed. To compare with Booth & Clarke (2016), we use our data to reproduce Figures **7** and **13** of their paper, that show a relationship between the dust velocity dispersion and $\beta_{\rm cool}$ and St. To do so, we divided the particles into equally spaced intervals of Stokes number and, for each particle, we computed the mean value of $c_d/c_g = \sqrt{\xi}$. The comparison is shown in Figure 10.9, where we show the results of simulations with $M_d/M_\star = 0.05$, for both standard and high resolution cases. The previously derived relationships with the Stokes number (the left panel) and with the cooling factor (the right panel) are well recovered. Using our two fluid algorithm, it is too computationally expensive to analyse properly the case of ${\rm St} < 1$. However, in this case we expect that as the aerodynamical coupling with the gas is stronger, c_d/c_g should increase, eventually reaching $c_d = c_g$ for ${\rm St} \to 0$. This growth for ${\rm St} < 1$ has been shown by Booth & Clarke (2016).

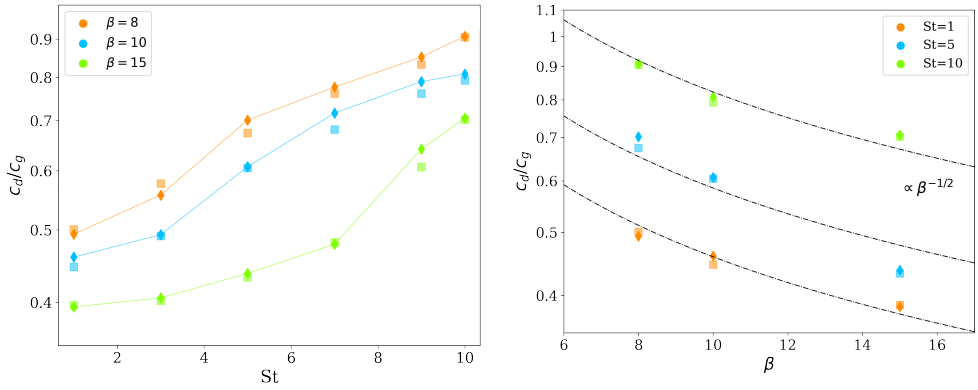

Figure 10.9: Comparison with Booth & Clarke (2016). The left panel shows how dust dispersion velocity depends on the Stokes number, for different values of cooling factor. The right panel, shows how dust dispersion velocity depends on the cooling factor, for different values of Stokes number, compared to the expected relationship $\propto \beta_{\rm cool}^{-1/2}$. All the simulations shown in these plots have $M_d/M_\star = 0.05$. The diamonds are the values obtained from the standard resolution simulations, while the squares from the high resolution ones.

10.2.3 Two fluid instability

In this section, we apply the two fluid instability theory presented in Chapter 9. The gas-only and gas-and-dust models for gravitational instability have both been developed within a linear framework; hence, in principle, the quantities ϵ, ξ and St should be evaluated in the unperturbed state. However, in this work, we are evaluating them in the perturbed one. Although not completely self-consistent, it gives us an idea of the most unstable regions of the disc. Figure 10.10 shows the distribution of large (blue) and small (orange) dust particles in the (ξ, ϵ) diagram: the black lines corresponds to the dust driven GI threshold for $\mathrm{St} = \infty$ (solid line) and for $\mathrm{St} = 0.5$ (dashed line), using eq. (9.13). We choose $\mathrm{St} = 0.5$ as a minimum value since the number of particles with Stokes number lower than this is negligible. The particles above the region are in a dust driven GI regime. We find that the number of small particles for which the instability is dust driven is greater compared to large ones: this is because small particles have both larger dust to gas ratio and lower dispersion velocity. In addition, the number of dust driven particles increases with the cooling factor and with the disc to star mass ratio, as already discussed in previous sections. To understand the spatial location of these particles in the disc, Figure 10.11 shows the particles that satisfy condition $\epsilon > \sqrt{\xi}$ superimposed on the total density map. As expected, the most unstable regions of the disc are not randomly distributed, but correspond with the spiral arms.

Figure 10.12 shows the value of the Jeans mass for $M_d/M_\star = 0.05$ as a function of the Stokes number. The Jeans mass has been computed from the two component fluid model with drag force, as shwon in Chapter 9.

The curve can be divided into two parts: for $\mathrm{St} \in (0, 5)$, the Jeans mass is decreasing with the Stokes number, reaching its minimum at about $\mathrm{St} \sim 3$. This happens because for $\mathrm{St} \to 0$, the particles are indistinguishable, and the instability is gas driven. It is important to notice that the number of particles with small Stokes number is low, hence the binning in Stokes number presents a considerable scatter. By increasing the Stokes number, ξ decreases and the two fluids behave more and more differently. When the

Stokes number is approximately 1, the relative temperature is a minimum and the dust to gas ratio is high, so the instability becomes dust driven. Otherwise, for St > 5, the Jeans mass increases with the Stokes number. Indeed, the relative temperature increases, and the dust to gas ratio decreases. Hence, the system transitions from dust into gas driven instability, again, eventually reaching the gas-only component model value.

10.3 Discussion

10.3.1 Dust collapse

The simulations with $M_d/M_\star = 0.2$ and small dust particles do not reach 5 outer orbits, since the simulation stops due to the onset of dust collapse. This happens because the stopping time of collapsing dust particles becomes smaller than the time step of the code. Indeed, the stopping time is inversely proportional to the total density $\rho_{\text{tot}} = \rho_g + \rho_d$, and since the dust density is increasing, because of the collapse, the stopping time tends to zero. The top panel of Figure 10.13 shows the maximum dust density as a function of time for small and large dust particles, in the run with $M_d/M_\star = 0.2$ and $\beta = 15$. While large dust particles reach a quasi-steady state, the small particle density exponentially increases in the first orbit. This is the signature of dust collapse. This phenomenon is visible in simulations **S16**, **S17** and **S18**, and happens only in the dust component. The bottom panel of Figure 10.13 shows a comparison between gas and small dust averaged density as a function of time, for $M_d/M_\star = 0.2$ and $\beta = 15$. At $t = 0$, $\langle\rho_d\rangle = 10^{-2}\langle\rho_g\rangle$. Whereas the gas average density is constant with time, the dust density increases because of dust trapping, eventually exceeding that of the gas. This means that any clumps forming from this mechanism would be substantially made up of solids, and would likely be identified with the rocky core of a giant planet. However, in this work we do not want to characterize the outcome of this collapse, which is a complex topic. Indeed, simulations of planetesimal collapse (Nesvorný et al. 2021) show that a rotating self-gravitating cloud of dust does not monolithically collapse, meaning that it is not possible to directly equate the cloud mass with the planetary core one.

To identify and analyse dust clumps in more detail, we define the numerical conditions that should be respected for a clump to be physical and not affected by resolution. For a clump radius r_{clump} the smoothing length of the dust particle h_i should be less than a fraction of the clump radius, in order to be resolved. This condition translates into $h_i < \eta r_{\text{clump}}$, where η is less than unity. We take $\eta = 1/2$. Physically, a gravitationally bound clump is a collection of particles whose thermal support does not balance the gravitational one. We define the thermal and gravitational energy of particles inside r_{clump} as follows:

$$e_{\text{th}} = \sum_{i}^{i\in r_{\text{clump}}} m_i c_i^2, \tag{10.7}$$

$$e_{\text{gr}} = -\frac{1}{2}\sum_{i}^{i\in r_{\text{clump}}}\sum_{j=i}^{j\in r_{\text{clump}}} m_i m_j[\varphi(r_{ij}, h_i) + \varphi(r_{ij}, h_j)], \tag{10.8}$$

where φ is the gravitational softening kernel and $r_{ij} = |\mathbf{r}_i - \mathbf{r}_j|$. We used a cubic spline softening kernel, and the detailed expression can be found in the appendix of Price & Monaghan (2007). According to the virial theorem, if the force between any two particles can be described in terms of a potential energy $\Phi \propto r^n$, where r is the distance between

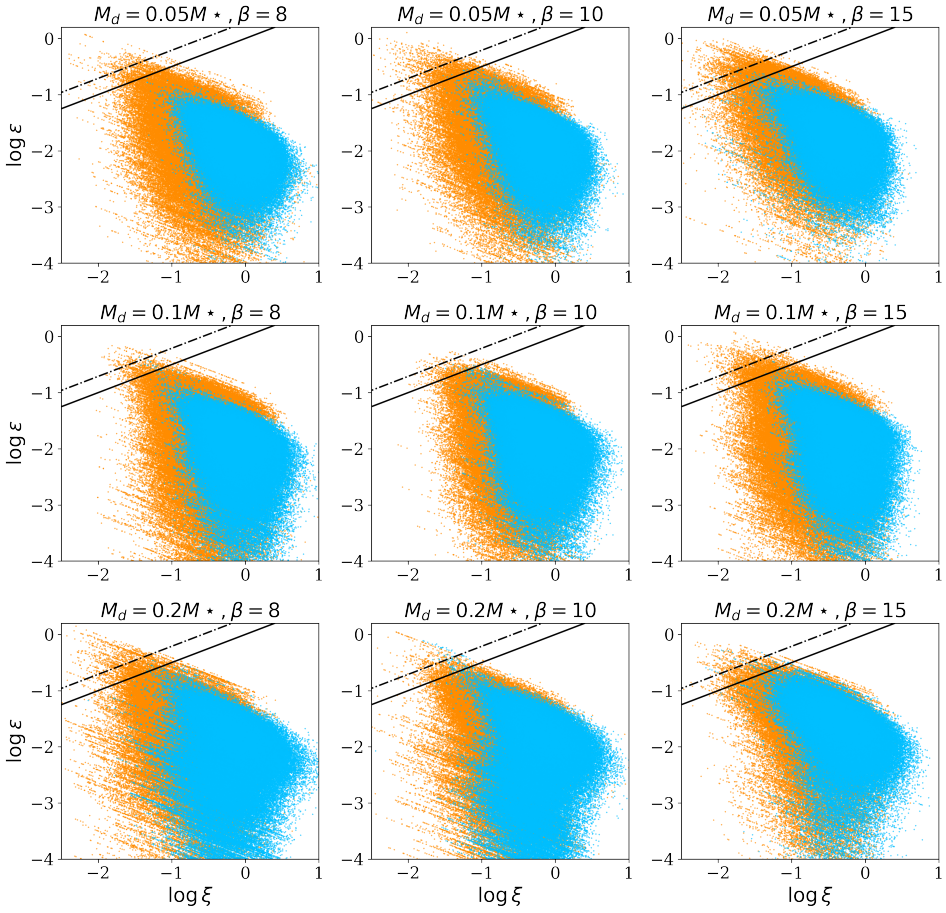

Figure 10.10: Distribution of large (blue) and small (orange) dust particles in the (ϵ, ξ) diagram, for different values of disc-to-star mass ratio and cooling factor. The black lines corresponds to the dust driven GI threshold for St $= \infty$ (solid line) and for St $= 0.5$ (dashed line), using eq. (9.13). We choose St $= 0.5$ as a minimum value since the number of particles with Stokes number lower than this is negligible. The particles above the region are in a dust driven GI regime.

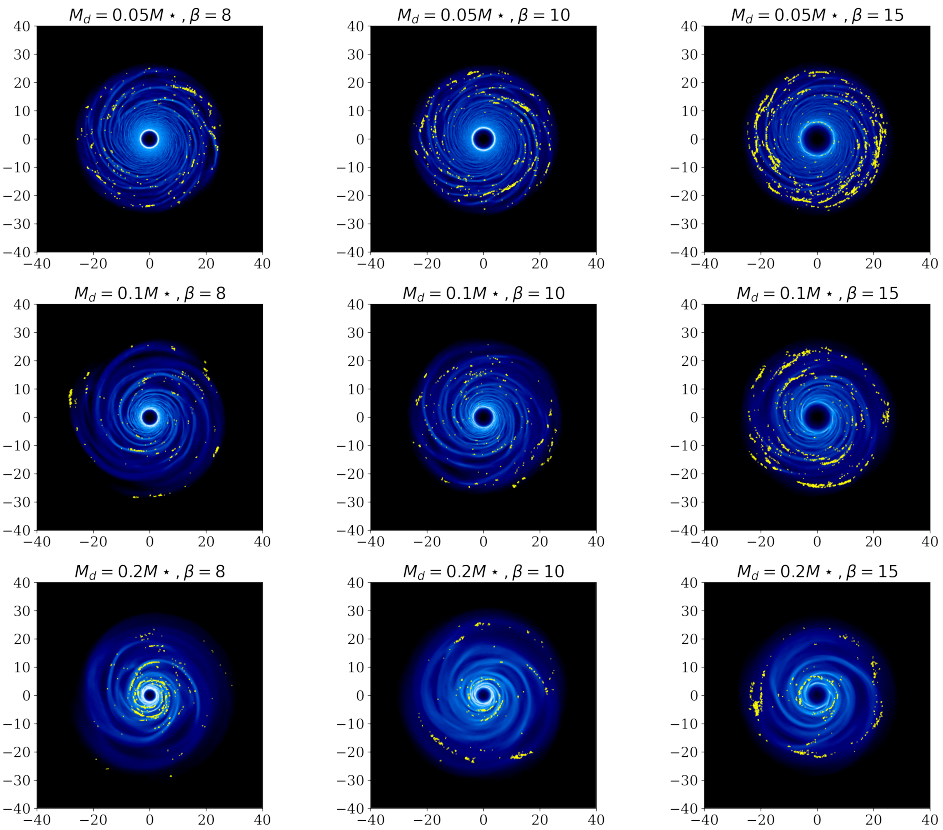

Figure 10.11: Total density maps for small dust particles simulations (**S4,S5,S6,S10,S11,S12,S16,S17,S18** in order). Yellow dots correspond to particles for which the instability is dust driven.

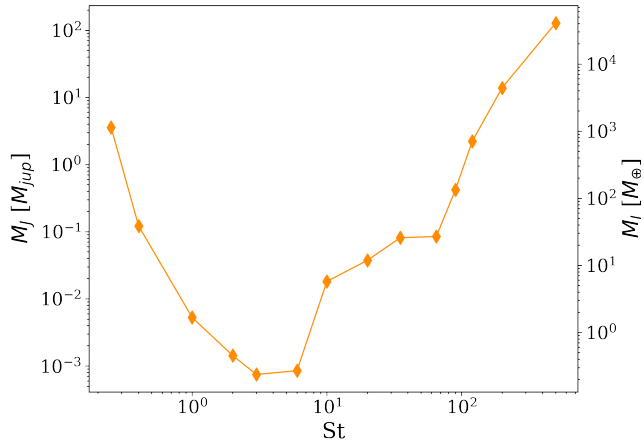

Figure 10.12: Jeans mass evaluated at each dust particle location as a function of the Stokes number, for $M_d/M_\star = 0.05$ and $\beta_{\rm cool} = 8$.

Table 10.3: Comparison between the expected and the observed Jeans Mass in the simulations where dust collapse happens.

#	**Expected M_J [$M_\oplus$]**	**Simulation [$M_\oplus$]**
S16	2	0.6
S17	2.2	1.
S18	4.5	3.2

two particles, the equilibrium state respects the following condition

$$2\langle T\rangle = n\langle\Phi\rangle, \tag{10.9}$$

where T is the kinetic energy. In the case of gravitational interaction, the virial theorem reads $\langle T\rangle/\langle\Phi\rangle = -1/2$. We define a clump as a region of the space where the dimensionless quantity $\alpha_J = -e_{\rm th}/e_{\rm gr} < 1/2$. Then, in order to be sure that the collapse is physical, and not artificial, we verify that $h_g < h_d$ in the region where there is the dust clump. The last condition requires that the resolution of the gas in the region where there is a possible clump should be higher compared to the dust resolution.

To summarize, the conditions under which we define a dust clump are the following

- $h_{g,i} \leq h_{d,i}$,
- $h_{d,i} < \eta r_{\rm clump}$,
- $\alpha_J < 1/2$.

In simulations **S16**, **S17** and **S18** there are particles that respect the previous conditions, implying that dust collapse has happened. Table 10.3 shows the mass of the clumps, obtained by summing the mass of each particle that is gravitationally bound and the one obtained from analytical theory of Longarini et al. (2023a). The masses are broadly in agreement with analytic expectations. For **S16**, for example, the derived Jeans

Table 10.4: Stopping, dynamical and free fall timescales for the simulations that show dust collapse

#	t_s [yr]	$t_{\rm dyn}$ [yr]	$t_{\rm ff}$ [yr]	$t_s/t_{\rm dyn}$	$t_s/t_{\rm ff}$
S16	2.7	7.9	0.4	0.3	6
S17	5.6	14.1	0.7	0.4	8
S18	7.2	17.7	1.6	0.4	4

mass is of the order of an Earth mass. In general, the mass of the clump computed from the simulation is smaller compared to the one expected from the analytical theory: this is not surprising, since with the simulation we are only able to appreciate the initial phase of the collapse. Indeed, as soon as the stopping time is smaller than the time step, the simulation stops. To avoid this problem, one could decrease the time step of the code, but it is computationally expensive. Otherwise, one could not consider the dust density when computing the stopping time: this procedure has been applied in previous works to increase the velocity of the simulations (Poblete et al. 2019; Longarini et al. 2021a) but this approximation is valid only for small dust to gas ratios. While there this was justified, here this is not possible, since dust is collapsing and the dust to gas ratio becomes higher than unity. Finally, to study the early evolution of clumps with an SPH code, it would be possible to simulate them as sink particles: so far, the creation of dust sink particles is not possible in PHANTOM.

Gas-dust coupling during the collapse

The bottom panel of Figure 10.13 shows that the collapse happens only in the dust component, and the gas is not influenced. This could sound surprising: indeed, in high density regions, we expect the stopping time to be small. So, why is the dust collapse not influencing the gas? The degree of coupling is measured with the Stokes number, that compares the strength of the drag force with the ones that are acting on the particle. Usually, in a flat protoplanetary disc, the Stokes number is computed as the ratio of the stopping time and the dynamical time, that is the typical timescale of a particle orbiting around a central object at a distance R. However, in this situation, the dust clump is driving the dynamics of the surrounding particles, and hence we should compare the stopping time with the free fall time in order to understand the degree of coupling of particles. The typical timescale of the infall of a spherically-symmetric distribution of mass is

$$t_{\rm ff} = \sqrt{\frac{3\pi}{32G\rho}}. \tag{10.10}$$

Comparing the stopping time and the free fall time in the simulations where dust collapse is happening (Table 10.4), we obtain that the particles in the collapsing region are uncoupled, since the ratio between the two timescales is higher than one.

It is possible to quantify the critical density a clump should reach so that $t_{\rm ff} < t_{\rm dyn}$, that is

$$\rho_{\rm crit} = \frac{3\pi}{32}\frac{M_\star}{R^3}\ : \tag{10.11}$$

when a clump reaches this density, the evolution of the surrounding particles is determined by the clump, and not by the star anymore. From that point, the aerodynamical coupling should be quantified by taking the ratio between the stopping time and the free fall time. Hence, for $\rho < \rho_{\rm crit}$, ${\rm St} \propto \rho^{-1}$, since the dynamical time does not depend on the

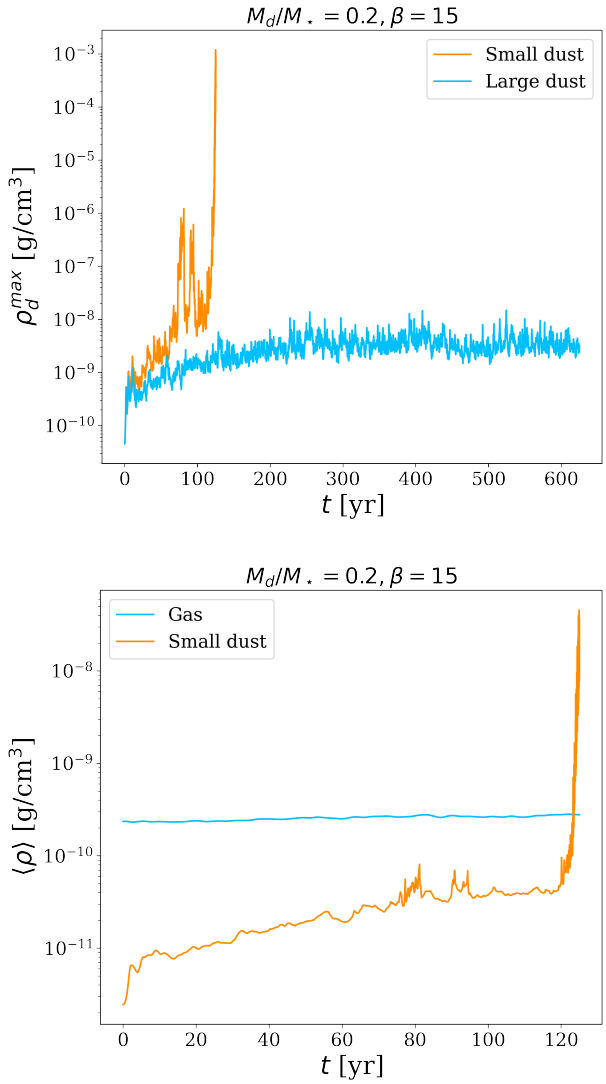

Figure 10.13: Maximum dust density as a function of time for simulations S15 ($M_d/M_\star = 0.2, \beta = 15$, large dust particles, blue line) and S18 ($M_d/M_\star = 0.2, \beta = 15$, small dust particles, blue line).

density. For $\rho > \rho_{\rm crit}$, the scaling changes since the free fall time depends on the density St $\propto \rho^{-1/2}$, and so does the degree of coupling.

10.3.2 Gravitational instability in the context of protoplanetary disc evolution

In this work, we focused on cooling driven GI, but it is also possible to trigger it through infall. Kratter et al. (2008) found that in the infall-driven case the strength of the spiral perturbation is controlled by two dimensionless parameters, a thermal one, that relates the infall mass accretion rate $\dot{M}_{\rm inf}$ to the characteristic sound speed of the disc, and a rotational one, that compares the relative strength of rotation and gravity in the core. Obviously, the higher the accretion rate, the stronger is the spiral perturbation in the disc. We can naively associate the dust evolution we have modelled in the limit of fast (slow) cooling with high (low) infall rate. This association is expected to be qualitatively correct, however a detailed comparison between these two regimes is given by Kratter & Lodato (2016).

By studying the non-linear evolution of gas and dust in protoplanetary discs, we found that the instability conditions for the two components are different. It is well established that spiral fragmentation occurs in fast cooling gas discs, and it is possible to define a critical value of $\beta_{\rm cool}$ below which fragmentation occurs. Simulations of cooling-driven fragmentation (Gammie 2001; Rice et al. 2005; Lodato & Clarke 2011; Meru & Bate 2012) currently suggest that $\beta_{\rm min} \simeq 3$ (Deng et al. 2017). For the dust, Booth & Clarke (2016) found that dust becomes more unstable for higher $\beta_{\rm cool}$, and we confirm this trend with 3D simulations. The differing behaviour of gas and dust suggests an interesting evolution in the outcome of gravitational instability within protoplanetary discs. During a first stage, at the beginning of the disc lifetime, we expect a very massive disc system characterized by strong GI, caused by the high infall rate from the molecular cloud. If conditions allow gas fragmentation, because of the high Jeans mass, low mass stellar companions can be formed (Kratter et al. 2008). A second stage is characterized by a less massive disc, with lower infall rate, or equivalently longer cooling time. If conditions during this epoch trigger gravitational instability, it will lead to *dust-driven* fragmentation that could be responsible for the formation of rocky cores of giant planets. Then, in the third stage, there is a protostar surrounded by a planet hosting disc, characterized by substructures such as gaps, rings or planetary spirals. In this stage, GI is not effective anymore because the disc mass is small and the transport of angular momentum is controlled by disc winds (Tabone et al. 2022) or other, non-self-gravitating, sources of turbulence (Lesur et al. 2022). A schematic view of these stages is given by figure 10.14.

10.3.3 Application to an actual case: HL Tau

HL Tau is a young (< 1Myr) protostellar system that shows axisymmetric structures (gaps and rings) in dust continuum emission (ALMA Partnership et al. 2015). The origin of rings and gaps is usually attributed to planet disc interaction (Lin & Papaloizou 1986), with Dipierro et al. (2015b) finding that three protoplanets with masses $M_{p1} = 61 M_\oplus$, $M_{p2} = 83 M_\oplus$, $M_{p3} = 170 M_\oplus$ at $R_{p1} = 13.2$au, $R_{p2} = 32.3$au and $R_{p3} = 68.8$au best match the observations. The formation of super-Earth mass planets at large radii, in such a young system, is a challenge for core accretion theory. If planets can form via the dust-induced collapse mechanism we have discussed in this work, HL Tau is a plausible example of what the resulting planetary system might look like. We note that the inferred trend of increasing mass with radius can be interpreted within our model. In a simplistic

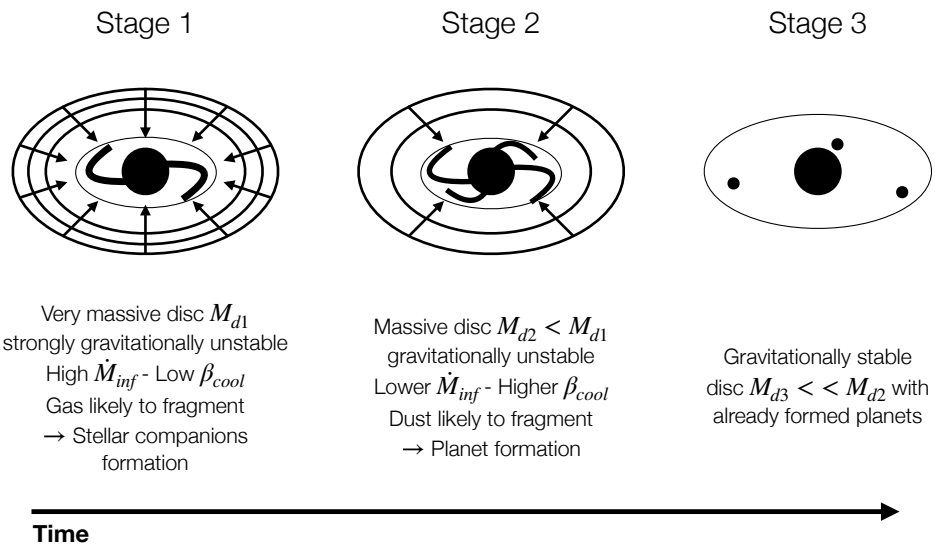

Figure 10.14: Scheme of the three stages of disc lifetime

way, we assume that $\mathrm{St} \propto \Sigma^{-1} \propto R$, and that $\xi \propto \beta_{\mathrm{cool}}^{-1}\mathrm{St} \propto R^{4.5}R = R^{5.5}$, where we have supposed a realistic cooling law, according to which $\beta_{\mathrm{cool}} \propto R^{-4.5}$ (Rafikov 2009; Clarke 2009). Supposing that the dust to gas ratio is constant, the Jeans mass of the gas-and-dust fluid model will be an increasing function of the radius, since the relative temperature is smaller for particles closer to the central star. So, within this hypothesis, we expect that the mass of the dust driven GI protoplanets will be an increasing function of the radius. We want to point out that this is just a qualitative argument. Indeed, to thoroughly investigate whether HL Tau planets can be formed through dust driven GI, one should properly model the system. In addition, planet migration and planet accretion should also be considered.

10.4 Conclusions

Self-gravitating gas discs may be ubiquitous during the Class 0/I phases of YSO evolution. Observations suggest that the self-gravity can in some systems be strong enough as to trigger fragmentation (Tobin et al. 2016), while in other cases, such as the massive disc of the more evolved IM Lup system (Lodato et al. 2023) the instability is expected to be more gentle. If that fragmentation occurs in the gas, as in the L1448 IRS3B system, the outcome is typically star or brown dwarf formation. Lower mass objects can be formed if the fragmenting fluid is instead the solid component of a two-fluid self-gravitating disc, given disc conditions that allows the collisional growth of dust to small macroscopic dimensions while the disc remains self-gravitating. Analytic estimates suggest that planetary cores of $\sim 1 - 10\ M_{\oplus}$ could form from this mechanism at large orbital radius, with properties that could be identified with the population of ALMA-inferred disc-embedded planets (Andrews 2020).

In this paper, we presented the results of SPH simulations of gas and dust in protoplanetary discs, studying the role of aerodynamic coupling in the context of gravitational

instability. We analysed our results in the framework of two fluid gravitational instability, and compared our findings with previous numerical works, finding generally good agreement.

Our main results can be summarized as follows:

1. We studied the relationship between the dust to gas ratio ϵ, the relative temperature between gas and dust ξ and the cooling factor $\beta_{\rm cool}$, the disc to star mass ratio and the Stokes number. We found that the dust to gas ratio increases with the cooling factor and decreases with the Stokes number, and that the relative temperature increases with the Stokes number and decreases with the cooling factor and the disc to star mass ratio. It is possible to explain these relationships by considering the interaction between dust particles and gas spiral arms. We compared our findings with Booth & Clarke (2016) and found good agreement.

2. We investigated the role of dust in gravitational instability, and found that the most unstable regions of the disc are the spiral arms, where the instability tends to be dust driven. In addition, we studied the relationship between the theoretical Jeans mass and the Stokes number. We found that the Jeans mass — when the instability is dust driven — can reach values of the order of the Earth mass.

3. We observe three cases of dust collapse in our set of simulation, which occur (as expected) in the high disc mass models. The values of the clump masses obtained numerically are close to those predicted by linear theory.

In applying our results to the possibility of early planet formation in Class $0/{\rm I}$ discs, the main prerequisite is the requirement that dust is able to grow via coagulation to a large enough Stokes number, with a top-heavy particle mass function, in a short enough time. Our simulations that explicitly exhibited dust collapse had solid particles with an average Stokes number $\langle {\rm St} \rangle = 16$, which would correspond (rescaling our simulations to a disc size of $R_{\rm out} = 250$au) to particles with sizes between a few cm and a few metres. Fragmentation and radial drift pose barriers to growth to the required sizes (Birnstiel et al. 2016), and further work is needed to assess whether there are circumstances where the required Stokes numbers can be reached. Simulations with a constant Stokes number, along with runs with ${\rm St} \sim 1$ (a regime which is numerically difficult to access using our code), would also help to better define the regime where dust can fragment in a gas disc that is itself stable against fragmentation.

In an evolutionary context, our results imply that planet formation — if it is able to occur via the mechanism of dust-dominated gravitational disc instability — is likely to occur toward the end of the self-gravitating phase. This is when the competing effects of particle trapping and particle excitation are jointly most favourable for collapse. The masses and orbital radii of the planets formed via dust collapse are qualitatively in agreement with those inferred for the HL Tau system, and we speculate that they may form from the collapse of solids in the spiral arms of a formerly self-gravitating protostellar disc.

CHAPTER 11

Conclusions and future directions

In this thesis, I explored the role of self-gravity and gravitational instability on the evolution of protostellar discs and planet formation. There is a growing evidence suggesting that planet formation is already underway in young systems, particularly when the disc exhibits significant mass, and self-gravity plays a crucial role in its dynamics. Consequently, understanding the effects of self-gravity on the evolution of these systems is essential to develop a comprehensive view of the planet formation process. Historically, gravitational instability has lost favour as a planet-forming scenario, primarily due to the higher likelihood of forming stellar companions rather than planets. However, in this thesis, we consider the synergy between gravitational instability and dust dynamics, opening new pathways for forming planets in young protostellar stages.

The two macro topics of this dissertation aim at characterizing (i) gas kinematics and (ii) dust dynamics in self gravitating discs. The first part builds a bridge between theory and observations, describing the expected effects of self-gravity and gravitational instability on molecular line emission, and then applying these results to actual cases. The second part, instead, is focussed on the theoretical side, analytically and numerically modelling the dynamics of solid particles in young protoplanetary discs. The main results of this work can be summarized as follows

- **Investigating the kinematic signatures of gravitational instability.**

  The outcome of gravitational instability is the formation of a large scale spiral structure that shapes the density field of the protostellar disc. In addition to the density, also the velocity field is influenced by the spiral, displaying a discernible perturbed pattern on a global scale. These kinematic signatures are visible in molecular line emission of CO isotopolgues, and they are called "GI Wiggles" (Hall et al. 2020). My contribution to this topic involves analytically deriving the velocity perturbations, as presented in chapter 6. I carried out a first order perturbation analysis to the fluid equations, and I found that for a gravitationally unstable disc in thermal saturation regime, the kinematic deviations depend on the structure of the spiral density wave, namely its amplitude (connected to the cooling and to the disc mass) and its radial frequency (connected to the pitch angle and to the azimuthal wavenumber). Measuring the amplitude of the GI Wiggle offers an incredible opportunity to quantify the cooling time, that is crucial in determining the amount of angular momentum transported by gravitational instability.

- **Quantifying the amount of angular momentum transport in a gravitational unstable disc: Elias 2-27.**

  There is convincing evidence that the protoplanetary disc Elias 2-27 is gravitationally unstable. In addition to two large scale spiral arms in dust continuum emission

(Pérez et al. 2016), it shows global kinematic perturbations (Paneque-Carreño et al. 2021). In the work presented in chapter 8, I verified that the shape of the velocity perturbations is compatible with the GI predictions, displaying a shift with the density spiral. Then, relying on the knowledge of the disc mass (Veronesi et al. 2021), I constrained the cooling factor of the system through the amplitude of the GI wiggle. I found a value of $\beta = 10.5$, corresponding to an effective $\alpha-$viscosity of 0.046. Assuming the self-similarity solution for the surface density of the disc, I computed the expected accretion rate, that is in good agreement with the observed one.

- **Measuring the self gravitating contribution to the rotation curve through high resolution kinematic observations.**

  When a disc is massive enough, its gravitational potential contributes to the gas rotation curve, making it super-Keplerian. High resolution ALMA observation are able to probe this effect, as shown in Veronesi et al. (2021) and Lodato et al. (2023). Measuring the self gravitating contribution to the rotation curve provides an effective way to determine the disc mass. This method does not rely on tracers-to-H_2 ratios, giving an accurate estimate of this quantity. In chapter 7 I benchmark this method with hydrodynamical and radiative transfer simulations. The minimum mass that is measurable through this approach is 5% of the star mass, with an uncertainty of about 25%. Afterwards, I relax the hypothesis of vertical isothermal disc, studying how the rotation curves changes when thermal stratification is taken into account, and I apply the new model to the MAPS sample. I show that the quality of the fit significantly increases when thermal stratification is included.

- **Investigating the dynamical role of dust in the gravitational stability of a protoplanetary disc.**

  In the context of galactic dynamics, it is well established since the '80s that the gravitational stability of a multi-fluid system can be substantially different from the one-fluid case (Kwok 1975; Jog & Solomon 1984; Bertin & Romeo 1988). In particular, the presence of a second cold component can drive gravitational instability at short wavelengths, characterized by a higher value of the critical Toomre parameter Q. In the context of galactic dynamics, this becomes important when considering the galactic fluid composed of stars and gas, where the gas is the second "cold" component, according to its lower dispersion velocity. In chapter 9 I adapt this framework to protoplanetary discs, where the two components are gas and dust. In particular, the gas is the most abundant and hot component, while the dust is less abundant and cold. Additionally, I generalize the galactic model by including the aerodynamical interaction between the two components, fundamental in protostellar discs, while negligible in galactic ones. I obtain the dispersion relation for such system, and I find that the stability threshold is determined by three parameters: the local dust-to-gas density ratio, the dust relative temperature and the Stokes number. In a region of parameters space, where young protoplanetary discs are likely to be found, the instability can be driven by dust, occurring at small wavelengths. In this regime, the Jeans mass is much smaller than the one predicted by the standard gravitational instability model, being of the order of $\sim 10 M_\oplus$. This mechanism can be a viable way to form planetary cores in young protostellar discs.

- **Assessing the viability to form planetary cores in young protostellar discs through dust collapse.**

Gas spiral arms effectively collect dust inside them (Dipierro et al. 2014), reaching concentrations for which the influence of dust self-gravity becomes significant. Young protostellar discs are likely to be both self-gravitating, and to support grain growth to sizes where the particles are marginally coupled with the gas, suggesting that dust trapping is likely at its peak. Concurrently, gas spiral arms have the capacity to excite solid particles, inducing a "kicking" effect during each interaction. The potential for dust to undergo gravitational collapse within spiral arms, giving rise to planetary cores, depends on the interplay between these two effects. In chapter 10, I use three-dimensional smoothed particle hydrodynamics simulations of two-fluid discs, focussing on the regime where the Stokes number of the particles St $\gtrsim 1$. The aim is to study the interplay between dust concentration and dust excitation, and understand how the formation of solid clumps depends on the disc to star mass ratio, the strength of gravitational instability (i.e. cooling time), and the Stokes number. I find that the ability of the spiral structures to concentrate solids increases with the cooling time, and decreases with the Stokes number, while the relative dynamical temperature between gas and dust of the particles decreases with the cooling time and the disc-to-star mass ratio, and increases with the Stokes number. I observe dust collapse in a subset of our simulations, yielding clumps whose mass is close to linear theory estimates, namely $1 - 10 M_\oplus$. Our results suggest that if planet formation occurs via this mechanism, the best conditions correspond to near the end of the self-gravitating phase, when the cooling time is long and the Stokes number close to unity. If these planetary cores are able to survive in such environments, they could form giant planets in the outer disc, serving as the embryos of class II protoplanets.

To summarize, taking into account the role of the disc self-gravity in young protoplanetary discs is crucial to understand the long term evolution of such systems and planet formation. Self-gravity is a powerful way to measure the disc mass, with the lowest number of assumptions, yielding accurate results. In addition, characterizing gravitational instability in protoplanetary discs offers a unique way to investigate fundamental questions in accretion disc theory, such as the amount of angular momentum transported within it. Finally, accounting for the dynamical role of dust in gravitationally unstable discs is of paramount importance. The physical conditions within these discs can lead to the gravitational collapse of the dust component, potentially forming the embryos of class II planets.

Future perspectives

Starting from the work presented in this thesis, I have identified several perspectives that I would like to address in the future. These developments are divided into two parts, the first one is related to gas kinematics and the second one to dust dynamics.

Gas kinematics

- **Kinematic signatures of the interaction between disc and environment:**

  In chapter 6 I investigated the kinematics of young protostellar discs, focussing my attention on the signatures generated by gravitational instability. However, young systems are strongly influenced by the environment, through infall from the molecular cloud or dynamical interactions with nearby protostars. These interactions shape the discs, determining their morphology and characteristics. While

gas dynamics is well understood in such environments (Kratter & Matzner 2006; Kratter et al. 2010; Cuello et al. 2023), a comprehensive study of gas kinematics is still lacking. A possible direction to follow is to characterize kinematic signatures of flybys, binary disc interaction and infall. Since for these phenomena an analytical derivation of the velocity field is not feasible, I intend to perform numerical simulations and then post process them with radiative transfer codes, to assess the nature of the kinematic signatures and their observability.

- **Investigate thermal stratification in gravitationally unstable discs:**

  The topic of thermal stratification in gravitationally unstable discs has never been explored so far. Currently, hydrodynamical simulations of gravitationally unstable discs use cooling prescriptions to trigger GI, and hence they are not suitable to study the thermal stratification. As a matter of fact, by imposing a cooling prescription, the disc is forced to behave as vertically isothermal. A possible path to follow in this context would be to couple a radiative transfer code to the hydrodynamical simulation, to compute live the temperature structure. In this way, the disc will cool due to radiative cooling, triggering gravitational instability without imposing any cooling prescription. In such a system, it is possible to investigate whether GI discs show peculiar thermal profiles. In case they are, this characteristic may be used as an observational evidence of gravitational instability. Indeed, the vertical thermal structure of protoplanetary disc can be easily probed with optically thick lines.

- **Infer the disc thermal structure from the rotation curves:**

  In chapter 7, we have shown that there are distinct kinematic signatures of thermal stratification when comparing rotation curves of multiple molecular species. So far, in our methodology we have fixed a 2D thermal structure of the disc, to correctly interpret rotation curves and determine the relevant parameters $(M_d, M_\star, R_c)$. In principle, if rotation curves from various molecular tracers or different transitions are available, it becomes viable to directly investigate the 2D thermal structure, without fixing it. The exoALMA dataset potentially offers three rotation curves (^{12}CO J=3-2, ^{13}CO J=3-2, and CS), and when combined with archival data, it provides an opportunity to evaluate the feasibility of this approach. The advantages of such method is that rotation curves of any molecular tracer can be used, without making assumptions about the optical depth. In contrast, when extracting the thermal structure channel by channel at a specific height $z = z(R)$, the emission must be optically thick.

Dust dynamics

- **Investigate the interplay between planetary accretion and migration in young protoplanetary discs:**

  In chapter 10 we showed that planetary cores can form in the outer disc from dust concentration and collapse in the spiral structure of a gravitationally unstable disc. This mechanism potentially solves the conundrum of planetesimal formation, overcoming the radial drift barrier to planet formation. However, the fate of planetary cores in massive protostellar discs has not been investigated. On one hand, a planetary object embedded into a gas disc tends to migrate towards the central object, with a rate that depends on its mass. For low mass planets, the migration timescale is very rapid (type I migration) while massive objects can open a

gap, slowing down this process (type II migration). On the other hand, the planetary core accretes disc material, potentially undergoing runaway accretion (Pollack et al. 1996) and becoming a gaseous giant. The interplay between these two mechanisms ultimately determines the fate of the planetary cores. Investigating the likelihood of a planetary core surviving in a young protostellar disc is essential to establish whether the collapse of dust in gravitationally unstable spirals is a viable way for generating the embryos of Class II ALMA planets.

In this context, a viable concept is to integrate into hydrodynamical codes, like PHANTOM, the capability to generate a sink particle originating from the dust component, a feature currently unavailable. Presently, the creation of sink particles is limited to those composed of gas, given the well-established clumping conditions (i.e., comparison between gas pressure and self-gravity). Regarding the dust, as outlined in chapter 10, we established its dispersion velocity within an SPH framework. Employing this definition enables the extension of clumping conditions to pressureless particles. Implementing this feature allows running long term simulations, investigating both the formation and the early evolution of planetary cores.

- **Study dust dynamics in thermally stratified discs:**

  As discussed in this thesis, protoplanetary discs exhibit thermal stratification. We have presented a methodology to probe the 2D thermal structure and modeling gas kinematics within such systems. However, a comprehensive model for the dynamics of dust in stratified discs is still lacking. In a study by Takeuchi & Lin (2002), the radial migration of dust particles in vertically isothermal protoplanetary discs was examined. A notable finding was that at high altitudes from the disc midplane, gas rotates faster than particles due to the inward pressure gradient force, causing particles to move outward radially. My objective is to address the issue of dust dynamics in thermally stratified discs. With the analytical model developed in chapter 7, it becomes feasible to calculate the gas velocity at any radial and vertical position in the disc, accounting for thermal stratification. Building upon this foundation, I will compute the drag force acting on dust particles and investigate their evolutionary dynamics. A semi-analytical approach is viable for this study, and I also plan to compare the obtained results with numerical simulations.

Appendices

APPENDIX A

Numerical methods: Smoothed particle hydrodynamics

A.1 Two different approaches

In astrophysics, numerical simulations are deeply exploited in order to test theoretical models, to model observed systems and to investigate physical mechanisms. As a matter of fact, most of the time is it not possible to set up a laboratory experiment and the observations are limited in space and time. Historically, two principal methodologies have been pursued in numerical hydrodynamics: the Eulerian and Lagrangian approaches.

Within the Eulerian framework, the observer tracks the evolution of fluid variables at specific points in space. Consequently, numerical Eulerian codes make use of geometric grids, which can either be fixed or adaptive. An example of an Eulerian code applied in the context of planet formation is exemplified by FARGO3D (Benítez-Llambay & Masset 2016). Conversely, the Lagrangian approach considers the evolution of the fluid variables for any given fluid element. These elements, in general, do not maintain constant positions. Hence, Lagrangian codes compute fluid properties at positions that move with the fluid's motion. A typical approach consists in using discrete particles that move with the flow, and hydrodynamic properties are evaluated at the particle positions and calculated by means of weighted averages. In this way, each particle is smoothed over a finite volume of fixed mass. From here, the name "Smoothed Particle Hydrodynamics" (SPH).

Both these approaches come with their own set of advantages and disadvantages in comparison to each other. The core distinction lies in the presence of a grid, which serves as both an asset and a drawback. On one hand, when we have prior knowledge of the problem's geometry, we can design a suitable grid that yields accurate results at a relatively low computational cost. On the other side, once the grid is chosen, it remains fixed and cannot be adjusted. This limitation can result in the grid failing to capture changes in the fluid flow. Another concern is grid resolution: once the spacing between grid cells is established, it remains unalterable. Consequently, if there are abrupt variations in fluid properties, our ability to precisely track the fluid diminishes. To address this challenge, Adaptive Mesh Refinement (AMR) techniques can be employed, though they tend to be intricate. Nevertheless, AMR codes offer superior resolution with a given number of grid cells compared to SPH codes using an equivalent number of particles. Additionally, they can be configured to adapt to diverse flow parameters, albeit with some complexity, whereas SPH primarily adapts based on density and excels in handling shocks. Conversely, SPH naturally manages vacuum boundary conditions, while AMR codes require large grids to prevent the flow from escaping the computational domain's edges, as previously mentioned. SPH, being a Lagrangian method, deals with the advection of flow properties, a task that presents challenges for AMR codes. Similarly, SPH codes can be implemented in a manner that inherently conserves mass, momentum,

angular momentum, and energy, and, unless explicitly accounted for in shocks, they also conserve entropy. In summary, we can characterize SPH and Eulerian methods as somewhat complementary; each excels in areas where the other encounters limitations.

A.1.1 Equations of hydrodynamics

The equation of hydrodynamics can be written in two different forms, Eulerian and Lagrangian. The continuity equation expresses the mass conservation, and in the Eulerian form is

$$\frac{\partial \rho}{\partial t} + \boldsymbol{\nabla} \cdot (\rho \mathbf{u}) = 0, \tag{A.1}$$

while in Lagrangian one is

$$\frac{\mathrm{D}\rho}{\mathrm{D}t} = -\rho \boldsymbol{\nabla} \cdot \mathbf{u}, \tag{A.2}$$

where $\mathrm{D}/\mathrm{D}t$ is the Lagrangian derivative

$$\frac{\mathrm{D}}{\mathrm{D}t} := \mathbf{u} \cdot \boldsymbol{\nabla} + \frac{\partial}{\partial t}. \tag{A.3}$$

The Euler equation expresses momentum conservation for an inviscid fluid, in Eulerian form is

$$\rho \left[\frac{\partial \mathbf{u}}{\partial t} + (\mathbf{u} \cdot \boldsymbol{\nabla}) \mathbf{u} \right] = -\boldsymbol{\nabla} P + \mathbf{f}, \tag{A.4}$$

where $\mathbf{f}$ is contains non fluid external forces, while in Lagrangian form is

$$\rho \frac{\mathrm{D}\mathbf{u}}{\mathrm{D}t} = \boldsymbol{\nabla} P + \mathbf{f}. \tag{A.5}$$

Finally the energy equation expresses energy conservation for a dissipationless fluid, in Eulerian form is

$$\frac{\partial e}{\partial t} + \mathbf{u} \cdot \boldsymbol{\nabla} e = -\frac{P}{\rho} \boldsymbol{\nabla} \cdot \mathbf{u} + \dot{q}, \tag{A.6}$$

where e is s the internal thermal energy and $\dot{q}$ is the external heat, while in Lagrangian form is

$$\frac{\mathrm{D}e}{\mathrm{D}t} = -\frac{P}{\rho} \boldsymbol{\nabla} \cdot \mathbf{u} + \dot{q}. \tag{A.7}$$

The meaning of the lagrangian derivative is the following. When we consider a fluid quantity in Lagrangian formalism, its temporal derivative needs to take into account the fact that the quantity at the particle location is changing because of both physical mechanisms (i.e. the density changes because a planet is perturbing it) and the fact that the particle is moving.

Now, we will focus our attention on Lagrangian SPH codes.

A.2 How to calculate density in SPH

SPH algorithms have as a starting point a fundamental question, that is *"how does one compute the density from a distribution of point mass particles?"* (Price 2012). This is a fundamental problem because, answering this question, makes us able to deal with problems coming from different field of physics, as solving the Poisson equation $\nabla^2 \Phi = 4\pi G \rho$ starting from a collection of point-like masses.

Three common approaches to compute density from an arbitrary collection of point mass particles are shown in figure A.1.

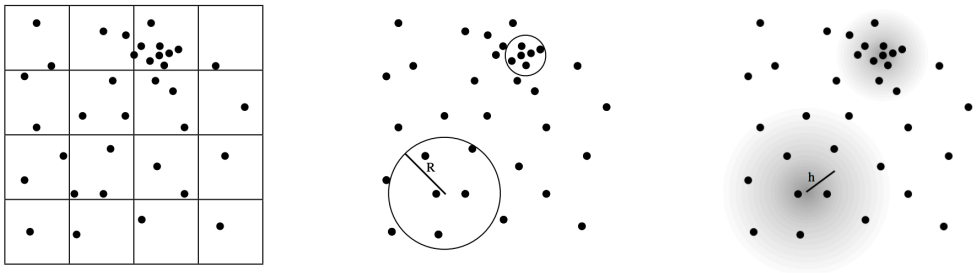

Figure A.1: Three common approaches to compute density from an arbitrary collection of point mass particles (Price 2012)

- Particle-mesh methods: the density is computed by interpolating the mass to a grid; this method tends to over/under resolve clustered/sparse regions.
- Adaptive sampling: the density is computed by constructing a volume around the sampling point, whose dimension depends on the local number density of the considered region.
- SPH approach: the density is computed by means of weighted sums over neighbouring particles, with the weight scaled according to a factor h.

We focus on the third approach, that is the basis of SPH. The density estimator in this case is

$$\rho(\mathbf{r}) = \sum_{b=1}^{N_{\text{neigh}}} m_b W\left(\mathbf{r} - \mathbf{r}_b, h\right), \tag{A.1}$$

where W is a weight function, h is a scale parameter determining the rate of decay of W, m_b is the mass of the b-th particle and $\mathbf{r}_b$ is its position. The conservation of total mass reads

$$\int_V \rho \mathrm{d}V = \sum_{b=1}^{N_{\text{neigh}}} m_b, \tag{A.2}$$

that implies the normalisation of the weight function (hereafter referred to as the smoothing kernel)

$$\int_{\mathrm{V}} W\left(\mathbf{r}' - \mathbf{r}_b, h\right) \mathrm{dV}' = 1. \tag{A.3}$$

It is clear that the accuracy of the density estimation depends on the choice of the smoothing kernel, that must have some properties

- it is positive, it decreases monotonically with distance, and it has smooth derivatives;
- it is symmetric with respect to $\mathbf{r} - \mathbf{r}'$, i.e. $W\left(\mathbf{r}' - \mathbf{r}, h\right) \equiv W\left(\left|\mathbf{r}' - \mathbf{r}\right|, h\right)$;
- it has a flat central region in which the density is not affected by a small change in position.

The most natural choice that respects all the requests is a Gaussian smoothing kernel, however it has the disadvantage of requiring interaction with all the particles in the domain, that means a big computational effort. In practise, it is useful to use a Gaussian-like kernel truncated at a finite radius; the most used smoothing kernels are the B-Spline functions (Monaghan & Lattanzio 1985) M_n. These functions give a better approximation to the Gaussian at higher n, both by increasing the radius of truncation and by increasing the smoothness.

As far as the smoothing length is concerned, it has to adapt to the local numerical density of particles, in order to resolve both sparser and denser region. Hence, it is computed as

$$h(\mathbf{r}) \propto n(\mathbf{r})^{-1/d}; \quad n(\mathbf{r}) = \sum_b W\left[\mathbf{r} - \mathbf{r}_b, h(\mathbf{r})\right], \tag{A.4}$$

with d the space dimension. Since the density is a function of the smoothing length and, in turn, the smoothing length depends on the density, at the location of particle a, we have to solve simultaneously two equations

$$\rho\left(\mathbf{r}_a\right) = \sum_b m_b W\left(\mathbf{r}_a - \mathbf{r}_b, h_a\right); \quad h\left(\mathbf{r}_a\right) = \eta\left(\frac{m_a}{\rho_a}\right)^{1/d}, \tag{A.5}$$

where η is a constant, that represents the smoothing length in unit of $(m/\rho)^{1/d}$. It is usually assumed $\eta = 1.2$.

A.3 Equations of motion

So far, we have discussed the density estimate because this is the only freedom we have if we want to obtain a fully conservative SPH algorithm. Indeed, the entire algorithm can be derived only by means of the density estimate. To implement an SPH algorithm, we must be able to calculate spatial derivatives of any given quantity. It can be shown that all derivatives of arbitrary quantities can be computed by means of the kernel derivatives. Although this argument is not needed to derive SPH equations, it is important for two main reasons: it allows us to interpret SPH equations and to study dissipative effects, that involve second derivatives. In this work, we avoid deriving the spatial derivatives, that can be found in Price (2012).

A.3.1 The discrete Lagrangian

For a system of point-like masses with velocity $\mathbf{v}$, internal energy per unit mass e and entropy per unit mass s, the discrete Lagrangian can be written as

$$L = \sum_b m_b \left[\frac{1}{2} v_b^2 - e_b\left(\rho_b, s_b\right)\right]. \tag{A.1}$$

According to the least action principle, we can derive the equations of motion, given by Euler-Lagrange equations

$$\frac{d}{dt}\left(\frac{\partial L}{\partial \mathbf{v}_a}\right) - \frac{\partial L}{\partial \mathbf{r}_a} = 0. \tag{A.2}$$

Substituting the expression of the Lagrangian, we have

$$\frac{\partial L}{\partial \mathbf{v}_a} = m_a \mathbf{v}_a; \quad \frac{\partial L}{\partial \mathbf{r}_a} = -\sum_b m_b \left.\frac{\partial e_b}{\partial \rho_b}\right|_s \frac{\partial \rho_b}{\partial \mathbf{r}_a}, \tag{A.3}$$

where to obtain the last equation, we made two important assumptions: the first one is that we derived it non considering explicitly the discrete nature of the time integral, the second one is that we assumed that the Lagrangian is differentiable, completely excluding the possibility of discontinuous solutions.

A.3.2 Thermodynamics of the fluid

To obtain an expression for the internal energy, we consider the first principle of thermodynamics

$$dE = TdS - PdV, \tag{A.4}$$

that, in unit mass, is

$$de = Tds + \frac{P}{\rho}d\rho. \tag{A.5}$$

At constant entropy, the variation of thermal energy is

$$\left.\frac{\partial e_b}{\partial \rho_b}\right|_s = \frac{P_b}{\rho_b^2}, \tag{A.6}$$

and, from the last equation, it follows that

$$\frac{de_a}{dt} = \frac{P_a}{\rho_a^2}\frac{d\rho_a}{dt}. \tag{A.7}$$

Taking the time derivative of the density, we obtain the evolution equation for e

$$\frac{de_a}{dt} = \frac{P_a}{\Omega_a \rho_a^2}\sum_b m_b \left(v_a - v_b\right)\cdot \nabla_a W_{ab}\left(h_a\right). \tag{A.8}$$

A.3.3 Density gradients

In equation (A.3) it appears the gradient of the density, that can be computed from the smoothing kernel (see Price (2012)). Its expression is

$$\frac{\partial \rho_b}{\partial \boldsymbol{r}_a} = \frac{1}{\Omega_b}\sum_c m_c \boldsymbol{\nabla}_a W_{bc}\left(h_b\right)\left(\delta_{ba} - \delta_{ca}\right), \tag{A.9}$$

where $W_{bc}(h_b) = W(\mathbf{r}_b - \mathbf{r}_c, h_b)$, ∇_a is the gradient with respect to the position of the particle a and

$$\Omega_a \equiv \left[1 - \frac{\partial h_a}{\partial \rho_a}\sum_b m_b \frac{\partial W_{ab}\left(h_a\right)}{\partial h_a}\right]. \tag{A.10}$$

A.3.4 Equations of motion

We are now able to derive the equations of motion by substituting relations (A.6) and (A.9) in (A.3)

$$\frac{\partial L}{\partial r_a} = -\sum_b m_b \frac{P_b}{\Omega_b \rho_b^2}\sum_c m_c \nabla_a W_{bc}\left(h_b\right)\left(\delta_{ba} - \delta_{ca}\right), \tag{A.11}$$

that, in a simplified form can be written as

$$\frac{d\mathbf{v}_a}{dt} = -\sum_b m_b \left[\frac{P_a}{\Omega_a \rho_a^2} \frac{\partial W_{ab}(h_a)}{\partial \mathbf{r}_a} + \frac{P_b}{\Omega_b \rho_b^2} \frac{\partial W_{ab}(h_b)}{\partial \mathbf{r}_a} \right]. \tag{A.12}$$

We underline an important result, without showing the mathematical demonstration (see Price (2012)): global quantities, as momentum, angular momentum and energy, are all simultaneously conserved. This feature derives directly from the Lagrangian nature of SPH. Since the particles move according to the Euler-Lagrange equations for the discrete Lagrangian, for every symmetry in the Lagrangian there is a corresponding conserved quantity.

Continuity equation

In order to obtain the continuity equation, we take the time derivative of the SPH density, and we obtain

$$\frac{d\rho_a}{dt} = \sum_b m_b (\mathbf{v}_a - \mathbf{v}_b) \cdot \boldsymbol{\nabla}_a W_{ab}(h_a), \tag{A.13}$$

where, for simplicity, we assumed constant smoothing length and $\Omega = 1$. Expanding the last equation, we obtain the continuity equation in Lagrangian form

$$\begin{aligned} \frac{d\rho_a}{dt} = v_a \cdot \sum_b \frac{m_b}{\rho_b} \rho_b \nabla_a W_{ab} - \sum_b \frac{m_b}{\rho_b} (\rho_b v_b) \cdot \nabla_a W_{ab} \approx \\ \approx \mathbf{v}_a \cdot \boldsymbol{\nabla}\rho - \boldsymbol{\nabla} \cdot (\rho \mathbf{v}) \approx -\rho_a (\boldsymbol{\nabla} \cdot \mathbf{v})_a. \end{aligned} \tag{A.14}$$

Thus, SPH enforces naturally the continuity equation. This is not surprising, since the continuity equation is the conservation of mass, that is fixed, because the particle masses do not change in time.

Euler equation

In order to obtain the Euler equation, we rewrite the first left side term of equation (A.12)

$$-\sum_b m_b \left(\frac{P_a}{\rho_a^2} + \frac{P_b}{\rho_b^2} \right) \boldsymbol{\nabla}_a W_{ab} \approx -\frac{P}{\rho^2} \nabla\rho - \boldsymbol{\nabla} \left(\frac{P}{\rho} \right) \approx -\frac{\boldsymbol{\nabla} P}{\rho}, \tag{A.15}$$

where we considered the smoothing length constant. As expected, we have obtained the pressure term of the Euler equation.

Energy equation

As far as the energy equation is concerned, we can substitute the continuity equation in (A.7) and get

$$\frac{de_a}{dt} = -\frac{P_a}{\rho_a} \boldsymbol{\nabla} \cdot \mathbf{u}, \tag{A.16}$$

that is the energy equation in Lagrangian form.

A.4 Focus on PHANTOM: dust and GI

The dust formulation is based on the continuum fluid equations in the form

$$\frac{\partial \rho_{\rm g}}{\partial t} + (\mathbf{v}_{\rm g} \cdot \nabla)\, \rho_{\rm g} = -\rho_{\rm g}\, (\nabla \cdot \mathbf{v}_{\rm g})\,, \tag{A.1}$$

$$\frac{\partial \rho_{\rm d}}{\partial t} + (\mathbf{v}_{\rm d} \cdot \nabla)\, \rho_{\rm d} = -\rho_{\rm d}\, (\nabla \cdot \mathbf{v}_{\rm d})\,, \tag{A.2}$$

$$\frac{\partial \mathbf{v}_{\rm g}}{\partial t} + (\mathbf{v}_{\rm g} \cdot \nabla)\, \mathbf{v}_{\rm g} = -\frac{\nabla P}{\rho_{\rm g}} + \frac{K}{\rho_{\rm g}}\, (\mathbf{v}_{\rm d} - \mathbf{v}_{\rm g})\,, \tag{A.3}$$

$$\frac{\partial \mathbf{v}_{\rm d}}{\partial t} + (\mathbf{v}_{\rm d} \cdot \nabla)\, \mathbf{v}_{\rm d} = -\frac{K}{\rho_{\rm d}}\, (\mathbf{v}_{\rm d} - \mathbf{v}_{\rm g})\,, \tag{A.4}$$

where the subscripts g and d refer to gas and dust properties. We define the stopping time, that is given by

$$t_s \equiv \frac{\rho_{\rm g}\rho_{\rm d}}{K(\rho_{\rm g} + \rho_{\rm d})}, \tag{A.5}$$

where the drag coefficient K depends on the physical drag regime the system is in. In general, it is given by

$$K = \rho_{\rm g}\rho_{\rm d}\frac{1}{2}C_{\rm D}\frac{\pi s^2}{m_{\rm d}}|\Delta v|, \tag{A.6}$$

where C_D is defined as before.

In the PHANTOM implementation, the two phases are modelled as two distinct sets of particles: hereafter, we adopt the convention of Price et al. (2018b), and refer to gas particles with the subscripts a, b, c and to dust particles with i, j, k. Gas and dust densities are computed by weighted summation over the particles of the same type according to

$$\rho_a = \sum_b m_b W_{ab}\,(h_a)\,; \quad h_a = h_{\rm fact}\left(\frac{m_a}{\rho_a}\right)^{1/3}, \tag{A.7}$$

$$\rho_i = \sum_j m_j W_{ij}\,(h_i)\,; \quad h_i = h_{\rm fact}\left(\frac{m_i}{\rho_i}\right)^{1/3}, \tag{A.8}$$

where the kernel W is the same for gas and dust, h is the smoothing length and $h_{\rm fact} = 1/2$. The drag terms of the equations of motion are discretized by using a "double hump" kernel (Laibe & Price 2012a) that, instead of the bell-shaped kernel, goes to zero at $r = 0$ and has a peak at $r/h \lesssim 1$. [1]

A.4.1 Heating and cooling

In order to take into account the effect of cooling or heating phenomena, we write the complete equation for the evolution of gas internal energy e

$$\frac{\partial e}{\partial t} + (\mathbf{v}_{\rm g} \cdot \nabla)\, e = -\frac{P}{\rho_{\rm g}}\,(\nabla \cdot \mathbf{v}_{\rm g}) + \Lambda_{\rm shock} - \frac{\Lambda_{\rm cool}}{\rho_g} + \frac{\Lambda_{\rm drag}}{\rho_g}, \tag{A.9}$$

[1] Laibe & Price (2012a) showed that using a double-hump kernel gives a factor of 10 better accuracy at no additional computational cost. For further information, see Section **2.13.4** of Price et al. (2018b).

where the first term on the RHS is the $P\mathrm{d}V$ work, the second is a heating term due to the shock viscosity, the third is the cooling of the disc and the last term is the drag heating term. Usually, an adiabatic equation of state is assumed. For an ideal gas, it is possible to link pressure and density as follows

$$P = (\gamma - 1)\rho_g e = \frac{c_g^2 \rho_g}{\gamma}, \tag{A.10}$$

where $\gamma = 5/3$ and c_g is the gas sound speed, that is initialized as a power law $c_g \propto R^{-0.25}$.

The shock viscosity term can be written as

$$\Lambda_{\text{shock}} = c_1 \alpha^{\text{AV}} \frac{h_g}{H} + c_2 \beta^{\text{AV}} \left(\frac{h_g}{H}\right)^2, \tag{A.11}$$

where c_1, c_2 are two numerical factors, whose dimension is a specific energy per unit time, α^{AV} and β^{AV} are respectively the linear and the quadratic viscosity coefficients, and h_g/H_g is related to the numerical resolution[2]. The viscosity term is dissipative, so it heats the disc. We did so since in these systems the main driver of angular momentum transport is GI.

For the cooling we use the prescription from Gammie (2001) and Rice et al. (2004), in which the cooling time t_{cool} is proportional to the dynamical time, with a factor of proportionality β_{cool}

$$t_{\text{cool}} = \beta_{\text{cool}} \Omega^{-1} \tag{A.12}$$

Under the assumption that the transfer of angular momentum driven by gravito-turbulence occurs locally (Lodato & Rice 2004), we can relate the cooling parameter to an effective $\alpha-$viscosity parameter

$$\alpha_{\text{GI}} = \frac{4}{9} \frac{1}{\gamma(\gamma - 1)\beta_{\text{cool}}}. \tag{A.13}$$

We need to introduce a cooling prescription for the system in order to trigger GI. Finally, the drag heating term is

$$\Lambda_{\text{drag}} = K|\mathbf{v}_d - \mathbf{v}_g|^2. \tag{A.14}$$

Currently, PHANTOM neglects any thermal coupling between the dust and the gas, aside from the drag heating.

[2]This quantity tells how many smoothing lengths are included in the disc thickness.

APPENDIX B

Two fluid dispersion relation

In this appendix we present the calculations to obtain the dispersion relations for axisymmetric perturbations, with and without taking into account the backreaction.

We consider an infinitesimally thin disc composed of two fluids (gas and dust, henceforth with the subscripts g and d). The two components interact through gravitational and drag force. We call Σ_i the surface density, v_i the radial velocity, u_i the azimuthal velocity, h_i the enthalpy. In a two-dimensional polar system of coordinates (R, ϕ), the fluid equations are

$$\partial_t \Sigma_g + R^{-1} \partial_R \left(\Sigma_g R v_g\right) + \frac{1}{R} \partial_\phi (\Sigma_g u_g) = 0, \tag{A.1}$$

$$\partial_t v_g + v_g \partial_R v_g - \frac{u_g^2}{R} + \frac{u_g}{R} \partial_\phi v_g = -\partial_R \left(\Phi + h_g\right) + \frac{\Sigma_d}{\Sigma_g t_s} \left(v_d - v_g\right), \tag{A.2}$$

$$\partial_t u_g + v_g \partial_R u_g - \frac{u_g v_g}{R} + \frac{u_g}{R} \partial_\phi u_g = -\frac{1}{R} \partial_\phi \left(\Phi + h_g\right) + \frac{\Sigma_d}{\Sigma_g t_s} \left(u_d - u_g\right), \tag{A.3}$$

$$dh_g = c_g^2 \frac{d\Sigma_g}{\Sigma_g}, \tag{A.4}$$

$$\partial_t \Sigma_d + R^{-1} \partial_R \left(\Sigma_d R v_d\right) + \frac{1}{R} \partial_\phi (\Sigma_d u_d) = 0, \tag{A.5}$$

$$\partial_t v_d + v_d \partial_R v_d - \frac{u_d^2}{R} + \frac{u_d}{R} \partial_\phi v_d = -\partial_R \left(\Phi + h_d\right) - \frac{1}{t_s} \left(v_d - v_g\right), \tag{A.6}$$

$$\partial_t u_d + v_g \partial_R u_d - \frac{u_d v_d}{R} + \frac{u_d}{R} \partial_\phi u_d = -\frac{1}{R} \partial_\phi \left(\Phi + h_d\right) - \frac{1}{t_s} \left(u_d - u_g\right), \tag{A.7}$$

$$dh_d = c_d^2 \frac{d\Sigma_d}{\Sigma_d}, \tag{A.8}$$

$$\nabla^2 \Phi = 4\pi G \delta(z) (\Sigma_g + \Sigma_d). \tag{A.9}$$

The basic state we consider is characterized by uniform surface densities Σ_{g0}, Σ_{d0}, azimuthal velocity $u_{g0} = u_{d0} = R\Omega$, zero radial velocity $v_{g0} = v_{d0} = 0$ and constant dispersion velocities c_g, c_d.

We now perform a first order perturbation analysis of the previous equations: we consider a perturbation to the basic equilibrium state $X_0 + X_1(R, \phi, t)$ that have spatial

and temporal dependence like $X_1 \propto \exp[i(kR - \omega t + m\phi)]$. We focus our attention on axisymmetric perturbations ($m = 0$): we substitute the perturbed quantities into the fluid equations, and we discard any term that is quadratic in them: the six first order perturbed equations are

$$-i(\omega - m\Omega)\Sigma_{g1} + ik\Sigma_{g0}v_{g1} = 0, \tag{A.10}$$

$$-i(\omega - m\Omega)v_{g1} - 2\Omega u_{g1} - \frac{\Sigma_{d0}}{\Sigma_{g0}}\frac{1}{t_s}(v_{d1} - v_{g1}) = -\partial_R\left(\Phi_1 + h_{g1}\right), \tag{A.11}$$

$$-i(\omega - m\Omega)u_{g1} - 2Bv_{g1} - \frac{\Sigma_{d0}}{\Sigma_{g0}}\frac{1}{t_s}(u_{d1} - u_{g1}) = 0, \tag{A.12}$$

$$-i(\omega - m\Omega)\Sigma_{d1} + ik\Sigma_{d0}v_{d1} = 0, \tag{A.13}$$

$$-i(\omega - m\Omega)v_{d1} - 2\Omega u_{d1} + \frac{1}{t_s}\left(v_{d1} - v_{g1}\right) = -\partial_R\left(\Phi_1 + h_{d1}\right), \tag{A.14}$$

$$-i(\omega - m\Omega)u_{d1} - 2Bv_{d1} + \frac{1}{t_s}\left(u_{d1} - u_{g1}\right) = 0, \tag{A.15}$$

where $B(R) = -\frac{1}{2}\frac{\mathrm{d}(\Omega R)}{\mathrm{d}R} + \Omega$ is the Oort parameter and $4B\Omega^2 = -\kappa^2$. Once we know the form of the density perturbation, it is possible to solve the Poisson equation and get the potential perturbation: it is possible to show that

$$\Phi_1 = -\frac{2\pi G}{|k|}\left(\Sigma_{g1} + \Sigma_{d1}\right), \tag{A.16}$$

and the enthalpy can be written as

$$h_{i,1} = c_i^2\frac{\Sigma_{i,1}}{\Sigma_{i,0}}. \tag{A.17}$$

Hence, it is possible to write the r.h.s of Euler equations as a function of the perturbed densities

$$-\partial_R(\Phi_1 + h_{i,1}) = ik\Sigma_{i,1}\left(\frac{2\pi G}{|k|} - \frac{c_i^2}{\Sigma_{i,0}}\right) + ik\frac{2\pi G}{|k|}\Sigma_{j,1}, \quad i \neq j. \tag{A.18}$$

Now, we'll consider the case of axisymmetric perturbations ($m = 0$).

Without backreaction

Here, we do not take into account the backreaction, so the drag terms appear only in dust equations. In this case, we can write the matrix of coefficients of $\mathbf{x} = (\Sigma_{g1}, v_{g1}, u_{g1}, \Sigma_{d1}, v_{d1}, u_{d1})$ that is

$$A = \begin{pmatrix} -i\omega & i\Sigma_{g0}k & 0 & 0 & 0 & 0 \\ -ik\left(\frac{2\pi G}{|k|} - \frac{c_g^2}{\Sigma_{g0}}\right) & -i\omega & -2\Omega^2 & -ik\frac{2\pi G}{|k|} & 0 & 0 \\ 0 & -2B & -i\omega & 0 & 0 & 0 \\ 0 & 0 & 0 & -i\omega & i\Sigma_{d0}k & 0 \\ -ik\frac{2\pi G}{|k|} & -\frac{1}{t_s} & 0 & -ik\left(\frac{2\pi G}{|k|} - \frac{c_d^2}{\Sigma_{d0}}\right) & \frac{1}{t_s} - i\omega & -2\Omega^2 \\ 0 & 0 & -\frac{1}{t_s} & 0 & -2B & \frac{1}{t_s} - i\omega \end{pmatrix}, \tag{A.19}$$

such that $A\mathbf{x} = 0$. In order to compute the dispersion relation, we impose that the determinant of A is zero: for simplicity, we express the relationship as a function of $y = -i\omega$. To be consistent with (Bertin & Romeo 1988), we define

$$\alpha_i = \kappa^2 - \lambda_i = \kappa^2 + c_i^2 k^2 - 2\pi G \Sigma_{i0} |k|, \tag{A.20}$$

and

$$\beta_i = 2\pi G \Sigma_{i0} |k|, \tag{A.21}$$

and we get

$$\begin{array}{l} y^5 + 2t_s^{-1} y^4 + y^3(\alpha_g + \alpha_d + t_s^{-2}) + t_s^{-1} y^2 (2\alpha_g + \alpha_d - \kappa^2 - \beta_d) + \\ + y[\alpha_g \alpha_d - \beta_g \beta_d + t_s^{-2}(\alpha_g - \beta_d)] + t_s^{-1}[\alpha_g \alpha_d - \beta_g \beta_d - \kappa^2(\alpha_g - \beta_d)] = 0. \end{array} \tag{A.22}$$

With backreaction

Starting from the same basic state as before, now we consider the backreaction, i.e. the effect of the drag force onto the gas component. In this case, the coefficients' matrix is

$$A_{\mathrm{B}} = \begin{pmatrix} -i\omega & i\Sigma_{g0}k & 0 & 0 & 0 & 0 \\ -ik\left(\frac{2\pi G}{|k|} - \frac{c_g^2}{\Sigma_{g0}}\right) & \epsilon\frac{1}{t_s} - i\omega & -2\Omega^2 & -ik\frac{2\pi G}{|k|} & -\epsilon\frac{1}{t_s} & 0 \\ 0 & -2B & \epsilon\frac{1}{t_s} - i\omega & 0 & 0 & -\epsilon\frac{1}{t_s} \\ 0 & 0 & 0 & -i\omega & i\Sigma_{d0}k & 0 \\ -ik\frac{2\pi G}{|k|} & -\frac{1}{t_s} & 0 & -ik\left(\frac{2\pi G}{|k|} - \frac{c_d^2}{\Sigma_{d0}}\right) & \frac{1}{t_s} - i\omega & -2\Omega^2 \\ 0 & 0 & -\frac{1}{t_s} & 0 & -2B & \frac{1}{t_s} - i\omega \end{pmatrix}, \tag{A.23}$$

where $\epsilon = \Sigma_{d0}/\Sigma_{g0}$. As before, by imposing that the determinant of A_B is zero, we obtain

$$\begin{array}{l} y^5 + 2t_s^{-1} y^4 (1+\epsilon) + y^3 \left[\alpha_g + \alpha_d + t_s^{-2}(1 + 2\epsilon + \epsilon^2)\right] + y^2 t_s^{-1} \left[(2\alpha_g + \alpha_d - 1)(1+\epsilon) - \beta_d - \epsilon\beta_g\right] + \\ + y\left[\alpha_g \alpha_d - \beta_g \beta_d + t_s^{-2}\left(\alpha_g - \beta_d + \epsilon(\alpha_g + \alpha_d - \beta_g - \beta_d) + \epsilon^2(\alpha_d - \beta_g)\right)\right] + \\ + t_s^{-1}\left[(\alpha_g \alpha_d - \beta_g \beta_d)(1+\epsilon) - (\alpha_g - \beta_d) - \epsilon(\alpha_d - \beta_g)\right] = 0. \end{array} \tag{A.24}$$

Bibliography

Adams, F. C., Lada, C. J., & Shu, F. H. 1988, *Astrophys. J.*, 326, 865

ALMA Partnership, Brogan, C. L., Pérez, L. M., et al. 2015, *Astrophys. J. Lett.*, 808, L3

Andre, P., Ward-Thompson, D., & Barsony, M. 2000, in Protostars and Planets IV, ed. V. Mannings, A. P. Boss, & S. S. Russell, 59

Andrews, S. M. 2020, , 58, 483

Andrews, S. M., Huang, J., Pérez, L. M., et al. 2018, *Astrophys. J. Lett.*, 869, L41

Andrews, S. M. & Williams, J. P. 2007, *Astrophys. J.*, 659, 705

Andrews, S. M., Wilner, D. J., Hughes, A. M., Qi, C., & Dullemond, C. P. 2009, *Astrophys. J.*, 700, 1502

Ansdell, M., Williams, J. P., Trapman, L., et al. 2018, *Astrophys. J.*, 859, 21

Armitage, P. J. 2013, Astrophysics of Planet Formation

Bae, J., Isella, A., Zhu, Z., et al. 2022, arXiv e-prints, arXiv:2210.13314

Bae, J., Teague, R., & Zhu, Z. 2021, *Astrophys. J.*, 912, 56

Baehr, H. & Zhu, Z. 2021a, *Astrophys. J.*, 909, 135

Baehr, H. & Zhu, Z. 2021b, *Astrophys. J.*, 909, 136

Baehr, H., Zhu, Z., & Yang, C.-C. 2022, *Astrophys. J.*, 933, 100

Balbus, S. A. & Hawley, J. F. 1991, *Astrophys. J.*, 376, 214

Balbus, S. A. & Papaloizou, J. C. B. 1999, *Astrophys. J.*, 521, 650

Bell, K. R. & Lin, D. N. C. 1994, *Astrophys. J.*, 427, 987

Benisty, M., Bae, J., Facchini, S., et al. 2021, *Astrophys. J. Lett.*, 916, L2

Benítez-Llambay, P. & Masset, F. S. 2016, The Astrophysical Journal Supplement Series, 223, 11

Bertin, G. & Cava, A. 2006, *Astron. Astrophys.*, 459, 333

Bertin, G. & Lodato, G. 1999, *Astron. Astrophys.*, 350, 694

Bertin, G. & Romeo, A. B. 1988, *Astron. Astrophys.*, 195, 105

Binney, J. & Tremaine, S. 1987, Galactic dynamics

Birnstiel, T., Fang, M., & Johansen, A. 2016, , 205, 41

Bollati, F., Lodato, G., Price, D. J., & Pinte, C. 2021, *Mon. Not. R. Astron. Soc.*, 504, 5444

Booth, R. A. & Clarke, C. J. 2016, *Mon. Not. R. Astron. Soc.*, 458, 2676

Booth, R. A. & Clarke, C. J. 2019, *Mon. Not. R. Astron. Soc.*, 483, 3718

Boss, A. P. 1997, Science, 276, 1836

Bouwman, J., Meeus, G., de Koter, A., et al. 2001, *Astron. Astrophys.*, 375, 950

Cadman, J., Rice, K., & Hall, C. 2021, *Mon. Not. R. Astron. Soc.*, 504, 2877

Cadman, J., Rice, K., Hall, C., Haworth, T. J., & Biller, B. 2020, *Mon. Not. R. Astron. Soc.*, 492, 5041
Calcino, J., Hilder, T., Price, D. J., et al. 2022, *Astrophys. J. Lett.*, 929, L25
Chandrasekhar, S. 1943, *Astrophys. J.*, 97, 255
Chiang, E. I. & Goldreich, P. 1997, *Astrophys. J.*, 490, 368
Clarke, C. & Carswell, B. 2014, Principles of Astrophysical Fluid Dynamics
Clarke, C. J. 2009, *Mon. Not. R. Astron. Soc.*, 396, 1066
Clarke, C. J. & Pringle, J. E. 1988, *Mon. Not. R. Astron. Soc.*, 235, 365
Cleeves, L. I., Öberg, K. I., Wilner, D. J., et al. 2016, *Astrophys. J.*, 832, 110
Cossins, P., Lodato, G., & Clarke, C. J. 2009, *Mon. Not. R. Astron. Soc.*, 393, 1157
Cuello, N., Dipierro, G., Mentiplay, D., et al. 2019, *Mon. Not. R. Astron. Soc.*, 483, 4114
Cuello, N., Louvet, F., Mentiplay, D., et al. 2020, *Mon. Not. R. Astron. Soc.*, 491, 504
Cuello, N., Ménard, F., & Price, D. J. 2023, European Physical Journal Plus, 138, 11
Curone, P., Izquierdo, A. F., Testi, L., et al. 2022, *Astron. Astrophys.*, 665, A25
Cuzzi, J. N., Dobrovolskis, A. R., & Champney, J. M. 1993, , 106, 102
Cuzzi, J. N. & Hogan, R. C. 2003, , 164, 127
Dartois, E., Dutrey, A., & Guilloteau, S. 2003, *Astron. Astrophys.*, 399, 773
de Gregorio-Monsalvo, I., Ménard, F., Dent, W., et al. 2013, *Astron. Astrophys.*, 557, A133
Deng, H., Mayer, L., & Meru, F. 2017, *Astrophys. J.*, 847, 43
Dipierro, G., Lodato, G., Testi, L., & de Gregorio Monsalvo, I. 2014, *Mon. Not. R. Astron. Soc.*, 444, 1919
Dipierro, G., Pinilla, P., Lodato, G., & Testi, L. 2015a, *Mon. Not. R. Astron. Soc.*, 451, 974
Dipierro, G., Price, D., Laibe, G., et al. 2015b, *Mon. Not. R. Astron. Soc.*, 453, L73
Dipierro, G., Ricci, L., Pérez, L., et al. 2018, *Mon. Not. R. Astron. Soc.*, 475, 5296
Disk Dynamics Collaboration, Armitage, P. J., Bae, J., et al. 2020, arXiv e-prints, arXiv:2009.04345
Dong, R. & Fung, J. 2017, *Astrophys. J.*, 835, 38
Dong, R., Liu, S.-y., Eisner, J., et al. 2018, *Astrophys. J.*, 860, 124
Dong, R., Zhu, Z., Rafikov, R. R., & Stone, J. M. 2015, *Astrophys. J. Lett.*, 809, L5
Draine, B. T. 2011, Physics of the Interstellar and Intergalactic Medium
Draine, B. T. & Lee, H. M. 1984, *Astrophys. J.*, 285, 89
Drażkowska, J. & Dullemond, C. P. 2014, *Astron. Astrophys.*, 572, A78
Dullemond, C. P., Isella, A., Andrews, S. M., Skobleva, I., & Dzyurkevich, N. 2020, *Astron. Astrophys.*, 633, A137
Dullemond, C. P., Juhasz, A., Pohl, A., et al. 2012, RADMC-3D: A multi-purpose radiative transfer tool, Astrophysics Source Code Library, record ascl:1202.015
Dutrey, A., Semenov, D., Chapillon, E., et al. 2014, in Protostars and Planets VI, ed. H. Beuther, R. S. Klessen, C. P. Dullemond, & T. Henning, 317–338
Facchini, S., Birnstiel, T., Bruderer, S., & van Dishoeck, E. F. 2017, *Astron. Astrophys.*, 605, A16
Facchini, S., Teague, R., Bae, J., et al. 2021, *Astron. J.*, 162, 99
Fan, Z. & Lou, Y.-Q. 1999, *Mon. Not. R. Astron. Soc.*, 307, 645
Fassio, F. & Probstein, R. F. 1970, AIAA Journal, 8, 772
Fedele, D., Tazzari, M., Booth, R., et al. 2018, *Astron. Astrophys.*, 610, A24
Fedele, D., Toci, C., Maud, L., & Lodato, G. 2021, *Astron. Astrophys.*, 651, A90
Flaherty, K., Hughes, A. M., Simon, J. B., et al. 2020, *Astrophys. J.*, 895, 109

Flaherty, K. M., Hughes, A. M., Rose, S. C., et al. 2017, *Astrophys. J.*, 843, 150
Foreman-Mackey, D., Hogg, D. W., Lang, D., & Goodman, J. 2013, *Publ. Astron. Soc. Pac.*, 125, 306
Fux, R. 1999, *Astron. Astrophys.*, 345, 787
Gaia Collaboration, Brown, A. G. A., Vallenari, A., et al. 2018, *Astron. Astrophys.*, 616, A1
Gammie, C. F. 2001, *Astrophys. J.*, 553, 174
Goldreich, P. & Tremaine, S. 1979, *Astrophys. J.*, 233, 857
Goldreich, P. & Tremaine, S. 1980, *Astrophys. J.*, 241, 425
Goldreich, P. & Ward, W. R. 1973, *Astrophys. J.*, 183, 1051
Gonzalez, J. F., Laibe, G., & Maddison, S. T. 2017, *Mon. Not. R. Astron. Soc.*, 467, 1984
Goodman, J. & Rafikov, R. R. 2001, *Astrophys. J.*, 552, 793
Guidi, G., Tazzari, M., Testi, L., et al. 2016, *Astron. Astrophys.*, 588, A112
Haisch, Karl E., J., Lada, E. A., & Lada, C. J. 2001, *Astrophys. J. Lett.*, 553, L153
Hall, C., Dong, R., Teague, R., et al. 2020, *Astrophys. J.*, 904, 148
Hall, C., Forgan, D., Rice, K., et al. 2016, *Mon. Not. R. Astron. Soc.*, 458, 306
Hall, C., Rice, K., Dipierro, G., et al. 2018, *Mon. Not. R. Astron. Soc.*, 477, 1004
Hammond, I., Christiaens, V., Price, D. J., et al. 2023, *Mon. Not. R. Astron. Soc.*, 522, L51
Hartmann, L. 2009, Accretion Processes in Star Formation: Second Edition
Hartmann, L., Calvet, N., Gullbring, E., & D'Alessio, P. 1998, *Astrophys. J.*, 495, 385
Haworth, T. J., Facchini, S., Clarke, C. J., & Cleeves, L. I. 2017, *Mon. Not. R. Astron. Soc.*, 468, L108
Hennebelle, P., Lesur, G., & Fromang, S. 2017, *Astron. Astrophys.*, 599, A86
Hildebrand, R. H. 1983, , 24, 267
Hohl, F. 1973, *Astrophys. J.*, 184, 353
Huang, J., Andrews, S. M., Dullemond, C. P., et al. 2018a, *Astrophys. J. Lett.*, 869, L42
Huang, J., Andrews, S. M., Pérez, L. M., et al. 2018b, *Astrophys. J. Lett.*, 869, L43
Huang, J., Bergin, E. A., Öberg, K. I., et al. 2021, *Astrophys. J. Suppl.*, 257, 19
Isella, A., Guidi, G., Testi, L., et al. 2016, , 117, 251101
Isella, A., Huang, J., Andrews, S. M., et al. 2018, *Astrophys. J. Lett.*, 869, L49
Izquierdo, A. F., Facchini, S., Rosotti, G. P., van Dishoeck, E. F., & Testi, L. 2022, *Astrophys. J.*, 928, 2
Izquierdo, A. F., Testi, L., Facchini, S., Rosotti, G. P., & van Dishoeck, E. F. 2021, *Astron. Astrophys.*, 650, A179
Izquierdo, A. F., Testi, L., Facchini, S., et al. 2023, *Astron. Astrophys.*, 674, A113
Izquierdo et al. in prep, in prep, 2, 2
Jog, C. J. & Solomon, P. M. 1984, *Astrophys. J.*, 276, 114
Kato, S. 1972, *Publ. Astron. Soc. Jpn.*, 24, 61
Kessler-Silacci, J., Augereau, J.-C., Dullemond, C. P., et al. 2006, *Astrophys. J.*, 639, 275
Kokubo, E. & Ida, S. 1998, , 131, 171
Kratter, K. & Lodato, G. 2016, , 54, 271
Kratter, K. M. & Matzner, C. D. 2006, *Mon. Not. R. Astron. Soc.*, 373, 1563
Kratter, K. M., Matzner, C. D., & Krumholz, M. R. 2008, *Astrophys. J.*, 681, 375
Kratter, K. M., Matzner, C. D., Krumholz, M. R., & Klein, R. I. 2010, *Astrophys. J.*, 708, 1585
Kwok, S. 1975, *Astrophys. J.*, 198, 583
Lada, C. J. & Wilking, B. A. 1984, *Astrophys. J.*, 287, 610

Laibe, G. & Price, D. J. 2012a, *Mon. Not. R. Astron. Soc.*, 420, 2345
Laibe, G. & Price, D. J. 2012b, *Mon. Not. R. Astron. Soc.*, 420, 2365
Lau, Y. Y. & Bertin, G. 1978, *Astrophys. J.*, 226, 508
Law, C. J., Crystian, S., Teague, R., et al. 2022, *Astrophys. J.*, 932, 114
Law, C. J., Teague, R., Loomis, R. A., et al. 2021, *Astrophys. J. Suppl.*, 257, 4
Lee, S., Lee, J.-E., Aikawa, Y., Herczeg, G., & Johnstone, D. 2020, *Astrophys. J.*, 889, 20
Lesur, G., Ercolano, B., Flock, M., et al. 2022, arXiv e-prints, arXiv:2203.09821
Lesur, G., Hennebelle, P., & Fromang, S. 2015, *Astron. Astrophys.*, 582, L9
Lin, C. C. & Shu, F. H. 1964, *Astrophys. J.*, 140, 646
Lin, D. N. C. & Papaloizou, J. 1986, *Astrophys. J.*, 309, 846
Lin, M.-K. & Kratter, K. M. 2016, *Astrophys. J.*, 824, 91
Lodato, G. 2008, , 52, 21
Lodato, G. & Clarke, C. J. 2011, *Mon. Not. R. Astron. Soc.*, 413, 2735
Lodato, G., Dipierro, G., Ragusa, E., et al. 2019, *Mon. Not. R. Astron. Soc.*, 486, 453
Lodato, G., Rampinelli, L., Viscardi, E., et al. 2023, *Mon. Not. R. Astron. Soc.*, 518, 4481
Lodato, G. & Rice, W. K. M. 2004, *Mon. Not. R. Astron. Soc.*, 351, 630
Lodato, G., Scardoni, C. E., Manara, C. F., & Testi, L. 2017, *Mon. Not. R. Astron. Soc.*, 472, 4700
Löhnert, L., Krätschmer, S., & Peeters, A. G. 2020, *Astron. Astrophys.*, 640, A53
Longarini, C., Armitage, P. J., Lodato, G., Price, D. J., & Ceppi, S. 2023a, *Mon. Not. R. Astron. Soc.*, 522, 6217
Longarini, C., Lodato, G., Bertin, G., & Armitage, P. J. 2023b, *Mon. Not. R. Astron. Soc.*, 519, 2017
Longarini, C., Lodato, G., Toci, C., & Aly, H. 2021a, *Mon. Not. R. Astron. Soc.*, 503, 4930
Longarini, C., Lodato, G., Toci, C., et al. 2021b, *Astrophys. J. Lett.*, 920, L41
Lynden-Bell, D. & Kalnajs, A. J. 1972, *Mon. Not. R. Astron. Soc.*, 157, 1
Lynden-Bell, D. & Pringle, J. E. 1974, *Mon. Not. R. Astron. Soc.*, 168, 603
Macías, E., Espaillat, C. C., Ribas, Á., et al. 2018, *Astrophys. J.*, 865, 37
Mayor, M. & Queloz, D. 1995, *Nature*, 378, 355
Mejía, A. C., Durisen, R. H., Pickett, M. K., & Cai, K. 2005, *Astrophys. J.*, 619, 1098
Meru, F. & Bate, M. R. 2010, *Mon. Not. R. Astron. Soc.*, 406, 2279
Meru, F. & Bate, M. R. 2011, *Mon. Not. R. Astron. Soc.*, 411, L1
Meru, F. & Bate, M. R. 2012, *Mon. Not. R. Astron. Soc.*, 427, 2022
Meru, F., Juhász, A., Ilee, J. D., et al. 2017, *Astrophys. J. Lett.*, 839, L24
Mestel, L. 1963, *Mon. Not. R. Astron. Soc.*, 126, 553
Min, M., Rab, C., Woitke, P., Dominik, C., & Ménard, F. 2016, *Astron. Astrophys.*, 585, A13
Miotello, A., Bruderer, S., & van Dishoeck, E. F. 2014, *Astron. Astrophys.*, 572, A96
Monaghan, J. J. & Lattanzio, J. C. 1985, *Astron. Astrophys.*, 149, 135
Montesinos, B., Eiroa, C., Mora, A., & Merín, B. 2009, *Astron. Astrophys.*, 495, 901
Natta, A., Testi, L., & Randich, S. 2006, *Astron. Astrophys.*, 452, 245
Nayakshin, S. 2017, , 34, e002
Nesvorný, D., Li, R., Simon, J. B., et al. 2021, PSJ, 2, 27
Öberg, K. I., Guzmán, V. V., Walsh, C., et al. 2021, *Astrophys. J. Suppl.*, 257, 1
Offner, S. S. R., Kratter, K. M., Matzner, C. D., Krumholz, M. R., & Klein, R. I. 2010, *Astrophys. J.*, 725, 1485
Oort, J. H. 1927, , 3, 275

Ormel, C. W. & Cuzzi, J. N. 2007, *Astron. Astrophys.*, 466, 413
Ostriker, E. C. 1999, *Astrophys. J.*, 513, 252
Ostriker, J. P. & Peebles, P. J. E. 1973, *Astrophys. J.*, 186, 467
Paardekooper, S.-J. 2012, *Mon. Not. R. Astron. Soc.*, 421, 3286
Paardekooper, S.-J., Dong, R., Duffell, P., et al. 2022, arXiv e-prints, arXiv:2203.09595
Paardekooper, S. J. & Mellema, G. 2006, *Astron. Astrophys.*, 453, 1129
Paneque-Carreño, T., Pérez, L. M., Benisty, M., et al. 2021, *Astrophys. J.*, 914, 88
Pérez, L. M., Carpenter, J. M., Andrews, S. M., et al. 2016, Science, 353, 1519
Pérez, S., Casassus, S., Baruteau, C., et al. 2019, *Astron. J.*, 158, 15
Pickett, B. K., Mejía, A. C., Durisen, R. H., et al. 2003, *Astrophys. J.*, 590, 1060
Pinilla, P., Birnstiel, T., Ricci, L., et al. 2012, *Astron. Astrophys.*, 538, A114
Pinilla, P., Kurtovic, N. T., Benisty, M., et al. 2021, *Astron. Astrophys.*, 649, A122
Pinte, C., Harries, T. J., Min, M., et al. 2009, *Astron. Astrophys.*, 498, 967
Pinte, C., Ménard, F., Duchêne, G., & Bastien, P. 2006, *Astron. Astrophys.*, 459, 797
Pinte, C., Ménard, F., Duchêne, G., et al. 2018a, *Astron. Astrophys.*, 609, A47
Pinte, C., Price, D. J., Ménard, F., et al. 2020, *Astrophys. J. Lett.*, 890, L9
Pinte, C., Price, D. J., Ménard, F., et al. 2018b, *Astrophys. J. Lett.*, 860, L13
Pinte, C., Teague, R., Flaherty, K., et al. 2022, arXiv e-prints, arXiv:2203.09528
Pinte, C., van der Plas, G., Ménard, F., et al. 2019, Nature Astronomy, 3, 1109
Poblete, P. P., Cuello, N., & Cuadra, J. 2019, *Mon. Not. R. Astron. Soc.*, 489, 2204
Pollack, J. B., Hubickyj, O., Bodenheimer, P., et al. 1996, , 124, 62
Powell, D., Murray-Clay, R., Pérez, L. M., Schlichting, H. E., & Rosenthal, M. 2019, *Astrophys. J.*, 878, 116
Prialnik, D. 2009, An Introduction to the Theory of Stellar Structure and Evolution
Price, D. J. 2012, Journal of Computational Physics, 231, 759
Price, D. J., Cuello, N., Pinte, C., et al. 2018a, *Mon. Not. R. Astron. Soc.*, 477, 1270
Price, D. J. & Monaghan, J. J. 2007, *Mon. Not. R. Astron. Soc.*, 374, 1347
Price, D. J., Wurster, J., Tricco, T. S., et al. 2018b, , 35, e031
Rafikov, R. R. 2002, *Astrophys. J.*, 569, 997
Rafikov, R. R. 2009, *Astrophys. J.*, 704, 281
Ragusa, E., Alexander, R., Calcino, J., Hirsh, K., & Price, D. J. 2020, *Mon. Not. R. Astron. Soc.*, 499, 3362
Ragusa, E., Dipierro, G., Lodato, G., Laibe, G., & Price, D. J. 2017, *Mon. Not. R. Astron. Soc.*, 464, 1449
Rice, W. K. M. & Armitage, P. J. 2009, *Mon. Not. R. Astron. Soc.*, 396, 2228
Rice, W. K. M., Lodato, G., & Armitage, P. J. 2005, *Mon. Not. R. Astron. Soc.*, 364, L56
Rice, W. K. M., Lodato, G., Pringle, J. E., Armitage, P. J., & Bonnell, I. A. 2004, *Mon. Not. R. Astron. Soc.*, 355, 543
Rice, W. K. M., Lodato, G., Pringle, J. E., Armitage, P. J., & Bonnell, I. A. 2006, *Mon. Not. R. Astron. Soc.*, 372, L9
Riols, A., Roux, B., Latter, H., & Lesur, G. 2020, *Mon. Not. R. Astron. Soc.*, 493, 4631
Rosenfeld, K. A., Andrews, S. M., Hughes, A. M., Wilner, D. J., & Qi, C. 2013, *Astrophys. J.*, 774, 16
Rosotti, G. P., Teague, R., Dullemond, C., Booth, R. A., & Clarke, C. J. 2020, *Mon. Not. R. Astron. Soc.*, 495, 173
Safronov, V. S. 1960, Annales d'Astrophysique, 23, 979

Safronov, V. S. 1969, Evoliutsiia doplanetnogo oblaka.
Sargent, A. I. & Beckwith, S. 1987, *Astrophys. J.*, 323, 294
Schwarz, K. R., Calahan, J. K., Zhang, K., et al. 2021, *Astrophys. J. Suppl.*, 257, 20
Shakura, N. I. & Sunyaev, R. A. 1973, *Astron. Astrophys.*, 24, 337
Shi, J.-M., Zhu, Z., Stone, J. M., & Chiang, E. 2016, *Mon. Not. R. Astron. Soc.*, 459, 982
Shu, F. H. 1970, *Astrophys. J.*, 160, 99
Stadler, J., Benisty, M., Izquierdo, A., et al. 2023, *Astron. Astrophys.*, 670, L1
Stamatellos, D., Hubber, D. A., & Whitworth, A. P. 2007, *Mon. Not. R. Astron. Soc.*, 382, L30
Stevenson, D. J. 1982, , 30, 755
Suriano, S. S., Li, Z.-Y., Krasnopolsky, R., & Shang, H. 2018, *Mon. Not. R. Astron. Soc.*, 477, 1239
Tabone, B., Rosotti, G. P., Cridland, A. J., Armitage, P. J., & Lodato, G. 2022, *Mon. Not. R. Astron. Soc.*, 512, 2290
Takahashi, S. Z. & Inutsuka, S.-i. 2014, *Astrophys. J.*, 794, 55
Takeuchi, T. & Lin, D. N. C. 2002, *Astrophys. J.*, 581, 1344
Teague, R. 2019, The Journal of Open Source Software, 4, 1220
Teague, R., Bae, J., Aikawa, Y., et al. 2021, *Astrophys. J. Suppl.*, 257, 18
Teague, R., Bae, J., Bergin, E. A., Birnstiel, T., & Foreman-Mackey, D. 2018, *Astrophys. J. Lett.*, 860, L12
Teague, R., Law, C. J., Huang, J., & Meng, F. 2021, Journal of Open Source Software, 6, 3827
Terry, J. P., Hall, C., Longarini, C., et al. 2022, *Mon. Not. R. Astron. Soc.*, 510, 1671
Testi, L., Birnstiel, T., Ricci, L., et al. 2014, in Protostars and Planets VI, ed. H. Beuther, R. S. Klessen, C. P. Dullemond, & T. Henning, 339–361
Tobin, J. J., Kratter, K. M., Persson, M. V., et al. 2016, *Nature*, 538, 483
Tobin, J. J., Sheehan, P. D., Megeath, S. T., et al. 2020, *Astrophys. J.*, 890, 130
Toci, C., Lodato, G., Christiaens, V., et al. 2020a, *Mon. Not. R. Astron. Soc.*, 499, 2015
Toci, C., Lodato, G., Fedele, D., Testi, L., & Pinte, C. 2020b, *Astrophys. J. Lett.*, 888, L4
Tominaga, R. T., Takahashi, S. Z., & Inutsuka, S.-i. 2020, *Astrophys. J.*, 900, 182
Toomre, A. 1964, *Astrophys. J.*, 139, 1217
Toomre, A. 1969, *Astrophys. J.*, 158, 899
van Boekel, R., Waters, L. B. F. M., Dominik, C., et al. 2003, *Astron. Astrophys.*, 400, L21
van der Marel, N., van Dishoeck, E. F., Bruderer, S., et al. 2013, Science, 340, 1199
Vandervoort, P. O. 1970, *Astrophys. J.*, 161, 87
Veronesi, B., Lodato, G., Dipierro, G., et al. 2019, *Mon. Not. R. Astron. Soc.*, 489, 3758
Veronesi, B., Paneque-Carreño, T., Lodato, G., et al. 2021, *Astrophys. J. Lett.*, 914, L27
Veronesi, B., Ragusa, E., Lodato, G., et al. 2020, *Mon. Not. R. Astron. Soc.*, 495, 1913
Veronesi et al. in prep, in prep, 2, 2
Verrios, H. J., Price, D. J., Pinte, C., Hilder, T., & Calcino, J. 2022, *Astrophys. J. Lett.*, 934, L11
Walmswell, J., Clarke, C., & Cossins, P. 2013, *Mon. Not. R. Astron. Soc.*, 431, 1903
Weaver, E., Isella, A., & Boehler, Y. 2018, *Astrophys. J.*, 853, 113
Weidenschilling, S. J. 1977, *Mon. Not. R. Astron. Soc.*, 180, 57
Whipple, F. L. 1972, in From Plasma to Planet, ed. A. Elvius, 211
Woitke, P., Min, M., Pinte, C., et al. 2016, *Astron. Astrophys.*, 586, A103

Youdin, A. N. 2011, *Astrophys. J.*, 731, 99
Youdin, A. N. & Lithwick, Y. 2007, , 192, 588
Zhang, K., Booth, A. S., Law, C. J., et al. 2021, *Astrophys. J. Suppl.*, 257, 5
Zhu, Z., Hartmann, L., Nelson, R. P., & Gammie, C. F. 2012, *Astrophys. J.*, 746, 110

List of Publications

As of November 2023

Refereed publications

First author publications

- "Dynamical dust traps in misaligned circumbinary discs: analytical theory and numerical simulations", **Cristiano Longarini**, Giuseppe Lodato, Claudia Toci, Hossam Aly, Monthly Notices of the Royal Astronomical Society, Volume 503, Issue 4, pp.4930-4941, (2021)

- "Investigating Protoplanetary Disk Cooling through Kinematics: Analytical GI Wiggle", **Cristiano Longarini**, Giuseppe Lodato, Claudia Toci, Benedetta Veronesi, Cassandra Hall, Ruobing Dong, Jason P. Terry, The Astrophysical Journal Letters, Volume 920, Issue 2, id.L41, 9 pp., (2021)

- "The role of the drag force in the gravitational stability of dusty planet forming disc - I. Analytical theory", **Cristiano Longarini**, Giuseppe Lodato, Giuseppe Bertin, Philip J. Armitage, Monthly Notices of the Royal Astronomical Society, Volume 519, Issue 2, pp.2017-2029, (2023)

- "The role of the drag force in the gravitational stability of dusty planet forming disc - II. Numerical simulations", **Cristiano Longarini**, Philip J. Armitage, Giuseppe Lodato, Daniel J. Price, Simone Ceppi, Monthly Notices of the Royal Astronomical Society, Volume 522, Issue 4, pp.6217-6235, (2023)

Co-author publications

- "Dust traffic jams in inclined circumbinary protoplanetary discs - I. Morphology and formation theory", Hossam Aly, Jean-Francois Gonzalez, Rebecca Nealon, **Cristiano Longarini**, Giuseppe Lodato, Daniel J. Price, Monthly Notices of the Royal Astronomical Society, Volume 508, Issue 2, pp.2743-2757, (2021)

- "Constraining protoplanetary disc mass using the GI wiggle", Jason P. Terry, Cassandra Hall, **Cristiano Longarini**, Giuseppe Lodato, Claudia Toci, Benedetta Veronesi, Teresa Paneque-Carreño, Christophe Pinte, Monthly Notices of the Royal Astronomical Society, Volume 510, Issue 2, pp.1671-1679, (2022)

- "Mapping the Complex Kinematic Substructure in the TW Hya Disk", Richard Teague, Jaehan Bae, Sean M. Andrews, Myriam Benisty, Edwin A. Bergin, Stefano Facchini, Jane Huang, **Cristiano Longarini** and David Wilner, The Astrophysical Journal, Volume 936, Issue 2, id.163, 16 pp., (2022)
- "Dynamical mass measurements of two protoplanetary discs", Giuseppe Lodato, Luna Rampinelli, Elena Maria Viscardi, **Cristiano Longarini**, Andrés F. Izquierdo, Teresa Paneque-Carreno, Leonardo testi, Stefano Facchini, Anna Miotello, Benedetta Veronesi and Cassandra Hall, Monthly Notices of the Royal Astronomical Society, Volume 518, Issue 3, pp.4481-4493, (2023)
- "Precession and polar alignment of accretion discs in triple (or multiple) stellar systems", Simone Ceppi, Cristiano Longarini, Giuseppe Lodato, Nicholás Cuello and Stephen H. Lubow, Monthly Notices of the Royal Astronomical Society, Volume 520, Issue 4, pp.5817-5827, (2023)

Publications under review

- "Weighing protoplanetary discs with kinematics: physical model, method and benchmark" Benedetta Veronesi, **Cristiano Longarini**, Giuseppe Lodato, Guillaume Laibe, Cassandra Hall, Stefano Facchini and Leonardo Testi, submitted to Astronomy & Astrophysics
- "Rotation curves in protoplanetary discs with thermal stratification", Paola Martire, **Cristiano Longarini**, Giuseppe Lodato, Giovanni Rosotti, Andrew Winter, Stefano Facchini, Caitlyn Hardimann, Myriam Benisty, Jochen Stadler, Andr es Felipe Izquierdo and Leonardo Testi, submitted to Astronomy & Astrophysics.

Publications in preparation

- "Angular momentum transport through gravitational instability in Elias 2-27", **Cristiano Longarini** et al.

Acknowledgments

Below, I report for completeness the formal acknowledgements sections of the individual projects presented in this thesis

- **Chapter 6: Kinematic signatures of gravitational instability**

  The authors thank the anonymous referee for insightful comments and suggestions, and Richard Booth, Cathie Clarke and Pietro Curone for useful discussions. This project has received funding from the European Union's Horizon 2020 research and innovation programme under the Marie Skłodowska-Curie grant agreement No 823823 (DUSTBUSTERS RISE project). BV acknowledges funding from the ERC CoG project PODCAST No 864965.

- **Chapter 8: Weighing and sizing protoplanetary discs with gravity**

  This work has received funding from the ERC CoG project PODCAST No 864965, and from the European Union's Horizon 2020 research and innovation programme under the Marie Skłodowska-Curie grant agreement No 823823 (RISE DUSTBUSTERS project). We used the EMCEE algorithm (Foreman-Mackey et al. 2013), the CORNER package to produce corner plots, and PYTHON-based MATPLOTLIB package for all the other figures. Computational resources were provided by the PSMN (Pôle Scientifique de Modélisation Numérique) of the ENS de Lyon, and the INDACO Platform, a project of High Performance Computing at the Università degli Studi di Milano. The authors thank Pietro Curone, Andrés F. Izquierdo, Sean Andrews, Richard Teague, Giovanni Rosotti and Enrico Ragusa for useful discussions.

  This paper makes use of the following ALMA data: ADS/JAO.ALMA#2018.1.01055.L. ALMA is a partnership of ESO (representing its member states), NSF (USA), and NINS (Japan), together with NRC (Canada), NSC and ASIAA (Taiwan), and KASI (Republic of Korea), in cooperation with the Republic of Chile. The Joint ALMA Observatory is operated by ESO, AUI/NRAO, and NAOJ. This work has received funding from the European Union's Horizon 2020 research and innovation programme under the Marie Sklodowska-Curie grant agreement # 823823 (RISE DUSTBUSTERS project). G.R. is funded by the European Union under the European Union's Horizon Europe Research & Innovation Programme No. 101039651 (DiscEvol) and by the Fondazione Cariplo, grant no. 2022-1217. S.F. is funded by the European Union (ERC, UNVEIL, 101076613). Views and opinions expressed are however those of the author(s) only and do not necessarily reflect those of the European Union or the European Research Council. Neither the European

Union nor the granting authority can be held responsible for them. S.F. acknowledges financial contribution from PRIN-MUR 2022YP5ACE. CH is funded by a Research Training Program Scholarship from the Australian Government, and acknowledges funding from the Australian Research Council via DP220103767. The authors thank Pietro Curone and Claudia Toci for useful discussions.

- **Chapter 9: The interplay between drag force and gravitational instability**

  The authors thank the anonymous referee for suggestions and comments, that significantly improved the quality of this work. This project and the authors have received funding from the European Union's Horizon 2020 research and innovation programme under the Marie Skłodowska-Curie grant agreement N. 823823 (DUSTBUSTERS RISE project). CL acknowledges funding from Fulbright Commission through VRS scholarship. CL thanks Callum Fairbairn for fruitful discussions.

- **Chapter 10: Planetary cores formation through dust collapse in gravitationally unstable discs**

  The authors thank the referee for useful comments and suggestions that significantly improved the quality of the work. In this work we used SPLASH to create figures of the hydrodynamical simulations. This project and the authors have received funding from the European Union's Horizon 2020 research and innovation programme under the Marie Skłodowska-Curie grant agreement N. 823823 (DUSTBUSTERS RISE project). CL acknowledges support from Fulbright Commission through VRS scholarship. PJA acknowledges support from NASA TCAN award 80NSSC19K0639, and from award 644616 from the Simons Foundation. DJP acknowledges Australian Research Council funding via DP220103767 and DP180104235. The authors thank Sahl Rowther, Benedetta Veronesi, Cathie Clarke and Richard Booth for useful discussions. We thank Stony Brook Research Computing and Cyberinfrastructure, and the Institute for Advanced Computational Science at Stony Brook University for access to the SeaWulf computing system, supported by National Science Foundation grant # 1531492.

Firstly, I would like to thank my supervisor Prof. Giuseppe Lodato. Thank you for the guidance during these PhD years. I believe that working together taught me a lot and shaped my methodology and critical thinking. I am extremely grateful for all the opportunities you offered me, and for the support you gave me during my PhD journey. Being your student will always be my pride, and I am sure we will keep collaborating in the future. I find it natural to seek your input and guidance, and I don't plan on stopping anytime soon!

I am deeply grateful to Prof. Philip Armitage. Thank you very much for accepting to be my host during my Fulbright experience. I can affirm that most of the ideas presented in the second part of this thesis were born during our discussions at the 11th floor of the Flatiron Institute. Working closely with you has been an invaluable educational experience, and I am truly grateful for the knowledge and insights gained during my stay in New York.

I wish to express my profound gratitude to Prof. Daniel Price for his exceptional support during my "upside-down" period in Melbourne. The experience of collaborating with you has been nothing short of extraordinary. Your vast knowledge and unwavering passion really inspired me. Being in the author list of PHANTOM, although undeservedly, is one of my greatest boast! And finally, the beautiful cover of this thesis exists because of you!

I want to thank Cathie Clarke and Myriam Benisty for their valuable comments and suggestions that improved the quality of the manuscript and for accepting to be the examiners of my thesis defence.

I warmly thank Giovanni Rosotti and Stefano Facchini for countless scientific discussions and for all the help you gave me during the postdoc research. I really admire you as persons and as scientists, and I really hope to keep collaborating with you in the future.

I thank Claudia for launching me inside Giuseppe's office when I was looking for a Master Thesis, for the countless Skype calls to teach me how to use PHANTOM, for keeping me company in the snowy Stony Brook, and many many other things. You're a wonderful person, and I am very lucky to know you.

A very special thank goes to my PhD colleagues Pietro and Simone. I can firmly say that without you two, my PhD would not have been the same. Thanks for reading my drafts, abstracts, for listening to my talks and revising slides. Pietro, thank you for teaching me how to do plots, even though I still have to learn many things! Simo, thanks for the countless programming advices and for all the discussions we had. It will be difficult not to call you once I have a new result or something to discuss. But, apart from "science", thank you for being my friends. I promise that the Imperia Summer School will still take place, regardless of the distance between us!

Thank you Giovanni for sharing every step in our academic journey, from Precorsi di Matematica back in 2015 to the PhD. I owe you more than you can imagine, I am sure that without your help I would still be struggling with Meccanica and Analisi 2. I won't ever find classes notes better than yours, and funnier email subjects.

Thanks Marina for being the Office's interior designer, our guru and for taking care of Annamaria. Without you, I would have missed all the PhD deadlines, birthdays and Transferable Skills.

Thank you Rossella for being so nice and kind, except for your comments on my cooking skills! Apart from jokes, when I think about our office, it seems that you have always been there! You are a wonderful scientist, and I am waiting to work together on SPH sooner or later!

I have a couple of words for the new generation, Alessandro, Luigi, Luna and Vi-

viana. You have three wonderful years in front of you, and you are lucky enough to be together. Take advantage of this, share the funny and the sad moments and have fun! I am very happy that I met you before leaving, and I am sure I will see you again very soon.

I would like to thank all the people I met during these three years, but it would take too many pages, so I just mention them. Thanks Benni, Marti, Nico, Hossam, Enri, Gullo, Chiara, Alessia, Francesco, Yihan, the Laboratorio di Astronomia crew Alessia and Alice, Cass, Ruobing, Jess, Christophe, Andrew, Paola, Charles, the Kinky Kids, the Misterrs Joe and Andrés, the exoALMA crew, my favourite Australians Caitlyn, Iain and Tom. I am probably forgetting someone!

A deep thanks to my non-academic friends, who have always been on my side during my journey, making jokes about my "work", and being jealous about my trips! Thanks Paolo for the countless beers, Matte for humiliating me at video games, Fabri for sharing pain and joy since Analisi 1, Enri for being the toughest reviewer of my works, Boss for all the funny moments, including the first time you saw the snow, Albi in honor of the room 519 and the Prosecco bottle I destroyed, Sofia for always laughing at my bad jokes, Veronica for being the only one who appreciates Vegemite, Alice for taking care of my dear Enrico and Bea for making our lives noisier and funnier. Without you, everything would be different! Thanks also to the Giulias and Flavia for knowing me since I was born and still putting up with me! By the way, thank all of you for paying my salary during the last three years with your taxes! See you in Cambridge!

I want to express my gratitude to my parents, who always supported me in everything I did, and who trusted me when back in 2015 I told them I wanted to study Physics. Even though you don't clearly understand what I have been doing during the last three years, I assure you that it makes sense!

Last but certainly not least, I want to express my gratitude to Marghe, to whom this thesis is dedicated. You have consistently been my anchor, keeping me grounded while my head wandered through the clouds (which has happened and still happens quite often!). From the very first day in the canteen, you've been by my side on this journey. Your unwavering determination has always inspired me, and your support has been my saviour during the toughest days.

That wraps it up, folks!